Experimental Study on the Influence of ITZ on the Durability of Concrete Made with Different Kinds of Blended Materials

Kai Wu

Promotors: Prof. G. De Schutter, PhD, Prof. H. Shi, PhD
Doctoral thesis submitted in order to obtain the academic degrees of
Doctor of Civil Engineering (Ghent University) and
Doctor of Engineering (Tongji University)

Department of Structural Engineering
Head of Department: Prof. L. Taerwe, PhD
Faculty of Engineering and Architecture

Institute of Environmental Materials
Head of Institute: Prof. H. Shi, PhD
College of Material Science and Engineering

Academic year 2013 - 2014

ISBN 978-90-8578-701-3
NUR 955, 956
Wettelijk depot: D/2014/10.500/47

Acknowledgements

At this point I would like to thank everyone who assisted and supported me in the preparation of this thesis. The financial supports from the Chinese Scholarship Council (CSC) and special research fund of Ghent University are highly appreciated.

First and foremost I would like to express my sincere gratitude to my promoter Prof. Geert De Schutter not only for his continuous supervision and suggestions throughout this investigation, but also for his endless support, tutelage and encouragement, which I needed to fulfill the requirements of this work faraway from university ambience. Much of what I have learned about science and the scientific world I owe to him, and I am eternally grateful.

I would like to extend my sincere gratitude to my co-promoter Prof. Guang Ye for all his excellent supervision, tireless assistance and encouragement. He has walked me through all the stages of the preparation of this thesis. Without his consistent and illuminating instruction, this thesis would not have been possible. I am also grateful for the chance he and Prof. Geert De Schutter gave me to do research in Magnel lab.

I would like to express my sincere gratitude to my co-promoter Prof. Huisheng Shi for the invaluable assistance, advice and encouragement he gave me since the first day I have met him. My heartfelt gratitude goes to him, who led me into the world of scientific research.

Special thanks go to the jury members of this thesis, Prof. Luc Taerwe, Prof. Veerle Boel, Prof. El-Hadj Kadri, for spending their valuable time evaluating this thesis and providing comments.

I would like to thank Prof. Luc Taerwe, Prof. Nele De Belie, Prof. Stijn Matthys and Prof. Robby Caspeele for the discussions and helpful critics during the research related to this thesis. I am also greatly indebted to the professors from Tongji University: Prof. Zhongping Wang, Prof. Zhenghong Yang, Prof. Weimin Ye, Prof. Peiming Wang, Assoc. Prof. Xiaolu Gu, who have helped me a lot in the past six years.

I would like to thank all my colleagues in Magnel, especially, Zhijun Tan, Jianyun Wang, Kunpeng Zheng, Lijie Wang, Ioan Pop, Mathias Maes, Jeroen Dils, Philip Van den Heede, Didier Snoeck, Dr. Eleni Arvaniti, Hugo Eguez Alava, Corina Şoşdean, Hai-Dang Le, Farid Van Der Vurst, Pieterjan Criel, for their support, discussions and friendship throughout the duration of this thesis. Special thanks go to Dr. Yun Gao, Yong Zhang, Yang Lv and Zhuqing Yu for their invaluable help in the experimental work and discussions. All in all, without their continued perseverance, dedication and friendship, the work in this thesis would not have been ready in time to submit.

Special appreciation goes to Nicolas Coppieters, Tommy De Ghein, Bart De Waele, Tom Stulemeijer, Nathan Lampens and Dieter Hillewaere, for their assistance in performing experiments. I would like to thank secretaries Christel Malfait, Marijke Reunes and Viviane Van Gaver I also would like to thank all the people from the lab for creating a pleasant and dynamic atmosphere that made these two years to pass so quickly. I will never forget the memorable time I have spent in Ghent

My sincere appreciation goes to Yun Gao, Yanan Xi, Zhijun Tan and Limin Lu, for their helps in the early period of my study in Ghent. It really means a lot to me. I would like to express my many thanks to all my dear friends in Ghent, which are too many to mention in this list, for their friendship and assistance during the time my lived in Belgium. You are always in my mind.

Last but not least, I would like to thank my parents and my family for their constant, heartfelt, and unconditional support and love throughout my life. I owe this thesis to Linglin Xu for her companion through many ups and downs. I will always be grateful for everything they have done and owe them a debt that never can be repaid.

最后谨以此文献给所有帮助和关心我的人！

Kai Wu 吴凯

May 2014

Table of contents

Chapter 1

Chapter 2

Chapter 3

Chapter 4

Influence of GGBS and LF on the microstructure of ITZ in relation to

Chapter 5

Chapter 7

Glossary

ITZ	Interfacial transition zone
Bulk cement matrix	Region outside aggregate and ITZ
S_{RH}	Water saturation degree
V_{agg}	Aggregate volume fraction
k_{a}	Gas permeability, m^2
I	Water absorption, mm
S_{i}	Initial sorptivity, $mm/s^{1/2}$
S_{s}	Secondary sorptivity, $mm/s^{1/2}$
x_d	Average value of the chloride penetration depth, mm
D_{nssm}	Non-steady state chloride migration coefficient, m^2/s
E_{d}	Dynamic elastic modulus, GPa
D	Chloride diffusion coefficient, m^2/s
erf	Error function
C_{t}	Total chloride concentration, %
C	Free chloride concentration, %
C_{b}	Bound chloride concentration, %
C_{i}	Initial chloride content, %
C_{s}	Surface chloride content ，%
V_{tot}	Total porosity
d_{mean}	Mean pore diameter, nm
d_1、d_2	Critical pore diameter, nm
PC	Portland cement
GGBS	Ground granulated blast-furnace slag
LF	Limestone filler

EDX	Energy Dispersive X-ray spectroscopy
BSE	Backscattered electron
MIP	Mercury intrusion porosimetry
CH	Calcium hydroxide
AFt	Ettringite
AFm	Monosulfoaluminate hydrates

Samenvatting

De overgangszone tussen granulaat en cementmatrix, in de literatuur aangeduid met ITZ (*Interfacial Transition Zone*), heeft een belangrijke invloed op de sterkte en de duurzaamheid van beton. Door zijn gewijzigde microstructuur in vergelijking met de cementmatrix, gekenmerkt door een hogere porositeit, een lagere cementconcentratie, en een preferentiële oriëntatie van portlandietkristallen in beton op basis van Portlandcement, wordt de ITZ vaak beschouwd als een afzonderlijke fase. Methoden ter verbetering van de ITZ zijn cruciaal voor het verbeteren van de betoneigenschappen. Het aanwenden van bijkomende cementachtige materialen, aangeduid met SCM (*Supplementary Cementitious Materials*), gekenmerkt door geringere korrelafmetingen en puzzolane reactiviteit, kan een effectieve en economische oplossing zijn. Bovendien wordt de aanwending van SCM aangemoedigd in het kader van het beperken van de ecologische impact van beton.

Deze thesis presenteert een studie van de relatie tussen de microstructuur van de ITZ en de globale betonperformantie. De microstructurele eigenschappen van de ITZ van beton op basis van Portlandcement en op basis van samengestelde bindmiddelen (met hoogovenslak en kalksteenmeel) werden bestudeerd door middel van beeldanalyse van elektronenmicroscopische opnamen (BSE – *Backscattered Electron Microscopy*), EDX-analyse (*Energy Dispersive X-ray analysis*), en kwikporosimetrie (MIP – *Mercury Intrusion Porosimetry*). De dikte en de volumefractie van de ITZ werden bestudeerd in relatie tot de volumefractie en specifieke oppervlakte van de granulaten in het beton. De invloed van de ITZ op transporteigenschappen (gaspermeabiliteit, waterabsorptie, chloridemigratie en –diffusie), mechanische eigenschappen, en sulfaatweerstand van het beton werd bestudeerd door proefnemingen op mortel en beton met variabele granulaatgehaltes en –afmetingen. Bovendien werd het effect van een verbeterde ITZ door de toepassing van een samengesteld bindmiddel geëvalueerd.

Bij de studie van het effect van de ITZ op de transporteigenschappen van het beton dienen naast de variatie in granulaatvolume en –eigenschappen verschillende factoren beschouwd te worden: (i) dilutie en tortuositeit van de cementmatrix leiden bij een verhoogd granulaatvolume of kleinere korrelafmetingen tot een verlaagde permeabiliteit; (ii) densificatie van de cementmatrix, gerelateerd aan de aanwezigheid van de ITZ, leidt eveneens tot een verlaagde permeabiliteit; (iii) het aanwezige ITZ-volume, en vooral een eventuele percolatie heirvan, verhogen de permeabiliteit. Bovendien kunnen bijkomende factoren zoals uitzweten (*bleeding*) en microscheuren door krimpeffecten een belangrijke invloed hebben op de resulterende transporteigenschappen. Microscheuren geïnduceerd tijdens het drogen van het beton in een oven kunnen bijvoorbeeld in zuivere cementpasta over een grotere afstand doorlopen, terwijl ze in beton met granulaten gestopt kunnen worden door de granulaten, of omheen de granulaten kunnen lopen. De invloed hiervan is belangrijker voor gaspermeabiliteit, gedomineerd door stroming onder druk, dan voor absorptie en migratie. Een gecontroleerde vervaardiging en nabehandeling van de proefstukken bij de experimentele studie van de invloed van de ITZ op de transporteigenschappen van mortel en beton is dan ook van groot belang.

Het relatieve belang van de ITZ voor de globale transporteigenschappen hangt af van de heersende transportmechanismen. Voor de serie vervaardigd op basis van portlandcement en met een water/cement-factor gelijk aan 0.5, wordt een dalende gaspermeabiliteit en een dalende absorptie (initieel en in latere fase) vastgesteld wanneer het relatieve granulaatvolume toeneemt van 0 tot 0.6. De chloridemigratie lijkt een andere afhankelijkheid van het granulaatgehalte te vertonen. Een verhoogd zandgehalte, tot een relatief volume van 0.35, leidt tot een daling van de migratiecoëfficiënt door de densificatie, dilutie en tortuositeit. Voor hogere gehaltes, toenemend van 0.35 tot 0.60, wordt een opmerkelijke stijging van de migratiecoëfficiënt vastgesteld, wegens het toenemend ITZ-volume en percolatie hiervan. De verhouding van massatransport in de ITZ tot deze in de cementmatrix neemt toe met toenemend ITZ-volume en –dikte. De invloed van de ITZ is opmerkelijk zodra deze percoleert. Uit microstructurele analyse blijkt dat het verschil in porositeit tussen ITZ en cement matrix in de buurt van grove granulaatkorrels (16 mm en 20 mm) ongeveer gelijk is in vergelijking met de situatie bij kleinere granulaatkorrels, terwijl echter een relatief hogere porositeit en grotere poriënafmetingen waargenomen kunnen worden aan de onderzijde van grove granulaatkorrels. Deze contrasterende microstructuur, ten gevolge van het positie-effect, is in beelden soms duidelijk waarneembaar. Bijgevolg is het beschouwen van een constante ITZ niet geheel correct bij de analyse van het effect van de ITZ in proefstukken met grove granulaatkorrels.

Kwantitatieve BSE beeldanalyse kan aangewend worden voor de studie van de ontwikkeling van de microstructuur in de ITZ. De kleinste evolutie in het gehalte niet-gehydrateerd cement treedt op in de eerste 5 µm vanaf het granulaatoppervlak, en dit gedurende de gehele meetperiode van 1 dag tot 6 maanden. De verder gelegen zones worden gedomineerd door grotere cementkorrels, die trager hydrateren. Na 1 dag is tussen 15 µm en 20 µm een piek te noteren in het gehalte niet-gehydrateerd cement. Verder dan 25-30 µm van het granulaatoppervlak is de korrelverdeling van het aanwezige cement nagenoeg deze van de cementmatrix. Voor mortels met een granulaatgehalte gelijk aan 55% is één van de meest opmerkelijke vaststellingen de aanwezigheid een kritieke poriëndiameter d_2 groter dan 0.1 µm. Het poriënvolume met kritieke diameter d_2 is groter in proefstukken met fijnere granulaatkorrels, terwijl de kritieke poriëndiameter d_2 groter wordt in proefstukken met grovere granulaatkorrel (gecombineerd 0/2 en 2/5.6). Het totale geïntrudeerde poriënvolume neemt toe met toenemend granulaatgehalte, of met afnemende afmetingen van de granulaatkorrels.

De implementatie van een beperkt gehalte kalksteenmeel (5%) leidt tot een verdichting van de microstructuur van de ITZ en van de cementmatrix, wegens het vuleffect en verbeterde nucleatie. In dit geval leidt de reductie van het volume poriën >0.1 µm tot de grootste reductie in totaal poriënvolume. Een kalksteenmeelgehalte van 10% leidt daarentegen tot een verhoging van de totale porositeit, met een verhoging van het volume poriën tussen 10 nm en 100 nm, doch met een reductie in het volume poriën >0.1 µm. De toevoeging van 35% hoogovenslak reduceert de porositeit op alle afstanden van het granulaatoppervlak, en leidt tot een dichtere microstructuur

zowel in de ITZ als in de cementmatrix. Een hoog slakgehalte (70%) kan de totale porositeit verhogen, doch leidt tot een verfijning van de poriën. In het geval van ternaire mengsels kan in de ITZ een synergetisch effect waargenomen worden tussen kalksteenmeel en hoogovenslak wanneer een gematigd gehalte aan slak (30%) en kalksteenmeel (5%) gecombineerd worden ter vervanging van Portlandcement.

De vervanging van Portlandcement door hoogovenslak en kalksteenmeel leidt niet tot een verhoging van de druksterkte van de zuivere cementpasta. De sterktetoename in mortel en beton zijn vermoedelijk te wijten aan de dichtere microstructuur in de ITZ. Anderzijds lijkt de verbetering inzake water- en ionentransport in mengsels met hoogovencement ook deels te wijten aan de verbeterde microstructuur in de ITZ, doch in meer belangrijke mate aan de densificatie van de cementmatrix.

Bij de studie van de sulfaatweerstand is het effect van de ITZ beter merkbaar wanneer de proefstukken blootgesteld worden aan magnesiumsulfaat. In het geval van natriumsulfaat is het negatieve effect van de ITZ duidelijk merkbaar na een blootstellingsduur van 12 maanden, terwijl de expansie na 6 maanden onafhankelijk lijkt te zijn van de ITZ. In het geval van magnesiumsulfaat is het negatieve effect van de ITZ reeds merkbaar na een blootstellingsduur van 3 maanden, onafhankelijk van het type bindmiddel. Dit is merkelijk vroeger dan in het geval van natriumsulfaat. Op basis van deze proefmethodiek zou een gewenst granulaatgehalte ingeschat kunnen worden teneinde de sulfaatweerstand van het beton te optimaliseren.

Kernwoorden: overgangszone (ITZ), hoogovenslak, kalksteenmeel, transporteigenschappen, sulfaatweerstand, microstructuur, elektronenmicroscopie, beeldanalyse, kwikporosimetrie

Summary

The interfacial transition zone (ITZ) between the aggregate and the bulk cement matrix is well known as one of the key factors that determine the concrete strength and durability. Due to its distinguishable microstructural features, such as higher porosity and lower cement content relative to the bulk cement matrix, preferential orientation of the CH crystals in ordinary Portland cement (OPC) concrete, the ITZ has been accorded as a separate phase during the concrete research. Methods of improving the ITZ are also crucial for enhancing the concrete properties. Among them, applying supplementary cementitious materials (SCMs) with finer particle size or high pozzolanic reactivity could be an effective and economic way. Furthermore, partially substituting SCMs for cement is encouraged due to the environmental benefits, such as less CO_2 emission, energy saving and waste products utilization.

This thesis addresses a study about the ITZ for establishing relationships between the microstructure and the overall performance. The microstructure features of ITZ in concrete made with pure PC and blended binders (slag-GGBS and limestone filler-LF) were determined by quantitative backscattered electron microscopy (BSE) image analysis, energy dispersive X-ray (EDX) analysis and mercury intrusion porosimetry (MIP) measurement. Besides its thickness, the volume fraction of ITZ was directly proportional to the aggregate volume fraction and surface area. Therefore, the role of ITZ on transport properties (gas permeability, water absorption, chloride migration and diffusion), mechanical properties and sulfate attack was evaluated by a comparison among mortars and concretes with systematically varied aggregate volume fraction and size. Moreover, the effect of an enhanced ITZ due to the application of blended binders on the overall performance of concrete has been evaluated.

For the study of the effect of ITZ and its percolation on the transport properties, several other factors should be considered with the variation in aggregate: (i) the dilution and tortuosity of the bulk cement matrix by

applying high aggregate volume fraction or finer aggregate size decreases permeability; (ii) the densification of bulk cement matrix associated with the presence of ITZ decreases permeability; (iii) the presence of ITZ and its percolation increases transport properties. Additionally, other parameters such as bleeding, cracks from drying exert significant effects on the overall transport properties. For example, the microcracks caused by oven-drying in the neat cement paste were able to span a longer distance without any obstruction, while it can be blocked or forced to circumvent the aggregates in concretes. This effect is more important for gas permeability which is dominated by pressure-induced flow than for the sorptivity and migration. To assess the effect of ITZ on the properties of mortars and concretes, a suitable preconditioning procedure, controlled compacting and suitable mixtures are necessary.

The relatively importance of ITZ to the overall transport properties depends on the mechanism governing the transport process. In the series prepared with pure PC and a w/c of 0.5, the gas permeability, initial and secondary sorptivity decreases continuously when the aggregate volume fraction increases from 0 to 0.6. The overall chloride migration coefficient appears to be dependent on the aggregate volume fraction. An increase of the sand volume fraction leads to a decrease of migration coefficient until 0.35 due to the densification, dilution and tortuosity effect. Then a significant increase in the migration coefficient is observed when the aggregate fraction increases from 0.35 to 0.60 due to the increased ITZ and percolation effect. The ratio of mass transport between ITZ and bulk cement matrix increases while ITZ volume fraction and width increases. The influence of ITZ is also becoming remarkable as the adjacent ITZ percolates. From the microstructure analysis, the visual difference in the porosity between the region of ITZ and that of bulk cement matrix at the side of coarse aggregate (16 mm and 20 mm) is fairly similar to the case of smaller particles, while a relatively higher porosity and larger pore size could be easily observed at the bottom of these coarse aggregates. A contrast microstructure is obtained in one image with respect to the position effect. Therefore, a fixed ITZ thickness is not correct for analyzing the ITZ effect in samples containing coarse aggregates.

The quantitative BSE image analysis can be used to infer the origin and the development of ITZ microstructure. The least change in the anhydrous content occurs at the first 5 μm from the interface throughout the whole measurement period from one day to 6 months. The regions further away are dominated by the larger particles, which hydrate slowly and present a peak in the region between about 15 and 20 μm for the anhydrous profiles of one day. The particle size distribution beyond about 25-30 μm from the interface is similar to that of the bulk cement matrix. For the mortars prepared with 55% of aggregate, one of the most important observations is the presence of a critical pores diameter d_2 superior to 0.1 μm. The pore volume with critical diameter d_2 is more remarkable for samples with finer aggregate, while the critical diameter d_2 is becoming larger for samples with coarser aggregates (combined 0/2 mm and 2/5.6 mm). The total intruded pore volume increases with increasing aggregate volume fraction, or with decreasing average aggregate size.

The incorporation of moderate amount of LF (5%) is able to compact the microstructure of both ITZ and bulk matrix by filling effect and nucleation sites effect. In this case, the reduction in the pore (>0.1 μm) volume contributes to the largest decrease in the total pore volume. However, the addition of 10% LF by mass of total binders results in an increase in total porosity and pore (ranged from 10 to 100 nm) volume, but a decrease in the pore (>0.1 μm) volume. The addition of 35% of GGBS reduces the porosity at all distances from the aggregate surface and produces a denser microstructure both in the ITZ and the bulk cement matrix. A high amount of GGBS substitution (70%) can increase total porosity but refine the pore size from coarser (>0.1 μm and 10-100 nm) to finer (<10 nm) size. For the ternary binders, a synergy effect of combined GGBS and LF is observed on the ITZ when moderate amount of GGBS (30%) and LF (5%) substitutes for PC.

Incorporating of GGBS and LF as a partial substitute for PC does not show enhancement in the compressive strength of neat paste. The increase in the strength of the mortars and concretes are presumably due to the densification of the ITZ. On the contrary, the observed improvement of limiting the movement of water and chloride ions for GGBS blended

samples is due in part to the improvement of the microstructure of the ITZ, but more importantly, to the densification of the bulk cement matrix.

With regard to sulfate attack, the effect of ITZ is more notable when the interior structure of samples is exposed to magnesium sulfate. In sodium sulfate attack, the negative effect of ITZ is prominent at the exposure age of 12 months, and the expansion seems to be independent of the ITZ after 6 months of exposure. In magnesium sulfate attack, the negative effect of ITZ starts to be appreciable at the exposure age of 3 months regardless of the binders. This point is much earlier than that in the sodium sulfate attack. According to these findings, one may use a similar approach to estimate the desirable aggregate proportion for improving the sulfate resistance during the mix design.

Keywords: ITZ, slag, limestone filler, transport properties, sulfate attack, microstructure, BSE image analysis, MIP

Chapter 1

Introduction

Concrete is by far the most important civil engineering material in the world. This is largely due to the abundance of raw materials, low relative cost and the versatility and adaptability of concrete in forming various structural shapes and environments. However, the lack of knowledge about the long-performance and the severity of environmental impacts has caused serious problems. Increasingly, repair and replacement costs of structures arising from materials failure have become a substantial portion of the total construction budget. For example, it is estimated that, in industrially developed countries, about 40% of the total resources of the construction industry are being applied to repair and maintenance of existing structures and only 60% to new installations. The escalation in replacement costs of structures and the growing emphasis on the life-cycle cost rather than the first cost are forcing engineers to pay serious attention to durability issues [1]. Moreover, there is a realization that a close relation exists between durability of materials and ecology. Conservation of natural resources by making the construction materials last longer is therefore an ecological step. The use of wrong materials or false design, improper detailing, insufficient quality control and etc., have reduced the service life of the structures or have forced extensive repairs with a huge economic cost [2-4].

The economic and security impact of the durability problem has led to extensive research and has initiated the way to produce better and durable concrete structures. Achieving adequate levels of concrete durability in order to improve the performance and reduce the life cycle costs of concrete structures continues to be a serious problem facing engineers and scientists. All we can do is to promote the developments towards making concrete a high-tech material with enhanced characteristics and durability and lead it to be a more ecological material with a longer life cycle.

Traditionally, investigation on the property of concrete assesses and compares the information in relation to the concrete as a whole. However, in order to more fully understand the behaviour of concrete, information on how the individual constituents within concrete behave is important to consider. Concrete is fundamental a composite material, consisting of the hydraulic binder paste diluted with coarse and fine aggregates, and the interfacial transition zone between them. The properties of aggregate and bulk cement paste have been studied extensively. However, the influence of the ITZ on the overall performance of concrete remains uncertain, particularly in the study of durability. Due to lack of understanding about this weak link in concrete, very little information has been given to improve them. Moreover, there is no simple method of predicting how much improvement can be made in the overall performance of concrete through enhancing the ITZ.

In terms of concrete durability, using additional binder materials are well established and the use of supplementary cementitious materials are now considered commonplace. The utilization of SCMs, particularly the industrial by-products, such as blast furnace slag from the steel industry, fly ash from the coal electricity plants, limestone powder and micronized sand, and/or by merging regular types of materials towards composite cements, is not only beneficial for the improvement of concrete performance, but also for saving energy and reducing CO_2 emission. Previous researches on concrete containing SCMs have been conducted mainly with focus on the overall properties or on the properties of the bulk cement paste. However, very limited information has been given with respect to the improvement of the weak ITZ region.

1.1 Thesis objectives

The ITZ between aggregate and bulk cement matrix in concrete has long been considered as a zone of weakness, both in terms of strength and in terms of the transport of fluids. However relative information is known about the actual relationship between this zone and the overall performance. The objective of this work is to study the ITZ for establishing relationships between the microstructure and overall performance. The role of ITZ on transport properties (gas permeability, water absorption, chloride migration and diffusion), mechanical properties and sulfate attack is evaluated by a comparison among mortars and concretes with systematically varied aggregate volume fraction and size. Moreover, the improvement in the overall performance of concrete with blended binders is mainly due to the enhanced ITZ, or to the densification of the bulk cement matrix is discussed. It will contribute to enhance the understanding of the link between microstructure and durability, and enable more effective controlling the properties of concrete via using SCMs. In specific, the main objective of this thesis can be summarized as follows:

(1) To evaluate the influence of ITZ on different transport coefficients. The relatively importance of ITZ, preconditioning regime, aggregate volume content and size on gas permeability, capillary water absorption and non-steady-state chloride migration will be investigated. Three transport measurements are considered, as their main mechanisms governing the transport process and the effect of ITZ hereon might be different.

(2) To study the effect of different types of SCMs on the microstructure features of ITZ. The influence of GGBS and LF on the porosity and anhydrous distribution within the ITZ will be determined by quantitative BSE image analysis. A systematic MIP experiment on samples with varying aggregate volume fractions and sizes will be performed to provide the direct information for the presence of ITZ.

(3) To determine if/how the improvement of the overall performance of concrete is due to the densification of ITZ. The effects of GGBS and LF on strength development, chloride migration and diffusion, water absorption of mortars and concrete with systematically varied aggregate volume fractions and sizes, hence, varied proportions of ITZ, will be examined. Whether the improvement in the overall properties is mainly due to the enhanced ITZ, or due to the densification of the bulk matrix will be determined.

(4) To study the role of ITZ in sulfate attack from both macro- and micro-level. In sodium sulfate and magnesium sulfate attack, the mass change, expansions of samples with various aggregate volume fractions will be compared. The microstructure features including deterioration patterns and the qualitative element distribution, particular within ITZ, will be determined by SEM and EDX analysis. The relationships between the ITZ and the variation in overall properties will thus be established. From this study, it is to assess to what extent the ITZ are involved in the degradation of concrete under sulfate attack.

1.2 Outline of the thesis

The thesis composes of seven chapters and the appendix. For each chapter, it composes of an introduction, experimental methods applied, results and discussion, and conclusions. Owing to the fact that for each chapter, a background and literature review regarding that study, and the aim is given. The literature review in chapter 2 has been presented briefly to avoid repetitions. Besides the introduction (chapter 1), literature review (chapter 2) and the conclusive remarks (chapter 7), the main scopes of the other five chapters can be summarized as follows:

Chapter 3 presents the results of the effect of ITZ, preconditioning regime on the gas permeability, capillary water absorption and chloride migration. The effects of aggregate size on the microstructure of ITZ due to bleeding are evaluated by performing the BSE image analysis at the top, bottom and side positions of coarse aggregates. The others parameters associated with the presence of ITZ, such as dilution, tortuosity and densification of bulk cement matrix are also discussed.

Chapter 4 shows the investigation of the effect of GGBS and LF on the microstructure of ITZ in relation to the macro-properties of the paste, mortar and concrete. Correlating the mechanical properties, chloride migration coefficients and water sorptivities with the variations in the microstructure, the relatively importance of the improved ITZ to the enhancement of the overall properties are determined.

Chapter 5 deals with the chloride diffusivity in various blended systems. The chloride resistance of samples with varying aggregate volume fractions and sizes are determined. The relation between free chloride and bound chloride is estimated in relation to the aggregate volume fraction and size.

Chapter 6 is focus on the role of ITZ in the process of degradation under sulfate attack. This is obtained by a comparison of resistance to sulfate among samples prepared with different aggregate volume fractions and sizes. The different degradation behavior of blended binders under sodium sulfate attack and magnesium sulfate attack is discussed. This chapter includes systematical macroscopic and microscopic measurements. The information for the onset of negative ITZ effect on the sulfate resistance is presented.

Chapter 2

Literature review

The primary phases in cement-based materials are aggregate and bulk cement paste. Further experimental studies on the ITZ suggested that the interfacial transition zone has a distinguishable microstructure which differs from that of bulk cement matrix. Hence, it is expected that ITZ has a strong influence on the overall performance of concrete materials. By improving the properties of the ITZ, for example by adding admixtures, one can improve the properties of concrete. Thus, further experimental studies on ITZ should enable the scientific design and the development of high performance concrete mixes.

2.1 Formation of the ITZ

The so-called wall effect has been extensively presented to explain the special features of the ITZ. The difference in size scale between cement grains and aggregate particles means that each aggregate particle is a mini wall which disrupts the packing of the cement grains. The result is that a zone closest to the aggregate contains predominately small grains and has a significantly higher porosity, while larger grains are found further out [5]. A complementary explanation has been proposed [6]: During casting, the spatial arrangement of anhydrous grains becomes looser in the vicinity of aggregate particles. Consequently, in fresh concrete the porosity and the w/c ratio increase from the bulk to the surface of aggregate particles. During the vibration of concrete and before setting, micro-bleeding leads to an accumulation of water under the aggregate. The fresh cement paste which surrounds the aggregate grains exhibits a gradient of water and a complementary gradient of anhydrous cement. Due to the second effect, certain heterogeneity of the gradient around the particles may be foreseen.

2.2 Microstructure features of the ITZ

According to the introduction above, the modelled ITZ is not a single shell with uniform property, but has gradients extending out to its width, which depends on the initial mixture proportions and evolves with hydration. However, the real ITZ microstructure is spatially variable, its width and phase distribution are not exhibited uniformly around each and every aggregate particle. Although its local property is highly variable, its average property taken over many locations shows well-defined gradients. The mobility of calcium ions in solution results in preferential nucleation and growth of calcium hydroxide on the aggregate surface, so that the porosity of the ITZ in many locations may be very low due to the presence of these deposits. Bleeding effects may also increase porosity in other locations. In normal concrete or mortar, the ITZ is generally believed to be characterized by a higher concentration of calcium hydroxide crystals and an increased porosity relative to the matrix paste [7-10].

The microstructure of ITZ has been presented in detail in Ref. [11-13] as follows: (i) at the immediate vicinity of the aggregate surface is a duplex film of $Ca(OH)_2$ topped by or ocassionally intermixed with C-S-H. Sometimes this duplex film occurs in close intimacy with the aggregate. At early ages of hydration, this duplex film is relatively porous. With increase in age, the film modifies into a dense layer, sometimes bonding with the surrounding cement paste. The side of the film in contact with the aggregate is a layer of crystalline $Ca(OH)_2$ of 0.5 μm thick. Following this layer is a thin deposit of C-S-H gel, in the form of short fiber, which extends into the cement paste. The total extend of the duplex film is 1.0μm. (ii) Next to the duplex film is the ITZ. This region is relatively larger with a thickness of around 50 μm, including the duplex film. Generally, this zone contains a large number of hollow-shell hydration grains, and enriched in larger $Ca(OH)_2$ crystals and ettringite (AFt). The occurrence of a large number of hollow-shell hydration grains suggested that cement hydration is accelerated in the ITZ. This is presumable because of an availability of excess water at the vicinity of the aggregate particles. Moreover, since the growth of large crystals of calcium hydroxide and ettringite is enhanced in a more open system, the occurrence of such large crystals at the ITZ is an indication of the existence of higher porosity.

Zimbelmann [14] performed a combination of tensile bond strength tests and SEM studies on debonded paste-rock composites at various ages. Based on the work, a model of the microstructure of the ITZ was also presented [14-15]: (i) Directly at the surface of the aggregate is a dense layer of 2-3μm thick and composed essentially of $Ca(OH)_2$ covering a network of ettringite crystals. After about 12 hours the $Ca(OH)_2$ forms a continuous closed layer which referred to as the contact layer. (ii) Directly adjacent to the contact layer is a zone of the intermediate layer with a thickness of 5-10 μm. This layer consisted for the most part of needle-shaped ettringite crystals, leaf- or flake-like $Ca(OH)_2$, sporadic needle-shaped C-S-H and hexagonal $Ca(OH)_2$ crystals aligned steeply with respect to the aggregate surface. (iii) The ITZ with a thickness of 10 μm which is characterized by dense paste which merged into the bulk cement paste. Zimbelmann [14] attributed the origin of the ITZ to the formation of thin films of water on cement grains and around large aggregate particles in fresh concrete. A schematic representation of the ITZ is shown in Fig. 2.1.

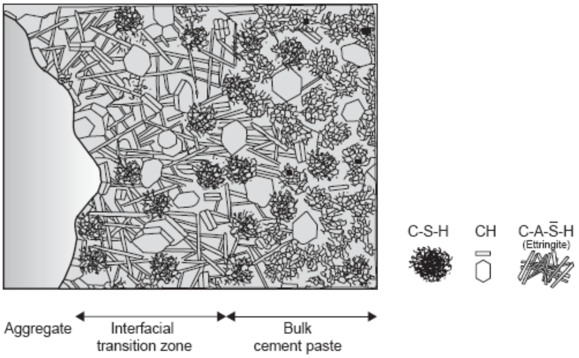

Fig. 2.1 Diagrammatic representation of the ITZ [1].

The ITZ is heterogeneous on the same scale as the cement grains. Since there is no clear-cut transition from ITZ to the bulk cement matrix, the distributions of different phases within this region are more meaningful for the study. Therefore, several researches have been carried out with respect to the phase distribution in the ITZ.

Porosity

Because of the locally higher w/c ratio and wall effect, the rate and characteristics of hydration in the vicinity of aggregate differ from that of the bulk paste, and result in higher porosity in this area. The higher porosity in the ITZ can also be attributed to the micro-bleeding under coarse aggregate particles as shown in Fig. 2.2. The porosity in the ITZ also evolves with the hydration time. Scrivener et al. [5] found that on the mixing the porosity adjacent to the interface is higher than that in the bulk. After the first day this difference is reduced and the gradient is less steep. At greater ages the porosity in the ITZ reduces by about the same amount as it is reduced in the bulk. As there is much less anhydrous material remaining in the ITZ, this reduction must be attributed to the deposition of hydrates from the migration of ions from the reaction of cement further from the interface. Besides, the pores in this ITZ were generally larger than those in bulk material. Thus it seems quite plausible that these ITZ pores could be the major reason for the observed differences in porosity features between paste and concrete specimens.

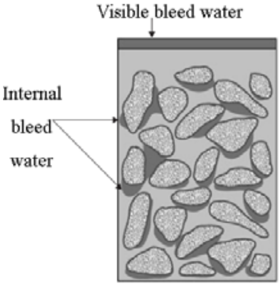

Fig. 2.2 Diagrammatic representation of bleeding [1].

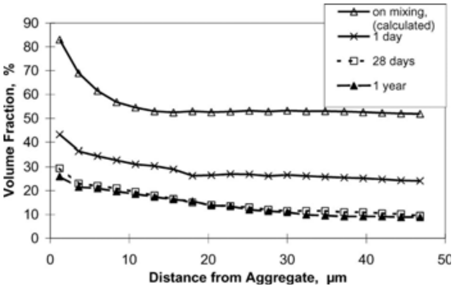

Fig. 2.3 Average porosity in the ITZ at various ages [5].

Anhydrous

The microstructure of the ITZ is determined by the packing of the anhydrous cement grains against the much larger aggregate particles. The well known ‘wall effect’ leads to a depletion of anhydrous cement in the ITZ, approaching zero at the aggregate surface. Previous research indicated that a deficit in anhydrous grains is only significant in a region of about 15 μm adjacent to the aggregate, similar to the size of the average cement grain [5].

The small grains quickly hydrate completely, while the larger grains have a core of unhydrated cement. At any given time the thickness of each grain that has reacted will be the roughly the same, so the unhydrated fraction will be greater for larger grains [16].

C-S-H and ettringite

In the ref. [5], there is a significant redistribution of the C-S-H between the ITZ and the bulk cement matrix during the first day. The C-S-H content was relatively low in the region of ITZ. After the first day, there is little further change over 1 year. These observations confirmed the lower mobility of silica (needed to form C-S-H) compared to calcium [17-18].

Monteiro and Mehta [19] measured an increase in ettringite in the ITZ. The small crystals of ettringite can not be easily resolved in BSE images, so it has not been possible to confirm this measurement in real concretes. The ions forming ettringite are highly mobile in cement pastes, as witnessed by the recrystallisation of ettringite in pores and voids in mature concretes. Therefore an increased concentration of this phase in the ITZ would be expected.

Calcium hydroxide

Large crystals of CH were sometimes formed adjacent to the aggregate particles, and tended to predominate on fracture surfaces because of their cleavage, their orientation relative to the aggregate surface varied considerably [20]. The packing of cement grains leaves an initially more porous zone around the aggregate. This favors the deposition of more calcium hydroxide in this region as can be seen from the experimental results shown in Fig. 2.4. In addition to these, particularly large crystals or extensive deposits of CH were found in places where local bleeding was considered to have been likely. The other characterizations of the formed CH also include the development of large well-formed CH crystals near the surface of aggregate with their c-axes roughly parallel to it, development of stacked-platelet secondary CH in open spaces, and hydration leading to the presence of hollow-shell hydration grain in the ITZ.

As the quantity of anhydrous material in the ITZ is low, most of this CH must form from calcium ions coming from the reaction of anhydrous cement outside the ITZ. This would result in a reduction in the calcium ions available in the bulk cement matrix.

Fig. 2.4 SEM of the calcium hydroxide crystals in the ITZ [1].

Thickness of the ITZ

The thickness of the ITZ is usually taken to be the distance from the surface of the aggregate where the cement paste has a distinctive microstructure. It is variable depending on the type of aggregate and cement used, the w/c ratio, the age of the composite, and the method used to estimate it. Scrivener et al [10, 21-22] have proved that the thickness of the ITZ affected by the packing of the cement grains by analysis of backscatter electron (BSE) images.

Since there is no clear-cut transition from ITZ to matrix, the changes are progressive and are most significant in the first 15-20μm. Therefore in good quality concretes the ITZ is not apparent as distinct band of higher porosity, the reported thickness of the ITZ varies, but is typically in the range of 15-50 μm [5, 23-24]. In order to compare ITZ thickness of the different concrete mixtures, Leemann et al. [25] proposed that the ITZ thickness is defined as the zone close to the aggregates where the current porosity exceeds the average of the bulk paste by 15%.

Khokhrin [26] reported a 60 μm thickness of ITZ between lightweight aggregate and paste by using SEM. Bentur and Cohen [27] found that the thickness of ITZ is around 50 μm. Winslow et al [28] proposed a value in the range of 15 to 20 μm as measured by MIP. Mehta and Monteiro [29] suggested a range of 10 to 50 μm for the thickness of ITZ. Based on the investigation of roughness number, Zanpini et al. [30] proposed a range of 96 to 128 μm. However, regardless of the actual value of this, it is difficult to measure directly the mechanical properties of ITZ.

Methods for the ITZ microstructure investigation

The use of X-ray diffraction to detect the preferential orientation of calcium hydroxide in ITZ was first proposed by Hadley [31], and modified and developed by Grandet and Ollivier [32]. Yuan and Odler [33] studied CaO to SiO_2 molar ratio in the ITZ by microprobe analysis. In the vicinity of aggregate, C/S is about 6 at about 120 μm from the aggregate surface. The C/S of C-S-H gel found in ITZ is in the range of 3.5 to 4, instead of 1.5 to 2 in the bulk cement paste.

The porosity of ITZ is mainly studied using two techniques: SEM and MIP. Scrivener et al. [21] are pioneers in applying quantitative SEM analysis to measure the porosity of the ITZ. The results showed that the degree of porosity in high near the surface of the aggregate and drops to a relatively constant level after about 30 μm from the aggregate surface. Scrivener and Gartner [22] further used the SEM technique to measure variation in the amount of porosity, CH, and anhydrous as a function of the distance from the aggregate surface. It was found that the porosity increases in the paste close to the surface of the aggregate, while the content of anhydrous decreases. The similar method was also successfully performed in the study of ITZ in other ref. [25, 34-39].

It is known that MIP measures the volume of pores of ITZ only if the ITZ porous system forms an interconnected cluster through the specimen. Winslow et al. [28] studied the percolation of ITZ by MIP, and interpreted the results with an aid of a hard core/soft shell computer model. A similar work based on combining MIP data and a simulated result of percolation of a three-dimensional mortar model, has been presented by Bourdette et al. [40]. These researches on percolation suggested that the percolation may increase porosity of concrete and mortar. There were also studies indicated the presence of ITZ by performing MIP on mortar and pastes, although these experiments were not specially designed for the study of ITZ [41-43].

Scrivener and Nemati [10] studied the porosity of concrete by intruding Wood's metal into a concrete sample with a pressure of 1500 psi. This allows wood's metal to penetrate pore down to 0.08 μm. This investigation combined with the SEM images indicated that the pores in ITZ are interconnected and permeated preferentially, rather than the bulk paste. But it must be borne in mind that the samples treated with wood's metal were dried prior to the experiment and heated to 80℃, which could have led to microcracking, linking pores which were not connected in the original state.

Nanoindentation was also used to determine the difference in the microhardness between the ITZ and the region further away from the aggregate [44-45]. By studying the microhardness, Duan et al. [44] found that microhardness of ITZ varies with the type of mineral admixture. With the addition of slag, silica fume and metakaolin, microhardness of ITZ increases gradually and the microhardness at later days is higher than that at early days.

In summary, ITZ, which is different from the bulk paste from the view of microstructure, could be one of the key factors that influence concrete strength and durability and its characterization has been a crucial parameter in concrete technology.

2.3 Effect of ITZ on the mechanical properties

The ITZ is the weakest constituent in concrete, and therefore, it exerts a great influence on the mechanical behavior of concrete than can be expected based on its size [36, 46-56]. It is because of the presence of ITZ that concrete fails at a considerably lower stress level than the strength of either of the other two constituents. The microcracks formed at the ITZ are the cause of pre-peak nonlinear behavior and the transition form liner to nonlinear response of a cementitious material under loading is primarily governed by the extent of available microcracks of the ITZ [57-59].

From a mechanical property point of view, the extent of microcracks in ITZ is governed by the degree of strain mismatch between aggregate and bulk cement paste under the applied loading [60]. For a stress equilibrium condition, the strain differences among aggregate, bulk cement paste and ITZ can be related to the discrepancy of modulus of elasticity and shear modulus. This also introduces the stress concentration phenomenon between two constituents with different moduli [59]. In fact, the ITZ serves as a bridge between aggregate particle and bulk cement paste. Even when the individual components are of high stiffness, the stiffness of the concrete may be low because of the broken bridge's effect that does not permit stress transfer [15].

The presence of easily cleavable and highly soluble CH crystals and the coarser porosity can affect the mechanical performance of the ITZ [59]. The plate-like CH crystals tend to form in oriented layers with the c-axis perpendicular to the aggregate surface. Thus, the microcracks are formed easily in the direction perpendicular to the c-axis. Besides, the large CH crystals possess less adhesion capacity, not only because of the lower surface area and correspondingly weaker van der waals forces of attraction, but also because they serve as preferred cleavage sites owing to their oriented structure. In addition to the oriented CH crystals, the larger volume of capillary voids and the presence of microcracks in the ITZ even before the concrete is subjected to external stresses are responsible for the lower stiffness and strength of the ITZ compared to the bulk paste in the concrete and mortar.

In researches [58, 61-63] carried out to determine the influence of aggregate, matrix and ITZ properties on the tensile and compressive strengths of concrete, it was found that the interfacial bond was the deciding factor for the tensile strength and played little role on the compressive strength. The influence of the type and the surface texture of the aggregate, on the compressive strength of concrete, however, become paramount as the quality of the mortar is improved.

It is not until recent years that progress and improved availability of advanced instruments and techniques, such as depth-sensing micro/nanoindentation, have made it possible to study mechanical properties of various micro/nanoscale features in cement-based materials [64-65]. Microindentation testing was firstly used to characterize gradients in mechanical properties to determine the mechanical characteristics of microsize zones in various cement based composites [66-67]. By using the nanoindentation technique, better representation of heterogeneous features exhibited by cementitious materials can be obtained [68]. Until now, few research works were focused on the studying of the ITZ between a rigid inclusion and matrix [64, 66, 69]. Additionally, microhardness testing can also contribute to characterization of the properties of the ITZ relative to the bulk cement paste matrix and also provide one means of estimating the thickness of the ITZ [67, 70].

2.4 Effect of ITZ on the durability

From a theoretical point of view, the higher porosity of the ITZ should facilitate the ingress of external aggressive agents and favor the development of deleterious chemical reactions. Furthermore, the higher CH concentration usually found in the ITZ should also increase the potential risk of leaching caused by dissolution of CH, and therefore detrimentally affects the resistance of concrete to ion penetration [71].

2.4.1 Effect of ITZ on the transport properties

2.4.1.1 General information

The transport properties of cement-based materials involve a great number of reactions and transport processes in the pore and void system of the composites. For this reason, an evaluation of the transport properties should provide a valuable indication of the durability of concrete. The main parameters affecting the transport properties are summarized in Table 2.1 [72]. Most aggregates used in concrete are dense compared with the paste and so are assumed to allow negligible transport through them. In addition to these, enhanced the knowledge of the structure and properties of individual components of concrete and the relationship between these components can be used to control the properties of concrete.

Table 2.1 parameters related to transport properties [72]

<table>
<tr><th colspan="3">Solid components</th></tr>
<tr><td>Paste</td><td>ITZ</td><td>Solid Inclusion</td></tr>
<tr><td>Chemical and mineralogical composition</td><td>Mineralogy</td><td>Mineralogy</td></tr>
<tr><td>Pore structure</td><td>Texture</td><td>Pore structure</td></tr>
<tr><td>Microcracks</td><td>Porosity</td><td>(permeability and diffusion)</td></tr>
<tr><th colspan="3">Transmitted components</th></tr>
<tr><td colspan="3">Gas Vapors Liquid Ions, …</td></tr>
<tr><th colspan="3">Environment</th></tr>
<tr><td colspan="3">Temperature Humidity</td></tr>
<tr><th colspan="3">Loading conditions</th></tr>
<tr><td>Confinement</td><td>Shear stresses</td><td>Pore pressures</td></tr>
<tr><td>Curing</td><td></td><td></td></tr>
</table>

Introducing inert aggregate to the cement paste resulted in higher diffusivities and permeabilities even though the aggregate is relatively impenetrable compared with the cement paste. This is in agreement with the general observation that the permeability of concrete is one to two orders of magnitude higher than that of neat cement paste [73]. This suggests that the differences between the transport coefficients of the paste and mortar are due to the different pore structure developed by the presence of aggregate.

One of the fundamental assumptions of the conventional picture of the effects of the ITZ is that the movement of water and ions through the ITZ paste is much more rapid than through the bulk cement paste. More specifically, it is usually considered that when aggregates are sufficiently closely-spaced that the adjacent ITZs percolates, namely overlap in space, fluid and ion transport is significantly enhanced [74].

2.4.1.2 Model paste-aggregate composites

When studying the effect of the ITZ on the transport properties, it is of essential importance to clearly separate between the pure effect of the ITZ and the effect of other competing parameters (in Fig. 2.5 and Fig. 2.6), such as reduction in the paste fraction and total porosity (the dilution effect), the increase in the effective transport path length (the tortuosity effect), and the presence of denser bulk cement matrix as a result of water conservation in the microstructure, which may have been changed at the same time as the presence of more ITZ [75].

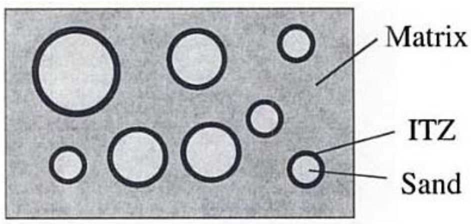

Fig. 2.5 Three-phase mortar model and dilution effect [75].

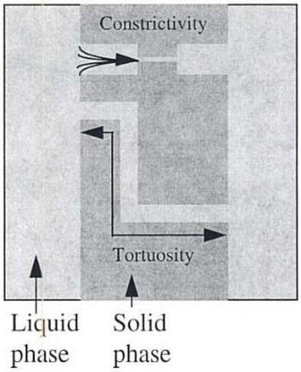

Fig. 2.6 Schematic of tortuosity and constrictivity [75].

Given the inherent difficulties of calculating the quantity of ITZ, some researchers have tested model paste-aggregate composites where the complex and random structure of concrete is approximated by simpler geometries [24, 76-78].

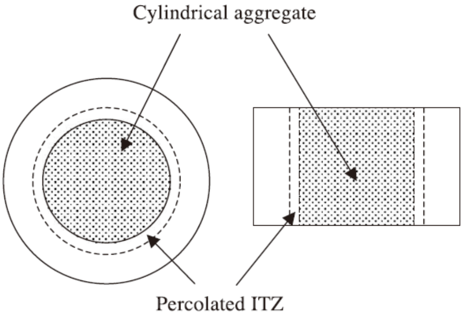

Fig. 2.7 Diagrammatic representation of percolated ITZ as a layer around the cylindrical aggregate [24, 78].

Recent studies by Breton et al. [79] and by Bourdette [40] indicate that the effective diffusion coefficient of chloride ions is 6 to 12 times greater in the ITZ than in the bulk paste. Working with a twin geometrical model and summing a 20 μm thickness of the ITZ, Ping et al. [77] have also calculated that the conductivity of the ITZ should be 10 times greater than that of the bulk paste. Yang et al. [24, 78] investigated the chloride migration coefficient of the percolated ITZ by using model concretes with cylindrical aggregates of the same height as the specimen (see an example in Fig. 2.7). The researchers also tested the chloride migration coefficient of mortar, using the specimens with different fine aggregate volume fractions, to assess the dilution, tortuosity and ITZ effects of aggregate in the cement-based composites [80]. Results showed that the approximate percolated ITZ migration coefficient is 40.6, 35.5, and 37.8 times of the altered migration coefficient of matrix mortar for the w/c ratio of 0.35, 0.45, and 0.55, and is 2.83, 1.76 and 1.55 times of the matrix migration coefficient for the ITZ with the thickness of 20, 40 and 50 μm, respectively.

While such studies reveal that the ITZ is indeed more penetrable than the bulk paste, they offer limited information on the overall performance of real mortars and concretes, where the microstructure is much more complicated and random. Available studies of real mortars and concrete samples where the aggregate content is systematically increased do not, however, provide a clear answer as to whether percolated ITZ result in higher transport properties [23, 71, 73, 81-82].

2.4.1.3 Percolation of the ITZ

The percolation theory deals with disordered multiphase media in which the disorder is characterized by the degree of connectivity of the phases. The microstructure of cement-based materials provides numerous examples of percolation phenomena, such as percolation of the CSH and CH phases, and percolation of the capillary pores [83]. In particular, the percolation of pores in the ITZ is of great interest for studying the transport properties in cement-based materials [9-10, 28, 84-85].

The ITZ has a definite effect on the pore size distribution due to its considerably higher porosity and the larger pore size. The effects of the ITZ on the transport properties should depend on the aggregate content. When the ITZ are isolated by a less porous bulk paste, the rate of transport should be significantly lower than if the ITZ overlap, which would create a continuous path of low resistance to penetration [73]. As evidence of such percolation, some researchers observed that the MIP results for mortar depend on the sand content, with the intrusion curves for sand contents higher than some critical value showing a disproportionate increase in the volume of larger pores [10, 28, 84].

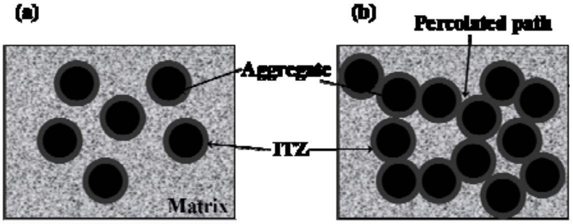

Fig. 2.8 Schematic of non-percolated ITZ (a) and percolated ITZ (b) in cement mortars [23].

A hard core-soft shell model has been proposed to simulate the overlap and percolation of the ITZ by Bentz [84]. ITZ was modeled as soft shells of a constant thickness surrounding each hard core aggregate particle. The ITZ may overlap one another and also may intersect the aggregate particles. The computer experiment results showed that both ITZ thickness and aggregate shape have significant effects on the percolation characteristics of the system. In coarsening the aggregate size, one finds that a greater volume of aggregate, but a smaller volume of ITZ pastes is needed to percolate the system. Based on a quantitative formula, Sun et al. [86] also indicate that the influencing order of three factors on the overlapping degree between neighboring ITZ in turn was the ITZ thickness, aggregate volume faction and the maximum aggregate diameter.

Whether or not ITZ percolation influences the transport property depends on the contrast between the ITZ property and that of the bulk matrix [23, 73, 87]. According to the results provided by Zheng et al. [88], the aggregate volume fraction, w/c ratio, and curing age are the most significant parameters, while the ITZ width, aggregate size and aggregate gradation have less influence on diffusivity. Additionally, Zheng et al. [88] indicated that the influence of ITZ on the overall diffusivity is not significant, despite it being on average more porous and itself having a diffusivity that is several times that of the bulk paste. A similar result provided by Wong et al. [89] also shows that the ITZ plays a more important role in fluid permeability than diffusivity. According to this theory, because permeability is a strong function of the pore size and the ITZ contains pores much larger than those in the bulk paste, the contrast in permeability between the ITZ and bulk paste would be very high. The contrast in diffusivity, however, is lower because diffusivity is only weakly dependent on pore size.

2.4.1.4 Theoretical calculation

Assumed that the ITZ was divided into a series of homogeneous concentric shell elements of equal thickness, some models were proposed to simulate the transport process in the ITZ. Researchers at National Institute of Standards and Technology (NIST) have developed numerical models to describe the microstructure of cement-based materials using digital image analysis techniques [90-91]. The models have applied to determine material properties and electrical conductivity of ITZ [87, 92-94]. Results obtained by Garboczi et al. [87] have also underlined the importance of the ration of conductivity $C_{\mathrm{ITZ}}/C_{\mathrm{paste}}$ on the overall transport properties. Using a similar approach, Bourdette et al. [40] studied the influence of the ITZ on the diffusivity of tritiated water in mortar samples. Results obtained by both models have clearly emphasized the fact that the concrete transport properties are influenced by the connectivity of ITZ and the excess in tortuosity introduced by increasing aggregate content in the mixture. Winslow et al. [28] investigated the percolation characteristics of cement-based materials ITZ by using a hard core/soft shell computer model. According to the results of Winslow et al. [28], Shane et al. [23] pointed out that the ITZ has become percolated between the sand volume fractions of 0.45 and 0.49, but did not affect the global electrical conductivity of mortar. Garboczi and Bentz [93] pointed out that the ITZ is modeled as a uniform property region of some conductivity, this conductivity depends on what thickness is chosen to represent the actual porosity gradient. Although some modeling works seems to be in agreement with experimental data, it is only strictly valid within the assumptions used and is not expected to be generally applicable. The model contains several empirical relationships and requires calibration with experimental data.

2.4.1.5 Conflicts results with respect to the ITZ effect

The microstructure of ITZ should facilitate the ingress of external aggressive agents and favor the development of deleterious chemical reactions in this region. However, available experimental studies on mortars and concretes, where the aggregate content is systematically increased to change the ITZ volume fraction, do not provide a clear answer as to whether the ITZ has a significant effect on the overall transport properties [88-89]. Some studies have found that the ITZ has a significant influence on the chloride diffusivity [73, 95], while results from others seem to suggest otherwise [71, 81-82, 88]. For example, Zheng et al. [88] indicated that the influence of ITZ on the overall diffusivity is not significant, despite it being on average more porous and itself having a diffusivity that is several times that of the bulk paste. According to the report of Hornain et al. [81], the diffusion coefficients of the various mixtures were apparently more influenced by the presence of solid inclusions that increased pore structure tortuosity than by the presence of ITZ. These result might be conflicted with the results of models of Winslow et al. [28] and that of Bourdette et al. [40]. In addition, the model proposed by Sun et al. [96] predicts that the chloride diffusivity of concrete composite materials depends on the chloride diffusion coefficient of the matrix and ITZ, volume fraction of the aggregate and ITZ. Different studies and the main findings are summarized in Table 2.2 to highlight this inconsistency.

It is interesting to note that these studies collectively involve a range of transport properties, sample type, maturity and moisture condition. However, the significance of the ITZ with regard to transport properties remains uncertain. These conflicting results from different sources underscore the difficulty in isolating the ITZ effect through experimental studies.

Table 2.2 Summary of the experimental studies on the effect of ITZ on the transport properties.

Transport properties	Main conclusions	Reference
Oil permeability	Permeability of concrete was about 100 times greater than for cement pastes, probably owing to presence of ITZ.	Watson and Oyeka [97]
Water permeability	Permeability increased with increasing sand content.	Nyame [98]
Chloride diffusivity, Water permeability	The diffusivity and permeability of mortars were higher than that of cement pastes; The ITZ percolation occurred between 35 and 45% sand volume fraction for the 0.4 w/c mortars.	Halamickova et al. [73]
Chloride diffusivity	Chloride diffusivity decreased with addition of sand and limestone filler, indicating that the presence of ITZ has only limited effect on diffusion of chlorides.	Hornain et al. [81]
Oxygen diffusivity, oxygen permeability, sorptivity, electrical conductivity, chloride diffusivity, carbonation resistance.	Transport resistance steadily decreased as cement content increased for all cases, equates to decreasing aggregate volume fraction.	Buenfeld and Okundi [82]
Chloride diffusivity	The increased tortuosity of the paste matrix owing to aggregate inclusion appeared to have a stronger influence than the interconnection of ITZ.	Delagrave et al. [71]

Electrical conductivity using impedance spectroscopy	ITZ did not affect the global electrical conductivity of mortar. However, significant differences in the conductivities of the ITZ and the bulk paste were presented.	Shane et al. [23]
Steady and non-steady-state chloride diffusivity	Chloride diffusivity of PC mortar increased with sand content.	Asbridge et al. [95]
Electrical conductivity	Results indicated the existence of a percolating pathway through the ITZ when the aggregate exceeded 60% vol. fraction.	Princigallo et al. [99]
Chloride ion binding and diffusion	The results indicated that the aggregates modify the pore structure of the cement paste and transport properties.	Care [100]
Air permeability, freeze-thaw/salt scaling resistance test, carbonation	As the proportion of larger size aggregate increased, the local porosity at the ITZ increases and the overall durability decreased.	Basheer et al. [101]
Oxygen diffusivity, oxygen permeability, water sorptivity	Permeability was far more sensitivity to the presence of microcracking and changes in total porosity. No critical threshold sand content linked to the ITZ percolation was found.	Wong et al. [89]
Mechanical proeprties, Chloride migration	The traditional notions of the adverse influence of the ITZ on the properties of conventional concretes may not be accurate.	Rangaraju et al. [74]
Water absorption	Samples containing higher volumes of cement paste absorbed more water. When the results are	Castro J. et al. [102]

	normalized by the volume of cement paste, the sample containing lower volumes of cement paste absorbed more water.	
Gas permeability	The gas permeability of mortars was higher than that of the cement paste. The permeability decreased with increasing ITZ volume content (or finer sand). This effect was all the more important as the aggregate volume content was low.	Care S. and Derkx F. [41]
Gas permeability	The gas permeability decreased with increasing fine aggregate content, due to the dilution and tortuosity effects, while the ITZ was less porous in the case of finer aggregates.	A.A. Hamami et al. [43]

2.4.2 Effect of ITZ on sulfate attack

The above discussion is mainly based on the physical principle. However, the durability of concrete is a complex phenomenon, where chemical and physical aspects should be considered simultaneously. Except for these physical properties, some chemical reactions are still of interest for the ITZ investigation.

The sulfate attack on Portland cement is a phenomenon involving several stages. According to the dominating mechanism in each stage, it can be divided into three stages: induction, gypsum formation and ettringite formation. Gypsum is formed from CH precipitated around aggregate during cement hydration. The importance of ITZ with respect to the chemical aggression of concrete is obvious when one considers the relations existing between porosity, permeability, chemical composition and the sulfate attack. For Portland cement, several reports have observed that gypsum is localized preferably at the ITZ leading to the increase of cracking in this zone and the consequent decrease of modulus, leading to expansion and cracking [103]. Irassar et al. [104] emphasized that the deposition of ettringite and gypsum around the aggregate indicates the vulnerability of the ITZ to chemical attack. Bonen [105] had also studied the replacement of CH by gypsum in the ITZ and they found thick deposits of gypsum up to 50 μm precipitating in this zone. These observations showed the important role of the ITZ that would be absent if the investigations was led on paste samples [106]. However, research specifically designed to study the effects of ITZ during sulfate attack is still limited.

2.5 Modification of the ITZ

Modification of the ITZ microstructure can be achieved by altering the spatial arrangement of the small grains, densifying the microstructure and reducing the micro-bleeding around aggregate particles. This can be generally done by using a finer supplementary cementitious material, superplasticizer and advanced mixing procedure [6, 21, 71, 107].

2.5.1 Effect of SCMs

Quantitative image analysis clearly showed that the ITZ is caused by the disruption of packing the anhydrous cement grains in this region. Thus the ITZ may be modified by changing the particle size distribution of the cementitious materials. Pozzolanic reaction between mineral admixtures and the CH deposited within ITZ would produce more finely dispersed products, thus, densifying the microstructure.

The published results have demonstrated that the mineral additions can produce a significant reduction in the thickness of the ITZ, besides the densification of such region, contributing to an improvement of the properties related to mechanical strength and durability [108-112]. Among them, silica fume is considered a very effective mineral addition in reducing the thickness of ITZ. The using of silica fume is effective in densifying the ITZ structure due to relatively fine particle size, and nucleation site effect for crystallization of hydration products and leads to the formation of small crystals of CH and reduction of its preferred orientation. Moreover, the pozzolanic reaction might reduce the content of calcium hydroxide in the ITZ and increase density of this layer [48, 52-53, 60, 113-114].

According to Bui et al. [115], partially replacement of cement with Rice Husk Ash (RHA), which has a similar chemical composition with that of silica fume but is not an ultra-fine material like SF, can also densify the ITZ and cause the development of a relatively homogeneous microstructure of ITZ. Asbridge et al. [95] also indicated that the use of metakaolin reduced the capillary porosity of the bulk paste and the ITZ due to the metakaolin-lime pozzolanic reaction, which result in the formation of silicate chains with higher molecular weight than those characteristic of the C-S-H phase of hydrated Portland cement. The results in ref. [52] showed that the microstructure of ITZ can be modified sufficiently by controlling the chemical components of the additives, even the use of fly ash consisted of relatively high CaO and low SiO_2. With the addition of slag, silica fume and metakaolin, the microhardness of ITZ increases gradually and the microhardness at later days is higher than that at early days. It indicates that the microstructure of ITZ has been optimized with increasing curing ages by mineral admixtures [44].

In general, limestone filler (LF) improves the hydration rate of cement compounds and consequently increases strength at early ages [116]. From a chemical point of view, LF does not have pozzolanic properties, but it reacts with the alumina phases of cement to form an calcium monocarboaluminate hydrate with no significant changes on the strength of blended cement [117]. The main effects of LF are of physical nature. It causes a better packing of cement granular skeleton and a larger dispersion of cement grains. Furthermore, LF acts as the crystallization nucleus for the precipitation of CH. These simultaneous effects produce an acceleration of the hydration of cement grains [118-119]. Additionally, replacing the expensive particles of cement by nonreactive economical particles of filler could offset the disadvantage of cracking.

Ground granulated blast-furnace slag (GGBS) is a glassy material from by-product of blast furnace iron making. Appropriate utilization of GGBS can result in better workability and pumpability, lower hydration heat, and reduce CO_2 emission for cement-based materials [120-121]. Generally, GGBS can refine the pore size distribution [42, 120, 122-124]. The beneficial effect of GGBS on pore refinement can improve the performance of materials, such as freezing action, carbonation, sulphate attack, gas penetration, chloride migration and reinforced bar corrosion [125-128].

Although the addition of LF and GGBS to Portland cement has been widely studied in pastes, mortars, and concretes, there is still less investigation related to the microstructure of ITZ.

2.5.2 Effect of chemical admixture

In the concrete modified with polymer, it is possible to observe an improvement in the ITZ characteristics, such as reduction of both quantity of CH and porosity, which can be attributed to the accumulation of polymer in this region [110]. The polymer in the freshly concrete is mainly dispersed in the liquid element. The ITZ presents a relatively higher water quantity compared with that of the bulk cement matrix, and consequently higher polymer quantity. Therefore, the reactions of the carboxylic group of the copolymer particles with calcium ions liberated during the cement hydration process thus reducing the calcium quantity available for the CH formation. The reduction of the CH quantity in the ITZ of polymer modified concrete has been proven in the literature [110, 129-130].

2.5.3 Effect of mixing procedure

On the macroscopic scale, the durability of self compacting concrete (SCC) structures is improved because SCC potentially leads to more homogeneous concrete properties due to the lack of vibration induced segregation [131-132]. On the microscopic scale, the type of mixing may have an influence on the porosity and width of ITZ. The absence of vibration in SCC reduces the volume of water accumulating around aggregates and leads to lower ITZ porosity and lower permeability [25, 107].

2.6 Conclusions

This brief literature review has been given to highlight the microstructure of the ITZ and the role it plays on the overall performance of the concrete. The published results have indicated the distinct microstructure of ITZ. Generally, it contains more CH with a preferred orientation with regard to the surface of the aggregate, a relatively high porosity and larger pore size compared with that of bulk cement matrix.

This review also showed that most of the studies regarding the characteristics of the ITZ have been approached from the micro-scale technique, including scanning electron microscopy with quantitative image analysis, mercury intrusion porosimety, wood’s metal penetration and energy dispersive spectrometry. All researchers agree on the existence of a relatively higher porosity within the ITZ. The efforts made by the investigator showed the possibility of improving the structure of the ITZ by using SCM, such as silica fume and metakaolin, and chemical additives such as polymer, and less compaction such as self-compacting concrete. However, there is no conclusion concerning if/how improvement can be made in the overall performance of concrete through improvement of the ITZ by using LF and GGBS.

Several studies and their main findings with respect to the effect of ITZ on the transport properties were also summarized in this review. However, the significance of the ITZ remains uncertain and the conclusion seemed to be inconsistency. These conflicting results from different sources underscored the difficulty in isolating the ITZ effect through experimental studies, where other important parameters that influence transport inevitably vary, when preparing and testing samples with different aggregate contents. Moreover, the information obtained about the ITZ has not been adequately translated to the overall performance of concrete.

Conclusively, the information mentioned above lays a solid foundation for the following experiments.

Chapter 3

Effect of ITZ on the transport properties of Portland cement-based composites

3.1 Introduction

The interfacial transition zone (ITZ) is the region surrounding each aggregate particle, where the microstructure is modified by the presence of aggregate. The origin of ITZ lies in the so called “wall effect”, by the packing of the anhydrous cement grains against the relatively flat aggregate surface [5]. The wall effect along with one side growth, flocculation and micro-bleeding which leads to the accumulation of water beneath the aggregate, results in a distinct microstructure within ITZ compared to that of the bulk paste [1]. Higher porosity and orientation deposition of calcium hydroxide, and fewer cement particles than in the bulk cement matrix[1] characterize the ITZ as the weakest link in the cement-based composites [5, 133-134]. Therefore the ITZ is an important consideration for durability aspects.

As a result of the distinguished microstructure, it is normally assumed that the ITZ should facilitate the ingress and movement of external aggressive agents into concrete. Additionally, it is expected that local transport properties within ITZ are higher than in the bulk paste due to its higher porosity. To investigate the influence of ITZ on the transport properties quantitatively, a number of studies have been performed on the artificial ITZ by casting neat cement paste against the plane surface of a large

---

[1] Note: bulk cement matrix means cement paste outside ITZ region.

aggregate [76-77]. Other studies were also carried out by using a rod-shaped aggregate positioned within a specimen of the same height, while the ITZ properties were modified by varying aggregate lateral surface and volume fraction. For example, Breton et al. [79] pointed out that the effective diffusion coefficient of chloride ion is 6 to 12 times greater in the ITZ than in the bulk paste. By using the accelerated chloride migration test, Yang et al. [24, 78] calculated that the migration coefficient of the ITZ is 40.6, 35.5, and 37.8 times the altered migration coefficient of the matrix for a water/cement (w/c) ratio of 0.35, 0.45, and 0.55, and is 2.83, 1.76 and 1.55 times the matrix migration coefficient for the ITZ thickness of 20, 40 and 50 μm, respectively.

Although these studies indicate that the ITZ is more penetrable than the bulk paste, they offer limited information on the overall properties of real materials where the microstructure is much more complicated and heterogeneous. The other challenge lies in how to extracting the influence of ITZ effect from other parameters, such as cracking, dilution and tortuosity of paste induced by the presence of aggregate and sample preparation. Therefore, some theoretical frameworks were proposed to enhance the understanding of the influence of ITZ on the transport properties of Portland cement concrete [90, 133]. The models were also validated with the electrical conductivity of mortar samples [23, 87]. By applying a twin geometrical model and assuming a 20 μm thickness of the ITZ, Ping et al. [77] have also calculated that the conductivity of the ITZ should be 10 times greater than that of the bulk paste. Using a semi-empirical three-phase composite sphere model, however, Zheng et al. [88] indicated that the influence of ITZ on the overall steady-state chloride diffusivity is small, despite it being on average more porous and having a diffusivity which is several times that of the bulk paste. In addition, a multi-scale model proposed by Sun et al. [96] predicts that the chloride diffusivity of concrete composite materials depends on the chloride diffusion coefficient of the bulk paste and ITZ. All these inconsistent results from different sources underscore the difficulty in isolating and determining the ITZ effect when preparing and testing samples with different aggregate content. Another important reason for these conflicting results is the sample treatment before measurement, which could cause damage to the microstructure and aggravate the ITZ effect. For example, some transport tests require preconditioning to a standard moisture degree. The most common method is oven-drying due to its fast drying rate and convenient operation. However, an increased drying rate will probably lead to more extensive microcracking, significantly influencing transport behaviour

When the samples are prepared with high aggregate contents, adjacent ITZs would be expected to interconnect and form a continuous path for the penetration of ions and water. Therefore, the percolation of pores in the ITZ is of great interest for studying the transport phenomena in Portland cement-based materials [10, 24, 84-85, 135]. By using mercury intrusion porosimetry (MIP) test, Winslow et al.[28] found that a sudden increase in intruded pore space was observed when the sand volume fraction increased from 45% to 49%. Other studies on mortars also attributed the increase in the paste porosity to the presence and percolation of ITZ [71]. Additionally, modeling work has also found that ITZ forms an interconnected network after a critical aggregate content even for a modest width of 10-20 μm [92, 136]. On the other side, some studies observed a decrease in transport properties with increasing aggregate volume fraction, indicating that the percolation of ITZ has limited effect on the overall properties [71, 74, 81, 89]. Therefore, the relationship between the percolation of ITZ and transport properties in real materials needs to be further understood.

Besides the factors mentioned above, there is another possible complication in determining the local transport properties of ITZ in real mortar or concrete. Due to the redistribution of cement particles and microbleeding, the lower cement content and higher w/c ratio in ITZ is accompanied by a denser bulk cement paste with higher cement content and lower w/c ratio than the nominal value [87, 100]. This redistribution makes the transport properties of bulk cement matrix different from the neat cement paste, and should be considered in determining the local transport properties of ITZ.

The relatively importance of ITZ, preconditioning regime, aggregate volume content and size on gas permeability, capillary water absorption and non-steady-state chloride migration is investigated in this chapter. The aim is to assess the effects of these variations in ITZ on transport properties such as ionic diffusion, water absorption and air permeability and to establish relationships amongst these transport coefficients and the properties of ITZ. Three transport measurements were considered as their main mechanisms governing the transport process and the effect of ITZ hereon might be different. Chloride migration is the transport of chloride ions induced by an external voltage. Permeability is the measure of the flow of oxygen under a pressure gradient, while absorption is the movement of water via capillary suction. Moreover, BSE imaging was performed at the top, bottom and side positions of coarse aggregates to examine other variables such as bleeding.

3.2 Experiment

3.2.1 Materials and mixtures

In order to study the effect of aggregate and ITZ on the transport properties, two series of mixtures were prepared. Series 1 were mortars with sand volume fractions ranging from 0% to 60%, while series 2 were concrete samples at a constant aggregate volume fraction of 60% with different coarse aggregate size and petrography. The mixture proportions are given in Table 3.1. A high w/c ratio of 0.5 was used to improve the workability of mixes with high sand content. Moreover, the difference in conditioning effects between paste, mortar and concrete are more remarkable for “normal” strength composites.

Nature sand (0-4 mm), gravel (2-8mm, 2-16mm) and crushed basalt (2-20mm) aggregates were used as fine and coarse aggregates, respectively. The gradation curves and physical properties of the aggregates are given in the Fig. 3.1 and Table 3.2. Ordinary Portland cement (PC) CEM Type I 52.5 N, complying with the European standard EN 197-1 (2000), was used for all mixtures. The compositions, physical properties and particle size distribution are given in Table 3.3 and Fig. 3.2, respectively.

Table 3.1 Paste, mortar and concrete mixture proportions.

Mixtures (kg/m^3)	Series 1				Series 2			
	M0	M10	M35	M60	C1 (M60)	C2	C3	C4
PC	1214.5	1093.0	789.4	485.8	485.8	485.8	485.8	485.8
Sand 0-4 mm	-	257.3	900.5	1543.8	1543.8	385.9	385.9	385.9
Gravel 2-8 mm	-	-	-	-	-	1184.4	-	-
Gravel 2-16 mm	-	-	-	-	-	-	1153.8	-
Basalt 2-20 mm	-	-	-	-	-	-	-	1170.0
Water	607.2	546.5	394.7	242.9	242.9	242.9	242.9	242.9
Agg. volume fraction (%)	0	10	35	60	60	60	60	60
Mean agg. Size (mm)	-	1.55	1.55	1.55	1.55	4.46	8.80	12.76

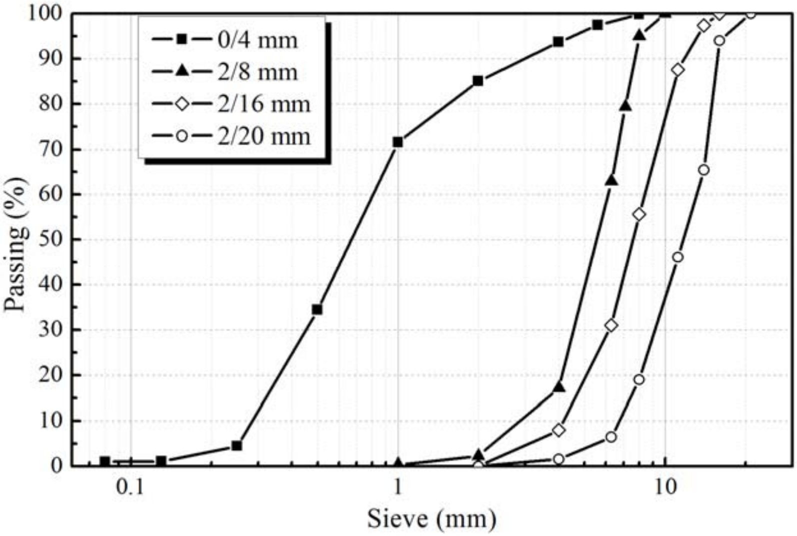

Fig. 3.1 Particle size distribution of aggregates.

Table 3.2 Physical properties of aggregates.

Aggregates	Density (kg/m^3)	Dry-rodded density (kg/m^3)	24h absorption (%)	Fineness (m^2/kg)	Specific surface area (×10^3m^2/m^3)
Sand (0-4 mm)	2573	1845	0.9	6.82	17.54
Gravel (2-8 mm)	2632	1832	1.1	1.76	5.61
Gravel (2-16 mm)	2564	1826	1.4	1.36	4.55
Crushed basalt (2-20 mm)	2600	1635	1.2	0.65	2.89

Table 3.3 Compositions (%) and Physical properties of ordinary portland cement.

CaO	SiO_2	Al_2O_3	Fe_2O_3	MgO	K_2O	Na_2O	SO_3	LOI
63.12	18.73	4.94	3.99	1.02	-	-	3.07	2.12
C_3S	C_2S	C_3A	C_4AF		Blaine (m^2/kg)	Density (kg/m^3)	Mean Particle size (μm)	
66.92	3.22	6.34	12.14		353	3092	15.675	

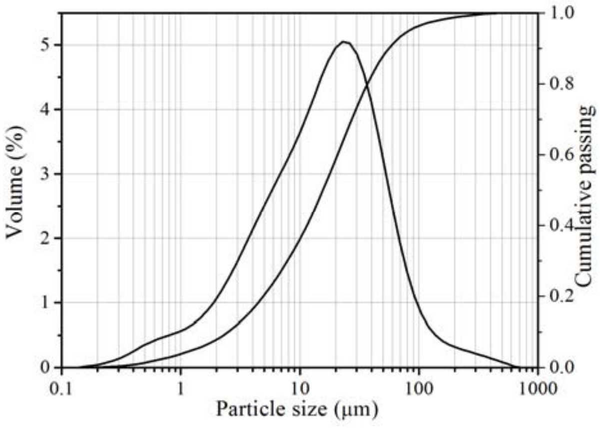

Fig. 3.2 Particle size distribution of PC.

3.2.2 Sample preparation and preconditioning

For each mix, two slabs (400×400×100 mm^3) slabs and a number of cubes (150×150×150 mm^3) were cast and placed with vibration. The intensity and duration of the vibration was adjusted according to the workability of each mix. Full compaction was considered to have been achieved when no significant amount of air bubbles escaped the top surface. All the samples were demolded after 24 h and then stored in the chamber with a constant temperature of 20±2°C and a relatively humidity of 95±5%. At the age of 28 days, six cylinder samples (Φ150×50 mm) were drilled out of the center of the slabs for gas permeability test, and a number of cylinder samples (Φ100×50 mm) were drilled and cut from the cubes for capillary water absorption and chloride migration tests. Subsequently, all the samples were divided into two equal groups, which were exposed to different preconditioning regimes in order to produce samples with a range of maturity and microcracks.

After cutting, samples from group #1 were slowly dried at 35°C for 1 week and then dried at 50°C until mass equilibrium, defined by a rate of mass loss below 0.01%/day. In order to prevent the formation of radial moisture gradients, the circumferential surfaces of the test specimens are sealed with an impermeable and tight material. Subsequent to the preconditioning, the specimens were sealed at a temperature of 50°C. Since no moisture exchange with the environment is possible, the elevated temperature will accelerate the redistribution of the axial moisture gradients towards a homogeneous distribution. Then, the specimens were moved to the lab condition (20±2°C) in the sealed state for a minimum of 24 hours before the measurement of gas permeability and water absorption.

In order to minimize the modification of pore structure and the influence of microcracks due to the oven-drying, another preconditioning regime was applied by placing the remaining cylinders (group #2) in an environmental chamber at 60% relatively humidity and 20°C until reaching the same saturation degree as acquired in group #1. The water saturation degree (S_{RH}) was calculated according to Eq. (3.1). The weight loss was recorded every week. Mixtures M60 (C1) required the longest period (12 months), and all the specimens were maintained in the chambers for 12 months to test them at the same age. After the permeability and water absorption measurements, all samples were firstly vacuum saturated [137] and conditioned until the pre-set weight of each of the specimens was obtained by using the same oven-drying procedure applied in group #1. The samples were sealed and moved to the lab condition (20°C) when each of the specimens reached the same weight at the end of 12 months of conditioning. Then all the measurements were carried out on these samples again.

$$S_{RH} = \frac{w_{RH}}{w_{sat}} \times 100\ (\%) \tag{3.1}$$

$$w_{RH} = \frac{m_{RH} - m_{dry}}{m_{dry}} \times 100\ (\%) \tag{3.2}$$

$$w_{sat} = \frac{m_{sat} - m_{dry}}{m_{dry}} \times 100\ (\%) \tag{3.3}$$

Where w_{RH} is the water content at equilibrium for RH, m_{RH} is the mass of the sample at equilibrium and m_{dry} the dried mass, obtained under oven-drying at 105°C until the equilibrium is reached.

3.2.3 Transport properties

3.2.3.1 Gas permeability

Gas permeability measurements were performed using the cembureau permeameter according to RILEM TC 116-PCD [138] (Fig. 3.3). Permeability tests were performed at 2, 3 and 4 bar pressure. The apparent oxygen permeability k_a (m^2) was determined from the steady-state gas flow rate Q (ml/s) at each pressure, and calculated according to the Eq. (3.4).

$$k_a = \frac{2P_a Q_i L \mu}{A(P_i^2 - P_a^2)} \tag{3.4}$$

Where Q_i is the volume flow rate of oxygen (in m^3/s) A is the cross-sectional area (in m^2), L is the thickness of the specimen (in m), μ is the viscosity of the fluid (2.02×10^{-5} N s m^{-2} for O_2 at 20°C), P_a is the atmospheric pressure (in bar) and P_i is the absolute inlet pressure (2, 3 and 4 bar).

(a) (b) (c)

Fig. 3.3 Schematic of CEMBUREAU gas permeameter (a), cell (b) and set-up (c) [139].

3.2.3.2 Capillary water absorption

In this study, a capillary water absorption test was carried out according to ASTM C 1585-04 [140] (Fig. 3.4). The preconditioned specimens were then covered with water-proof sheets, completely sealed on their circular sides and top to avoid evaporation and ensure unidirectional absorption. In order to ensure uniformity in the suction surface, the cutting face was chosen to be placed face down on two plastic rods in deionized water (about 2 mm above the base of the specimen). The water level was kept constant through addition of deionized water. The mass gain of a sample in contact with water was monitored at regular time intervals: 5, 10, 20, 30, 60 min, then at hourly intervals for the next 6 h and then daily until the sample reached saturation. Prior to weighing, the specimens were removed from the water and the surface was dried using a wet towel. Each weighing was completed within 30 s. The absorption was obtained by means of Eq. (3.5) [141-142].

$$I = \frac{\Delta m}{A \cdot \rho} \qquad (3.5)$$

Where I is the water absorption (in mm), Δm is the change in specimen mass at the time t (in g), A is the exposed area of the specimen (in mm^2) and ρ is the density of the water (in g/mm^3).

The rate of water absorption, sorptivity coefficient S (in mm/s$^{1/2}$), was determined from the slope of the line that is the best fit to I plotted against the square root of time t (in s$^{1/2}$):

$$I = St^{1/2} + b \tag{3.6}$$

The initial sorptivity is determined as the slope of the curve during the first 6 h, while secondary sorptivity is determined using the slope of the same measurements between 1 and 8 days.

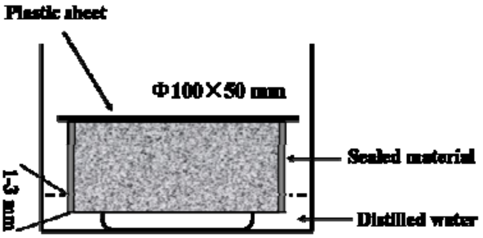

Fig. 3.4 schematic of water absorption set-up

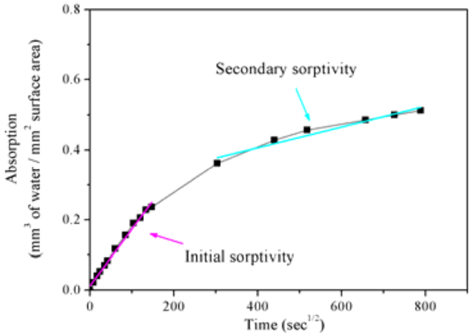

Fig. 3.5 Procedure to determine the initial and secondary sorptivity.

3.2.3.3 Rapid chloride migration

To investigate the influence of ITZ on the penetrability of chloride ions into concrete, a rapid test procedure is necessary to study this type of phenomenon without modifying the properties of ITZ. Therefore, a non-steady state migration test was carried out on the obtained mortar and concrete specimens at the age of 28 days. Prior to the migration test, the specimens were vacuum saturated with a saturated $Ca(OH)_2$ solution. Then a DC external electrical potential is applied on the specimens for a certain time period forcing the chloride ions from the 10% NaCl solution to migrate into the specimens. The schematic is presented in (Fig. 3.6). Due to the potential difference applied between the electrodes, chloride ions move from the upstream solution, through the specimens towards the downstream solution. The duration of the test yields between 6 and 96 h depending on the quality of the specimens expressed in terms of the initial current value when the external voltage is set to 30 V. After the migration, the specimens are split and sprayed with $AgNO_3$ - a colourimetric indicator for chlorides. Finally, the chloride penetration depth was measured and used for the D_{nssm}. Details concerning the testing procedure were explained elsewhere (1999) [143].

The general continuity equation for the chloride transport in concrete presents as:

$$\frac{\partial c_t}{\partial t} + u\nabla c + \nabla J = r \tag{3.7}$$

Where c_t is the total chloride concentration in concrete, u is the velocity of chloride ion, c is the concentration of chlorides, J is the total chloride flux and r is the reaction term. The total flux of chlorides for a combined process of diffusion and migration through saturated and uncharged porous medium can be given by the Nernst-Planck equation [144-146]:

$$J_x = -D(\frac{\partial c}{\partial t} - \frac{zF}{RT}c\frac{\partial \phi}{\partial x}) \tag{3.8}$$

Assuming: (i) a constant electrical field distribution across the samples; (ii) the convection term equal to zero (no pressure gradients during the process); (iii) zero reaction term, and a simplified equation can be applied to calculate the D_{nssm}:

$$D_{nssm} = \frac{RT}{zFE}\frac{x_d - \alpha\sqrt{x_d}}{t} \tag{3.9}$$

$$E = \frac{U-2}{L} \tag{3.10}$$

$$\alpha = 2\sqrt{\frac{RT}{zFE}}erf^{-1}(1-\frac{2c_d}{c_0}) \tag{3.11}$$

Where D_{nssm} is the non-steady-state migration coefficient (in m^2/s), z is the absolute value of ion valence (1 for chloride ions), F is the faraday constant (9.648×10^4 J/(V·mol)), U is the absolute value of the applied voltage (in V), R is the gas constant (8.314 J/(K·mol)), T is the average value of the initial and final temperatures in the anolyte solution (in K), L is the thickness of the specimen (in m), x_d is the average value of the penetration depth (in m), t is the test duration (in s), c_d is the chloride concentration at which the colour changes (0.07 mol/dm^3 or 2.48 g/dm^3), c_0 is the chloride concentration in the catholyte solution.

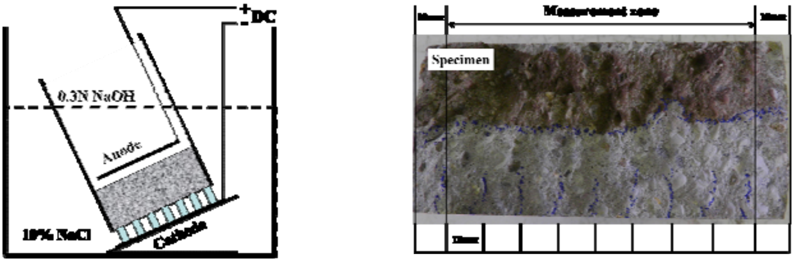

Fig. 3.6 Schematic of rapid chloride migration set-up (NT Build 492-1999) (a), and penetration depth measurement (b).

3.2.4 Microstructure

3.2.4.1 Average distance between adjacent aggregate

If the conventional assumptions of the effects of the ITZ on the transport properties are correct, the proportion of ITZ volume to bulk paste volume, and the extent of percolation between adjacent ITZs should determine the concrete properties to a great extent. Therefore, the average distance between adjacent aggregate grains can provide a useful index to evaluate the effects of ITZ on the transport properties. The average distance is determined by both the aggregate size distribution and aggregate content. The average distance between adjacent aggregate grains is reduced when the number of grains increases, or finer aggregates are used in the mixes. In this work, the average distance between aggregate was calculated by using the method proposed by Rangaraju [74]. This simplified method aims to represent the distance averaged over all directions in a three dimensional space, rather than the distance of closest approach measured on an arbitrary plane.

3.2.4.2 Water accessible porosity

For the determination of porosity accessible to water, an approximate method with a vacuum saturation and drying procedure was performed on the parallel mortar and concrete cores (Φ100 mm×50 mm) used in the transport measurements [139]. At 28 days, the specimens were placed in a vacuum container, and water was added afterward until the specimens were completely immersed. After one extra hour of vacuum preservation, the air pressure was re-loaded and the specimens were stored under water for 24 hours. The porosity was derived from the difference in mass of the water saturated sample to the dried sample [147]. Thereby, the specimens were transferred and kept into an oven at 50°C and 105°C until constant mass. The total porosity ($P_{105°\mathrm{C}}$) was calculated based upon the difference in mass of the water saturated sample and the dried (105°C) sample (Eq. (3.12)). The capillary porosity ($P_{50°\mathrm{C}}$) was similarly based upon the difference in mass of the water saturated sample and the sample dried at 50°C (Eq. (3.13)).

$$P_{105°\mathrm{C}} = \frac{m_{sat} - m_{105°\mathrm{C}}}{m_{sat} - m_{wat}} \tag{3.12}$$

$$P_{50°\mathrm{C}} = \frac{m_{sat} - m_{50°\mathrm{C}}}{m_{sat} - m_{wat}} \tag{3.13}$$

Where P is the water accessible porosity in volume (%), m_{sat} is the weight in air of saturated sample, m_{wat} is the weight measured in water of the saturated sample, and $m_{50°\mathrm{C}}$ and $m_{105°\mathrm{C}}$ is the constant weight of oven-dried samples at 50°C and 105°C, respectively.

Finally, the gel porosity was calculated from the mass difference of the dried (105°C) sample to the sample dried at 50°C.

3.2.4.3 Backscatter SEM imaging

The microstructure within interfacial regions may also vary significantly with position around the aggregate particles due to bleeding and segregation effects during casting and setting of the concrete. The trapping of water beneath coarse aggregates is an extreme case of heterogeneity and may be detrimental to both the strength and durability of the concrete. In this chapter, a field emission scanning electron microscope (SEM) in the backscattered electron (BSE) mode was used to investigate the effects of aggregate size on the microstructure of ITZ due to the bleeding and segregation, by measuring at the top, bottom and side positions of the aggregate separately. This measurement was qualitative here, but a more detailed quantitative analysis of the amount and distribution of porosity, unhydrated grains and hydration products will be performed in the following chapters.

To avoid the surface effect, slices (40×40×10 mm^3) were cut from the inner part of bulk mortar and concrete samples (150×150×150mm^3) by using a lime-water lubricated diamond-bladed wheel at 28 days. Two series of slices were obtained by cutting parallel to the casting direction (vertical) and perpendicular to the casting direction, respectively. Prior to the grinding and polishing, the obtained slices were submerged in liquid nitrogen for 5 min to stop further hydration. This quick quenching process at very low temperature prevents the growth of big ice crystals that form in larger pores and generate compressive stress in finer porosity zones. In such conditions, water drainage and finer pore retraction can be observed. Moreover, the smaller the pore access, the lower the water freezing temperature[148]. After freezing, the slices were transferred into a freeze-dryer (Fig. 3.7) in which temperature and vacuum were kept to -40°C and to 0.1 Pa, respectively. This process sublimates the ice trapped in the pores. During the sublimation operation, ice is converted directly into gas and thus the freeze-drying method softens the capillary stress effects and brings limited damage to the pore structure of samples [148-149]. However, the freeze-drying method removes less water than the oven drying method, especially in the case of low w/c ratio. In this work, the w/c ratio applied was 0.5 and the freeze-drying time was 14 days.

For BSE examination further sample preparation is necessary. The slices were vacuum impregnated with a low viscosity epoxy resin and heated for 24 h in an oven maintained at 30°C to reduce the setting time of the resin. After epoxy, the samples were ground with SiC paper 320, 500, 1200 and 2400 grit for about 4 min each. Subsequently, the samples were polished with a diamond paste of 3, 1 and 0.25 μm for around 2 min each and cleaned up with a low-relief polishing cloth. One example of the final prepared samples can be seen in the Fig. 3.8.

The polished samples were examined under the BSE detector in the environmental scanning electron microscope with a low acceleration voltage of 20 kV. The normal magnification used for evaluation is 500×, and the pixel resolution is 1424×968. Accordingly each pixel is approximately 0.18 μm in each direction.

Fig. 3.7 LTE Lyotrap freeze-dryer

Fig. 3.8 Impregnated, ground and polished samples for SEM examination (C2)

3.3 Results and discussion

3.3.1 ITZ volume fraction and inter-aggregate distance

3.3.1.1 ITZ volume fraction

In order to evaluate the effect of ITZ on the transport properties of cement-based composites, the first key step is to determine the ITZ content at a given aggregate volume fraction and size distribution. If the ITZ volume fraction is small, then this effect is also small, which would be the case for a small aggregate volume fraction. As the amount of the aggregate increases, the ITZ volume fraction also increase, and the ITZ effect becomes quite appreciable.

The microstructure of cement-based composites, especially the ITZ, is complex and heterogeneous, thereby some simplifications are inevitable. In this chapter, we aim to link the ITZ with transport properties. To simplify the analysis, several assumptions have been made: (i) The ITZ thickness is not a function of the aggregate size and aggregate volume content; (ii) the aggregates are approximated as spheres of various sizes and treated as being dispersed sufficiently to achieve their desired position, where the effect of gravity is neglected; (iii) the ITZ is modeled as shells of certain width that extend from the aggregate particles. Based on the aggregate size distribution present in Fig. 3.1, the volume fractions of the ITZ and bulk cement matrix can be determined analytically by using the 'void exclusion probability' denoted by Lu and Torquato [150], and well explained elsewhere [94]. In our case, the void exclusion probability $e_V(h)$ is basically the volume fraction outside of both the aggregates and the shell. While the hard aggregates may not overlap one another, the ITZ are allowed to overlap aggregates and each other, which would be general in real mortar and concrete. Accordingly, the ITZ volume fraction V_{ITZ} with ITZ thickness of h can be calculated as:

$$V_{\mathrm{ITZ}} = 1 - V_{\mathrm{agg}} - e_{\mathrm{V}}(h) \tag{3.14}$$

$$e_{\mathrm{V}}(h) = (1 - V_{\mathrm{agg}}) \exp[-\pi\rho(ch + dh^2 + gh^3)] \tag{3.15}$$

Where V_{agg} is the aggregate volume fraction, ρ is the total number of aggregate particle per unit volume, and the coefficients c, d, g are given in terms of average over the particle size distribution of the aggregate in terms of number. These coefficients can be determined from the sieve analysis with certain reasonable assumptions.

$$c = \frac{4\langle \mathrm{R}^2 \rangle}{1 - V_{\mathrm{agg}}} \tag{3.16}$$

$$d = \frac{4\langle \mathrm{R} \rangle}{1 - V_{\mathrm{agg}}} + \frac{8\pi\rho\langle \mathrm{R}^2 \rangle^2}{(1 - V_{\mathrm{agg}})^2} \tag{3.17}$$

$$g = \frac{4}{3(1 - V_{\mathrm{agg}})} + \frac{16\pi\rho\langle \mathrm{R} \rangle\langle \mathrm{R}^2 \rangle}{3(1 - V_{\mathrm{agg}})^2} + \frac{64\lambda\pi^2\rho^2\langle \mathrm{R}^2 \rangle^3}{27(1 - V_{\mathrm{agg}})^3} \tag{3.18}$$

Where <R> is the mean aggregate radius and $<R^2>$ is the mean square aggregate radius over the entire aggregate size distribution, the detailed process can be found in the ref. [94]. The parameter λ has different values (0, 2, or 3) depending on the analytical approximation used in the theory [150]. Garboczi and Bentz [94] observed that the actual values of λ did not make much difference to the calculated volume fraction, but λ=0 was always slightly better than λ=2 or 3 by comparing with the numerical simulation values. Therefore λ=0 was applied in the present study.

Along with the sieve analysis results in Fig. 3.1, the final calculated results are given in Table 3.4, in which the ITZ content is correlated to the ITZ width and aggregate volume fraction. It can be seen that the ITZ volume fraction increases with increasing width *h* and increasing aggregate volume fraction, or with decreasing grain size. It is still worth to mention that for the calculation a spherical aggregate geometry was assumed, which might not be correct for the case of C4 (basalt). The irregular surface would increase the surface area of aggregate, thereby the calculation applied in this work would lead to an underestimation of the ITZ volume fraction in this case.

Table 3.4 ITZ volume fraction calculated from void exclusion probability

Samples	V_{agg}	V_{ITZ}				
		h=5 μm	h=10 μm	h=15 μm	h=20 μm	h=30 μm
M0	0	0	0	0	0	0
M10	0.1	0.0013	0.0027	0.0041	0.0055	0.0084
M35	0.35	0.0047	0.0094	0.0142	0.0192	0.0294
M60 (C1)	0.60	0.0080	0.0161	0.0244	0.0328	0.0500
C2	0.60	0.0023	0.0045	0.0068	0.0092	0.0139
C3	0.60	0.0016	0.0031	0.0048	0.0064	0.0097
C4	0.60	0.0013	0.0026	0.0039	0.0053	0.0081

3.3.1.2 Average inter-aggregate distance

Besides the ITZ volume fraction, another determining parameter is the average distance between adjacent aggregates. If the conventional picture of the ITZ effect is correct, this effect should be more prominent for samples manufactured with finer grains or higher volume contents, in which the ITZs surrounding closely-spaced grains might effectively overlap (percolate) each other. Consequently, the average inter-aggregate distance can also provide something of a numerical index to the transport properties.

The average inter-aggregate distance was computed using the adjusted method proposed by Rangaraju et al. in ref. [74], which can be summarized as: (i) the volume of cement paste is introduced into the dry-rodded aggregate in two steps; (ii) the cement paste firstly fills the pore space between the grains in the dry-rodded condition; (iii) the excess paste beyond this volume serves to push the grains apart until all of the excess paste has been introduced and the final concrete volume is attained; (iv) It is assumed that all aggregate particles are enveloped by a shell of paste of uniform thickness. This thickness is simply the volume of the excess paste divided by the total surface area of the aggregate, and the average inter-aggregate distance is twice the thickness of the shell, and can be calculated by Eq. (3.19):

$$d = 2 \times \frac{1\text{-}V_{\mathrm{agg}}\text{-}V_{\mathrm{agg}} \cdot \; [\rho_{\mathrm{a}}/\rho_{\mathrm{p}}\text{-}1]}{SA} \tag{3.19}$$

Where V_{agg} is the aggregate volume fraction, SA is the total specific surface area of the combined coarse and fine aggregates (in $\mathrm{m}^2/\mathrm{m}^3$), ρ_{a} is the apparent density and ρ_{p} is the packing density under dry-rodded condition of the combined aggregate (in $\mathrm{kg/m}^3$).

The necessary data for these calculations are provided in Table 3.2, and the final results are given in Fig. 3.9. It can be seen that the average distance decreases with increasing aggregate volume fraction, and decreasing grain size at a constant volume fraction (0.6) except for the sample C4. This is attributed to the irregular geometry of aggregates in concrete C4, which create a poor packing and needs more paste to fill the voids. With this aggregate the average inter-aggregate distance is small, and large overlap could have existed between the adjacent ITZ. On the other hand, the gravel aggregate (2-16 mm) used has only a small surface area, thus would limit the ITZ content and its percolation.

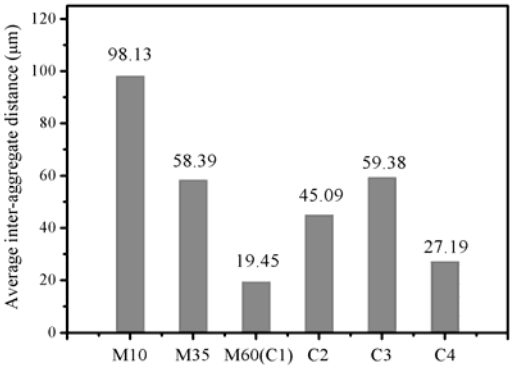

Fig. 3.9 Calculated average inter-aggregate distance of mortars and concretes.

3.3.2 Effect of aggregates on the porosity

Fig. 3.10 presents the porosity of samples in relation to aggregate volume content and grain size. The addition of aggregate tends to modify the porosity. The overall porosity decreases with increasing aggregate volume content due to the dilution effect by impermeable aggregate (Fig. 3.10 (a)). However, increasing grain size decreases porosity insignificantly. Comparing the capillary porosity of measured results with the dashed line obtained from $P_0 \times (1-V_{agg})$ (dilution effect，in Fig. 3.10 (b)), it can be seen that the capillary porosity values are above the theoretical line except for mortar M10. The higher capillary porosity than the normalized one may be attributed to the presence of high porous ITZ when grains were added into the neat cement paste. on the other hand, more porous ITZ is expected to be accompanied by denser bulk cement matrix [100], and lead to a decrease in the porosity. This effect could be more prominent for samples with low aggregate volume content (M10).

Additionally, the capillary porosity of samples prepared with varied grain size is in the decreasing order: M60(C1) > C4 > C3 > C2. If the average width of the ITZ around any grain does not vary with its size, the more porous ITZ would be proportioned to the surface areas, and the porosity should be decreased with increasing grain size at a constant aggregate volume fraction. However, another determinant factor which would enlarge the width of ITZ is bleeding and segregation, especially for the case of coarse and irregular aggregates. In this work, this effect was observed notably in C3 and C4 in which 2/16mm and 2/20mm coarse aggregate was used respectively. The trapping of water beneath coarse aggregates would increase thickness of the shell around the grains significantly. Therefore, this effect on the transport properties is evaluated by backscatter SEM image analysis and presented in section 3.6.

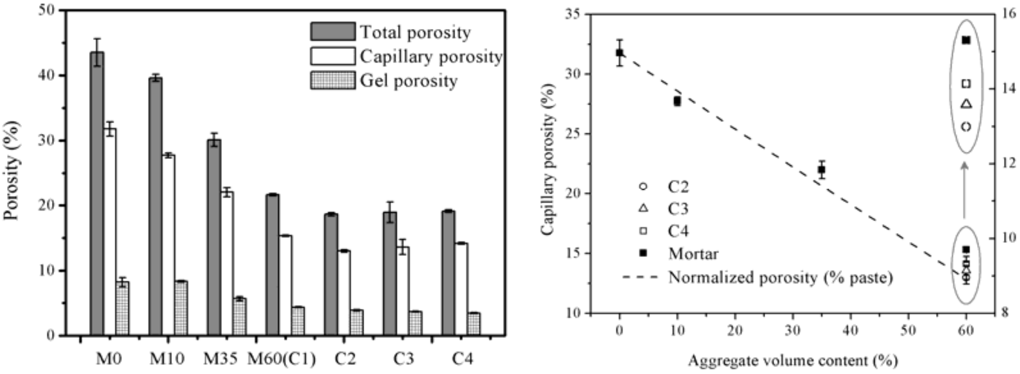

(a) (b)

Fig. 3.10 Effect of aggregate volume content on the porosity (a), normalized capillary porosity by volume of paste (b).

3.3.3 Effect of ITZ on the gas permeability

3.3.3.1 Preconditioning and curing age

The gas permeability k_a of all samples is given in Fig. 3.11. The y-axis scale of each graph is different for clarity. Samples from group #2 which are conditioned in a curing chamber have the lowest k_a for all mixtures. Regarding the results between 28 d and 12 months using the same oven-drying conditioning procedure, it can be seen that k_a decreases with increasing curing age due to continuous hydration of cement. Changes in k_a (Eq. (3.20)) from 28 d to 12 m in Fig. 3.12 show that the decreases are all the more remarkable as the aggregate volume fraction increases or the grain size decreases, and the highest decrease is observed in mortar M60(C1). According to the ITZ contents in Table 3.4, M60(C1) has the least bulk cement matrix which should be less sensitive to the hydration of cement in the later age. This contradictory result might be due to the damage brought by drying shrinkage.

$$\frac{k_{a,\text{28d-oven-drying}} - k_{a,\text{12m-oven-drying}}}{k_{a,\text{28d-oven-drying}}} \tag{3.20}$$

Results in ref. [89] indicated that drying even at moderate temperature (50°C) damages the microstructure. Drying shrinkage is restrained by the relatively rigid aggregates, causing a build-up of radial and tangential stresses, and finally relaxation when the local tensile strength is exceeded. Stresses are largest at the ITZ, therefore, cracks initiate here, then propagate and radiate from the aggregate surface into the bulk cement matrix[151]. In the work by Wong et al. [89] , the microcracks were divided into two classes, the bond cracks which appear at the ITZ and matrix cracks which propagate from the aggregate surface across the paste in an almost linear fashion until reaching a neighboring aggregate particle. The cracks in neat cement paste tend to span a longer distance without any obstruction, and leads to a higher permeability which is less sensitive to the further hydration. In samples containing more aggregate, the growing cracks would be arrested by or traverse around the aggregate [152]. Therefore, these cracks have more tortuous paths and longer effective lengths because they are easily blocked or forced to circumvent the aggregates. Additionally, the aggregates in concrete samples have larger size distribution and fewer grains per unit plane or volume, therefore, the mircrocracks in the concrete samples are less tortuous than those in mortars at a given aggregate volume content.

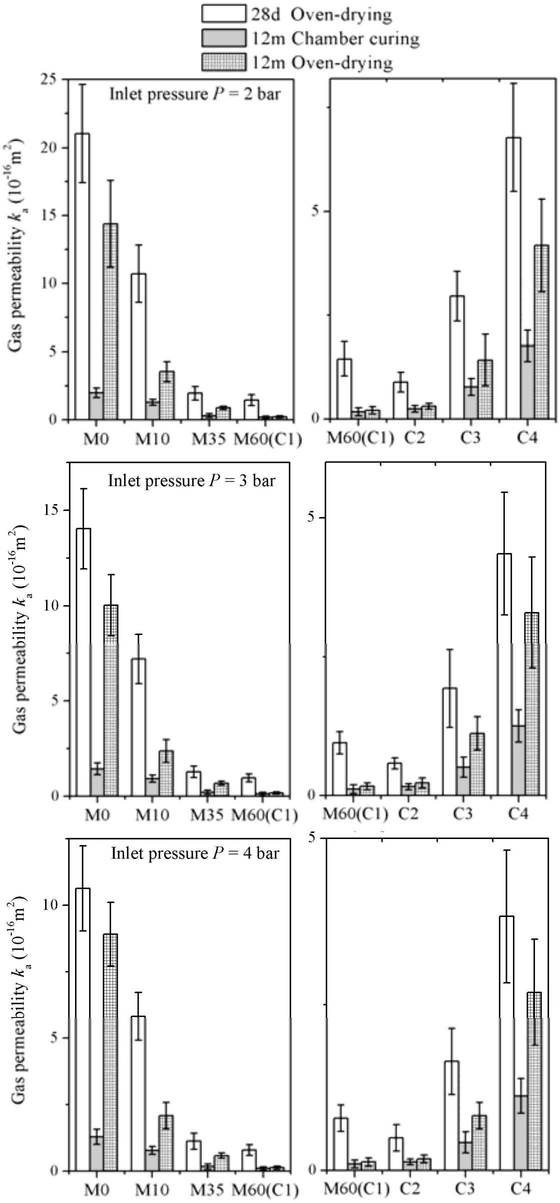

Fig. 3.11 Effect of aggregates, curing age and preconditioning regimes on the gas permeability measured at different inlet pressure. (oven-drying refers to drying at 35°C for 1 week and then at 50°C until mass equilibrium)

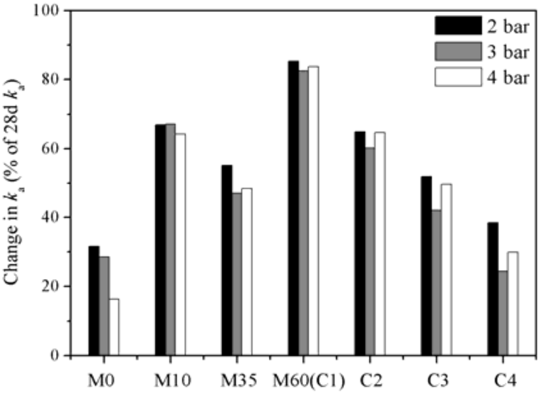

Fig. 3.12 Comparison of gas permeability k_a between 28d and 12m of oven-drying (% k_a of 28d oven-drying).

Concerning the effect of preconditioning regimes on the k_a at 12months, results from Fig. 3.11 indicate that drying at 50°C increases permeability to a large extent. This increase (Eq. (3.21)) is all the more notable as the cement matrix paste increases either by decreasing aggregate volume content or increasing grain size (Fig. 3.13). The largest increase is observed in the neat cement paste M0. This can be attributed to the same reason we have explained previously. Additionally, the gas permeability of concrete samples is more sensitive to the cracks caused by drying (Fig. 3.13). This is because a larger aggregate size at constant volume equates to lower surface area to bond with the paste, thereby any shrinkage produces larger stresses at the ITZ and a higher degree of cracking when they are exposed to the same preconditioning.

$$\frac{k_{a,\text{12m-oven-drying}} - k_{a,\text{12m-chamber curing}}}{k_{a,\text{12m-chamber curing}}} \tag{3.21}$$

Oven-drying is able to create a certain internal water saturation degree in a short term, however, bring more significant damage to the microstructure [41]. The increase in permeability due to this type of damage is all the more significant as the bulk cement matrix volume increases. These results suggest that the oven-drying conditioning would bring extra parameters in determining the permeability of mortars and concretes [41, 43, 148, 152-153]. In our work, this effect was more notable for neat cement paste in which cracks propagated without being obstructed by grains. It is critical to employ a suitable preconditioning procedure for studying the effect of ITZ on the permeability when neat cement paste is used as references. Therefore, results of samples preconditioned in chamber for 12months are employed for the following analysis.

3.3.3.2 Aggregate volume content, grain size and ITZ

The gas permeability of samples preconditioned in the chamber for 12 months, are plotted as a function of the aggregate volume fraction (in Fig. 3.14). The experimental results were compared with the dash line of $k_{\mathrm{a,paste}}$ $(1-V_{\mathrm{agg}})$ and the line of $k_{\mathrm{a,paste}}$ $(1-V_{\mathrm{agg}})^{3/2}$, which is the well-established Bruggeman-Hanai (B-H) law for the case of spherical, non-permeable aggregates in a permeable matrix and combines the tortuosity with the dilution effect [23, 154]. The law is exact in the case of a low volume content, and has also been found to be accurate for normal aggregate volume fractions. The derivation of this equation was also proved to better apply to concrete microstructure than other approximations and is to be chosen for this reason [23, 80, 154]. However, this equation does not consider the percolation threshold for the bulk paste or inclusions. Therefore, if the transport properties of bulk paste stay constant as more aggregate is added, and the effect of the ITZ on overall permeability is negligible, then the experimental data should follow the line. The results will go below the line if the presence of ITZ decreases transport properties, and above the line if the ITZ increases transport properties.

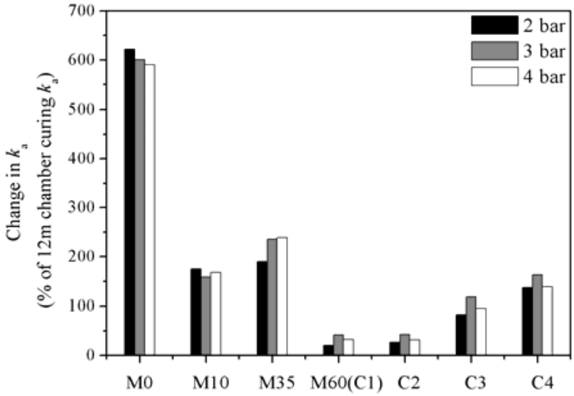

Fig. 3.13 Comparison of gas permeability k_a between oven-drying and chamber curing at 12months (%k_a of 12m chamber curing).

3.3.3.2 Aggregate volume content, grain size and ITZ

The gas permeability of samples preconditioned in the chamber for 12 months, are plotted as a function of the aggregate volume fraction (in Fig. 3.14). The experimental results were compared with the dash line of $k_{a,paste}$ $(1-V_{agg})$ and the line of $k_{a,paste}$ $(1-V_{agg})^{3/2}$, which is the well-established Bruggeman-Hanai (B-H) law for the case of spherical, non-permeable aggregates in a permeable matrix and combines the tortuosity with the dilution effect [23, 154]. The law is exact in the case of a low volume content, and has also been found to be accurate for normal aggregate volume fractions. The derivation of this equation was also proved to better apply to concrete microstructure than other approximations and is to be chosen for this reason [23, 80, 154]. However, this equation does not consider the percolation threshold for the bulk paste or inclusions. Therefore, if the transport properties of bulk paste stay constant as more aggregate is added, and the effect of the ITZ on overall permeability is negligible, then the experimental data should follow the line. The results will go below the line if the presence of ITZ decreases transport properties, and above the line if the ITZ increases transport properties.

From Fig. 3.14, it can be seen that the k_a decreases with increasing aggregate volume content and it is surprisingly observed that the experimental data are below the law to a certain extent. The difference between experimental data and model line decreases as the aggregate volume content increases to 60%. This result seems to be contradictory with the conventional assumptions of negative ITZ effect. In literature, the influence of aggregate on transport properties was also found to be sometimes low and sometimes strong. Haalamickova et al. [73] reported that water permeability increases with increasing aggregate volume content. Similarly, Hamami et al. [43] measured a decrease of gas permeability when the paste volume fraction decreases. However, Care and Derkx [41] observed that the gas permeability of mortars is higher than the gas permeability of the cement paste. For low relatively humidity (50%), the gas permeability measurements tended to the same value for all specimens. In our work, to explain this contradictory observation, several assumptions can be made when the aggregate is added to the neat cement paste. On the one hand, considering a fixed ITZ width, the ITZ volume increases with increasing aggregate content. This effect would increase permeability, considering the higher permeability of the ITZ zone. On the other hand, the impermeable aggregate decreases permeable cross section area of specimens and increases the effective lenth of the transport path. These effects are normally termed as dilution and tortuosity, and are expected to decrease transfer properties. Furthermore, while an increasing aggregate content produces more ITZ, it also leads to a more dense bulk cement matrix. The total amount of water and cement in the mortar is conserved, but more water can be adsorbed on the increased aggregate surface area in the ITZ. A lower amount of cement and greater amount of water in the ITZ will lead to a higher amount of cement and a lower amount of water in the bulk cement matrix. This redistribution of cement and water was confirmed by using a multiscale model in ref. [23, 155], in which the bulk cement matrix w/c ratio is reduced to 0.36 from a nominal value of 0.4 when the aggregate volume fraction reached the maximum amount of 50%. Therefore, the bulk cement matrix which mainly determines the permeability becomes denser with increasing aggregate volume content, but this was not taken into account in the B-H law. In this study, the dilution and tortuosity effects plus the densified bulk cement matrix are supposed to dominate permeability for samples with low aggregate volume content. These effects tend to be balanced by the ITZ effect and its percolation when the aggregate content reaches 60%, and the negative effect of ITZ becomes notable at high aggregate addition. Moreover, the high gas permeability of neat cement paste due to microcracking could also be the reason for the higher model line.

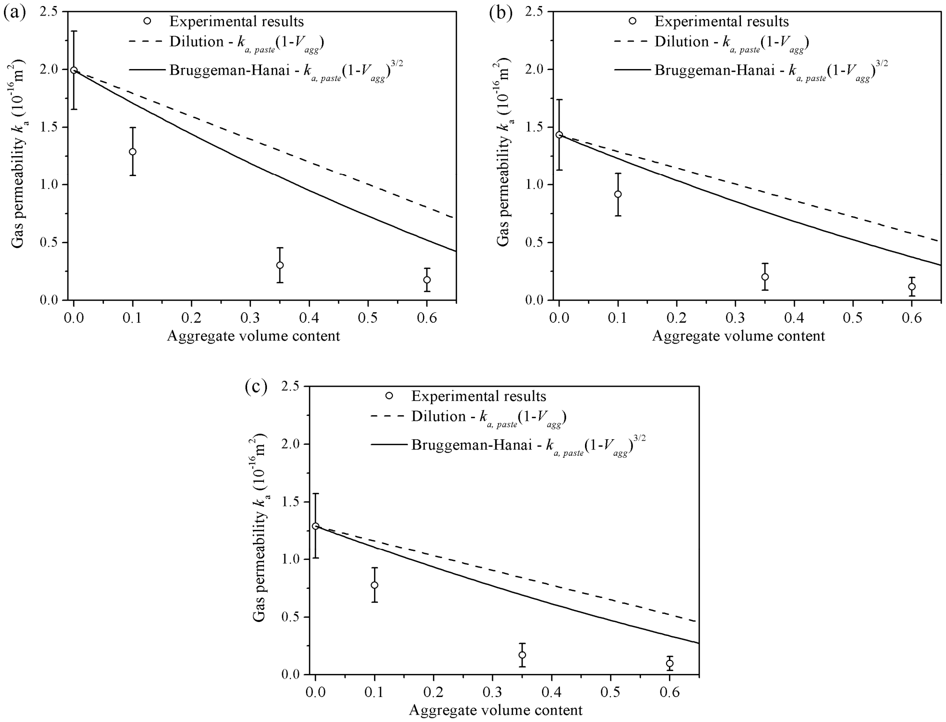

Fig. 3.14 Gas permeability measured at (a) 2 bar, (b) 3 bar and (c) 4 bar, versus aggregate volume content.

In order to determine the gas permeability of ITZ, a new approximation is proposed based on the B-H law and combine the dilution, tortuosity, densification and ITZ together, which can be expresses as:

$$k_a = \alpha k_0 e_{\mathrm{V}}(h)^{3/2} + k_{\mathrm{ITZ,I}} V_{\mathrm{ITZ}} \tag{3.22}$$

Where k_a is the overall gas permeability at a given aggregate volume fraction, a is the densification factor which is related to the aggregate volume fraction (a=1 for neat paste), k_0 is the gas permeability of neat cement paste, $e_V(h)^{3/2}$ is the combined dilution and tortuosity effect, and $k_{ITZ,I}$ is the intrinsic permeability of ITZ. According to measured k_a and calculated $e_V(h)$

and V_{ITZ} (in Table 3.4), the densification factor a and $k_{\mathrm{ITZ,I}}$ can be obtained by using the least square method. Taking the inlet pressure of 2 bar and a fixed ITZ thickness of 15 μm for instant, the fitted $k_{\mathrm{ITZ,I}}$ is 8.15×10^{-16} m^2.

The gas permeability versus the average grain size (in Table 3.1) is given in Fig. 3.15. At a constant aggregate volume content and fixed ITZ thickness, using a finer aggregate size creates more porous ITZ which would increase the permeability. However, the gas permeability varies slightly with increasing average grain size from 1.55 to 4.46 mm, and a significant increase in k_a is observed in samples C3 and C4. This is in agreement with the work done by Care and Derkx [41], in which the gas permeability is higher with coarser aggregate for preconditioning at RH=90%. Assumptions can be made to explain this result. Coarser sand is associated with larger pores in the ITZ phase due to bleeding and segregation. The trapping of water beneath coarse aggregates is an extreme case of inhomogeneity. Furthermore, this effect could be confirmed by the fact that the porosity is increased as the grain size increases from 4.46 to 12.76 mm (in Fig. 3.10). The detailed information about this effect is discussed in the section 3.6, and a fixed thickness of ITZ might not be correct for analyzing the ITZ effect in samples containing large grain size distribution.

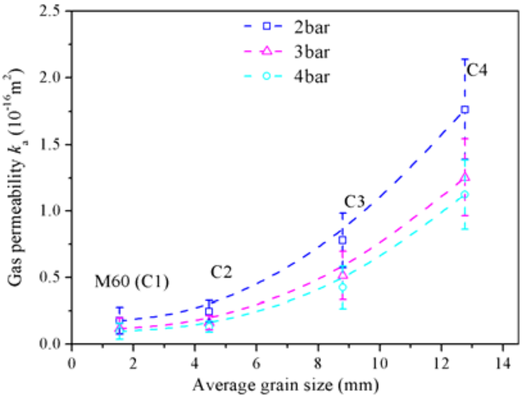

Fig. 3.15 Gas permeability versus average grain size.

3.3.3.3 Correlation between porosity and gas permeability

Permeability should depend on both porosity and connected pores size. The complexity due to the presence of porous ITZ and a modified microstructure of the matrix should also be taken into account in this work. Fig. 3.16(a) presents the apparent gas permeability for mortars versus the porosity of the bulk cement paste, which represent the ideal case of a porous paste diluted by nonporous aggregates. As expected, the cement paste porosity increases with increasing the aggregate volume fraction due to the presence of more porous ITZ. The k_a significantly decreases with increasing nomalised porosity from M0 to M35. This can be explained by the high permeability of cracked neat cement paste, the increase in the effective transfer path length (tortuosity) and the densified microstructure of matrix. These effects tend to be cancelled out by the enhanced ITZ and percolation effect with increasing aggregate volume content. It can be confirmed by the fact that no notable decrease in k_a is observed in M60 relative to M35, showing that the gas permeability varies only slightly when the aggregate volume content increases from 35% to 60%.

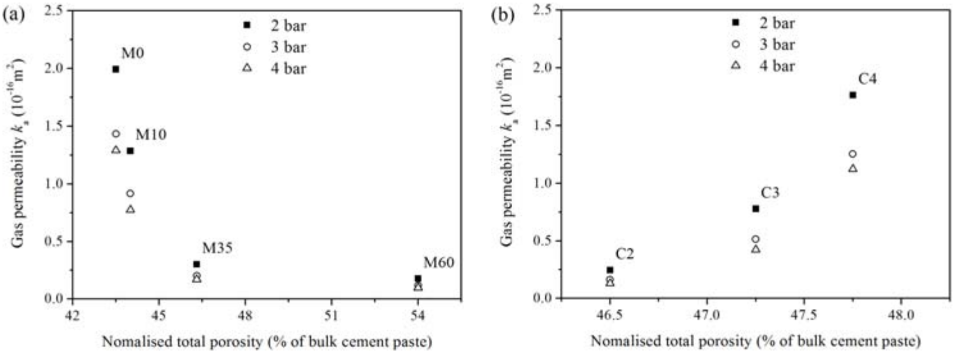

Fig. 3.16 Apparent gas permeability versus normalized porosity of bulk cement paste , (a) mortars and (b) concretes.

For a constant aggregate volume fraction, the apparent gas permeability increases with increasing nomalised porosity (Fig. 3.16(b)). At a given aggregate volume content, using a coarser grain size decreases the tortuosity of matrix which would reduce the effective flow path length and increase the permeability. As confirmed in section 3.3.2 and 3.3.3.2, coarser pores in the ITZ phase due to bleeding and segregation are expected in C3 and C4, which could increase the averaged ITZ thickness significantly and the permeability as a result. Therefore, a fixed thickness of ITZ is not suitable for analyzing the ITZ effect in samples containing large grain size distribution. In our work, significant bleeding and increasing in ITZ is observed in C3 and C4. This is assessed in the section 3.3.6.

3.3.4 Effect of ITZ on the capillary water absorption

3.3.4.1 Preconditioning and curing age

Fig. 3.17 shows the initial and secondary sorptivity calculated as the slope of the absorption versus the square root of time during the first 6 h and between 1-8 d of testing. Details about the water absorption data are given in the Appendix. Both the initial and secondary sorptivity decrease when the aggregate volume content increases. Regarding the effect of grain size, the sorptivity decreases with increasing average grain size from 1.55 (C1) to 4.46 (C2) mm. However, notable increases in initial and secondary sorptivity are observed in C3 and C4. These trends are all the more remarkable as the oven-drying preconditioning regime (35°C + 50°C) is employed. Samples preconditioned in the chamber with R.H. 60% for 12 months have the lowest sorptivity.

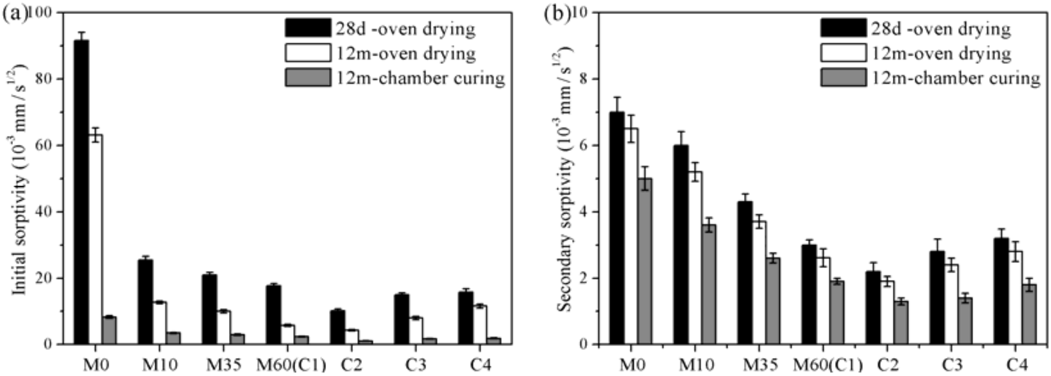

Fig. 3.17 Initial (a) and Secondary (b) sorptivity of samples preconditioned at different regimes.

Regarding the results between 28 d and 12 m employing the same oven-drying conditioning procedure, it can be seen that sorptivity decreases with increasing curing age due to further hydration (Fig. 3.17). Changes in the initial sorptivity (Eq. (3.23)) from 28 d to 12 m in Fig. 3.18 show that the decrease is all the more remarkable as the aggregate volume fraction increases (from M0 to M60) or the grain size decreases (from C4 to C1), and the highest decrease is observed in mortar M60(C1). Concerning the effect of preconditioning regimes on the initial sorptivity at 12 m, results from Fig. 3.17 indicate that drying at 50°C increases the sorptivity to a large extent, especially for the neat cement paste. The increasing ratio is calculated by using Eq. (3.24) and given in Fig. 3.19. This increase is all the more notable as the bulk cement matrix volume increases either by decreasing the aggregate volume content (from M60 to M0) or increasing grain size (C1 to C4). The largest increase is observed in the neat cement paste M0.

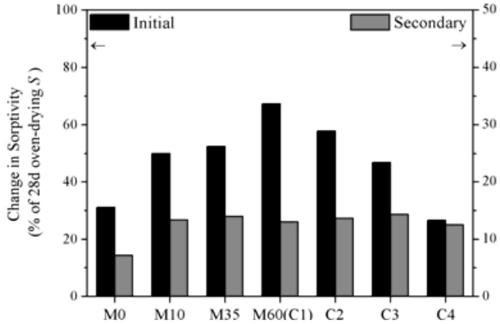

Fig. 3.18 Comparison of Sorptivity between 28 d and 12 m of oven-drying (% Sorptivity of 28 d oven-drying).

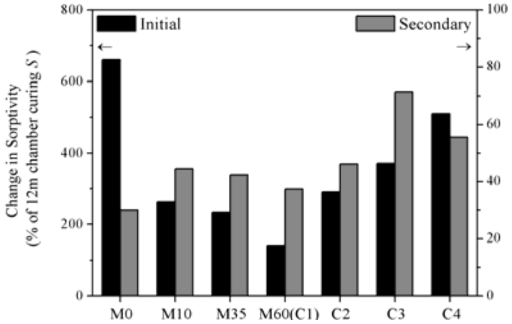

Fig. 3.19 Comparison of Sorptivity between 12 m of oven-drying and chamber curing (% Sorptivity of 12 m of chamber curing).

These observations are in consistence with the findings indicated in gas permeability, which can be due to the damage produced by the oven-drying. Oven-drying is able to create a certain intern water saturation degree in a short term, however, brings more significant damage to the microstructure regardless of the testing age. Increasing in the transport properties due to this type of damage is all the more significant as the bulk cement matrix volume increases. These results suggest that the oven-drying conditioning would bring extra parameters in analyzing the results. In our work, this effect was more notable for neat cement paste in which cracks propagated without being obstructed by grains. Therefore, results of samples preconditioned in chamber for 12 months are employed for the following analysis.

$$\frac{S_{\text{28d-oven-drying}} - S_{\text{12m-oven-drying}}}{S_{\text{28d-oven-drying}}} \tag{3.23}$$

$$\frac{S_{\text{12m-oven-drying}} - S_{\text{12m-chamber curing}}}{S_{\text{12m-chamber curing}}} \tag{3.24}$$

3.3.4.2 Aggregate volume content, grain size and ITZ

The water absorptions per unit of surface area of mortars preconditioned in the chamber for 12 m are given in Fig. 3.20. From Fig. 3.20(a), it can be seen that samples with higher volume of aggregate show lower absorption. The water absorption at 7 days decreases with increasing in aggregate volume content (Fig. 3.20(b)). The water absorption is mainly determined by the paste, thereby the results are normalized by the volume of bulk cement paste (1-V_{agg}), and a reversal order is observed in Fig. 3.21(a). Mortar M60 prepared with the highest aggregate volume content has the highest water absorption.

The effect of water absorption of the aggregate is not considered in the results. To better understand the effect of aggregate, the normalized water absorption at 7 days by volume of bulk cement paste is given in Fig. 3.21(b), in which the aggregates are assumed to be full saturated after 7 days of absorption and the absorptions of aggregates are subtracted according to its absorption in Table 3.2. From Fig. 3.21(b), it can be seen that for 0.9% sand absorption, the normalized water absorption at 7 days is in the increasing order: M60>M35>M0>M10, but the difference is not as remarkable as in the Fig. 3.20(b).

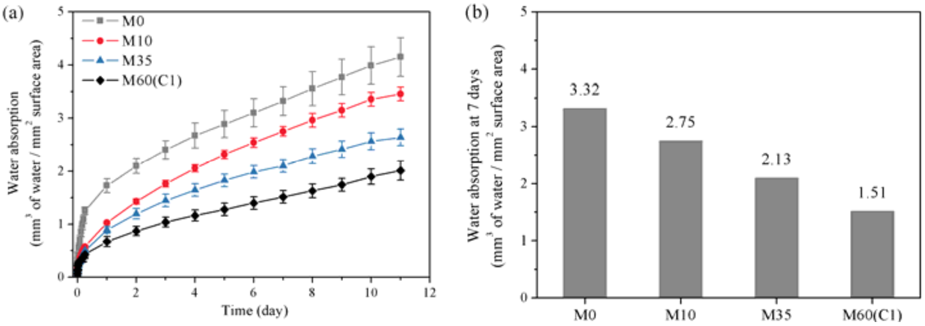

Fig. 3.20 Effect of aggregate volume content on the water absorption (a), and cumulative absorption at 7 days (b).

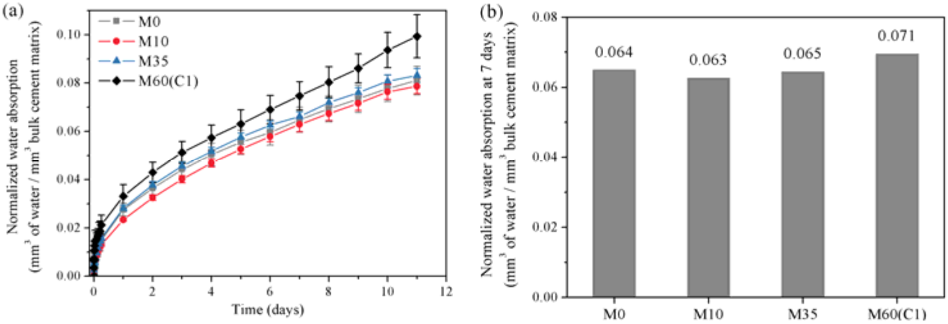

Fig. 3.21 Normalized water absorption in samples containing different aggregate content by volume of bulk cement paste(a), and cumulative normalized water absorption at 7 days.

The sorptivity of mortars versus the aggregate volume content are given in Fig. 3.22, and the experimental results are compared with the model dilution line and B-H law. As indicated in section 3.4.1, the initial and secondary sorptivity decreases when the aggregate volume content increases. In order to analyze the experimental results, several effects are taken into account with the presence of aggregate, namely, the dilution, tortuosity and densification effect reduce the sorptivity, while the presence of more porous ITZ increases it. From Fig. 3.22 (a), it can be seen that the initial sorptivity of M0, M10 and M35 is below the model line due to the further reduction by densified bulk cement matrix. This was also observed in the gas permeability measurement (Fig. 3.14) and explained in section 3.3. Different from the gas permeability, a higher initial sorptivity than the model line is observed in mortar M60 in which 60% of aggregate was added. This phenomenon starts from M35 for the secondary sorptivity (Fig. 3.22 (b)).

The addition of relatively impermeable aggregate tends to decrease the permeable area of specimens and to increase the effective transport path length, which would decrease the transfer properties. Although increasing aggregate content introduces more porous ITZ, this is accompanied by a more dense bulk cement matrix which has been explained in section 3.3. These positive effects of dilution, tortuosity and densification on sorptivity dominate the ITZ effect until an aggregate volume fraction of 0.60 for the initial sorptivity, and 0.35 for the secondary sorptivity, respectively. After that, these effects are canceled out by the ITZ effect and the experimental data is above the model line.

In order to get insight into the effect of ITZ on the sorptivity, an approximation is proposed based on the B-H law, which has been explained in Eq. (3.22) and can be expresses as:

$$S \ = \alpha S_0 e_{\mathrm{V}}(h)^{3/2} + S_{\mathrm{ITZ,\,I}} V_{\mathrm{ITZ}} \tag{3.25}$$

Where S is the sorptivity at a given aggregate volume fraction, a is the densification factor which is related to the aggregate volume fraction (a=1 in case of neat cement paste), S_0 is the gas permeability of neat cement paste, $e_{\mathrm{V}}(h)^{3/2}$ is the combined dilution and tortuosity effect, and $S_{\mathrm{ITZ,\,I}}$ is the intrinsic sorptivity of ITZ. According to measured S and calculated $e_{\mathrm{V}}(h)$ and V_{ITZ} (in Table 3.4), the densification factor a and S_{ITZ} can be obtained by using the least square method. Taking a fixed ITZ thickness of 15 μm for instance, the obtained initial $S_{\mathrm{ITZ,\,I}}$ and secondary $S_{\mathrm{ITZ,\,I}}$ is 12.32×10^{-3} mm/s$^{1/2}$ and 28.19×10^{-3} mm/s$^{1/2}$ respectively.

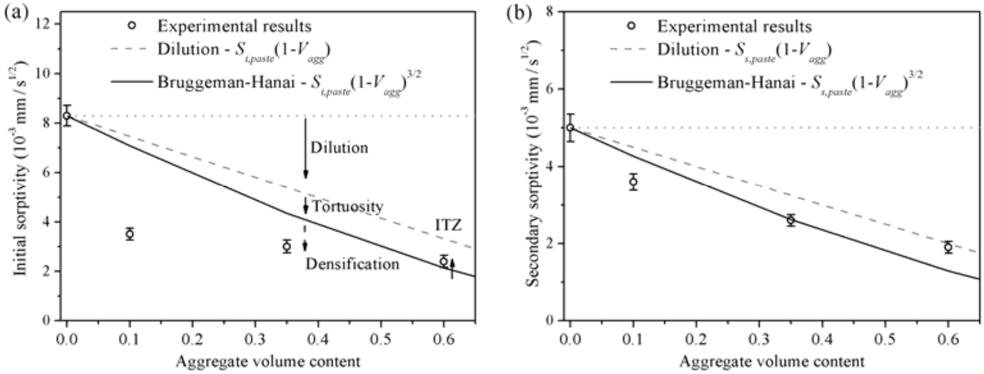

Fig. 3.22 Effect of aggregate volume content on the sorptivity (a) Initial, (b) Secondary.

The water absorption versus the average grain size (in Table 3.1) is given in Fig. 3.23. At a constant aggregate volume content and fixed thickness of ITZ, using a finer aggregate size increases the ITZ volume fraction which would increase the absorption. The water absorption is in the following increasing order: C4>C1>C3>C2. The water absorption at 7 days decreases from 1.51 to 1.05 mm with increasing average grain size from 1.55

to 4.46 mm, and a gradual increase in the absorption is observed in C3 and C4. This finding is consistent with the observation in gas permeability. In section 3.3, assumptions have been made that the coarser sand is associated with coarser pore in the ITZ phase due to bleeding and segregation. The trapping of water beneath coarse aggregates is an extreme case of inhomogeneity. The absorption and sorptivity is given versus the porosity in the following discussion. This would further suggest that a fixed thickness of ITZ might not be correct for analyzing the ITZ effect in samples containing large grain size distribution.

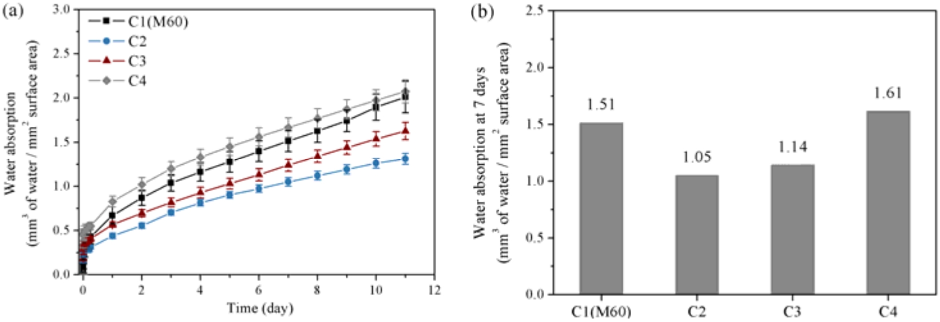

Fig. 3.23 Effect of grain size on the water absorption (a), and cumulative absorption at 7 days (b).

3.3.4.3 Correlation between porosity and water absorption, sorptivity

The transport of water through the specimens is also highly dependent on the pore structure. Fig. 3.24 (a) presents the initial and secondary sorptivity for mortars versus the porosity of bulk cement paste (normalized by the volume of paste), which represents the ideal case of a porous paste diluted by nonporous aggregates. The S_i and S_s decrease significantly with increasing nomalized porosity significantly from M0 to M10. This can be explained by the increase in the effective transfer path length (tortuosity) when the aggregate volume content is increased. These effects tend to be balanced by the enhanced ITZ effect with increasing aggregate volume content. At a given aggregate volume content (Fig. 3.24 (b)), using a coarser grain size decreases the tortuosity of paste which would reduce the effective flow path and increase the transport properties. As confirmed in sections 3.3.2 and 3.3.3, coarser pores in the ITZ phase due to bleeding and segregation are expected in C3 and C4, which could increase averaged ITZ width significantly and enhance its effect.

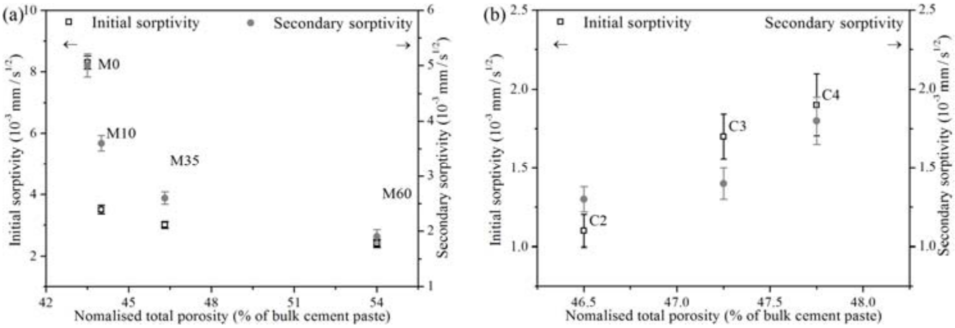

Fig. 3.24 Sorptivity versus normalized porosity of bulk cement paste, (a) mortars and (b) concretes.

Although the same trend is observed in both S_i and S_s, S_i is more sensitive to the variation of porosity: (i) the decrease in sorptivity with increasing porosity is more remarkable for S_i in Fig. 3.24 (a); (ii) the increase in sorptivity with increasing porosity is more notable for S_i in Fig. 3.24 (b). This can be explained by the fact that the initial sorptivity is highly dependent on the pore features closer to the exposed surface of the specimens. In contrast, the secondary sorptivity is a function of water transport through the bulk cement paste, and depends on the pore sizes and pore connectivity, resulting in a lower sensitivity to the total porosity [156]. As the water enters the pore space it encounters smaller pores, hence slowing the rate of absorption. The presence of porous ITZ and their percolation in the case of a high aggregate volume fraction forms an enhanced connected network. The ingress of water may still be slowed down as the air/water interface relaxes to a stable or metastable [142]. Then further movement of water and secondary sorptivity would be controlled by smaller pores. In the samples containing higher aggregate volume fraction or finer aggregate size, coarser pores with larger critical radius appear due to the presence of ITZ, while capillary pores with finer critical radius are also present which can be attributed to the denser matrix than the corresponding neat cement paste [41]. This could also be the reason for the enhanced sorptivity in M60(C1).

The amount of absorption is also dependent on the microstructure, a higher porosity would lead to a higher amount of water uptake. By plotting the normalized 7 days water absorption as a function of its porosity of bulk cement paste, this is confirmed in Fig. 3.25. A pronounced increasing relation exists between the normalized porosity and the absorption for both mortars and concretes. Therefore, an increase in the porous ITZ would increase the normalized water absorption by the volume of cement paste.

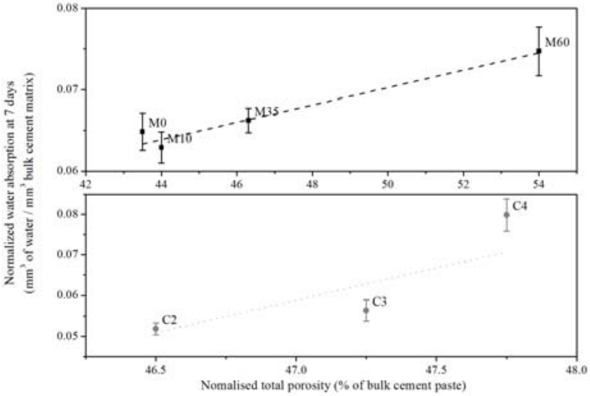

Fig. 3.25 Relationship between the normalized water absorption at 7 days and the normalized total porosity.

3.3.5 Effect of ITZ on the chloride migration

3.3.5.1 Aggregate volume content and grain size

The non-steady-state chloride migration test provides a comparative index of the relatively ease of movement of ions through the mortar and concrete. The results of the chloride migration coefficient obtained at 28 days are given in Fig. 3.26. The overall migration coefficient appears to depend on the aggregate content of the mixtures. An increase of the sand volume fraction leads to a decrease of the migration coefficient until 0.35 due to the dilution and tortuosity effect. Then a significant increase in the migration coefficient was observed when the aggregate content increased from 0.35 to 0.60. This marked increase in permeability was also observed in Halamickova et al. [73], when the aggregate volume increased from 0.45 to 0.55. This is also in agreement with the MIP results of Winslow et al. [28], which was an indication that the ITZ has reached a high connection degree.

The transport properties of mortar are determined by the transport properties and content of their constituents. In this study, mortar is considered as bulk cement matrix, aggregate and the interfacial region, ITZ. The aggregate has much lower transport properties. If the ITZ is impermeable, the transport properties of mortar will decrease with increasing aggregate content [78], which contradicts the test results in Fig. 3.26. Normally two opposite effects should be taken into account when aggregates are introduced into the hydrated cement paste [23, 71, 100]: The dilution, tortuosity and densification of bulk paste reduce concrete permeability while the ITZ and percolation effects increase permeability. More specifically, when aggregates are sufficiently closely-spaced that the adjacent ITZs overlap in space, fluid and ions transport is significantly enhanced [28, 74].

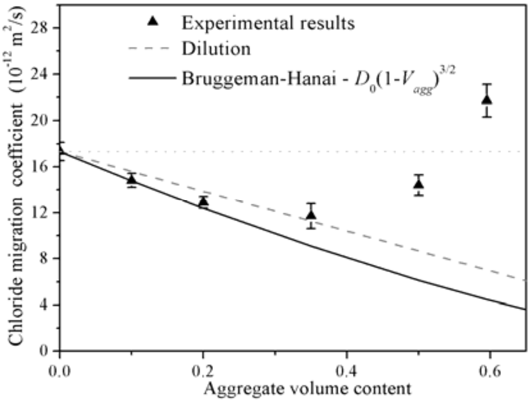

Fig. 3.26 Non-steady-state chloride migration coefficients versus aggregate volume content.

The experimental results plotted against the volume fraction of aggregate, and compared with the model line $D_0(1\text{-}V_{\text{agg}})$ and $D_0(1\text{-}V_{\text{agg}})^{3/2}$ are shown in Fig. 3.26. As indicated previously, the law does not consider two factors. One is the densification effect of bulk paste due to the redistribution of cement in mortar, and the other is the effect of ITZ, which could influence the transport due to its characteristics different from that of paste. In Fig. 3.26, it is found that and the ITZ effect does not seem to significantly influence the overall migration coefficient of the mortar at low aggregate content. However, the migration coefficient is affected by the ITZ at higher aggregate content. At V_{agg}=0.50, the D_{nssm} is increased from B-H law of

4.47×10^{-12} m^2/s to 14.40×10^{-12} m^2/s, and the ITZ effect would dominate the effect of the blocking aggregate, the densification and the tortuosity of bulk cement paste.

In order to get in side into the effect of ITZ on the migration, an approximation is proposed based on the B-H law, which has been explained in Eq.(3.22) and can be expressed as:

$$D_{nssm} = \alpha D_0 e_{\mathrm{V}}(h)^{3/2} + D_{\mathrm{ITZ,\,I}} V_{\mathrm{ITZ}} \tag{3.26}$$

Where D_{nssm} is the non-steady-state chloride migration coefficient, a is the densification factor which is related to the aggregate volume fraction (a=1 in case of neat cement paste), D_0 is the chloride migration coefficient of neat cement paste, $D_{\mathrm{ITZ,\ I}}$ is the intrinsic migration coefficient of ITZ. According to measured D_{nssm} and calculated $e_{\mathrm{V}}(h)$ and V_{ITZ} (in Table 3.4), the $D_{\mathrm{ITZ,\,I}}$ can be obtained by using the least square method. Taking a fixed ITZ thickness of 15 μm for instance, the obtained $D_{\mathrm{ITZ,\,I}}$ is 372.52×10^{-12} m^2/s.

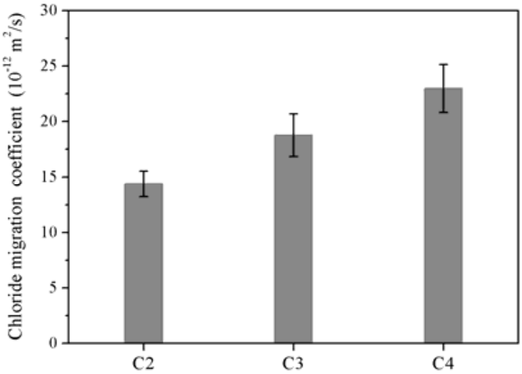

Fig. 3.27 Non-steady-state chloride migration coefficients of concretes.

The D_{nssm} of samples prepared with different grain size is shown in Fig. 3.27. At a constant aggregate volume content and fixed thickness of ITZ, using a finer aggregate size increases the ITZ content which would increase the transport properties. On the contrary, the experimental data are in the following order: C4>C3>C2. The D_{nssm} increases from 14.37×10^{-12} to 22.99×10^{-12} m^2/s with increasing average grain size from 4.46 to 12.76 mm. This finding is consistent with the observation in gas permeability and water absorption. In the previous discussion, assumptions have been made that the coarser sand is associated with coarser pore in the ITZ phase due to bleeding and segregation. The trapping of water beneath coarse aggregates is an extreme case of inhomogeneity.

3.3.5.2 Correlation between porosity and Dnssm

Fig. 3.28 (a) presents the D_{nssm} values for mortars versus the normalized porosity by the volume of bulk cement paste, which represents the ideal case of a porous paste diluted by nonporous aggregates. The D_{nssm} decreases significantly with increasing nomalized porosity significantly from M0 to M35. This can be explained by the increase in the effective transfer path length (tortuosity effect). These effects tend to be cancelled out by the pronounced ITZ effect with increasing the aggregate volume content to 0.5. At a given aggregate volume content (Fig. 3.28 (b)), using a coarser grain size decreases the tortuosity of paste which would reduce the effective flow path and increases the transport properties. As confirmed in section 3.2 and 3.3, coarser pore in the ITZ phase due to bleeding and segregation are expected in C3 and C4, which could increase averaged ITZ width significantly and enhance its effect.

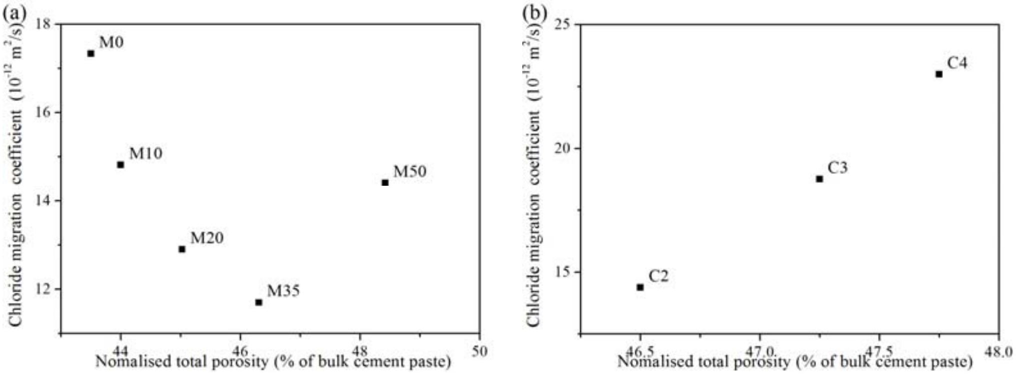

Fig. 3.28 D_{nssm} versus normalized porosity of bulk cement paste, (a) mortars and (b) concretes.

3.3.6 BSE image

To investigate the effects of aggregate size on the microstructure of ITZ due to the bleeding and segregation effect, BSE images were obtained at the top, bottom and side positions of the aggregate. The schematic of cutting plates and imaging point is given in Fig. 3.29. Within these images the unreacted anhydrous cement appears white, calcium hydroxide as light grey, and the porosity as black.

Fig. 3.30 presents the BSE images of mortar M60, it is found that the constituents in the region of ITZ at the side, top and bottom of the aggregate were fairly similar. The microstructure within ITZ is firstly determined by the packing of anhydrous. Prior to encountering an aggregate particle, the anhydrous predominantly move downwards in a vertical direction. Most of the anhydrous will stop moving entirely when they encounter an aggregate, and pack within the regions at the top of the aggregate. In the work by Crumbie [16], the distribution of all the cement constituents are highly dependent on the water to cement ratio. At low w/c ratio, the packing of the small anhydrous cement particles in the ITZ is fairly similar in both the top and bottom of the aggregate particles. On the contrary, there is a significantly lower amount of anhydrous cement remaining within ITZ at the bottom compared to that at the top of the aggregate. In this chapter, the aim is to assess the microstructure with the position around different particle sizes due to bleeding and segregation.

The images obtained for the ITZ in concrete C2 also show that the visible differences at the side, top and bottom are small (Fig. 3.31). This just confirms that no significant bleeding and segregation is presented for the samples containing a maximum grain size of 8 mm. Comparing the BSE images of C2 with that of C1(M60), the microstructure within ITZ is fairly similar at different positions. Therefore, the difference between C2 and C1 in the microstructure seems to be negligible concerning the position of ITZ. However, the details with respect to the distribution of porosity and anhydrous should be further analyzed.

The images within the ITZ in concrete C3 are given in Fig. 3.32. At the side of the coarse aggregate (Fig. 3.32(a)), a much lower amount of anhydrous in the region closest to the aggregate is observed. However, by visual observation, the porosity in the region of ITZ and the bulk cement matrix seems fairly similar. The most significant features are shown in the high porosity and large pore size at the bottom of the aggregate ((Fig.

3.32(b)). The migration of calcium ions to the ITZ is also reduced, since the products CH form more locally in the hydrating cement matrix [16]. The overall increased porosity and pore size decreases the initial overall amount of anhydrous cement, and therefore the amount of small anhydrous cement particles available to pack in this region. The porosity is unlikely to be minimized with further hydration, and would promote the movement of ions and exert detrimental influence on the transport properties. The combination of significant bleeding, reduced migration and significantly lower amount of anhydrous cement initially packing within the regions, results in the exaggerated “ITZ effects”.

Fig. 3.33 shows the BSE images of concrete C4 at different position. Similar microstructural features as for C3 are observed, but a lower magnification was used to obtain a wider visual area. The influences of bleeding and segregation during the casting are also significant for the microstructure of C4. This is in agreement with the highest transport coefficients in the durability tests. Compared with the aggregates used in C3, the surface of aggregates in C4 is more irregular and shows higher roughness. The rougher surface of the aggregate is able to retain more small anhydrous cement particles as the aggregate moves through the cement paste during casting and setting. The distribution of the microstrutural constituents within ITZ in C4 is expected to be denser than that of C3, but this is cancelled out by the significant bleeding and reduced migration. Additionally, a contrast microstructure was obtained in one image with respect to the position effect (Fig. 3.33(c)). This further confirms the redistribution of microstructure at the bottom of the aggregate, and suggests that future investigations with respect to the microstructure of ITZ in real concrete should also take the position effect into account.

For obtaining a quantitative distribution of phases within ITZ, a certain amount of images is required. This is difficult for samples containing large aggregate sizes and more slices are needed to be prepared. In this chapter, therefore, only visual differences were obtained whilst the quantitative distribution of microstructural phases was not involved. In our work, the significant bleeding and segregation were present in the samples containing a maximum grain size of 16 and 20 mm. This additional parameter should be considered during the analysis and increases the negative "ITZ effect". Therefore, the maximum grain size of 8 mm is employed in the following investigation and data concerning the distribution of phases within ITZ will be given in the following chapter.

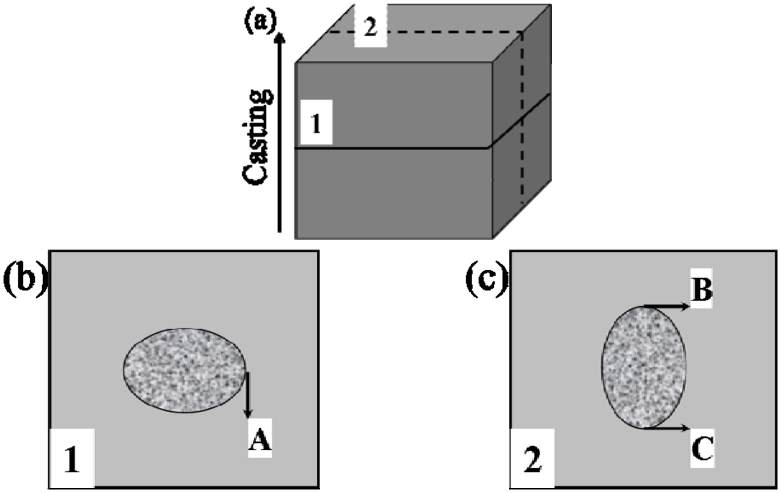

Fig. 3.29 Schematic of the cutting procedure (a) and the imaging point: A-side, B- top and C-bottom.

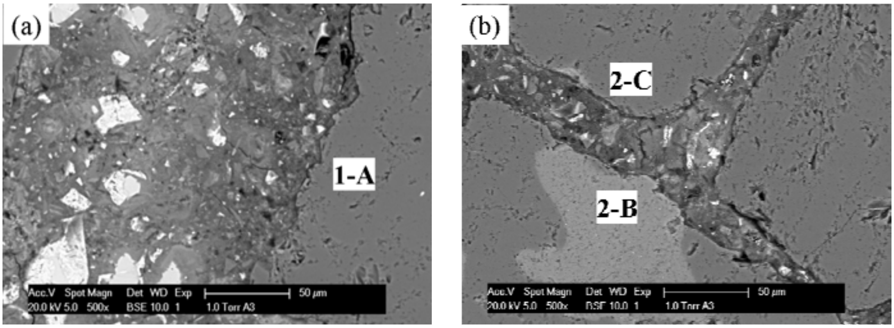

Fig. 3.30 BSE images of M60 (a) imaging point A and (b) imaging point B and C.

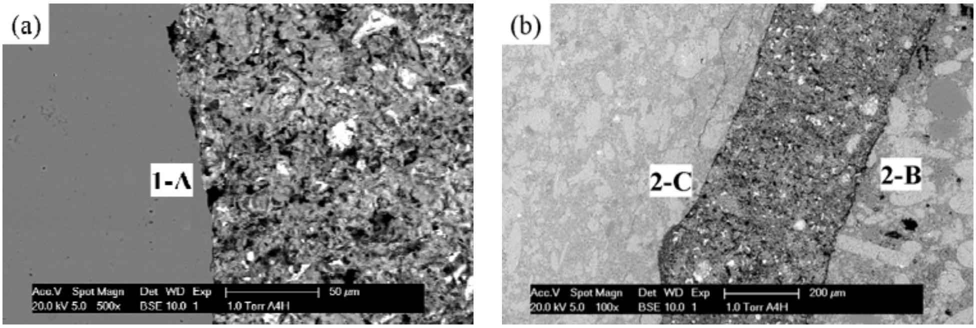

Fig. 3.31 BSE images of C2 (a) imaging point A and (b) imaging point B and C.

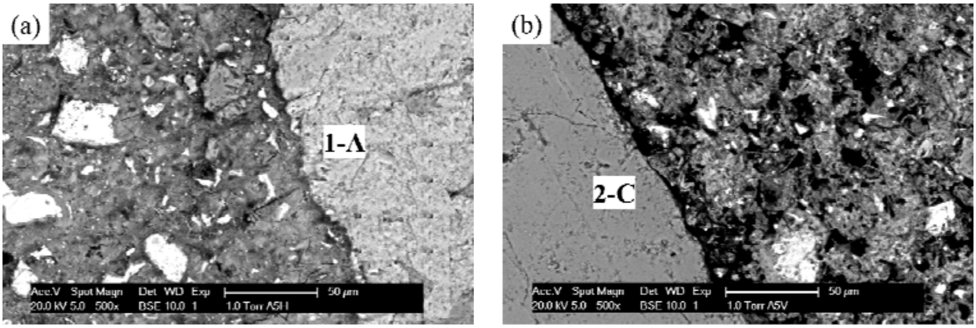

Fig. 3.32 BSE images of C3 (a) imaging point A and (b) imaging point C.

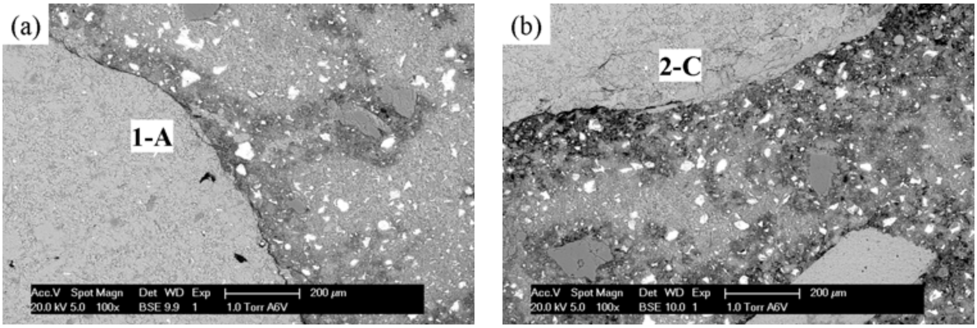

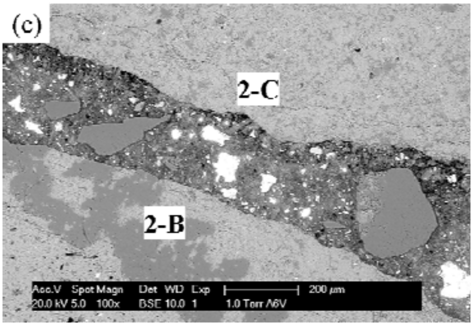

Fig. 3.33 BSE images of C4 (a) imaging point A, (b) imaging point C, (c) imaging point B and C.

3.3.7 Discussion

While analyzing the effect of ITZ on the transport properties, several parameters such as cracking and bleeding, will influence the final results significantly and should be taken into account. For example, the microcracks caused by drying shrinkage are one of them. In the measurement of gas permeability, comparing the experimental data with the model line, it is found that the typical ITZ effect which would increase the transport properties when the aggregate volume content increase is not obvious. This could be caused by the high permeability of neat cement paste, since the model line was calculated based on the sample without aggregate additions. The cracks formed in the neat cement paste are able to span a longer distance without any obstruction. In samples containing more aggregate, the growing cracks would be arrested by or traverse around the aggregate, theses cracks have more tortuous paths and larger effective lengths because they are easily blocked or forced to circumvent the aggregates [152]. Therefore, the concluded ITZ effect in relation to the gas permeability is underestimated. On the other side, the determined ITZ effect on sorptivity and migration coefficient is more remarkable. There are some theoretical and experimental studies indicating that microcracking has very little effect on diffusion compared with pressure-induced flow [43, 89, 142, 157]. It has been shown that for mortar, diffusivity scales as r and permeability scales as r^3, where r is a critical pore radius based on percolation ideas. Sorption in tube models predicts that the sorptivity scales as $r^{1/2}$. If effects due to the tortuosity of the porous medium are included, it can be shown that permeability scales as r^3. Then sorption should scale more closely with r. Therefore, the microcracks exert more influence on the permeability than on the diffusivity and sorption.

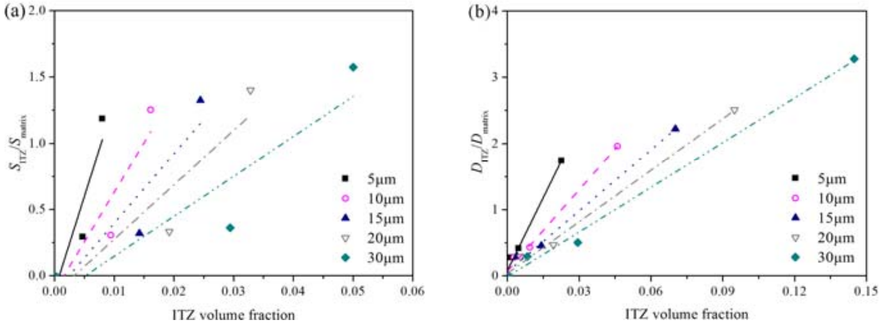

Fig. 3.34 Effect of ITZ width and volume fraction on the (a) $S_{\mathrm{ITZ}}/S_{\mathrm{matrix}}$ of secondary sorptivity, and (b) $D_{\mathrm{ITZ}}/D_{\mathrm{matrix}}$ ratio.

The influence of ITZ on the transport properties also depends highly on the contrast between the ITZ and that of the bulk cement matrix [23, 87]. For mortars with a w/c ratio of 0.5, a range of aggregate volume contents and assumed ITZ thicknesses, the sorptivity and migration coefficient ratio between the ITZ and bulk cement paste can be calculated by using Eq. (3.27) - (3.30). The obtained ratio versus ITZ volume content is given in Fig. 3.34. It can be seen that the ratio increases with ITZ volume fraction and ITZ width. For a given aggregate volume content and size (M50 and M60), the ratio between ITZ and bulk paste for a range of mass transport is given in Fig. 3.35. It can be observed that the ratio increases with ITZ width and the lowest contrast is the initial sorptivity. Recall that the amount of aggregate and ITZ thickness determine the volume fraction of ITZ and therefore determine the increasing effect of ITZ on the transport properties. Additionally, the transport properties of ITZ are approximated as the average of all the ITZ shell, although the real ITZ microstructure is spatially variable and its gradient is not uniform for each and every aggregate particles.

$$D_{\mathrm{nssm}}=D_{\mathrm{matrix}}+D_{\mathrm{ITZ}}=\alpha\cdot D_0\cdot e_{\mathrm{V}}(h)^{3/2}+D_{\mathrm{ITZ}} \qquad (3.27)$$

$$S=S_{\mathrm{matrix}}+S_{\mathrm{ITZ}}=\alpha\cdot S_0\cdot e_{\mathrm{V}}(h)^{3/2}+S_{\mathrm{ITZ}} \qquad (3.28)$$

$$\frac{D_{\text{ITZ}}}{D_{\text{matrix}}} = \frac{D_{\text{nssm}} - \alpha \cdot D_0 \cdot e_{\text{V}}(h)^{3/2}}{\alpha \cdot D_0 \cdot e_{\text{V}}(h)^{3/2}} \tag{3.29}$$

$$\frac{S_{\text{ITZ}}}{S_{\text{matrix}}} = \frac{S - \alpha \cdot S_0 \cdot e_{\text{V}}(h)^{3/2}}{\alpha \cdot S_0 \cdot e_{\text{V}}(h)^{3/2}} \tag{3.30}$$

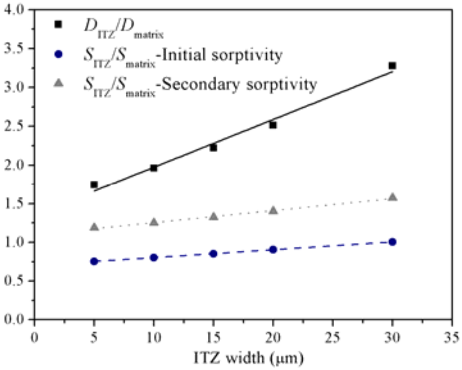

Fig. 3.35 Effect of ITZ width on the $S_{\text{ITZ}}/S_{\text{matrix}}$ and $D_{\text{ITZ}}/D_{\text{matrix}}$ ratio.

Although the ratio presented in Fig. 3.34 shows the same trend with increasing ITZ volume and ITZ width, the increased amplitude is varied in accordance with the sand content and ITZ thickness. The reason for this could be attributed to the interconnection of ITZ. Previous experimental and theoretical studies have also shown that ITZ percolates in samples when the adjacent aggregates are close enough [28]. The porous ITZ tends to interconnect at higher aggregate content with a fixed ITZ thickness, or at wider ITZ thickness with a fixed aggregate volume content. The degree of ITZ interconnection, *IC* is defined in this study as:

$$IC = 2h/d \tag{3.31}$$

Where *h* is the thickness of ITZ, *d* is the average distance between adjacent aggregate which has been given in Fig. 3.9.

When the *IC* is equal to 0 (either the thickness is 0 or the aggregate content is 0), the transport properties will be dominated by the bulk cement matrix and ITZ does not exert any influence on the overall properties. The ITZ will begin to percolate completely when the *IC* reaches 1. The ratio of chloride migration transport between ITZ and bulk cement matrix versus the degree of interconnection is given in Fig. 3.36. It is observed that the influence of ITZ increases with the increase of the degree of ITZ connection continuously until 1.0. Beyond 1.0, there is a sudden increase in $D_{\mathrm{ITZ}}/D_{\mathrm{matrix}}$ ratio, indicating the negative percolation effect when the adjacent ITZ start to interconnect. In this work, the critical aggregate content, at which the adjacent ITZ starts to percolate, can only be obtained after the exact ITZ thickness and inter-aggregate space are given. Although some positive information has been given, further investigation with respect to how much the percolation determine the overall properties of the composites need to be carried out.

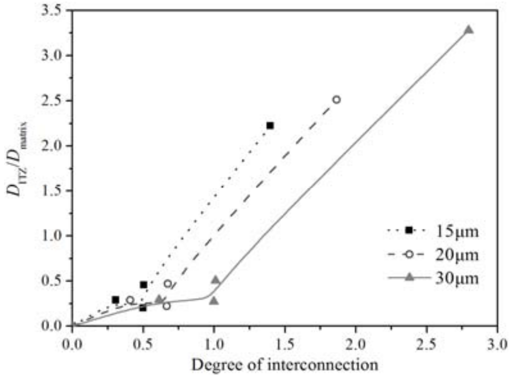

Fig. 3.36 Effect of the interconnection on the $D_{\mathrm{ITZ}}/D_{\mathrm{matrix}}$ ratio.

Another important parameter in the mortars is the air void systems, which is often badly controlled in samples containing a high amount of aggregate and depends strongly on the compacting procedure of the fresh mixtures. It is often assumed to play a negligible role in the mass transport, but large air voids would also have their associated ITZ and would be packed very close to the aggregate particles in certain cases [158]. In these cases, the region closest to the voids is potentially more porous than the ITZ around aggregates. The air voids may not be treated as inclusions with zero transport properties depending on their saturation degree [88]. The air voids in saturated samples are also able to exert some negative effect on the mass transport. However, there has been no systematic experimental study to assess the effect of the degree of saturation of air voids on the mass transport and needs to be future investigated.

The mortars and concretes used in the experiments are far more complicated than the three-phase model presented here. Real aggregate particles are not spheres, and thereby have a larger specific surface and create more ITZ than spherical aggregate particles at the same volume fraction. However, this approximation is not likely to have a huge influence on the estimated diffusivities, as evident from our work. In this study, the cracking due to drying conditioning, compacting, exaggerated ITZ width due to bleeding would dominate the mass transport to a high extent. This will also increase the ITZ effect. Therefore, to assess the effect of ITZ on the properties of cement based composites, a suitable preconditioning procedure, controlled compacting and suitable mixtures are necessary. In the following chapters, the maximum grain size of 8 mm, conditioning procedure without oven-drying, aggregate volume faction ranging from 0 to 0.55 and transport measurements which are not induced by pressure, are employed to evaluate the properties of ITZ and its relationship with durability.

3.4 Conclusions

In this chapter, the relatively importance of ITZ, preconditioning regime, aggregate volume content and size on gas permeability, capillary water absorption and non-steady-state chloride migration was investigated. Mortars and concretes were approximated as three-phases models representing the impermeable aggregates, bulk cement matrix and ITZ with assumed widths. To assess the effects of aggregate size on the microstructure of ITZ due to the bleeding and segregation, BSE imaging was performed at the top, bottom and side positions of coarse aggregates. The following main conclusions can be drawn as:

1) For the study of the effect of ITZ and its percolation on the transport properties, several other factors should be considered with the variation in aggregate: (i) the dilution and tortuosity of the bulk cement paste by using high aggregate volume fraction or finer aggregate size decreases the permeability; (ii) the densification of bulk cement matrix associated with the presence of ITZ decrease the permeability; (iii) the presence of ITZ and its percolation increases the transport properties.

2) The overall porosity decreases with increasing aggregate volume

content due to the dilution effect by impermeable aggregates. The capillary porosities are above the theoretical line obtained from $P_0 \times (1-V_{agg})$ (dilution effect) except for mortar M10, which can be attributed to the presence of high porous ITZ when grains were added into the neat cement paste. On the other hand, more porous ITZ is expected to be accompanied by a denser bulk cement matrix, which leads to a decrease in the porosity of mortar M10. The capillary porosity of samples prepared with varied grain size is in the following order: M60(C1)>C4>C3>C2.

3) An increase in gas permeability due to oven-drying induced cracks is all the more significant as the bulk cement matrix volume increases. The cracks formed in samples with higher aggregate volume content have more tortuous paths and larger effective lengths because they are easily blocked or forced to circumvent the aggregates. The cracks in neat cement paste tend to span a longer distance without any obstruction, and lead to a higher permeability which is less sensitive to the further hydration.

4) The microcracks exert more influences on the permeability than on the migration and sorption. Since the migration scales as r and permeability scales as r^3, where r is a critical pore radius based on percolation ideas. Sorption in tube models predicts that the sorptivity scales as $r^{1/2}$. The concluded ITZ effect in relation to the gas permeability is underestimated, while the ITZ effect on sorptivity and migration coefficient is more remarkable.

5) When the aggregate volume content increases from 0 to 0.6, the gas permeability, initial and secondary sorptivity decrease. The gas permeability and sorptivity of concretes made with different aggregate size are in the following order: C4>C3>C2>C1, while the water absorption showing the following order: C4>C1>C3>C2. An increase of the sand volume fraction leads to a decrease of migration coefficient until 0.35 due to the densification, dilution and tortuosity effect induced by the inclusions. Then a significant increase in the migration coefficient was observed when the aggregate content

increased from 0.35 to 0.60.

6) No visual differences were observed in BSE images obtained from the side, top and bottom of C1 and C2. The visual difference in the porosity between the region of ITZ and bulk cement matrix at the side of C3 and C4 is fairly similar, while high porosity and large pore size can be easily observed at the bottom of these samples. Additionally, a contrast microstructure was obtained in one image with respect to the position effect.

7) The ratio of mass transport between ITZ and bulk cement matrix increases with increasing ITZ volume and width. The influence of ITZ is also becoming remarkable as the adjacent ITZ percolates.

Chapter 4

Influence of GGBS and LF on the microstructure of ITZ in relation to mechanical properties, chloride migration and water absorption

4.1 Introduction

The literature review and previous chapter have highlighted the distinguishing microstructure of the ITZ and its role on the transport properties of concrete. For this reason, some efforts are needed to improve the quality of this so-called weak region. Monteiro [159] pointed out that studies which approach the improvement of the ITZ should be priorized before any systematic work is done to understand the cement matrix microstructure aiming to increase concrete properties. Since many important properties of the concrete are significantly influenced by the characteristics of that ITZ.

It has been stated that the bigger the difference between the strengths of the ITZ and the surrounding matrix, the higher the tendency of micro-cracking in the ITZ [58, 160]. In the study done by Bentz and Garboczi [161], increases in compressive strength of the concrete have been linked to an improved ITZ microstructure. Much denser, stronger and tougher ITZ would produce a stronger and tougher material. In special cement composites where very excellent properties are needed, the ITZ characteristics and their influences on the properties of the composite play a very crucial role [160]. Therefore, it is necessary to control and modify these characteristics to achieve optimum results. Moreover, the percolation or interconnection depends on the thickness of ITZ. By decreasing ITZ thickness or the porosity in the ITZ, the probability of ITZ percolation can be reduced. This also suggests that reducing the ITZ thickness is one method for decreasing the likelihood of ITZ percolation.

The microstructure of the ITZ is initially determined by the packing of the anhydrous cement grains against the much larger aggregate particles. The well known “wall effect” leads to a depletion of anhydrous cement in the ITZ, approaching zero at the aggregate surface. As a result of the anhydrous distribution there is an increase in the amount of porosity in the ITZ [5-6, 40, 93]. According to literature [6, 16, 29, 134, 162], the structural features can be described by the sequence of its development from the time concrete is placed as follows: (i) in freshly compacted concrete, water films form around the large aggregate particles. This would account for a higher water to cement ratio closer to the large aggregate than away from it; (ii) in the same way as in the bulk cement matrix, calcium, sulfate, hydroxyl and aluminate ions are produced by the dissolution of calcium sulfate and calcium aluminate compounds, and are then combined to form ettringite and calcium hydroxide. Owing to the higher water to cement ratio, these crystalline products in the vicinity of the coarse aggregate consist of relatively larger crystals. Therefore, they form a more porous framework than in the bulk cement matrix; (iii) with the progress of hydration, poor crystalline C-S-H and a second generation of smaller crystals of ettringite and CH start filling the empty space that exists between the framework created by the large ettringite and large flat CH crystals. This helps to improve the density and hence, the strength of the ITZ.

Based on the structural features, modification of the ITZ can be achieved by changing the spatial arrangement of the small grains, densifying the microstructure and reducing the mircrobleeding around aggregate particles. The modification process mainly has to do with densification and reducing the thickness of the ITZ, which can be done by using a finer cementitious material, pozzolanic materials, superplasticizer and advanced mixing procedure. These processes can be chiefly classified into two main types: (i) coating aggregate surfaces with some chemical reagents or polymers before mixing [111, 113]. However, the pre-treatment process before concrete production will lead to a higher cost, and the practical potential may be limited; ii) using mineral admixtures such as silica fume, fly ash, metakaolin for partial replacement of cement. Such materials participate in the particle packing and longer-term pozzolanic reactions which continue to densify the ITZ. Moreover, the fine particles can also act as growth nuclei for multiple generations of CH crystals which therefore have smaller size [8, 28, 44, 48, 50-52, 65, 113, 163-164].

As indicated in the literature review, most researchers found that silica fume is a highly effective admixture for improvement of concrete properties due to enhancement of the transition zone [48, 110, 113-114, 165]. It is argued that very fine silica fume particles behave as micro-filler and nucleation sites for crystallization of hydration products, leading to formation of small crystals of calcium hydroxide and a reduced tendency for preferred orientation [110, 113-114]. In addition, pozzolanic reaction between silica fume and calcium hydroxide reduces calcium hydroxide content and increases transition zone density [165]. Rossignolo [110] has shown that the usage of 10% of silica fume caused a reduction of 36% in the thickness of the matrix-aggregate ITZ, in relation to the reference concrete. It was also observed that addition of silica fume increased interfacial bond strength and interfacial fracture energy by about 100% [46]. The interfacial bond improvement effect of such materials is due to their small particle size and pozzolanic reactivity, leading to denser microstructures and stronger interfacial bond. Moreover, it was also found that the microstructure of ITZ can be modified by using metakaolin [65, 95], fly ash [50-52], rice husk ash [115] and etc.

Ground granulated blast-furnace slag (GGBS) is a glassy by-product of blast furnace iron making. It mainly contains calcium silicoaluminate with high reactivity [120]. Appropriate use of GGBS can result in better workability and pumpability, lower hydration heat, and reduced CO_2 emission for cement-based materials [120-121]. Generally, incorporating

GGBS into cementitious binders of cement-based composites can increase total porosity but refine the pore size [42,120,122-124]. The pore refinement by GGBS is attributed, at macro-scale, to the filling effect of GGBS particles in the binder particle packing, and, at micro-scale, to the pozzolanic reaction of active silica-alumina in GGBS particles [120, 124]. The beneficial effect of GGBS on pore refinement can improve the performance of materials, such as freezing action, carbonation, sulfate attack, gas penetration, chloride migration and reinforcement corrosion [125-128].

Previous researches on the concrete containing GGBS have been conducted mainly with focus on the overall properties or on the properties of the bulk cement paste. However, very limited information has been given with respect to the improvement by GGBS of the weak ITZ region. Additionally, there seems to be no data available about how much improvement can be made in the overall properties of concrete through improvements of ITZ. It is not clear whether properties enhancements are due principally to the improvement of ITZ or to bulk cement matrix itself.

Incorporating GGBS in binary blends to improve the performance of concrete may have associated limitations with its use, such as early age strength, extended curing periods [128, 166-167]. The use of appropriately proportioned ternary blends allows the effects of one powder to compensate for the inherent shortcomings of another [128, 168-169]. Among them, limestone filler (LF) is one of the potential materials which can offset the negative effects of GGBS especially on early-age [166, 170-171]. The use of limestone filler is a common practice in European countries due to its technical, economical, and ecological benefits [117, 119, 172-175]. In general, limestone filler improves the hydration rate of cement compounds and consequently increases the strength at early ages. Limestone filler does not have pozzolanic properties, but it reacts with the alumina phases of cement to form calcium monocarboaluminate hydrate with no significant changes on the strength [168-169, 176]. The main effects of limestone filler are of physical nature. It causes a better packing of the cement granular skeleton and a larger dispersion of cement grains. LF can also act as the crystallization nucleus for the precipitation of $Ca(OH)_2$ [117, 168, 170].

From the above description, it can be inferred that LF possesses the potential to alter the structure of the ITZ by changing the initial particle packing and facilitating the formation of smaller CH crystals with less crystallization tendency in preferential orientations. However, no quantitative information has been given on the influence of LF on the microstructure of ITZ. Moreover, the development of ternary binders, associating Portland cement, LF and GGBS, could be an alternative to modify the properties of ITZ, by combining their beneficial effects. Previous investigations have shown the advantages of such ternary blends for the overall properties of concrete and paste [166, 170-171]. More investigation needs to be done to further understand the mechanism underlying the effects on the structure of the ITZ, and to improve their utilization efficiency.

This chapter focuses on the role of GGBS and LF, used as partial cement replacement materials, on the thickness and porosity of the ITZ. The effects of these mineral additions on strength development, chloride migration and water absorption of mortars and concrete with systematically varied volume fraction and grain size of aggregate, hence, varied proportions of ITZ, are also examined. Moreover, whether the improvement in the overall properties is mainly due to the improvement of the ITZ, or due to the densification of the bulk matrix is also to be discussed. This would also help to achieve suitable mix proportions and facilitate the incorporation of more mineral additions.

4.2 Experiments

4.2.1 Materials and mixtures

This chapter considers ordinary Portland cement, GGBS and LF as binder components. The cement used is CEM Type I 52.5 N, the same as used in chapter 3. The GGBS originated from ORCEM company (the Netherlands), and the LF was offered by OMYA company (France). The chemical and physical characteristics of these materials are given in Table 4.1. As the fineness of the powder is an important parameter controlling the packing of binders, the particle size distribution curves of the materials were measured by the laser diffraction method (Mastersizer 2000) and are given in Fig. 4.1. The mineralogy of the slag was determined by quantitative X-ray powder diffraction analysis (QXRPD, Philips PW1830). Details about the quantitative analysis were explained elsewhere [177]. The results are indicated in Table 4.2. The sieve analysis of aggregates is given in Fig. 4.2. According to the conclusions in chapter 3, the maximum aggregate size of 8 mm was applied to minimize the bleeding effect.

Table 4.1 Chemical composition and physical characteristics of cement, slag and limestone filler

Composition	PC	GGBS	LF
	Weight (% by mass)		
CaO	63.12	40.10	-
SiO_2	18.73	35.40	0.80
Al_2O_3	4.94	11.25	0.17
MgO	1.02	7.82	0.50
Fe_2O_3	3.99	0.89	-
SO_3	3.07	0.61	-
Na_2O	0.73	0.33	-
K_2O	0.47	0.62	-
$CaCO_3$	-	-	98.00
Loss on ignition (LOI, %)	2.12	0.31	43.90
Blaine fineness (m^2/kg)	353	410	753
Specific density (kg/m^3)	3092	2890	2676
Median particle size (μm)	15.7	12.5	9.4

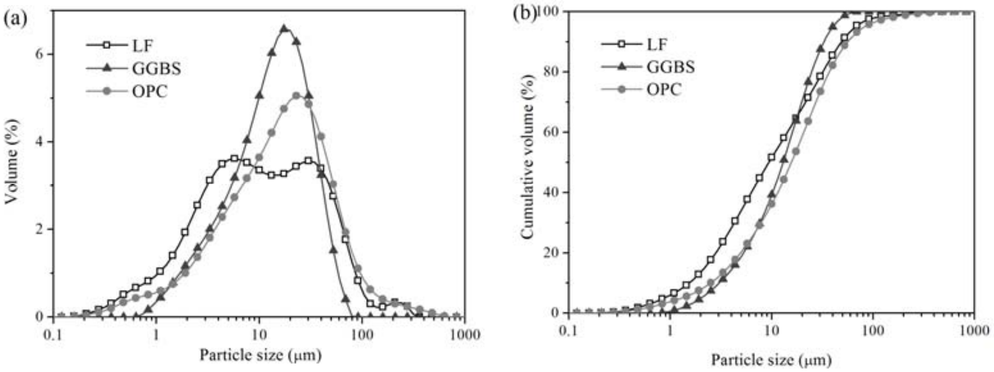

Fig. 4.1 Particle size distribution of the applied materials.

Table 4.2 Mineralogical phases of slag (XRD/Rietveld result) and PC (Bogue calculation) (% by mass)

Composition	Slag	Composition	PC
Akermanite	0.9	C_3S	66.92
Quartz	1.3	C_2S	3.22
		C_3A	6.34
		C_4AF	12.14

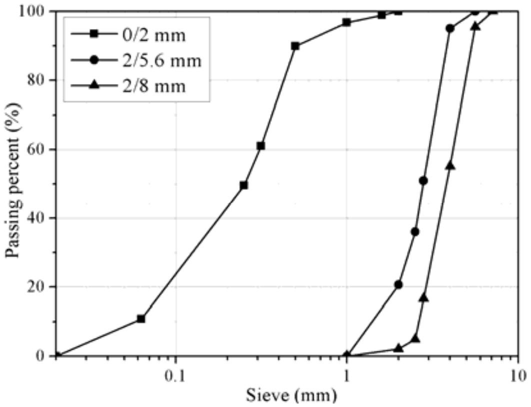

Fig. 4.2 Grain size distribution of aggregates.

Eight series of specimens were prepared in relation to the type and replacement levels of the SCMs. The percentage of different blended materials is given in Table 4.3. For each series, mortars and concretes with systematically varied volume fraction and grain size, hence, varied proportions of ITZs, were prepared (in Table 4.4). The mixtures are named "S**L**-Y" where "**" gives the SCMs substitution levels (C for reference samples without SCMs, "S" for samples with GGBS, "L" for samples with limestone filler), "Y" gives aggregate volume fraction and size features and "P" refers to the neat cement paste without aggregates. For instance, S60L10-4 corresponds to the binder containing 30% of PC, 60% GGBS and 10% LF, and the volume fraction of aggregate 0/2 mm and 2/8 mm is 0.2 and 0.35, respectively. Finally, this chapter comprises:

i) A control series of Portland cement-based samples and seven blended compositions prepared with binary and ternary binders.

ii) For each binder, one paste, four mortars and concretes are prepared by varying the aggregate volume content and aggregate size systematically.

iii) Forty mixtures were prepared in total.

All mixtures were prepared by mixing the binders with water at fixed water to binder (W/B) ratio of 0.45. After sufficient mixing and full compaction, the samples were cast into 150×150×150 mm^3. All the samples were demoulded after 24 h and then stored in the chamber with a constant temperature of 20±2°C and a relative humidity of 95±5% until designated testing age.

Table 4.3 Mixture proportions of blended materials

Mixtures (S**L**)	PC	GGBS	LF
C	100	-	-
S35	65	35	-
S70	30	70	-
L05	95	-	5
L10	90	-	10
S30L05	65	30	5
S65L05	30	65	5
S60L10	30	60	10

Table 4.4 Aggregate content and volume fraction for each blended system

Mixtures	Aggregate content (kg/m^3)			Aggregate volume fraction		
(-Y)	0/2 mm	2/5.6 mm	2/8 mm	0/2 mm	2/5.6 mm	2/8 mm
-P	-	-	-	-	-	-
-1	529.0	-	-	0.2	-	-
-2	1454.8	-	-	0.55	-	-
-3	529.0	919.1	-	0.2	0.35	-
-4	529.0	-	938.9	0.2	-	0.35

4.2.2 Tests and analysis method

4.2.2.1 BSE image analysis

There is still no consensus on the ITZ mineralogy and microstructure, because of the condition of the ITZ microstructure as a localized phenomenon that makes the process of identifying and analyzing the ITZ by bulk techniques very complicated. However, Scrivener and Gartner [21-22] established that backscattered electron microscopy is by far the best techniques to inspect these localized phenomena. The penetration of the electron beam into the specimen is in the order of a few microns, so that grayscale values at the interface may represent a mix of atomic number values from both aggregate and hydrated components. This technique was employed for its advances in providing a direct investigation and quantitative characterization, and has been proven useful for the study of ITZ microstructure [25, 36, 38, 160, 178-180]. However, there are still some challenges e.g. related to image analysis with regard to the porosity gradient distribution within ITZ. In this part, a new method for delineating strips from aggregate surface and porosity determination is applied [34].

Sample preparation

At the designated ages, core specimens were drilled from mortars-2 (prepared with 55% of aggregate volume fraction and 0/2 mm size). The acquired inner parts were split into small pieces. Thereafter, the obtained pieces were immersed in liquid nitrogen for 5 min to stop further hydration. After freezing, the specimens were transferred into a freeze-dryer in which temperature and vacuum were kept to -40°C and to 0.1 Pa, respectively. In this study, the freeze-drying time was 14 days.

For BSE image acquisition further sample preparation is necessary. The dried specimens were vacuum impregnated with low viscosity epoxy resin and heated in an oven of 30°C to reduce the setting time of the resin. After epoxy drying, the samples were ground with SiC paper of 320, 500, 1200 and 2400 grit for about 4 min each. Subsequently, the samples were polished with diamond paste of 3, 1 and 0.25μm for around 2 min each and cleaned up with low-relief polishing cloth.

BSE imaging

BSE images were acquired around random grains by using the BSE detector in the environmental scanning electron microscope with an acceleration voltage of 20 kV. Specifically, the images were captured at two magnifications, 100× and 500×. For each kind of specimen, 30 images with 500× magnification were captured and employed for quantitative analysis, since the field of view can usually be entirely filled with an interface. The images (500×) were digitized at 1424×968 pixels and each pixel is approximately 0.18 μm. Calibration of the image grayscale was optimized to provide best contrast across all images. Around 30 images were collected for each sample. Examples of original BSE images are presented in Fig. 4.3.

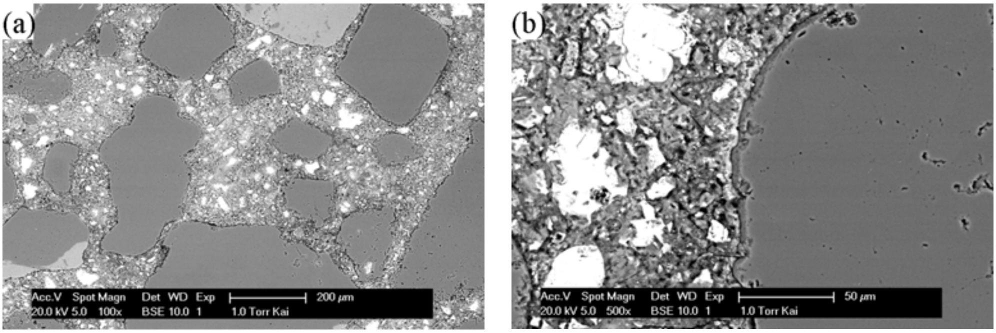

Fig. 4.3 BSE images on mortar C-2 at 2 months, (a) 100×, (b) 500×

Strip delineation

It was commonly believed that the components within ITZ exhibit a gradual distribution profile, such as the porosity and anhydrous. Therefore, a series of successive strips needs to be built starting from the surface of aggregate exactly. Within each strip, the fraction of the component versus the distance from the surface of aggregate can be given. Firstly, it was necessary to delineate the boundary of the aggregate to specify the ITZ. The BSE coefficient of hydration products was quite close to that of the aggregate, thereby it is difficult to specify the boundary automatically. Therefore, an artificial method by using image processing software was applied in this work. The delineated aggregate area was covered manually by white pixels (grey scale = 255).

After the aforementioned pre-treatment, positions of aggregate boundary pixels can be determined according to the grey scale difference between aggregate (255) and surrounding paste (<255). Subsequently, strips need to be delineated as the distance from the aggregate surface into the bulk cement matrix. In this study, a method named "concentric expansion" was employed to gain a simple definition of distance from aggregate surface. It is based on the concept of the surrounding layer of a circular aggregate. The least square method was used to fit over the aggregate boundary. With the fitted center, a concentric expansion is imposed on the original aggregate boundary. The expanded zone is taken as delineated strip. The algorithm of this method can be given by the Eq.(4.1) - (4.3) and the details about the mathematical algorithm were explained elsewhere [34].

$$(x_c, y_c, r) = cirfit\{(x_i, y_i); i = 1...n\} \tag{4.1}$$

$$X_i = x_i + s \cdot (x_i - x_c) / r \tag{4.2}$$

$$Y_i = y_i + s \cdot (y_i - y_c) / r \tag{4.3}$$

Where *circfit* is the least square fitting with respect to a circle, x_c, y_c, r is center coordinates and radius of the fitted circle, x_i, y_i the position coordinates of aggregate boundary pixels, X_i, Y_i is the boundary of a delineated strip, and s is the width of the strip. An example of aggregate boundary specification and strip delineation is given in Fig. 4.4, in which the width of the strip is 5 μm.

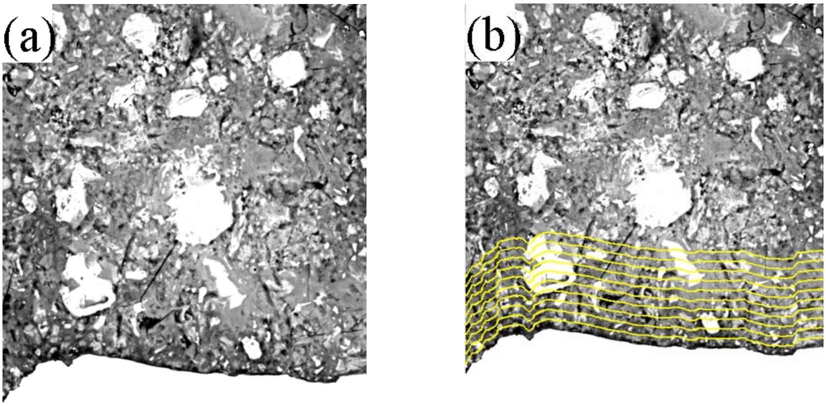

Fig. 4.4 Mortar C-2 at 2 months, (a) aggregate boundary specification, (b) strip delineation.

Phase segmentation

From literature, it is known that the most important features of ITZ are the phase redistribution within this region, such as the porosity and anhydrous. Within grey scale analysis, the determination of lower and upper threshold values in a histogram pattern are crucial for the further analysis. Several studies have also been conducted to segment different phases [181-182]. In this study, the overflow method is employed. Within this techniques, the slope of cumulative histogram of grey level displays three segmentations, i.e., pores, hydration products and anhydrous. More details on this method can be found in [181].

An example of phase segmentation procedure is indicated Fig. 4.5. Fig. 4.5 (b) is the frequency count histogram which is not able to achieve a satisfactory accuracy in differentiating pores and anhydrous simultaneously. The inflection point for capillary pores (Fig. 4.5 (c)) and anhydrous (Fig. 4.5 (d)) is determined in the cumulative grey level histogram (83 for the pore and 177 for the anhydrous). It is still worth to mention that the threshold values for each sample are averaged from selected images. Thereafter, pores and anhydrous segmentations can be conducted according to the thresholds and binary images. The corresponding examples are shown in Fig. 4.6.

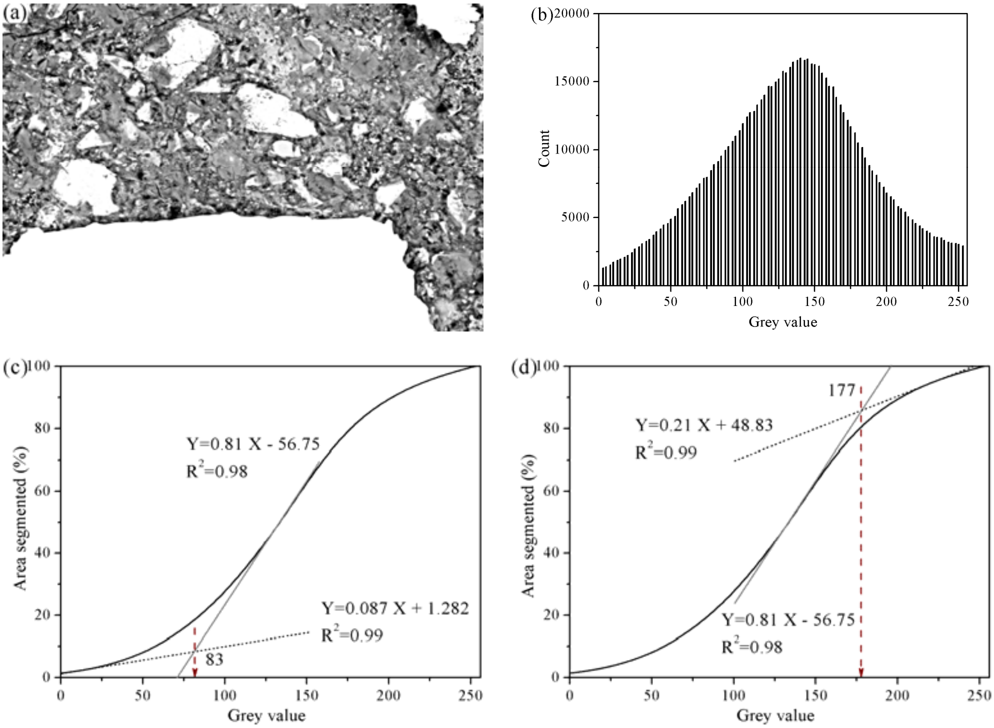

Fig. 4.5 Phase segmentation procedure for mortar C-2 at 2 months, (a) boundary specification, (b) frequency histogram, (c) inflection point for pores, (d) inflection point for anhydrous.

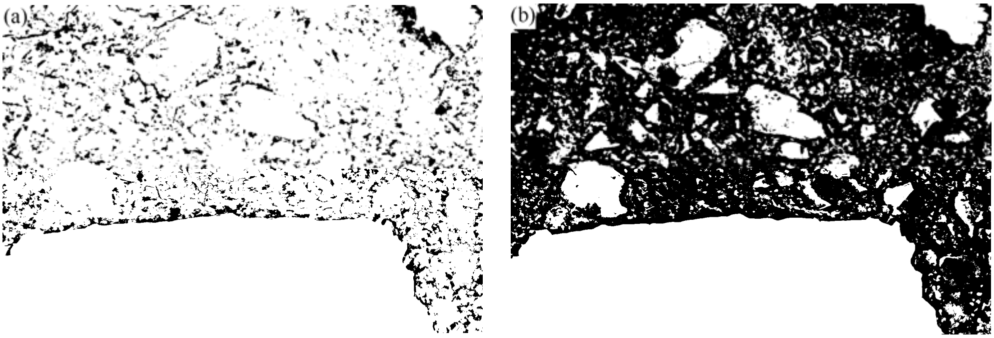

Fig. 4.6 Binary images from Fig. 4.5, (a) black pixels represent pores, (b) white pixels represent anhydrous.

Combining the strip delineation and phase segmentation, the phase distribution within the ITZ region can be obtained. Moreover, the anhydrous contains unhydrated cement, LF and GGBS. Fig. 4.7 presents an example of the phase distribution profile in 10 successive 5-μm strips from mortar C-2. It can be seen that both the porosity and anhydrous exhibit a gradual distribution profile. The porosity decreases while the anhydrous increases with increasing distance away from the aggregate surface.

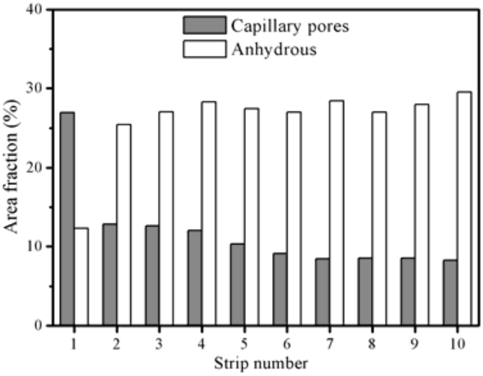

Fig. 4.7 phase distribution profile in 10 successive 5-μm strips from mortar C-2.

Energy Dispersive X-ray Spectroscopy

The Energy Dispersive X-ray analysis is expected to provide chemical evidence on the existence of calcium and silicon, which are the major elements of hydration products. In this study, the X-ray line analysis was performed on the mortar C-2 and S70-2 hydrated for 2 months to detect the presence of the various elements within the region of the ITZ. The detector dwelled 200-millisecond for each point. Ca/Si ratios were calculated and plotted against the distance from the interfaces. Final results are given by averaging 10 measurements. The samples containing LF powder were not involved due to the Ca/Si ratio of LF is close to the CH. This EDX analysis is supplementary to the SEM image analysis, and is able to further confirm the modification of the ITZ by pozzolanic reaction. An example of the analysis is given in Fig. 4.8.

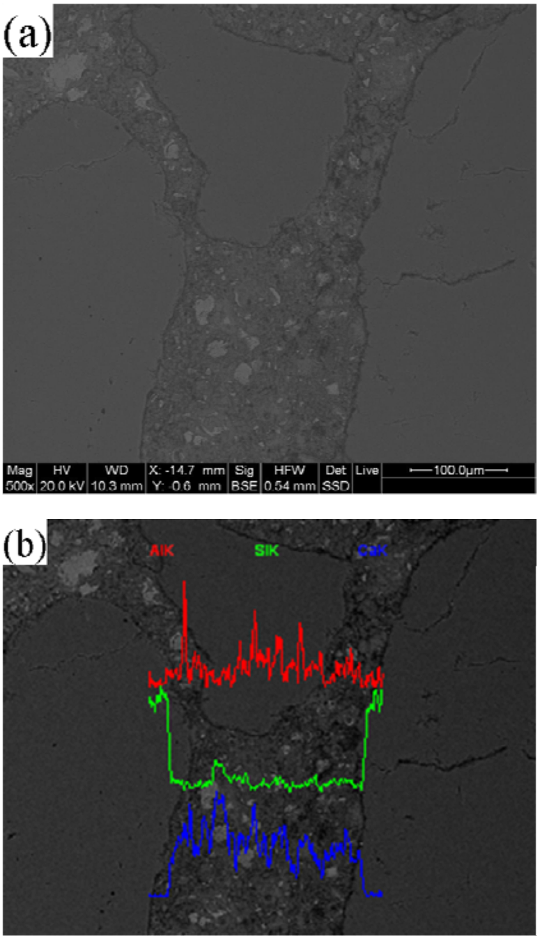

Fig. 4.8 EDX analysis in the ITZ of C-2 at 2 months (the spectrum refers to the corresponding element concentration).

4.2.2.2 Mercury intrusion porosimetry (MIP)

The principle of the MIP test lies in the fact that the intrusion volume of mercury depends on the applied external pressure to overcome the surface tension of mercury in pores [183]. The mercury intrusion and extrusion process can be quantified by intrusion (extrusion) volume versus increasing (decreasing) pressure. The total porosity is deduced from the total mercury intrusion volume and material apparent volume. The pore size distribution is usually expressed by the differential of the intruded volume in terms of pore diameter in logarithm scale.

MIP measurements were successfully performed on mortars with systematically varied aggregate volume fraction, to detect the influence of the ITZ on the pore size distribution [28, 41, 43]. This method is based on the assumption that the larger pores are essentially present in the ITZ region. It can not only indicate the pore size distribution, but also the connectivity or percolation of the pore system since only the continuous pores throughout the specimen can be reached. Therefore, a systematic MIP measurement is performed on the designed blended systems and samples of varying aggregate volume fraction and size. Due to the limitation for the sample size, the samples prepared with 2/8 mm aggregate were not involved in this study.

To avoid the boundary heterogeneity, the inner parts of the cubes were taken at designated testing age and reduced to particle samples of 1.5-3 g. Before the measurement, the collected pieces were dried by using the same freeze-drying procedure as in section 2.2.2.1. An automatic mercury porosimeter (Thermal Scientific PASCAL 140/440 series, Fig. 4.9) was used and the mercury intrusion and extrusion were performed with a minimum intruding pressure of 1.4 kPa and a maximum intruding pressure of 240 MPa. According to the Washburn-Laplace equation (Eq. (4.4)) given for a cylindrical pore, the corresponding detectable pore radius R ranges from 3.0 nm to 800 μm. The contact angle θ of 140° and the surface tension of mercury γ of 0.480 N/m were used in the calculations.

$$P = -\frac{2\gamma\cos\theta}{R} \tag{4.4}$$

Where P is the mercury intrusion pressure (in Pa), γ is the surface tension of mercury (in N/m), θ is the contact angle between solid and mercury, and R is the pore access radius (in m).

Based on the assumption of cylindrical shape of pores, several calculations were also carried out in this study. The total pore volume (V_{tot}) is the total intruded volume of mercury at the highest pressure determined. The pore size distribution is defined as the pore volume per unit interval of pore diameter according to Eq. (4.5)

$$D_V(d) = \frac{p}{d} \cdot \frac{dV}{dp} \tag{4.5}$$

The critical pore diameter d_c (in nm) is the diameter which corresponds to the maximum of porosity given by the pore size distribution or to the inflection point on the intrusion pore volume versus diameter curve. The mean pore diameter (d_{mean}) can be calculated by using Eq. (4.6).

$$d_{mean} = 4 \cdot \frac{V_{tot}}{S} \tag{4.6}$$

where S is the total pore surface area (in mm^3/g). It can be obtained by using Eq. (4.7).

$$S = \frac{1}{\gamma \left|\cos\theta\right|} \int_0^{V_{tot}} p dV \tag{4.7}$$

Fig. 4.9 Mercury porosimeter (Thermal Scientific PASCAL 140/440 series).

4.2.2.3 Strength and dynamic elastic modulus

For strength and ultrasound velocity test, specimens were cast into $40\times40\times160$ mm^3 prismatic moulds and mechanically compacted in two layers. After casting, the moulds were stored in the humid chamber at 20°C for 24 h. Specimens were demoulded after 1 day and stored in the fog room until designated testing age.

At 1, 3, 7, 28, 56 and 180 days, the flexural and compressive strength was determined according to the procedure of the European standard EN 196-1. Data reported represent the average values obtained on three specimens, corresponding to three flexural strength and six compressive strength values.

Using ultrasonic velocity measurements the dynamic elastic modulus can be estimated. Launch the ultrasonic wave through the concrete specimen and use the receiver to get the time. Then, set specimen length to calculate the supersonic speed for the test with both sides of the specimen daubed with lubricator. The dynamic elastic modulus was measured and calculated according to ASTM C 469 [19, 184].

4.2.2.4 Rapid chloride migration

To investigate the influence of GGBS and LF on the transport properties of concretes in relation to the ITZ, the non-steady state chloride migration test was performed following the NT build 492 standard [143]. The cylinder samples (Φ100×50 mm) were drilled and cut from the cubes at 14 days. The detailed procedure was explained in chapter 3 and elsewhere [143, 185].

4.2.2.5 Capillary water absorption

To investigate the influence of SCMs on the water absorption of samples in relation to the ITZ, the same method was applied as in chapter 3 [140]. The cylinder samples (Φ100×50 mm) were drilled and placed in an environmental chamber at 60% relative humidity and 20°C until 12 months. The preconditioned specimens were then covered with water-proof sheets, completely sealed on their circular sides and top to avoid evaporation and ensure unidirectional absorption. In order to ensure uniformity in the suction surface, the cutting face was chosen to be placed face down on two plastic rods in deionized water. The detailed procedure and calculation can be found in chapter 3.

4.3 Results and discussion

4.3.1 Microstructural investigation of the ITZ using BSE image analysis

4.3.1.1 Effect of LF

The BSE image examples of mortar L05-2 and L10-2 at the age of 2 months are shown in Fig. 4.10 and Fig. 4.11, respectively. The LF particles can be easily observed, especially in the high resolution images. Generally, LF does not posses pozzolanic properties. It can only react with the alumina phases of cement to form monocarboaluminate hydrate phases in relatively small quantities [168, 170]. This is the reason why the LF was still detected in the samples at the age of 2 months. It can be seen in the low resolution images (Fig. 4.10 (a) and Fig. 4.11 (a)) that the overall porosity tends to increase while increasing the LF content from 5 to 10%. This is mainly due to the dilution effect of LF, increasing local effective water to cement (W/C) ratio. Visually comparing the high resolution images of Fig. 4.10 (b) and Fig. 4.3 (b), it can be seen that the addition of 5% LF alters the microstructure to a certain extent. This will be confirmed by the quantitative analysis.

The calculated data for capillary porosity and anhydrous of each sample was obtained from 30 images and plotted against the distance from aggregate surface. The microstructural profile of each phase is illustrated in Fig. 4.12. Calculated results are in line with expected trends for the typical ITZ characteristics. The porosity reaches the highest value at the interface and reduces to around 10% at a distance of 50 μm. The anhydrous content is quite low at the interfaces, and rises with distance as the result of particle packing. From Fig. 4.12, it can be seen that there are remarkable differences between the reference mortar and the samples with LF. The porosity at each strip reduces with increasing LF content from 0 to 5%, and a significant increase in porosity is observed in the sample containing 10% of LF. Several effects need to be accounted for with the addition of LF powder, namely (i) filler effect which causes a better packing of cement granular skeleton and a larger dispersion of cement grains; (ii) nucleation effect which contributes to the formation of smaller CH crystals with less crystallization tendency in preferential orientations; (iii) dilution effect which reduces the quantity of cement and increase the effective W/C ratio at a fixed water to binder (W/B) ratio; (iv) chemical reactions between LF powder and the alumina phases of cement, which is not noticeable in the BSE image analysis [168, 170, 173, 175]. At 5% of LF addition, the filler effect and nucleation effect dominate the adverse dilution effect, and produce a denser microstructure. However, increasing LF addition to 10%, the dilution effect becomes prominent and leads to a more porous structure not only in the ITZ but also in the bulk cement matrix. Moreover, the reduction in the porosity from C-2 and L05-2 is more remarkable within the region close to aggregate (0-20 μm) than in the region farther away (>30 μm). This may be due to the differential particle size packing. The finer LF particles tend to squeeze themselves closer to the aggregate surface and alter the nearby region to a higher extent, such as replacing the large CH plates with smaller crystals showing less preferential orientation crystals, resulting in a denser structure.

On the other hand, the aforementioned effects simultaneously produce an acceleration of the hydration of cement grains. This is confirmed by Fig. 4.12 (b) in which the anhydrous content is lower for the samples containing LF powder at all distances. Interestingly, both anhydrous and porosity of L05-2 reaches constant values at a distance of 10-15 μm, while the porosity of C-2 reduces continuously with a distance up to around 25 μm. The significant changes occur within the first two strips for all the samples.

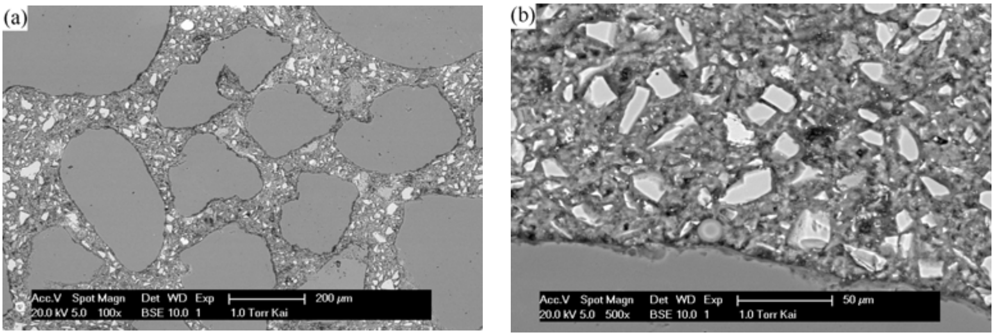

Fig. 4.10 BSE images of mortar L05-2 at 2months, (a) 100× and (b) 500×.

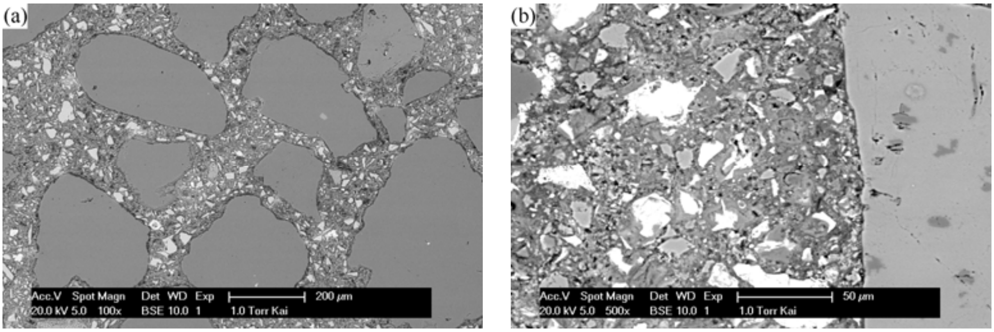

Fig. 4.11 BSE images of mortar L10-2 at 2months, (a) 100× and (b) 500×.

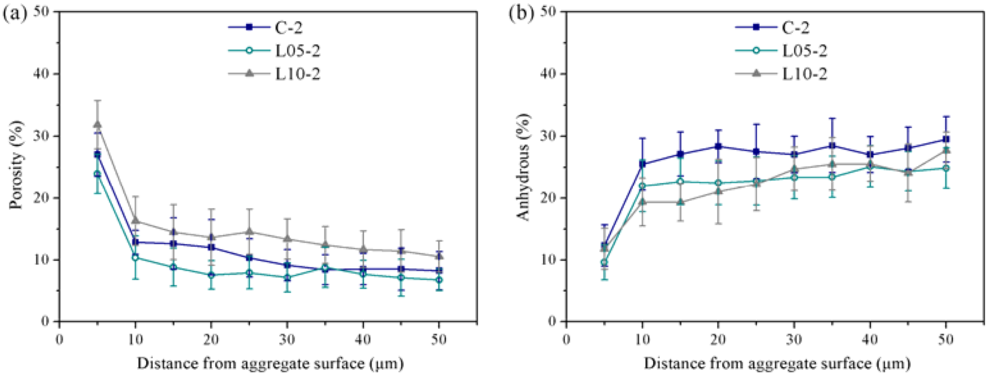

Fig. 4.12 Microstructural profiles in the ITZ (a) capillary porosity, and (b) anhydrous.

4.3.1.2 Effect of GGBS

The typical BSE images of mortar S30-2 and S70-2 at the age of 2 months are illustrated in Fig. 4.13 and Fig. 4.14, respectively. From the images at high resolution (500×), a reduced anhydrous content and size is seen in the region close to aggregate surface. The microstructure tends to compact while increasing GGBS content from 0 to 35%. On the contrary, the image in Fig. 4.14 (b) exhibits a more porous structure when the GGBS addition reaches to 70%.

Fig. 4.15 shows the microstructural profile in relation to the substitution amount of GGBS. It can be seen that the typical gradients of porosity and anhydrous exist for all samples containing GGBS. The porosity reaches the highest value at the interface, while the anhydrous content is quite low within the ITZ, and rises with distance. The porosity profiles in Fig. 4.15 (a) indicate that the addition of 35% of GGBS reduces the porosity at all distances and produces a denser microstructure both in the ITZ and bulk cement matrix. However, this improvement disappears when the substitution amount reaches to 70%. The main contribution of GGBS to the development of hardened cement paste is through the pozzolanic reaction. The pozzolanic particles produce a fast saturation balance of CH, with small crystal size in the ITZ, which results in formation of a dense cementitious matrix [164]. Usually, the mean size of CH crystals is larger than 10 μm in conventional PC concrete [8]. The pozzolanic reaction of GGBS significantly decreases the mean size of the CH crystal to 3-4 μm [164]. Therefore, the GGBS is able to decrease both the content and the arrangement of CH crystals. Moreover, the consumption of CH by pozzolanic reaction leads to a higher PC reaction degree, which is confirmed by a lower anhydrous fraction for mortar S35-2 compared with the reference sample (in Fig. 4.15 (b)).

On the other hand, the pozzolanic reaction of GGBS is limited by the amount of CH produced by cement hydration. With substitution of 70% GGBS, the available CH content for pozzolanic reaction will reduce. Therefore, the low GGBS reaction degree (Fig. 4.15 (b)) results in a more porous zone as observed in the BSE image and porosity profile.

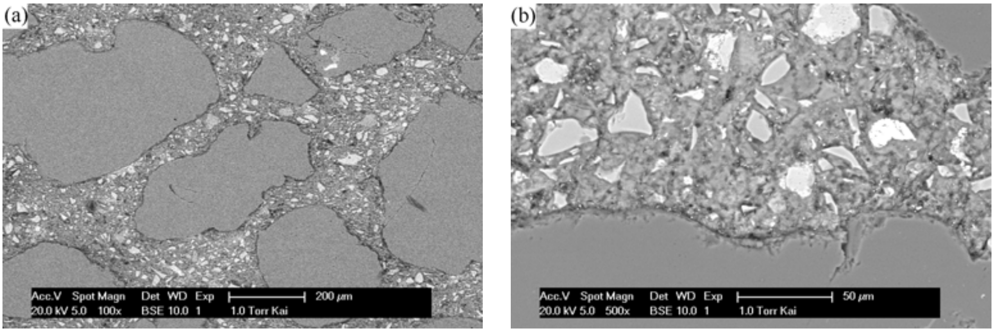

Fig. 4.13 BSE images of mortar S35-2 at 2months, (a) 100× and (b) 500×.

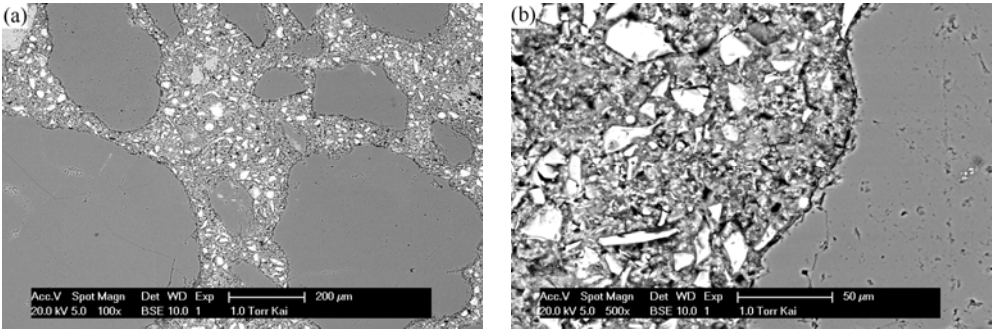

Fig. 4.14 BSE images of mortar S70-2 at 2months, (a) 100× and (b) 500×.

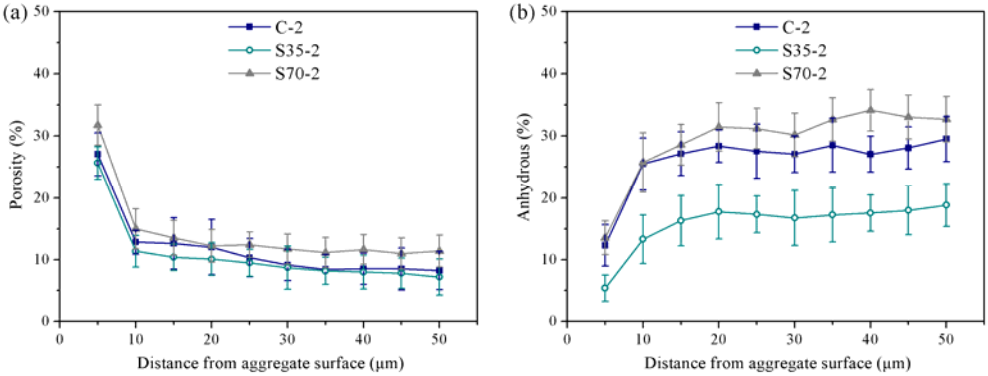

Fig. 4.15 Microstructural profiles in the ITZ (a) capillary porosity, and (b) anhydrous.

4.3.1.3 Combined effect of GGBS and LF

The BSE images of mortars prepared with PC-GGBS-LF ternary binders are given in Fig. 4.16. Corresponding phase distribution profiles are shown in Fig. 4.17 and Fig. 4.18, respectively. Compared with only GGBS partially replacing PC, the influence of GGBS and LF simultaneously substituting for a part of PC highly depends on the amount of LF. For binders with 35% replacement of PC by SCMs, the porosity of mortar S30L05-2 is marginally lower than that of S35. This reduction is more noticeable at the distance of 5 µm. It can be attributed to the increase in the reactivity of cement contributed by LF (nucleation site), which produces a higher formation rate of CH at early age and thus an increase in the pozzolanic reactions. Moreover, the smaller LF particles tend to pack themselves in the region close to the aggregate interface initially. It is possible to act as a dense skeleton which can be filled by hydration products, further densifying the microstructure within the ITZ. This could be the reason for the presence of relatively more remarkable reduction in the porosity at the distance of 5 μm. By contrast, the effect of LF on the anhydrous percentage displays a different trend (Fig. 4.17 (b)). The anhydrous fraction of S30L05-2 is higher than that of S35-2 at all distance, which could be explained by the presence of inert LF powders which was accounted for the anhydrous in this study. The majority of LF was not involved in the hydration and present as anhydrous in the BSE images (Fig. 4.16 (a)). Additionally, it is still worth to mention that the backscattering coefficient of CH is close to LF. It is possible that some CH was classified into anhydrous during the image analysis.

At a fixed 70% replacement by SCMs, the combination of the GGBS and LF has different effect on the phase concentration. From Fig. 4.18 (a), it can be seen that substituting of 5% LF for GGBS reduces the porosity at all distances. For a higher amount of LF substitution rate (10%), the porosity is higher than in case of S65L05 and the corresponding binary PC-GGBS series. Although it is believed that a higher LF content could increase the production rate of CH at a fixed PC content, this beneficial effect would be offset by the prominent dilution effect, which increases the local W/C ratio and results in a more porous structure. Concerning the anhydrous profiles, the highest anhydrous concentrations are observed in the mortar S60L10-2 at all distances, while the substitution of 5% LF for GGBS has a limited effect on the anhydrous content.

In this study, the work carried out suggests that partially substitution of GGBS by LF powder has an influence on the phase distributions. However, this effect appears to depend on the replacement level of LF. A synergy effect of combined GGBS and LF was observed in the porosity gradients when a moderate amount of GGBS (5%) was replaced by the LF.

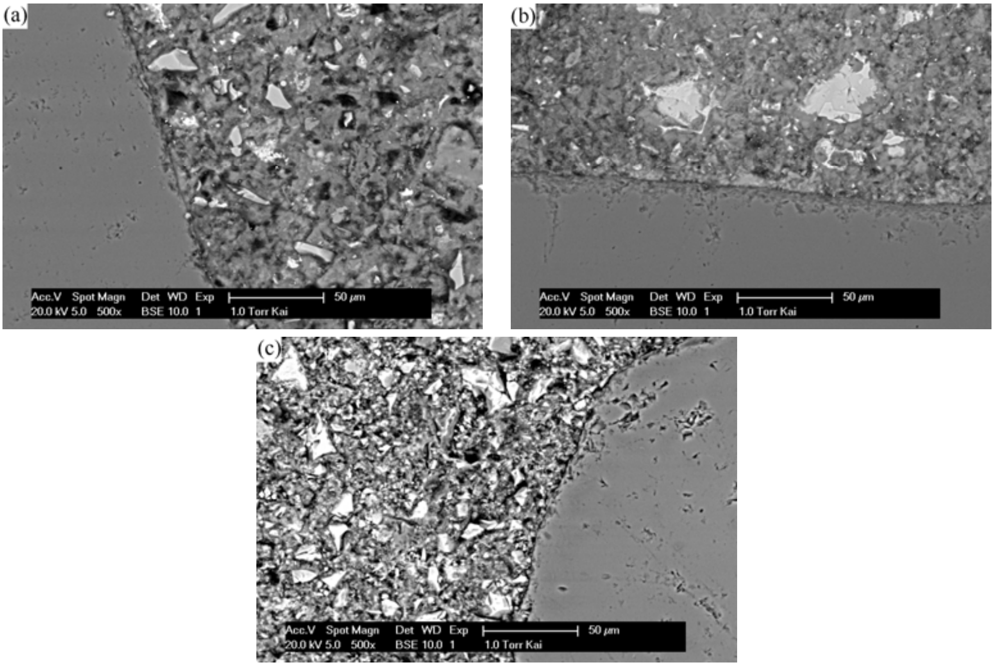

Fig. 4.16 BSE image examples at 500× magnification, (a) S30L05-2, (b) S65L05-2 and (c) S60L10-2.

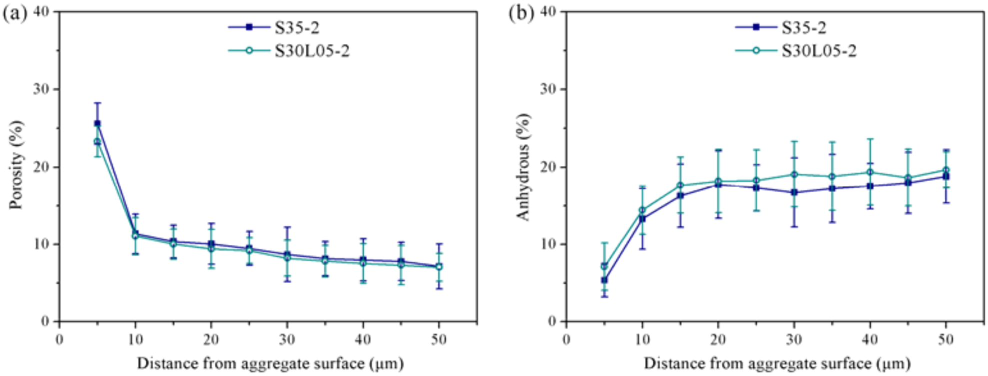

Fig. 4.17 Microstructural profiles in the ITZ (a) capillary porosity, and (b) anhydrous.

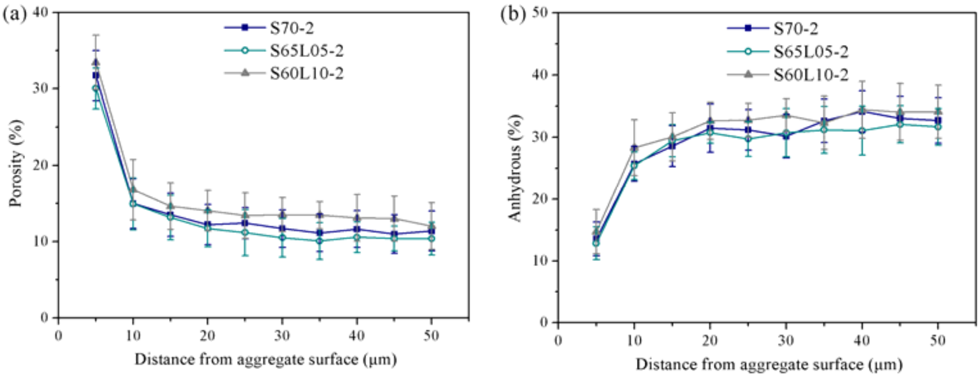

Fig. 4.18 Microstructural profiles in the ITZ (a) capillary porosity, and (b) anhydrous.

4.3.1.4 Curing ages

In order to study the effect of curing age and initial particle packing on the microstructure within the ITZ, two series of experiments were carried out by varying the testing ages and mixtures. Fig. 4.19 shows the BSE image examples for mortar C-2 obtained at different hydration time. The most noticeable features displayed are the densification in the microstructure and the decreases in anhydrous grains with hydration time. These changes are much clearer in the region close to the interfaces. Fig. 4.20 exhibits the percentage of anhydrous and pores versus distance from the aggregate interface. Concerning the porosity gradients in Fig. 4.20 (a), the porosity decreases significantly from 1 day to 2 months due to the formation of hydration products. However, this reduction is insignificant with subsequent hydration from 2 months to 6 months. Throughout the whole hydration period of 6 months, the least changes are observed at the distance of 5 μm. During the hydration period from 1 day to 2 months, the most significant reduction is observed at about 10 μm in distance from the interfaces. This distance transfers to 20-25 μm during the hydration period from 2 to 6 months. This difference could be explained by the initial particle packing due to “wall effect”. It is further confirmed by the anhydrous cement grains profile as given in Fig. 4.20 (b). In the region closest to the interface the amount of anhydrous is low, which is half the amount in the bulk regions. The anhydrous distribution of 1 day reached a fairly constant bulk value by about 25 µm distance from the aggregate, and a peak value is observed at the distance of 20-25 µm. With continuing hydration from 1 day to 2 months, the anhydrous fraction decreases and the peak disappears. From 2 to 6 months, the anhydrous fraction changes slightly at the distance of 5 µm and levels at about 20 µm. Throughout the whole hydration period, the changes in the anhydrous content at the first 5 µm vary little. This low variability indicates that mostly small particles packed in the region closest to the interface. Therefore, the width of this region depends on the proportions of smaller particles within the binders.

The results presented in this section are possibly a direct consequence of the packing of the anhydrous cement grains against the much larger aggregate surface due to the "wall effect". Small particles tend to pack close to the interface and larger ones tend to settle further away. The peak in the anhydrous gradient hydrated after 1 day suggests that the preferential packing of the small particles in the first 5-10 µm from the interface results in a higher concentration of larger cement particles in regions slightly further away (these hydrated more slowly to give the anhydrous peak between about 15 and 20 µm), and that only beyond about 25-30 µm from the interface the particle size distribution is similar to that expected from a bulk cement matrix. The smaller particles with a proportionally higher surface area per unit volume hydrated much more rapidly than larger particles, assuming that the reaction boundary moved at a constant rate at any given time. The small particles are expected to have a higher reaction degree than larger ones. Within the first day the anhydrous cement grains in the first 5-10 µm nearest to the interface hydrated rapidly, and show the least changes between 1 day and 6 months. With continuing hydration, the relatively larger particles at the distance about 15-20 µm hydrate continuously and the peak does not exist at later ages. The anhydrous particles in the regions further away than about 25 µm from the interface, hydrated more uniformly than those in the region between about 5-30 µm.

These observations are in agreement with the findings indicated in literature. Elsharief et al. [37] indicated that age effect on the ITZ normalized porosity depends on its initial microstructure. The amount of the anhydrous present at initial age controls the microstructure lately. Crumbie [16] classified the anhydrous particles into several region: In the region up to about 10 μm from the interface (A) there are mostly very small particles which hydrate rapidly and almost completely by 28 days. In the region between about 20 μm to 30 μm from the interface (B) there are predominantly larger particles since the accompanying smaller ones have packed closer to the interface. Further from the interface between about 30 μm to 40 μm away, region (C), there is again a slightly higher amount of smaller particles than in region (B). This suggests that the packing of the anhydrous cement particles in regions further than about 30 μm away, is less disrupted by the aggregate interface than that in closer regions, and is more similar to that of the bulk cement matrix.

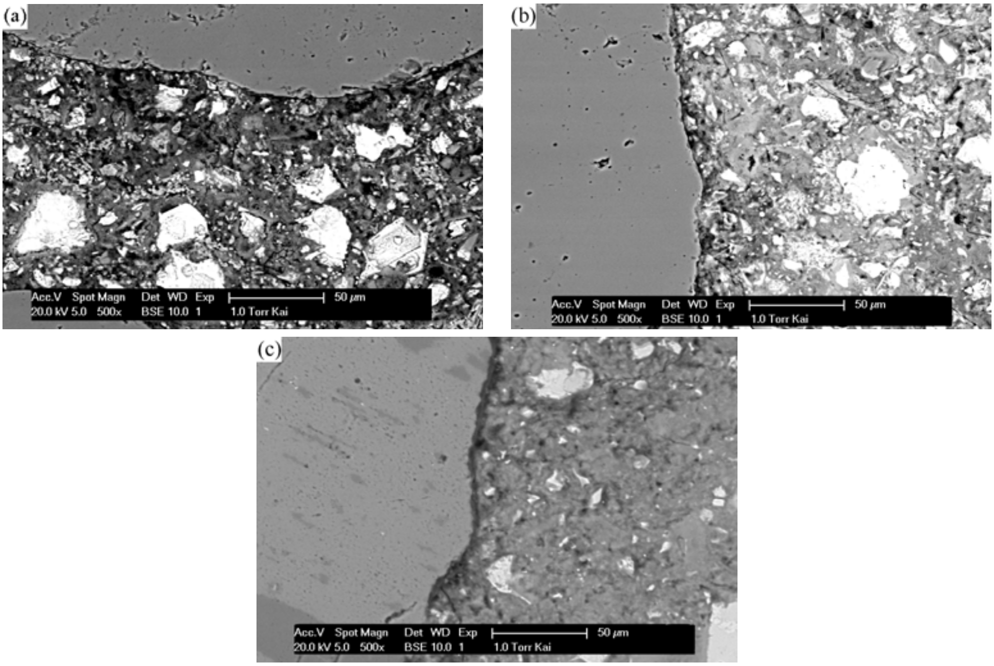

Fig. 4.19 BSE image examples (500×) of mortar C-2 at (a) 1 day, (b) 2 months and (c) 6 months.

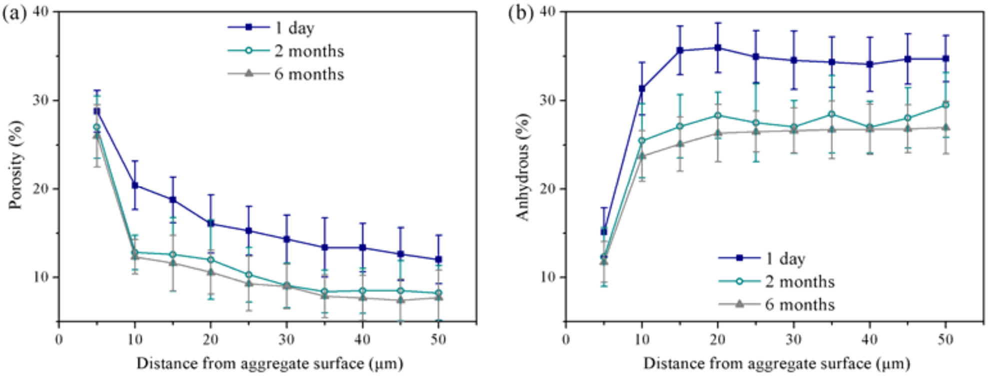

Fig. 4.20 Microstructural profiles of C-2 developed with hydration time (a) capillary porosity, and (b) anhydrous.

The influence of initial particle packing on the microstructure within ITZ was confirmed by comparing the phase distributions of mortar L05-2 hydrated after 1 day with those of the reference sample. From Fig. 4.21 (a), the addition of LF modifies the porosity in the region between 5-15 μm at the most. Regarding the anhydrous gradients, there is no clear peak existed in the mortar L05-2. This suggests that the addition of fine LF particle tends to modify the microstructure in the region close to the interface. Moreover, the anhydrous fractions of L05-2 are lower than those of the reference sample at all distances, which indicates that the acceleration of the cement hydration due to the addition of moderate LF (nucleation site effect) starts at very early age (earlier than 1 day in this study).

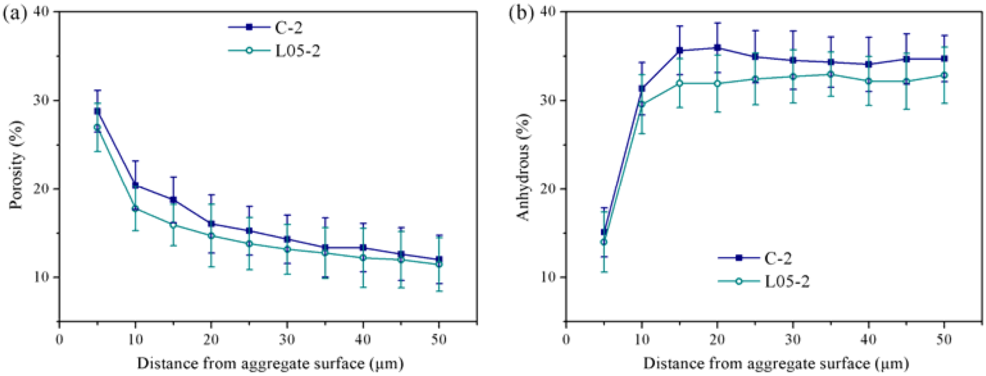

Fig. 4.21 Microstructural profiles in the ITZ obtained after 1 day of hydration (a) capillary porosity, and (b) anhydrous.

4.3.1.5 X-ray line scanning analysis

In order to detect the influence of GGBS on the chemical compositions in the region of ITZ, elemental composition in the ITZ was determined by using EDX line scanning analysis. If the presence of GGBS is able to modify the microstructure of the ITZ by consuming the deposited large CH crystals, it can be expected that the Ca/Si ratio within the ITZ of the reference mortar would decrease with the addition of GGBS. In previous studies [160], the following classification with respect to the Ca/Si ratio was used to distinguish hydrates rich in C-S-H, CH and monosulfate (AFm). The same classification was employed in this work.

C-S-H: $0.8 \leq \text{Ca/Si} \leq 2.5$, $(\text{Al+Fe}) / \text{Ca} \leq 0.2$

CH: $\text{Ca/Si} \geq 10$, $(\text{Al+Fe}) / \text{Ca} \leq 0.1$, $\text{S/Ca} \leq 0.04$

AFm: $\text{Ca/Si} \geq 10$, $\text{S/Ca} > 0.15$

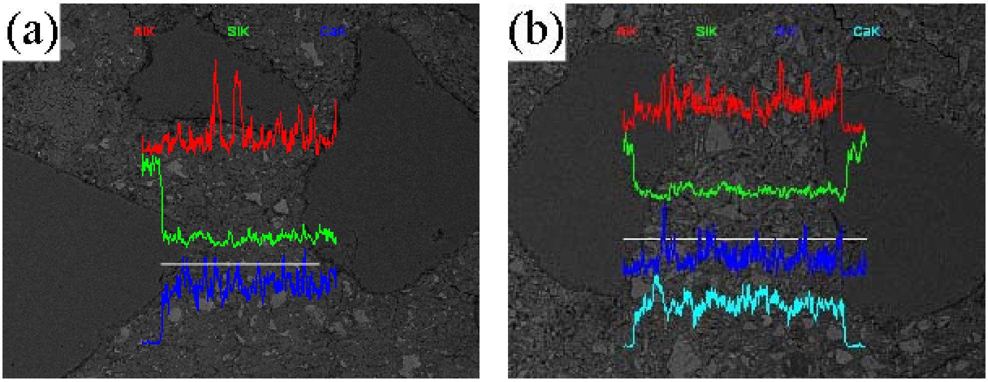

Fig. 4.22 EDX line scanning analysis at the age of 2 months (a) C-2, and (b) S70-2 (the spectrum refers to the corresponding element concentration).

The typical EDX line measurements of mortar C-2 and S70-2 are given in Fig. 4.22. Fig. 4.23 shows the variation in the Ca/Si ratio as a function of distance from the aggregate surface for both samples. The results of Ca/Si ratio within the aggregate parts were removed manually by using image analysis. The quantitative analysis for C-2 reveals that a higher build-up of CH is found in the ITZ. For the sample prepared with binary binders, however, there is a fairly constant Ca/Si ratio and a relatively large quantity of C-S-H throughout the structure. Such a phenomenon suggests that the chemical composition development is much more uniform.

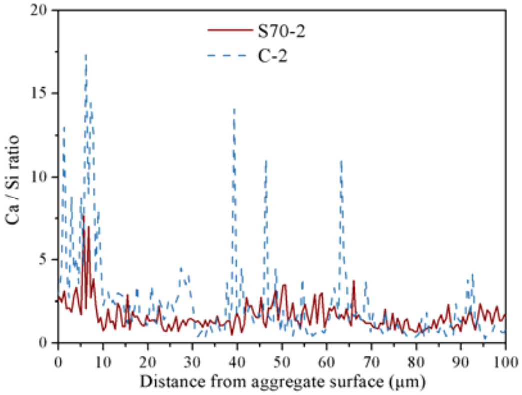

Fig. 4.23 Ca/Si ratio at the ITZ

4.3.2 Porosity characteristics from MIP

4.3.2.1 Effect of aggregate content

To investigate the effect of aggregate volume content on the microstructure, several series of MIP tests at the curing age of 2 months have been performed. Table 4.5 presents the total porosity, mean pore diameter and critical pore diameter of samples with various aggregate volume contents. These results indicate that the pore structure of specimens depends highly on the aggregate volume fraction. For all the binders, the mean pore diameter increases with increasing aggregate content. This can be explained by the presence of ITZ. The quantity of the ITZ is proportional to the aggregate volume fraction. Therefore, the presence of porous structure and large pore size within the ITZ cause a coarser mean pore diameter.

The relations between the critical pores with diameter d_1 and the aggregate volume fractions are not well defined. However, the pore diameters (d_1) of mortars prepared with 55% of aggregate are always less than the corresponding neat cement paste regardless the binders. This could be due to the fact that the bulk cement matrix is denser than the neat cement paste P because of the porous ITZ phase. Since the total amount of water and cement in the mortar is conserved. A lower amount of cement and greater amount of water in the ITZ would lead to a higher amount of cement and a lower amount of water in the bulk cement matrix [41, 43, 186]. This densification effect is not obvious in the case of low aggregate volume content.

One of the most important observations is the presence of critical pores with diameter d_2 for all the specimens prepared with 55% of aggregate. For the samples under this aggregate volume content, the value of d_2 is inferior to 0.5 μm. According to the previous studies [89, 152], the microcrack width is superior to 1 μm under severe curing condition. Thereby, the critical pores with diameter d_2 cannot be associated with the microcrack width and may be attributed to the presence of the ITZ.

The results concerning the total porosity show that the increase in the aggregate volume content decreases total porosity. This is mainly due to the reduction in the paste fraction, as the aggregates are non-porous. In order to present the results more clearly, the unit of the total porosity was transformed from mm^3/g to mm^3/mm^3 "paste". The volume of non-porous aggregate was subtracted and the "paste" includes the bulk cement matrix and the ITZ. The pore size distribution and the total intrusion pore volume versus the pore diameter are given in Fig. 4.24 - Fig. 4.30. Concerning the cumulative intrusion volume, a reverse trend is observed. The addition of aggregate increases total porosity (mm^3/mm^3 paste), particularly at diameters larger than the thresholds of the corresponding neat cement paste. These results are in line with previous studies. Winslow and Cohen [28] observed a sudden increase in the volume as the sand content reaches a critical value, which suggests the occurrence of percolation. The authors pointed out that as sand is added to the cement paste, ITZs are formed around each aggregate but remain relatively isolated due to the low sand content. For the mercury to reach these ITZ, it must intrude through the denser bulk cement matrix. Some increases in the total porosity are possible to be detected due to the overlap of some ITZ with the surface of the specimen, and the critical threshold for the neat cement paste will be lost (samples with 20% aggregate in this study). Subsequently, as more and more aggregates are added, the isolated ITZs start to connect one to another to greatly increase the volume of directly accessible ITZ. When enough aggregate is present, all the ITZ will be expected to percolate throughout the whole system. By using the Eq. (3.19) and the PSD of aggregates (Fig. 4.2), the average inter-aggregate distances for mortars prepared with 20% and 55% of aggregate are 60.2 and 21.5 μm, respectively. Therefore, the percolation of ITZ is possible to occur when the thickness of the ITZ is superior to 11 μm in case of 55% aggregate. This could be the reason why a significant increase in the total porosity is presented in mortar prepared with 55% aggregate, whatever the binders. However, some differences in the increasing ratio are still observed due to the modification of SCMs on the microstructure, which will be discussed in the following sections.

Table 4.5 Porosity features, V_{tot}: total porosity, d_{mean}: mean pore diameter, d_1 and d_2^*: critical pore diameter.

	V_{tot} (mm^3/g)	d_{mean} (nm)	d_1 (nm)	d_2 (nm)		V_{tot} (mm^3/g)	d_{mean} (nm)	d_1 (nm)	d_2 (nm)
C-P	104.7	20.1	46.0	-	S35-P	91.0	16.5	37.0	-
C-1	91.1	23.8	55.8	-	S35-1	85.6	18.3	51.2	-
C-2	54.3	27.5	42.8	424.7	S35-2	53.0	21.5	28.2	333.3
L05-P	96.8	26.2	43.5	-	S70-P	115.5	8.7	7.2	-
L05-1	81.4	27.1	50.7	-	S70-1	100.7	12.1	10.4	-
L05-2	60.6	33.2	40.9	277.3	S70-2	62.0	14.0	7.0	160.7
L10-P	119.3	20.0	53.1	-	S30L05-P	91.8	21.0	52.0	-
L10-1	101.5	23.9	60.8	-	S30L05-1	77.5	22.5	64.0	-
L10-2	67.3	46.4	46.0	339.4	S30L05-2	46.0	28.5	51.7	269.7
					S60L10-P	121.5	13.4	25.1	-
					S60L10-1	103.8	14.2	35.9	-
					S60L10-2	63.4	15.7	21.7	196.3

*d_1 is the diameter corresponds to the maximum dV / $d$log (D) in the range less than 100 nm.

d_2 is the diameter corresponds to the maximum dV / $d$log (D) in the range larger than 100 nm.

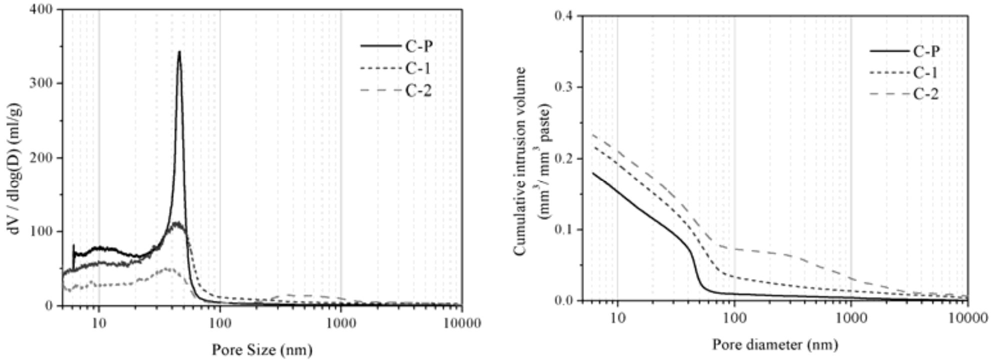

Fig. 4.24 PSD measured by MIP for the samples C with various aggregate volume fractions.

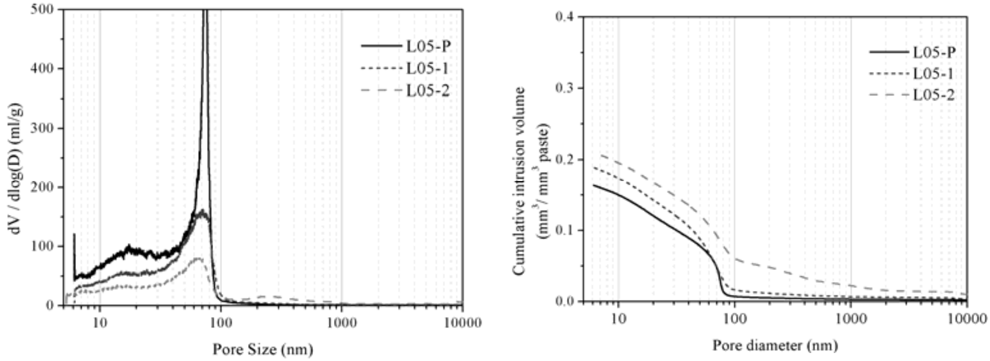

Fig. 4.25 PSD measured by MIP for the samples L05 with various aggregate volume fractions.

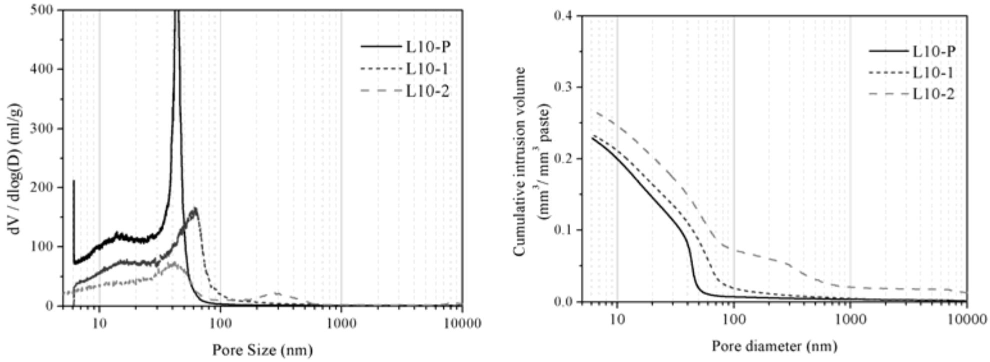

Fig. 4.26 PSD measured by MIP for the samples L10 with various aggregate volume fractions.

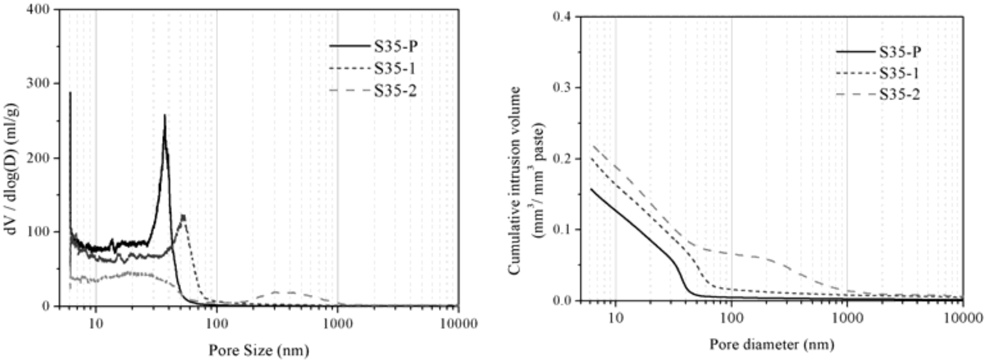

Fig. 4.27 PSD measured by MIP for the samples S35 with various aggregate volume fractions.

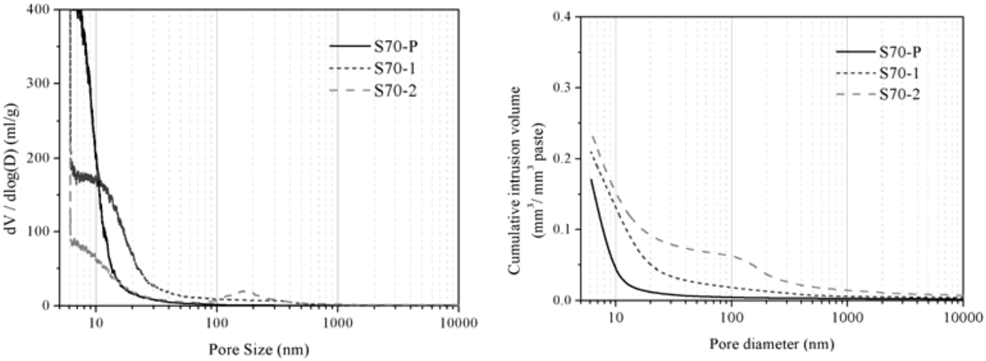

Fig. 4.28 PSD measured by MIP for the samples S70 with various aggregate volume fractions.

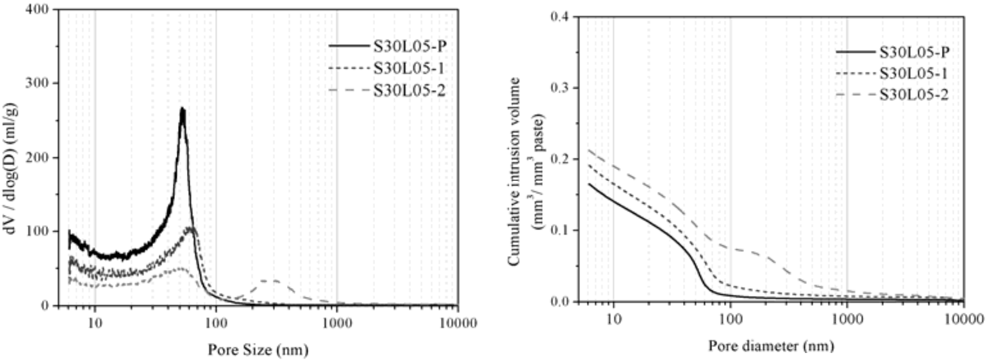

Fig. 4.29 PSD measured by MIP for the samples S30L05 with various aggregate volume fractions.

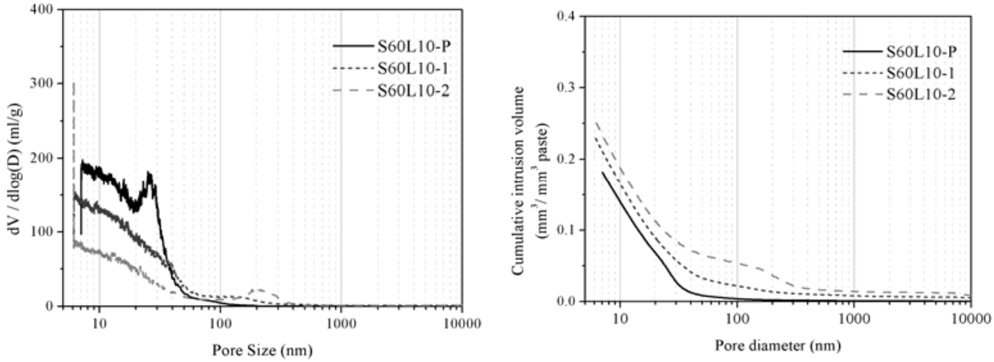

Fig. 4.30 PSD measured by MIP for the samples S60L10 with various aggregate volume fractions.

4.3.2.2 Effect of aggregate size

The pore size distributions of samples with various aggregate sizes are given in Fig. 4.31 - Fig. 4.35. Generally, the changes in the aggregate sizes tend to modify the pore structure. Firstly, coarser pores with critical diameter d_2 are more remarkable for samples with the small aggregate size 0/2 mm, while the critical diameter d_2 is becoming larger for samples with coarser aggregates (combined 0/2 mm and 2/5.6 mm). Secondly, the mode pores with diameter d_1 are slightly moved forward to finer pores. Moreover, the total porosity is higher for mortar prepared with only 0/2 mm aggregate.

These findings are in accordance with aforementioned results and previous studies [41]. The quantity of the ITZ is proportional to the surface area of aggregate. An increase in the average aggregate size would reduce its surface area, and thus the ITZ content with an assumption of a fixed ITZ thickness. Therefore, the amount of critical pores corresponding to diameter d_2, which can be attributed to the presence of the ITZ, is higher for samples prepared with finer aggregate size. The shifting of diameter d_2 towards coarser pores may be attributed to the presence of local micro-bleeding around some coarse aggregates, which could lead to the presence of coarser pores. The presence of more porous ITZ is normally accompanied by a denser bulk cement matrix. This could be the reason for the variation in the critical pore diameter of d_1. Although a similar trend is observed for all the binders, some differences are still presented due to the modification effect of

SCMs on the ITZ. Further investigations are explained in the next section.

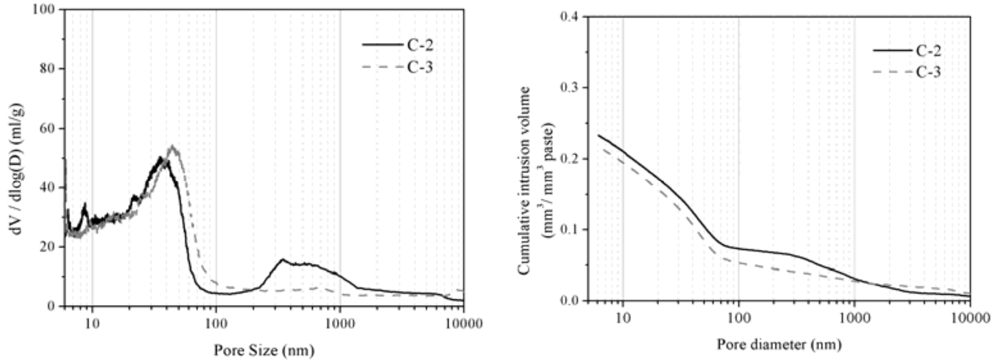

Fig. 4.31 PSD measured by MIP for the samples C with various aggregate sizes.

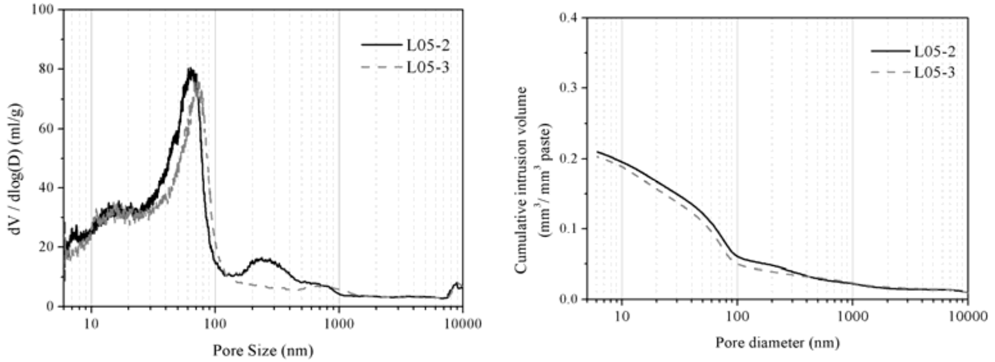

Fig. 4.32 PSD measured by MIP for the samples L05 with various aggregate sizes.

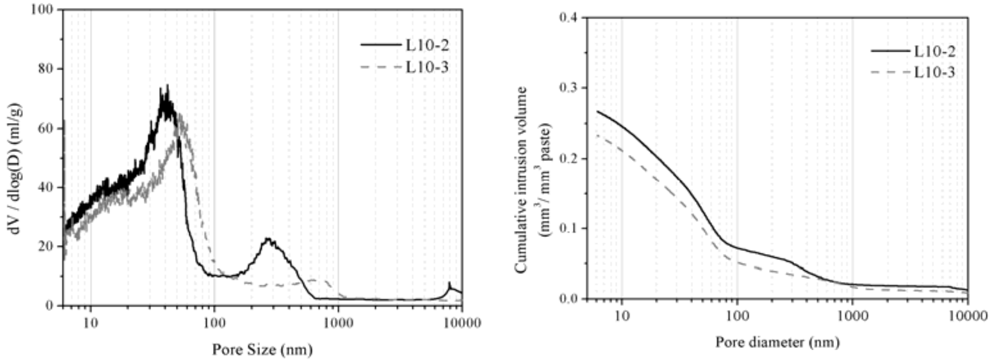

Fig. 4.33 PSD measured by MIP for the samples L10 with various aggregate sizes.

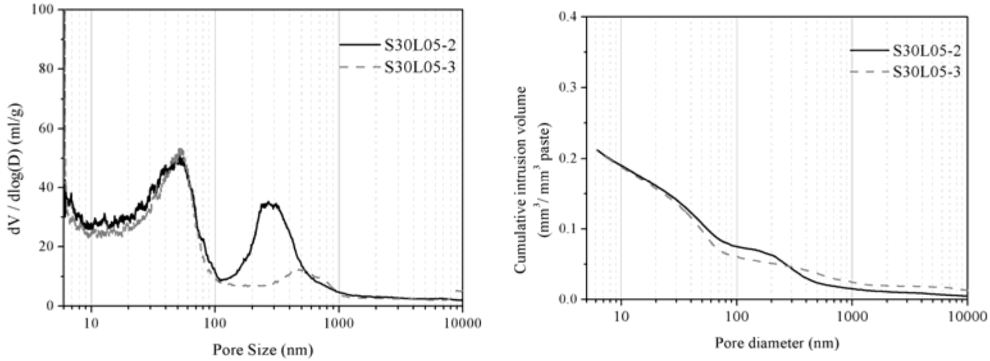

Fig. 4.34 PSD measured by MIP for the samples S30L05 with various aggregate sizes.

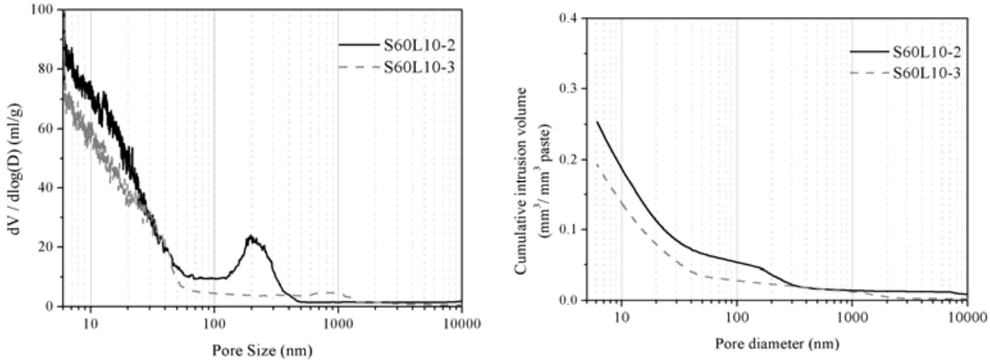

Fig. 4.35 PSD measured by MIP for the samples S60L10 with various aggregate sizes.

4.3.2.3 Effect of SCMs

Limestone filler

To clearly present the MIP results, the intruded pore volume in terms of three characteristic ranges is classified as: <10 nm (P1), 10 nm-100 nm (P2) and >100 nm (P3). An example of this classification is given in Fig. 4.36. From the intruded pore volume (Fig. 4.37), one can easily observe that the total pore volume increases with increasing aggregate volume content. This increase in the total porosity is mainly contributed by the pores in the scale larger than 100 nm. To investigate the influence of SCMs on the porosity of bulk cement matrix and ITZ, the relative differences between the intruded volume of L05, L10 and the reference samples C, are calculated and given in Fig. 4.38. A negative value represents a reduction, with a positive value represents an increase in the pore volume. The results show that the two LF additions have different effects on the intruded pore volume. For binders L05, 5% of LF addition results in a decrease in the total pore volume, P2 and P3. The reduction in P3 volume is 50% and 16% for mortar-1 (20% of aggregate) and mortar-2 (55% of aggregate) respectively, which contributes to the largest decrease in the total pore volume. This indicates that the addition of 5% LF is able to modify the pore structure superior to 100 nm significantly. This confirms the improvement of the ITZ by LF through disturbing the particle packing and facilitating the formation of smaller CH crystals with less crystallization tendency in preferential orientations.

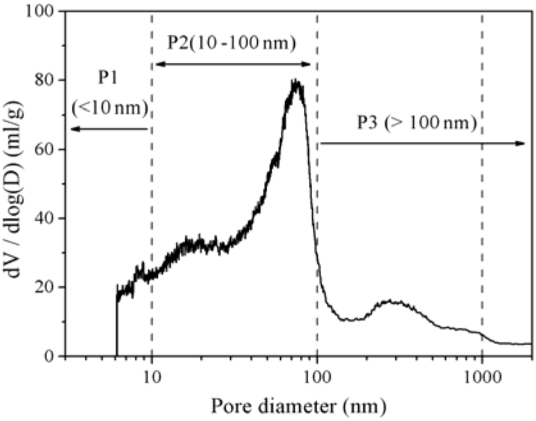

Fig. 4.36 An example for the classification of PSD curve.

Concerning the relative differences in the pore volume between mortars prepared with binders L10 and the reference samples, the incorporation of 10% LF as substitute for PC results in increases in the total porosity and P2 pore volume, but decreases in the P3 volume. The overall pore structure is weakened by the addition of high amount of LF due to dilution effect. However, it is still expected to have improvements in the microstructure of ITZ. The percentage of reduction in P3 pore volume is 22% and 1.4% for L10-1 and L10-2, respectively. This again confirms the ITZ modification of LF in binders.

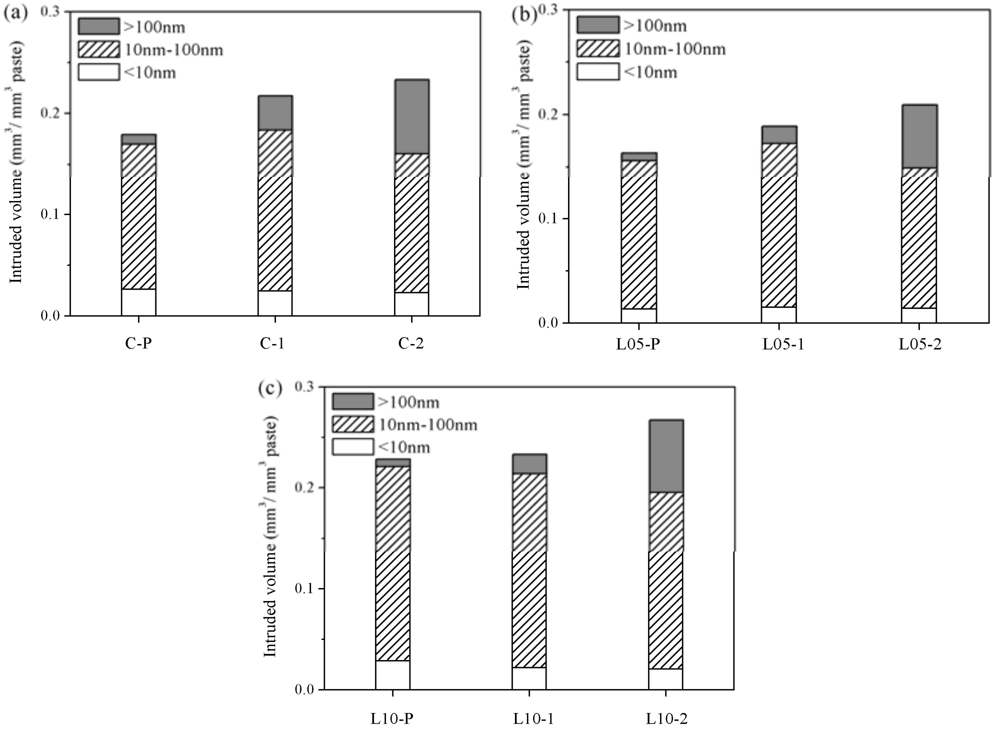

Fig. 4.37 Intruded pore volume in relation to three regions for, (a) C, (b) L05 and (c) L10.

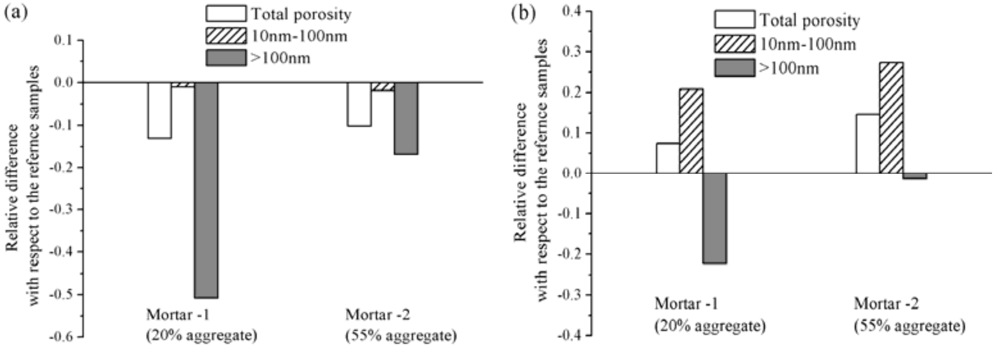

Fig. 4.38 Relative difference in intruded pore volume of mortars with (a) L05 and (b) L10 with respect to the reference mortars C.

GGBS

The intruded pore volume in terms of the three pore size regions for binders S35 and S70 are given in Fig. 4.39. Compared with the intruded volume of the reference samples (Fig. 4.37), the effects of GGBS on the porosity are highly dependent on the replacement level and the determined pore size classification. For 35% GGBS replacement (Fig. 4.39 (a)), the total porosity, P3 and P2 volume are less than that of GGBS-free samples, while the P1 volume is higher. Concerning the substitution of 70% GGBS for PC (Fig. 4.39 (b)), the total porosity reaches to 0.18, 0.22 and 0.24 mm^3/mm^3 for neat paste, mortar-1 and mortar-2, respectively. The P1 volume is increased significantly to 0.085, 0.078 and 0.086 mm^3/mm^3 for neat paste, mortar-1 and mortar-2, respectively. However, the coarser pores are refined and the P2 volume decreases to 0.08, 0.112 and 0.089 mm^3/mm^3 for neat paste, mortar-1 and mortar-2, respectively. The P3 volume arrives to 0.005, 0.031 and 0.069 mm^3/mm^3 for neat paste, mortar-1 and mortar-2. It can be concluded that the high amount of GGBS substitution can increase the total porosity but refine the pore size from the range of P3 and P2 to P1 size.

The relative differences in the pore volume between mortars prepared with GGBS and the reference samples are given in Fig. 4.40. As mentioned above, an overall decrease in the total porosity is observed in the binder S35 (Fig. 4.40 (a)), while an increase is captured for binder S70 (Fig. 4.40 (b)). The P2 and P3 volume decreases regardless of the amount of GGBS. The refinement for P3 pore size suggests that GGBS can densify the microstructure of ITZ by consuming the CH crystals due to pozzolanic reaction. It has been proven by previous report that the size and content of CH crystals in the ITZ of GGBS blended concretes are smaller and the microstructure of ITZ is denser [164]. In this study, another possible reason for the improvement of ITZ by GGBS is that the mean particle size is less, having a higher amount of fine particles than that in case of PC. This effect is all the more important as a higher amount of GGBS was blended.

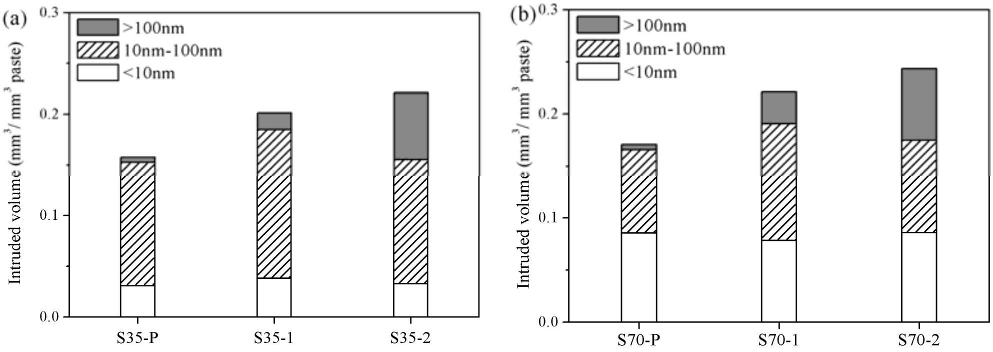

Fig. 4.39 Intruded pore volume in relation to three regions for (a) S35 and (b) S70.

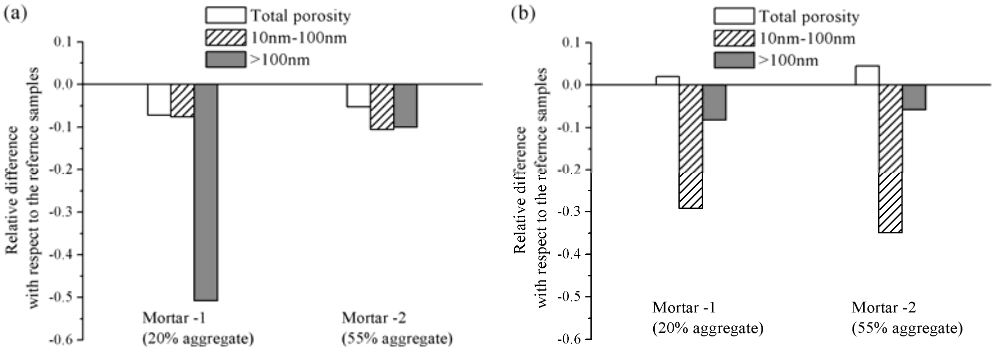

Fig. 4.40 Relative difference in intruded pore volume of mortars with (a) S35 and (b) S70 with respect to the reference mortars C.

Combined GGBS and LF

The combination effects of the GGBS and LF on the intruded pore volume in terms of three size ranges are given in Fig. 4.41. Compared with the corresponding binary binder, the S30L05 ternary binder enables to further refine the pore size distribution. Take the mortar-2 for instance, replacing 5% of GGBS by LF reduces the total porosity to 0.21 mm^3/mm^3, and increases the P2 volume to 0.11 mm^3/mm^3. Concerning the ternary S60L10, a reverse trend is captured of which the total porosity is increased with substituting 10% LF for GGBS. This result is in line with the previous observations. The positive effect of LF is offset by the prominent dilution effect, which increases local W/C ratio and results in a more porous structure.

Concerning the modification of the ITZ, the relative differences in the pore volume between the ternary binder and the reference samples are given in Fig. 4.42. Comparing the results of ternary binders (Fig. 4.42) with those of corresponding binary systems (Fig. 4.40), one can easily observe the further reduction in the P3 pore volume for all the samples, whatever the binders. This again suggests that a synergy effect of combined GGBS and LF can be expected to modify the microstructure of ITZ. This beneficial effect by the ternary binder could be explained by disturbing the particle packing within the ITZ, the acceleration of the cement hydration (nucleation site effect), the reduction in large flat CH crystals and providing more secondary C-S-H and other hydrates. In term of the overall porosity and local porosity features, the optimum binder is 65% PC, 30% GGBS and 5% LF blends.

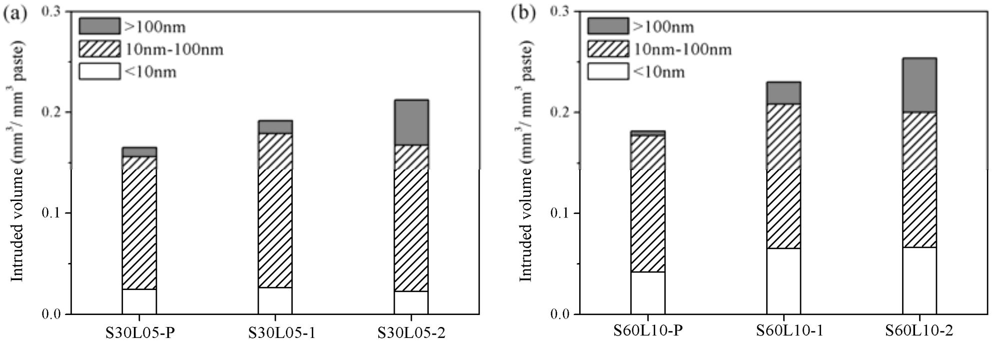

Fig. 4.41 Intruded pore volume in relation to three regions for (a) S30L05 and (b) S60L10.

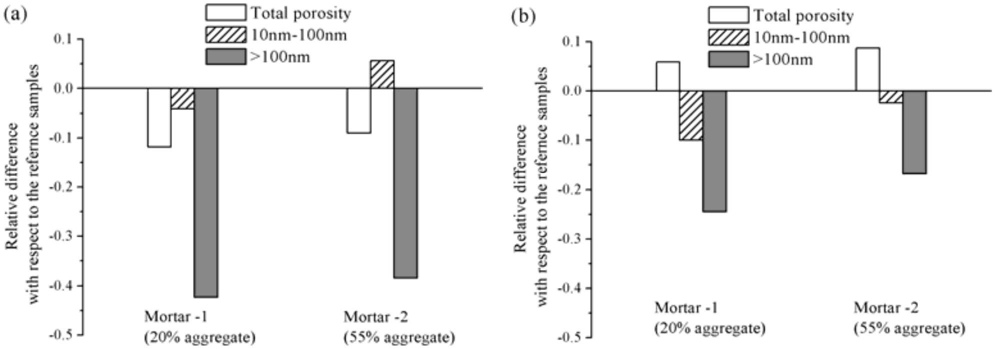

Fig. 4.42 Relative difference in intruded pore volume of mortars with (a) S30L05 and (b) S60L10 with respect to the reference mortars C.

4.3.3 Mechanical properties

4.3.3.1 Compressive strength

Limestone filler

To correlate the compressive strengths of all the samples with the effect of ITZ, several parameters have been determined in Table 4.6, i.e. aggregate volume fraction, mean aggregate size and average inter-aggregate distance. The detailed calculation was shown in chapter 3. Compressive strengths of samples at different LF replacement rates were determined at 2 months. The results are plotted against various aggregate properties in Fig. 4.43. The error bars are indication of the standard deviation. At 2 months, the results show that the highest compressive strength value is captured in the reference sample C-P. For the reference samples in relation to the aggregate volume content (Fig. 4.43 (a)), the compressive strength decreases as the volume of aggregate increases. However, there is no significant effect of the differences in aggregate volume content on compressive strength for the LF blended series, whatever the replacement rate.

The relationship between the compressive strength and the mean aggregate size given in Fig. 4.43 (b) indicates that the compressive strengths decrease slightly while increasing the aggregate size for the reference samples. Here there is no remarkable difference in the compressive strengths for binders containing LF with respect to the average aggregate size.

The compressive strengths of all the samples versus the average inter-aggregate distance are shown in Fig. 4.43 (c). A concave trend is observed for the compressive strength of reference samples, the strength value decreases firstly with increasing average distance up to 47.4 μm and increases with continuouly increasing distance. The compressive strengths of samples containing LF seem to be less sensitive to the difference in the average inter-aggregate distance, whatever the amount of LF used. Moreover, the substitution of 5% LF for PC increases the compressive strengths of mortars and concretes slightly, while the strengths of L10 blended mortars and concretes decrease due to the dilution effect.

Table 4.6 Aggregate properties for the mixtures

	Aggregate volume fraction	Mean aggregate size (mm)	Average inter-aggregate distance (μm)
Binder-P (neat paste)	0	-	-
Binder -1	0.2	0.36	60.1
Binder -2	0.55	0.36	21.5
Binder -3	0.55	1.97	47.4
Binder -4	0.55	2.88	53.3

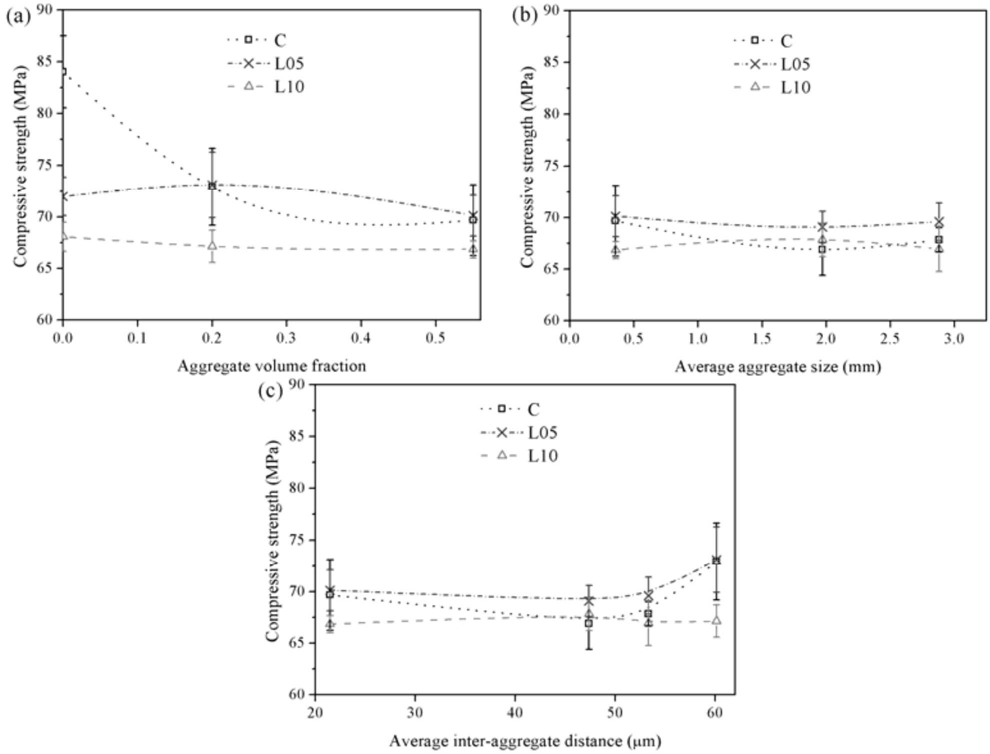

Fig. 4.43 Compressive strengths of samples at 2 months versus various aggregate properties: (a) volume fraction, (b) mean size and (c) average inter-aggregate distance.

GGBS

Fig. 4.44 presents the effects of the variation in GGBS replacement rates on the compressive strengths. From Fig. 4.44 (a), there is no appreciable difference in the strength of samples containing 35% GGBS with respect to the aggregate volume content. For the compressive strength of binders containing 70% GGBS, a similar trend is observed as for the GGBS-free reference samples.

Concerning the mean aggregate size in Fig. 4.44 (b), the compressive strengths of GGBS blended samples decrease with the size. This trend is more obvious for the S70 series samples. The relationships between the compressive strengths of GGBS blended samples and the average inter-aggregate distance are more complicated than those of the reference series (Fig. 4.44 (b)). A significant reduction is observed at the distance of 53.3μm, in case the coarsest aggregates were used. Generally, the compressive strengths of samples containing GGBS show less variation with the average inter-aggregate distance. Moreover, the incorporation of 35% GGBS as a partial substitute for PC improves the compressive strengths of mortars and concretes, while the strengths of S70 blended mortars and concretes reduce significantly. These results are in accordance with the microstrcutural analysis.

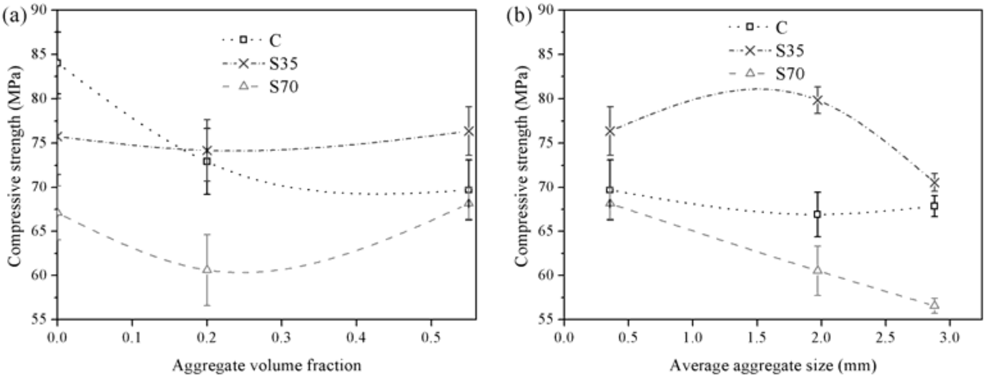

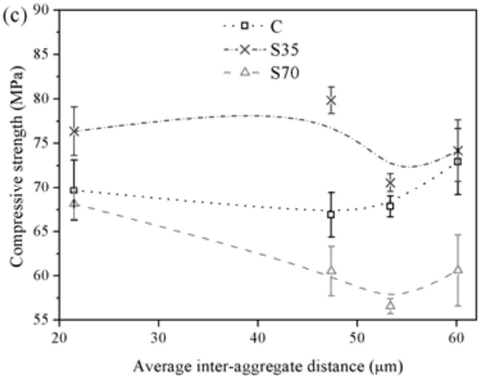

Fig. 4.44 Compressive strengths of samples at 2 months versus various aggregate properties: (a) volume fraction, (b) mean size and (c) average inter-aggregate distance.

Combined GGBS and LF

At a fixed SCMs replacement level (35%), partial substitution of 5% LF for GGBS tends to increase the overall compressive strengths except for the samples with an average inter-aggregate distance of 47.4μm (Fig. 4.45). Concerning the effect of average inter-aggregate distance on the strengths of S30L05 series, a similar trend is observed as in the references. However, the variation ratio is less than that of C series. Regarding the effect of aggregate volume fraction, there seems to be a subtle trend for S30L05 towards reducing compressive strength for the samples with the higher aggregate volume.

The effects of the aggregate properties on the compressive strengths of the incorporation of 70% SCMs are shown in Fig. 4.46. The compressive strengths of S65L05 show the least variation with the aggregate volume fraction. At a fixed total replacement rate, incorporating moderate amount of LF for GGBS increases compressive strength, particularly for the mortar-1 with 20% of aggregate. From Fig. 4.46 (b), there is no well defined effect of average inter-aggregate distance on the results. Generally, the variation ratio is less for the ternary blended systems.

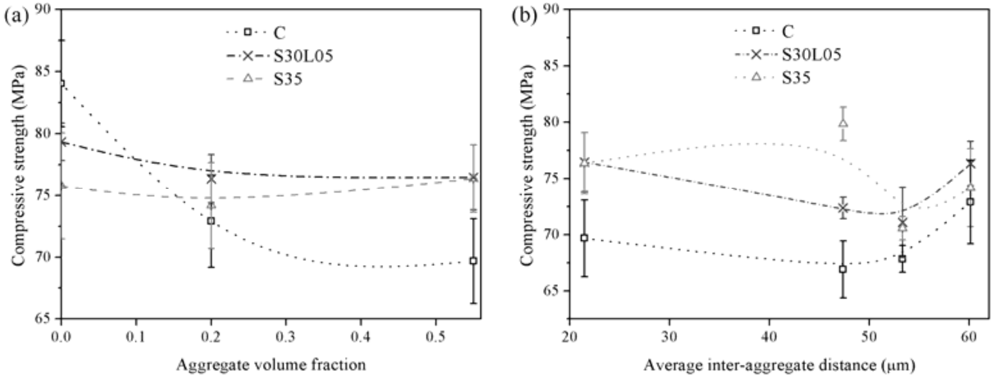

Fig. 4.45 Compressive strengths of ternary binders at 2 months versus various aggregate properties: (a) volume fraction and (b) average inter-aggregate distance.

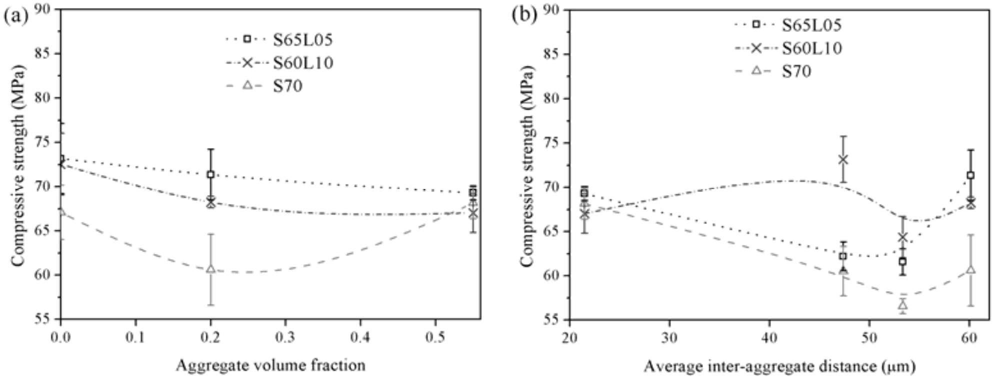

Fig. 4.46 Compressive strengths of ternary binders at 2 months versus various aggregate properties: (a) volume fraction and (b) average inter-aggregate distance.

ITZ

In order to evaluate the modification effect of SCMs on the ITZ in relation to the compressive strength, the results are presented versus the ITZ volume content in Fig. 4.47. To obtain the ITZ quantity, a similar method was used as did in chapter 3 and one additional approximation has been made: the thickness of ITZ corresponds to the mean particle size of the binders regardless of aggregate volume contents and sizes. For example, the mean particle size of S30L05 can be calculated by: 15.7×0.632+12.5×0.312+9.4×0.056=14.3 (μm), where 0.632, 0.312 and 0.056 is the volume fraction of PC, GGBS and LF.

For the reference series, there seems to be an obvious trend towards reduced compressive strength with higher ITZ quantity. Concerning the effect of the difference in the ITZ quantity on the compressive strengths, the variation is all the less appreciable as the amount of LF increases (Fig. 4.47 (a)). The L10 series show the least variation but the lowest overall strengths. For the GGBS incorporated binary systems (Fig. 4.47 (b)), the variation in strength is less for S35 than that for the reference series. At a fixed total SCM replacement level, the substitution of moderate amount of LF for the GGBS tends to reduce the variation in the strengths. However, the overall compressive strengths are reduced for a higher SCMs replacement level (70%). These results suggest that the use of GGBS and LF has a beneficial effect on the properties of ITZ. This modification effect of GGBS depends on its dosage. Additionally, a synergy effect is possible to obtain by combining the GGBS and LF at a moderate proportions. The ternary S35L05 series presents a relatively higher overall strength and a little variation with the ITZ quantity.

Interestingly, the neat cement paste C-P has the highest overall compressive strength compared with the mortars and concretes. It is likely to be due to the ITZ which result in a less effective transfer of stress from the bulk cement matrix to the aggregate grains. Larbi [15] pointed out that the presence of aggregate tends to lower the strength which can be attributed to inhomogeneities with respect to the elastic properties of mortar and to a modification of the mode of failure of cement paste in the presence of sand particles. Therefore, the strength decreases with the addition of the aggregate. For SCM incorporated series, the strengths of the neat pastes are always lower than the reference one mainly due to the dilution of the PC quantity. However, some improvements are captured in the mortars and concretes, such as group S35, L05 and S30L05. In mortars and concretes, the contribution of bulk matrix to the overall strengths is less and the effect of ITZ and aggregate becomes higher. This further suggests that the improvement in the compressive strength of mortars and concrete by the GGBS and LF are possibly due to the densification of the ITZ.

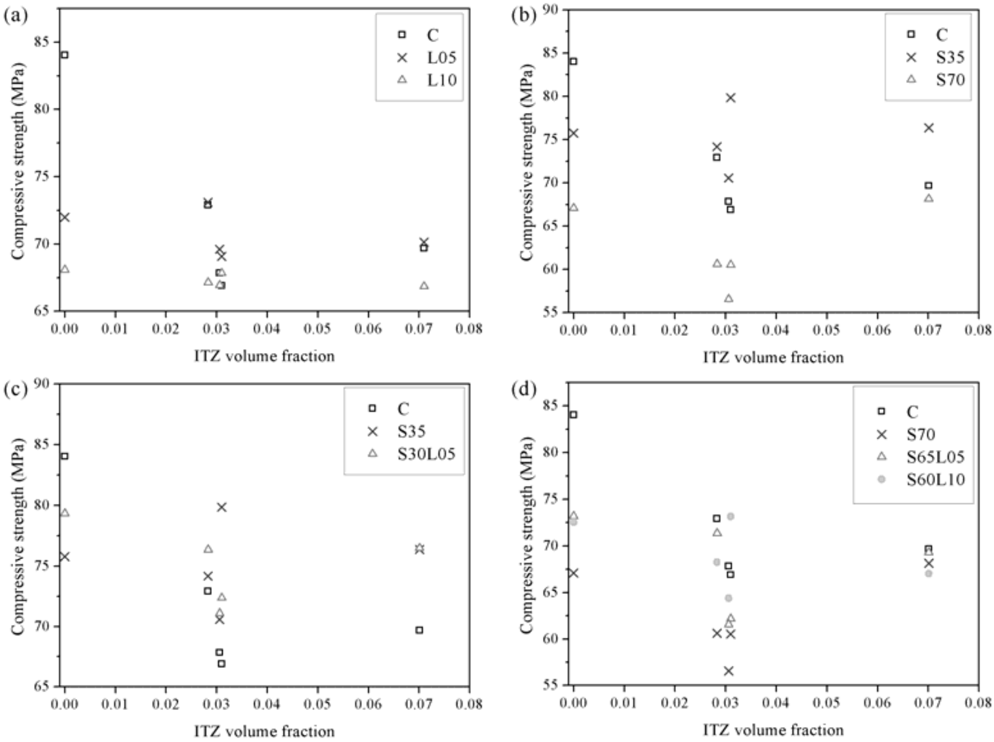

Fig. 4.47 Compressive strengths of all samples versus calculated ITZ quantity.

4.3.3.2 Dynamic elastic modulus

Limestone filler

The dynamic elastic modulus (E_d) at 2 months are obtained from the ultrasound velocity measurements and provided in Fig. 4.48. It is clear from Fig. 4.48 (a) that there is an apparent effect of the aggregate volume on the overall E_d for all the three groups, namely the E_d of the sample increases with the aggregate volume fraction. For the neat paste, the substitution of LF for PC tends to decrease E_d. However, this reduction by LF is less apparent for the mortar L05-1 and an improvement in the E_d is captured in the mortar L05-2.

Results in Fig. 4.48 (b) indicate that there is a slight trend towards increasing E_d for the samples with a coarser aggregate. The results from the binary groups seem to be less sensitive to the variation in the average aggregate size. The incorporation of 5% LF as a partial substitute for the PC increases E_d for all the samples. This enhancement depends on the aggregate size used in the samples, and a more remarkable increase is observed for the finer aggregate samples. On the contrary, a reverse trend is observed for 10% LF replacements, in which the E_d is reduced and the reduction is all the more apparent as the coarser aggregate is used. This can be simply explained by the following assumptions. If the dilution effect by the high amount of LF addition (10%) is the same for all the samples with various aggregate sizes, the reduction in E_d would be expected to have a similar order of magnitude. Therefore, the contrary observation in the measurement suggests that some improvements in the structure contributed by the LF occur at the substitution rate of 10%, particularly for the sample with a finer aggregate size.

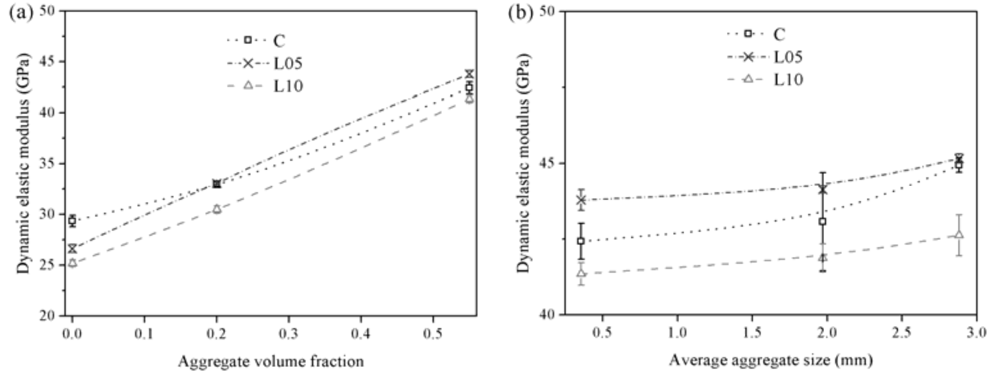

Fig. 4.48 E_d of samples at 2 months versus: (a) the aggregate volume content and (b) the average aggregate size.

The results of E_d were calculated from the measured ultrasound velocity which could be highly influenced by the properties of the aggregate. In order to evaluate the relations between the ITZ and the results, the differences between the E_d of the PC-LF binary groups and the reference samples are given against the ITZ volume fraction in Fig. 4.49. For the substitution of 5% LF, the dilution effect dominates only in the neat paste (ITZ = 0), and an improvement is observed in the mortars and concretes. Moreover, this improvement is all the more apparent as the ITZ volume fraction increases. For 10% of substitution, the E_d reduces for all the samples with various ITZ quantities mainly due to the prominent dilution effect. This negative effect is less apparent with increasing ITZ volume fraction. These results again confirm the improvement in the properties of ITZ by the LF powders even at a high substitution rate.

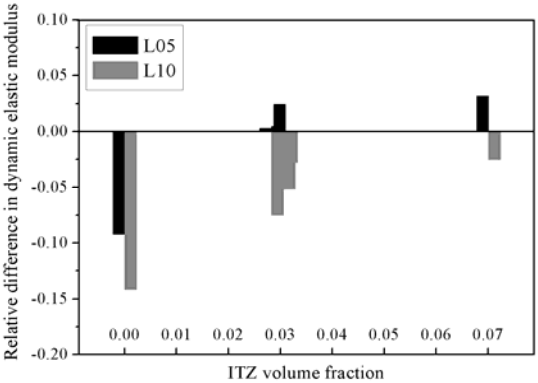

Fig. 4.49 Relative difference in E_d of PC-LF binary series with respect to the reference C set.

GGBS

Fig. 4.50 presents the E_d of the binary PC-GGBS series against the aggregate volume fraction and size. Concerning the effect of the aggregate volume fraction, there is a similar apparent trend as in the Fig. 4.48 (a), i.e. the E_d of the sample increases with the aggregate volume fraction. For the neat paste, the substitution of GGBS for PC tends to decrease E_d. However, this reduction by GGBS disappears in the S35 mortars and an improvement in the E_d is captured for the S35-1 and S35-2. For the replacement level of 70%, the differences in the E_d between the mortars of S70 and the reference samples are less apparent with increasing aggregate volume content.

Concerning the effect of aggregate size in Fig. 4.50 (b), there is a similar trend in the relation between the E_d and the average aggregate size. The results from the binary groups are less sensitive to the variation in the average aggregate size. The substitution of 35% GGBS for the PC increases E_d for all the samples. This enhancement is more remarkable for the finer aggregate samples. For 70% of GGBS replacements, the E_d is reduced and the reduction is all the more apparent as the coarser aggregate is used.

By comparing the E_d of the PC-GGBS binary groups with the reference samples (Fig. 4.51), the results of samples containing 35% of GGBS increase with the ITZ volume fraction. For 70% of substitution, the E_d reduces for all the samples. This negative effect is less apparent of the samples with a higher ITZ volume fraction. These results are in line with the previous results and further confirm the improvement in the properties of ITZ by the GGBS.

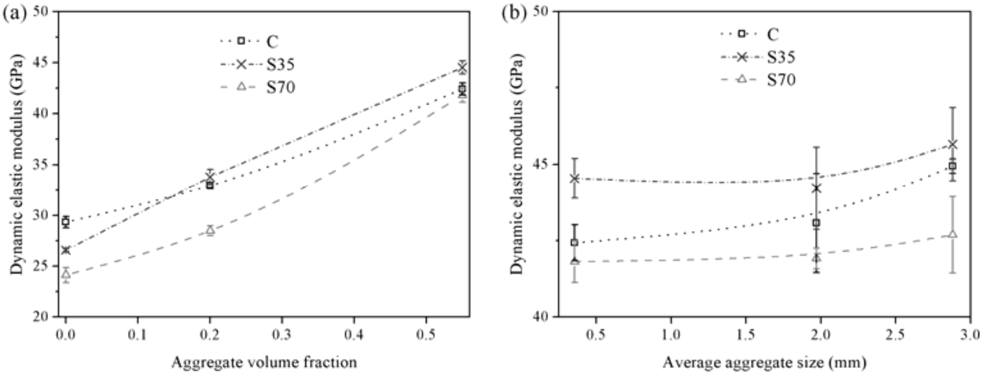

Fig. 4.50 E_d of samples at 2 months versus: (a) the aggregate volume content and (b) the average aggregate size.

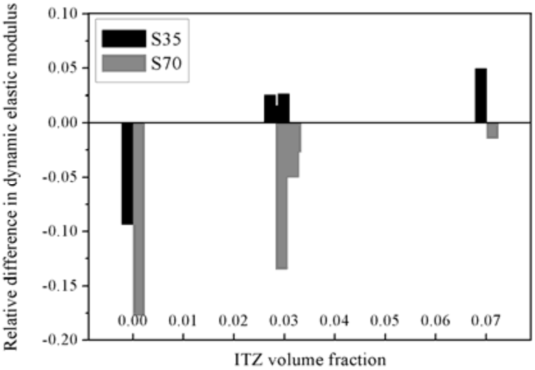

Fig. 4.51 Relative difference in E_d of PC-LF binary sets with respect to the reference C set.

Combined GGBS and LF

The relative differences between the E_d of the ternary groups and the reference samples are given in Fig. 4.52 and Fig. 4.53. At a fixed SCMs replacement level (35%), the increases in the E_d are higher for the samples prepared by substituting 5% LF for GGBS (Fig. 4.52). For 70% of substitution, both the results from the binary and ternary groups are lower than those of the references. This reduction is less apparent for a higher ITZ volume fraction (Fig. 4.53 (a)). Moreover, improvements occurred in the E_d for the S65L05 series compared with the corresponding binary group. These again confirm that the weak ITZ can be enhanced by combining GGBS and LF at moderate proportions. For the S60L10 group, the relative difference is reduced compared with the corresponding binary S70 except for the mortar-2 with the highest ITZ volume fraction. This unexpected phenomenon could be caused by experimental error, and others need to be further investigated.

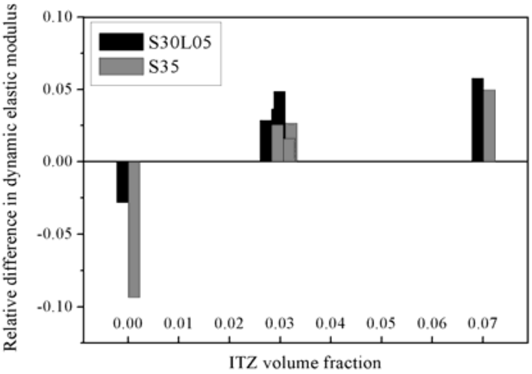

Fig. 4.52 Relative difference in E_d of binary and ternary sets at 35% replacement with respect to the reference C set.

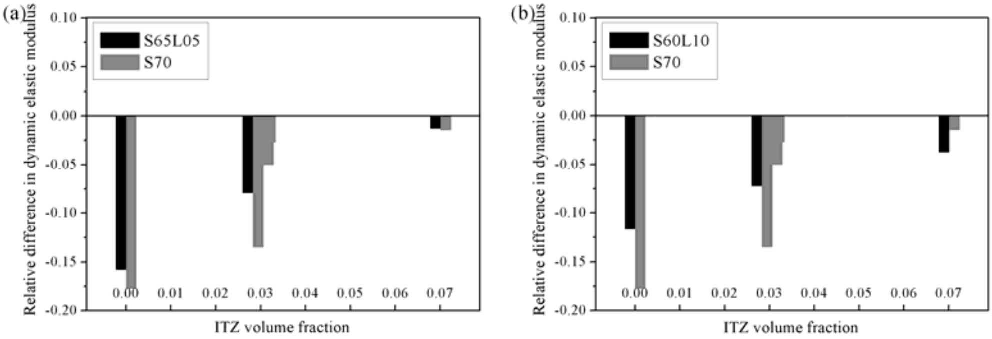

Fig. 4.53 Relative difference in E_d of binary and ternary sets at 70% replacement with respect to the reference C set.

Curing age

To evaluate the effect of LF and GGBS on the ITZ in terms of curing age, the E_d results of S35L05 and the reference C are presented against the mean aggregate size in Fig. 4.54. A similar analysis had been proposed in the previous report in which the effect of silica fume on the properties of ITZ was evaluated [48]. The initial distribution of the structure in the ITZ is of interest but is practically difficult to assess since the cement has not yet set. Therefore, the earliest results of 1 day are provided. The samples from C series have higher E_d values than the corresponding ternary samples until 7 days. After 2 months of hydration, the E_d results of S30L05 samples are higher than the corresponding references. This suggests that the pozzolanic reaction of GGBS mainly starts after the middle age (7 day). Moreover, even at very early age (1 day), the E_d results of the ternary blended groups are less sensitive to the variation of the aggregate size. This is presumably due to the ability of the LF powder to modify the ITZs. As mentioned above, the LF is able to disturb the initial particle packing and act as filler at very early age. This is especially important for the improvement in the ITZ, which is confirmed by the fact that the reduction in the E_d at 1 day is less significant for the samples with the finer aggregate size. To elucidate the effect of LF on the ITZ at very early age, the relation between E_d of the ternary group and the corresponding binary samples at 1 day is given in Fig. 4.55. There is a subtle trend toward increased E_d for the samples with the finer aggregates. This again confirms the ITZ modification contributed by the LF at the initial stage.

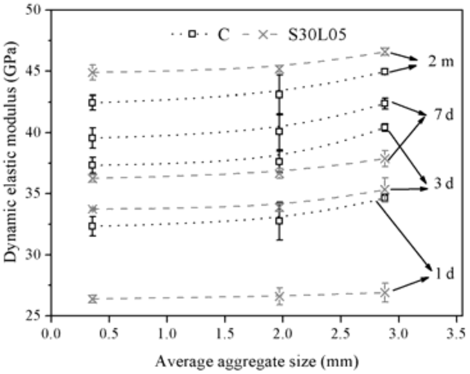

Fig. 4.54 Relation between E_d and the aggregate size with respect to the curing ages.

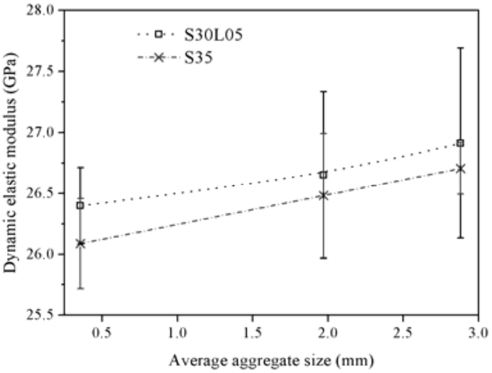

Fig. 4.55 Relation between E_d and the aggregate size at 1 day.

4.3.4 Chloride migration

4.3.4.1 Limestone filler

The rapid chloride migration test provides an acceptable comparative index (D_{nssm}, in m^2/s) of the relative ease of movement of ions through a given sample. Fig. 4.56 presents the chloride migration coefficient results of reference and LF blended binary series at 2 months versus the aggregate volume content. The results obtained were between 12-15×10^{-12} m^2/s for C series, 11-12×10^{-12} m^2/s for L05 series and 18-22×10^{-12} m^2/s for L10 series. For the reference series, the D_{nssm} value decreases slightly with the aggregate content until 0.2, and increases apparently with subsequent increase in aggregate volume content to 0.55. This trend is consistent with the previous findings and literature [24, 95, 185]. As the sand volume in the mortar increases, the number of ITZ formed per unit volume of mortar also increases. This effect would increase transport values. However, the presence of impermeable aggregates decreases permeable cross section area of specimens and increases effective transport path length, which would decrease transfer values. The more porous ITZ is normally accompanied by a more dense bulk cement matrix. In this study, the increase in the D_{nssm} value is supportive of the hypothesis that there will be a gradual predominance effect of the ITZ as the volume of aggregate in the mortar increases and some percolation may occur for samples with a higher aggregate content (see Table 4.6).

For the binary series, the effect of LF on the overall D_{nssm} values depends on the substitution rate. The incorporation of 5% LF as a partial substitute for PC decrease D_{nssm} of all the samples, while the D_{nssm} value increases significantly as the substitution rate of LF reaches to 10%. Additionally, the D_{nssm} shows little variation as the aggregate volume content increases from 0.2 to 0.55. This is presumable due to the modification effect of LF on the ITZ. To support this conclusion, the differences calculated between the D_{nssm} of the LF blended series and the reference samples are given in Fig. 4.57. For L05 series, the most significant reduction in the D_{nssm} occurs for the sample with 55% aggregate. Concerning L10 series, the least increase is observed for the mortar L10-2. This further confirms the relatively importance of LF to the modification of ITZ.

Fig. 4.58 presents the relation between the measured D_{nssm} values versus the average aggregate size. A similar trend is observed with respect to the effect of LF on the overall D_{nssm} as observed in Fig. 4.57. For the reference series, an increase in the aggregate size tends to increase the overall D_{nssm} value. The results seem to be contradicted with the fact that using a finer aggregate creates more porous ITZ which could lead to a higher transport value. This can be explained by three effects: (i) using coarser aggregates would reduce the tortuosity and thus the effective movement paths; (ii) a denser bulk cement matrix is possible to be obtained in the sample prepared with finer aggregate; (iii) although no significant bleeding was observed in the specimens, some local microbleeding is still possible to occur around the coarse aggregates, leading to the presence of coarser pores. The effects (ii) and (iii) have been well defined in the MIP results. Moreover, the relative difference of D_{nssm} in Fig. 4.59 shows more apparent variations with the aggregate size for the L05 group. This again confirms the modification of ITZ contributed by the LF.

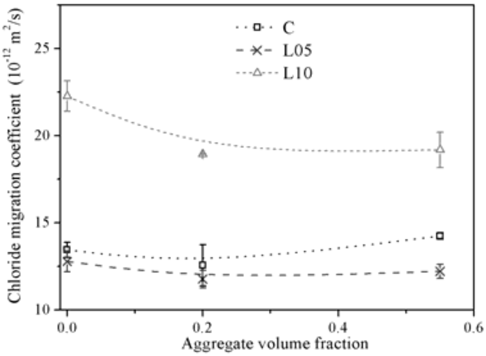

Fig. 4.56 Chloride migration coefficients of samples at 2 months versus aggregate volume content.

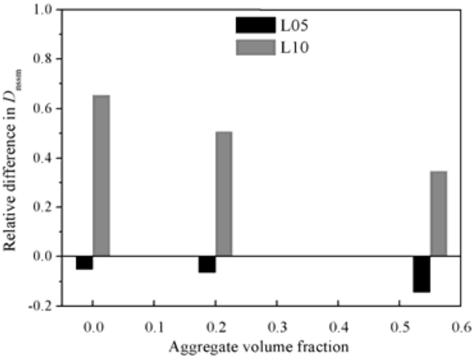

Fig. 4.57 Relative difference in D_{nssm} of LF blended series with respect to the reference series.

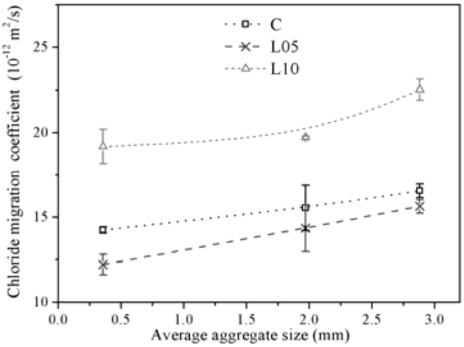

Fig. 4.58 Chloride migration coefficients of samples at 2 months versus mean aggregate size.

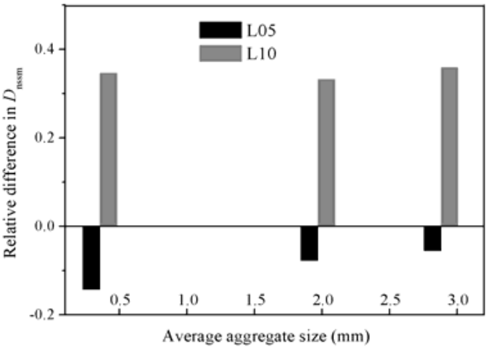

Fig. 4.59 Relative difference in D_{nssm} of LF blended series with respect to the reference series.

4.3.4.2 GGBS and GGBS-LF

The D_{nssm} of GGBS blended binary series versus the aggregate volume fraction and size are given in Fig. 4.60. The D_{nssm} values of the series containing GGBS decrease significantly when the replacement rate of GGBS increases regardless of aggregate volume fraction and size. The values obtained are of the order of 3×10^{-12} m^2/s for the S35 series, and about 2×10^{-12} m^2/s for the S70 series. Interestingly, the D_{nssm} increases continuously as the aggregate volume increases. Similar findings are also observed in the ternary series containing GGBS in Fig. 4.61(a) and Fig. 4.62 (a). This unexpected phenomenon seems to indicate that the adverse effects of ITZ in the GGBS blended mortars are more significant, which is contradicted with the previous findings. Therefore, this raises a controversy as to whether the improvement in the chloride resistance ability is predominantly controlled by (i) the modified bulk cement matrix, or (ii) the ability of GGBS to enhance the microstructure of the ITZ. This is discussed in the following section in detailed.

On the other hand, the D_{nssm} values of GGBS blended binary and ternary series show little sensitive to the average aggregate size (in Fig. 4.61 and Fig. 4.62). Additionally, the D_{nssm} increases when the incorporation rate of LF as a partially substitute for GGBS in the ternary series increases. This is more apparent for the mortars with a higher aggregate volume fraction.

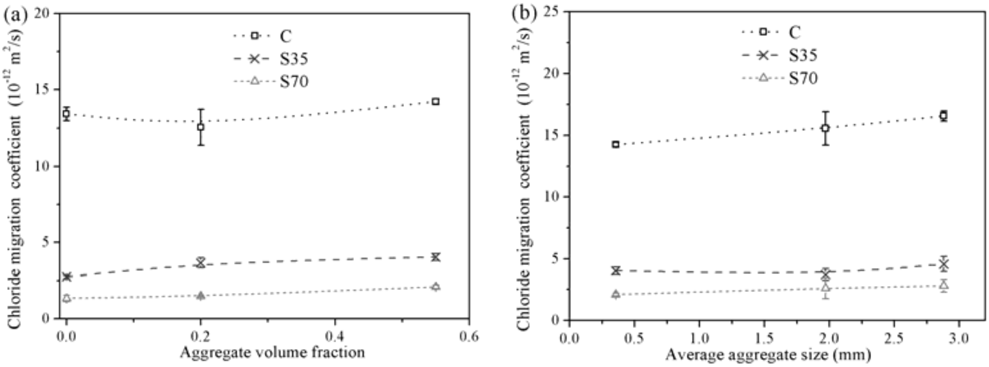

Fig. 4.60 D_{nssm} of PC-GGBS binary series at 2 months versus, (a) aggregate volume fraction and (b) mean aggregate size.

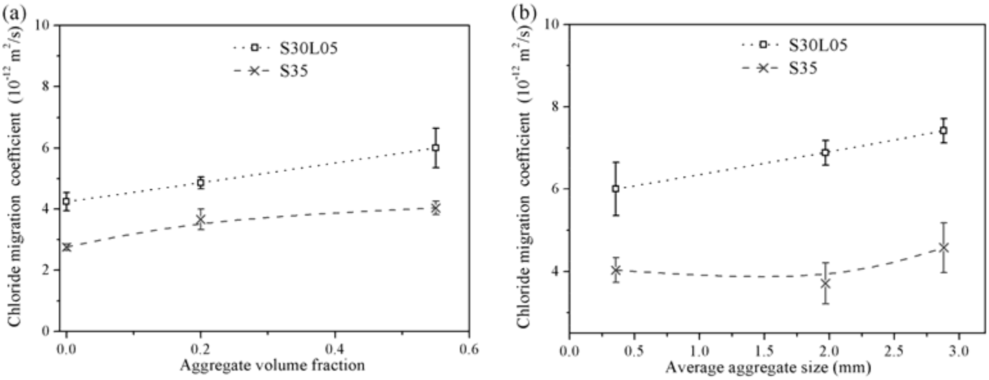

Fig. 4.61 D_{nssm} of PC-GGBS-LF ternary series at 2 months versus, (a) aggregate volume fraction and (b) mean aggregate size.

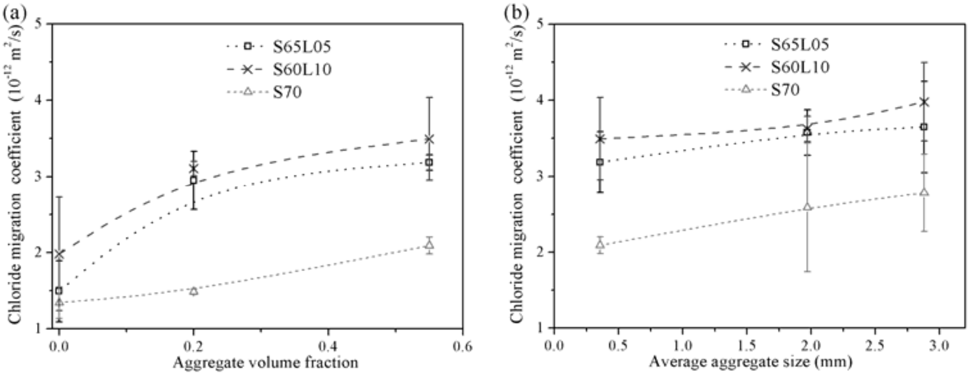

Fig. 4.62 D_{nssm} of PC-GGBS-LF ternary series at 2 months versus, (a) aggregate volume fraction and (b) mean aggregate size.

4.3.4.3 ITZ vs. bulk matrix

In the previous MIP investigations, it was found that one significant feature of ITZ is the relatively high pore volume in the range of P3 (>100 nm). In the reference series, the increases in the total pore volume with increasing aggregate volume are mainly contributed by the pores in the scale larger than 100 nm. The intruded pore volume in this range (P3) can be reduced by incorporating moderate amount of SCMs, i.e. GGBS and LF in this study. As a result, the microstructure of ITZ is compacted and improved. Meanwhile, the pore volume in the range of P2 ($10\,\text{nm} < d < 100\,\text{nm}$), which predominates in the bulk cement matrix, was also altered by the presence of SCMs. To evaluate whether the reductions in the D_{nssm} values of SCMs blended series are mainly contributed by the densification of the ITZ, or by the improvement of the bulk cement matrix, the relations between the relative difference in the D_{nssm} and the relative difference in the intruded pore volume are given in Fig. 4.63. The relative difference is calculated by (P_{SCMs}- $P_{ref.}$)/ $P_{ref.}$ and (D_{SCMs}- $D_{ref.}$)/ $D_{ref.}$, where P_{SCMs} are the intruded pore volume of the blended pastes and mortars, $P_{ref.}$ are the results from the corresponding reference paste and mortars, D_{SCMs} and $D_{ref.}$ are the non-steady state chloride migration coefficients of the blended pastes and mortars, and those of the corresponding reference paste and mortars. Negative values represent a decrease, while positive values represent an increase for the corresponding parameters.

From Fig. 4.63 (a), there is a fairly obvious linear relation between the variation of D_{nssm} and that of P2 ($10\,\text{nm} < d < 100\,\text{nm}$) volume. As shown in Fig. 4.63 (b), there is no clear relation between the difference in the D_{nssm} and the difference in the P3 (>100 nm) volume. On the contrary, some increases in the D_{nssm} values are captured when the P3 volume decreases from the L10 series. The variations of D_{nssm} are highly determined by the variations of P2 pores rather than those of P3 pores. Therefore, the observed improvement of chloride resistance of the GGBS blended samples in the former section must be due in part to the improvement of the microstructure of the ITZ, but more importantly, to the marked densification of the bulk cement matrix.

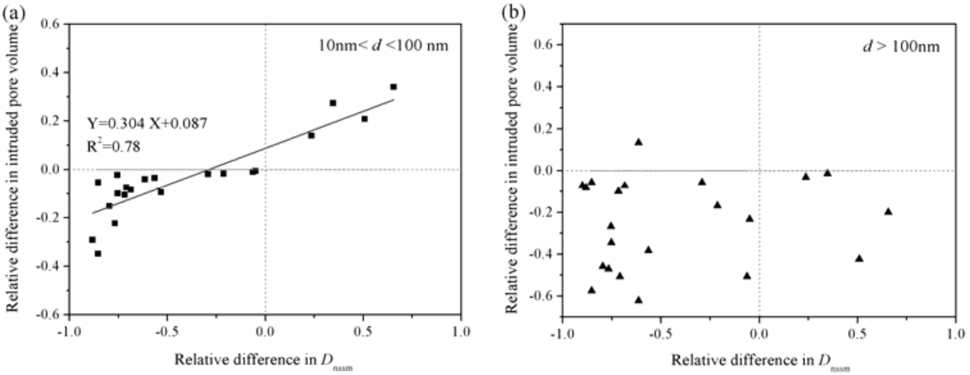

Fig. 4.63 Relation between the relative difference in the D_{nssm} values and, (a) the relative differences in the P2 (10 nm < d < 100 nm) volume and (b) the relative differences in the P3 (>100 nm) volume.

4.3.5 Water absorption

4.3.5.1 SCMs

Water absorption can be described as the ability to take in water by means of capillary suction, which is heavily influenced by the volume of pores as well as the connectivity [141, 187]. A large amount of concrete in service is only partly saturated and the initial ingress of water and dissolved salts is influenced by absorption. Therefore, it can be used as an important factor for evaluating the durability of the cementitious systems [102]. In this part, the main objective is to evaluate the relative significance of the improvement of the ITZ and the densification of the bulk cement matrix in relation to the absorption. Only initial sorptivities are analyzed. The detailed water absorption profiles are given in the Appendix and the discussion related to the effect of aggregate on the water absorption were presented in chapter 3. An example of water absorption measurement is given in Fig. 4.64, it can be found that the absorbed water decreases as the aggregate volume fraction increases. This is mainly due to the replacement of paste by the impermeable aggregates. On the other hand, the water absorption measured after 9 days is higher for the samples with finer aggregate (Fig. 4.64 (b)). This is in line with the MIP results in which the samples with finer aggregate had a higher porosity due to the increase in the ITZ quantity.

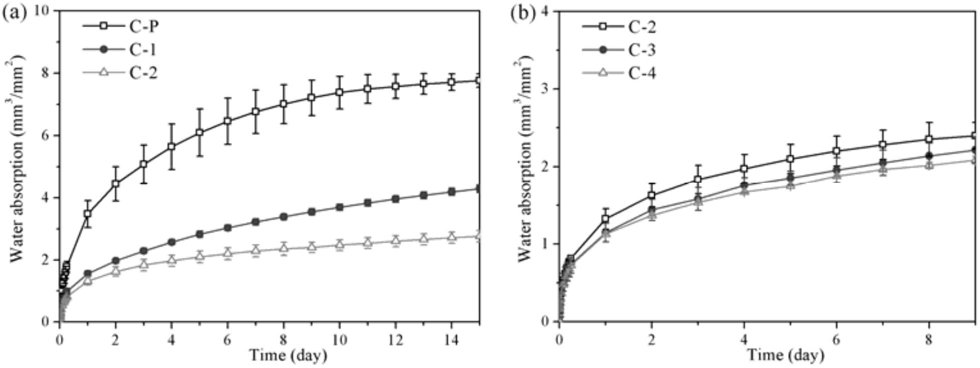

Fig. 4.64 Absorbed water of C series (tested at the age of 12 months) versus, (a) aggregate volume fraction and (b) aggregate size.

The calculated initial sorptivities (S_i) in relation to the SCMs and the aggregate volume fraction and size are given in Fig. 4.65 - Fig. 4.68. It is still worthy to recall that only the cutting face was chosen to place face down on two plastic rods in deionized water, and no surface effects are considered in the analysis. The results obtained are between 5-10×10^{-3} mm/s$^{0.5}$ for C and L05 series, 12-15×10^{-3} mm/s$^{0.5}$ for L10 series (Fig. 4.65). The incorporation of 5% LF as a partial substitute for PC decrease S_i of all the samples, while the S_i value increases significantly as the substitution rate of LF reaches to 10%. For the reference series and the LF blended groups, the S_i decreases with increasing aggregate content and shows little variations with subsequent increase of the aggregate volume content to 0.55. Concerning the effect of aggregate size in Fig. 4.65 (b), an increase in the aggregate size tends to increase the overall S_i value slightly. This could be explained by the increased tortuosity for a finer aggregate and a denser bulk cement matrix.

From Fig. 4.66, the S_i of the series containing GGBS decreases significantly when the replacement rate of GGBS increases. The values obtained are of the order of 2.5×10^{-3} mm/s$^{0.5}$ for the S35 series, and about 0.5×10^{-3} mm/s$^{0.5}$ for the S70 series. Compared with the reference series, the S_i of GGBS blended samples shows the least sensitivity to the variation of aggregate volume fraction, particularly for the S70 series (Fig. 4.66 (a)). Regarding the effect of aggregate size in Fig. 4.66 (b), a similar trend is observed in the S35 binary series, namely the S_i is higher for the samples with coarser aggregate. However, there is no detectable effect of the aggregate size on the S_i of the S70 series.

At a fixed SCMs replacement rate, substituting moderate amount of LF (10%) tends to increases S_i values for all the samples. Moreover, this increase is more apparent for the samples prepared with a coarser aggregate (Fig. 4.67 (b) and Fig. 4.68 (b)).

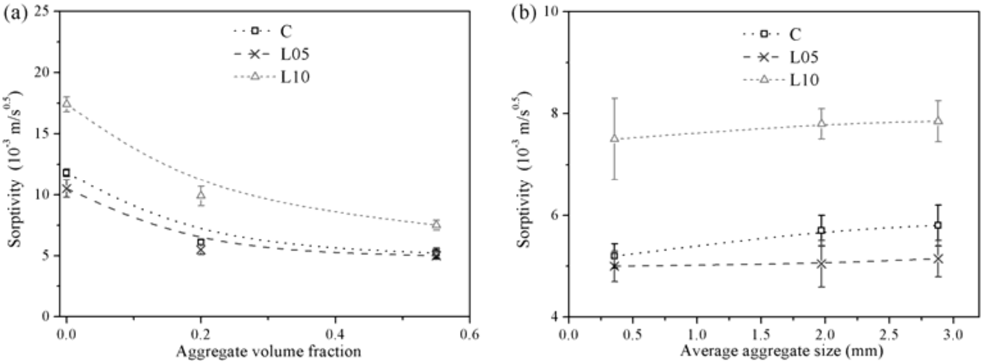

Fig. 4.65 Initial S_i of PC-LF binary series versus, (a) aggregate volume fraction and (b) aggregate size.

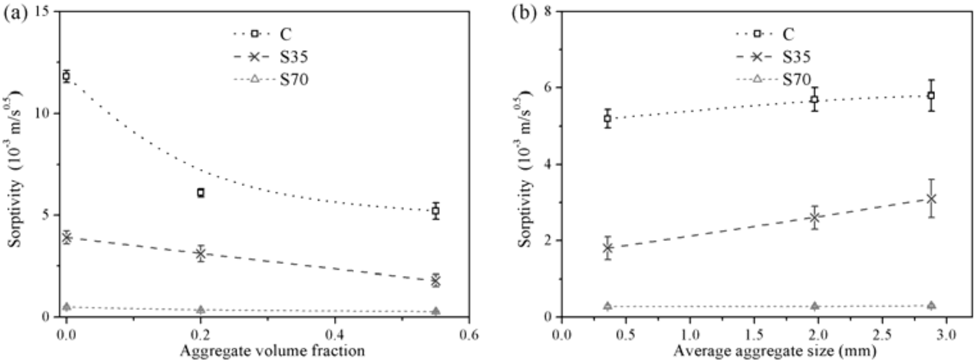

Fig. 4.66 Initial S_i of PC-GGBS binary series versus, (a) aggregate volume fraction and (b) aggregate size.

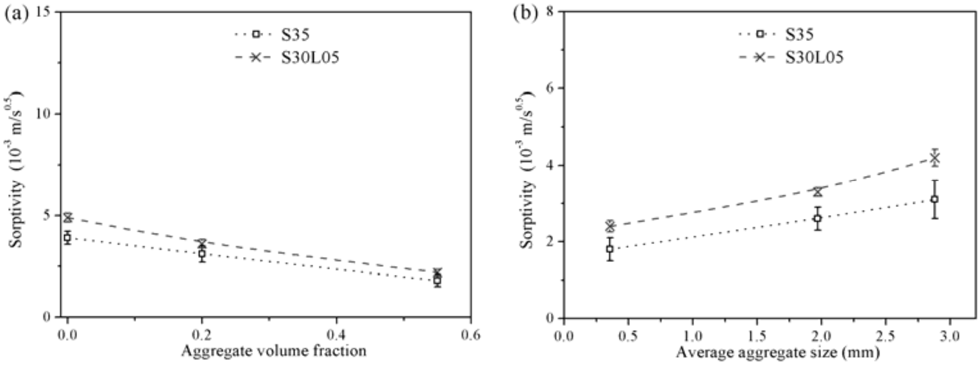

Fig. 4.67 Initial S_i of PC-GGBS-LF (35%) ternary series versus, (a) aggregate volume fraction and (b) aggregate size.

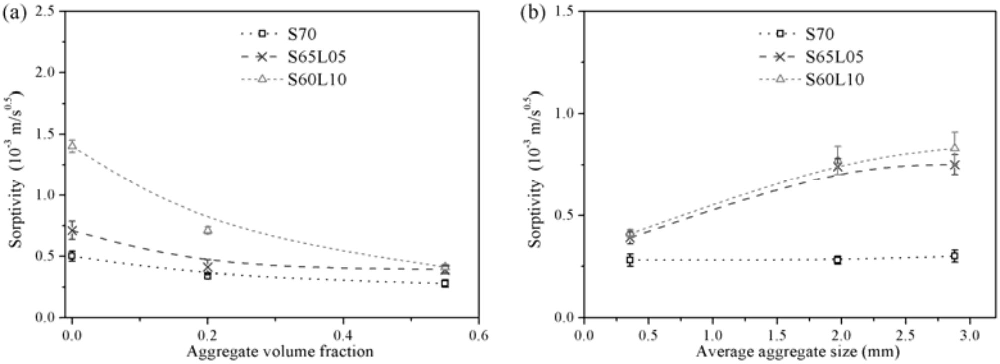

Fig. 4.68 Initial S_i of PC-GGBS-LF (70%) ternary series versus, (a) aggregate volume fraction and (b) aggregate size.

4.3.5.2 ITZ vs. bulk matrix

To evaluate whether the reductions in the S_i values of SCMs blended series are mainly contributed by the densification of the ITZ, or by the improvement of the bulk cement matrix, the relations between the relative difference in the S_i and the relative difference in the intruded pore volume are given in Fig. 4.69. There is a fairly obvious linear relation between the variation of S_i and that of P2 ($10\,\text{nm} < d < 100\,\text{nm}$) volume. As shown in Fig. 4.69 (b), there is no clear relation between the difference in the S_i and the difference in the P3 (>100 nm) volume. On the contrary, some increases in the S_i values are captured when the P3 volume decreases for the L10 series.

The variations of S_i are highly determined by the variations of P2 pores rather than those of P3 pores. Therefore, the observed improvement of water movement resistance of the GGBS blended samples in the former section must mainly be due to the marked densification of the bulk cement matrix.

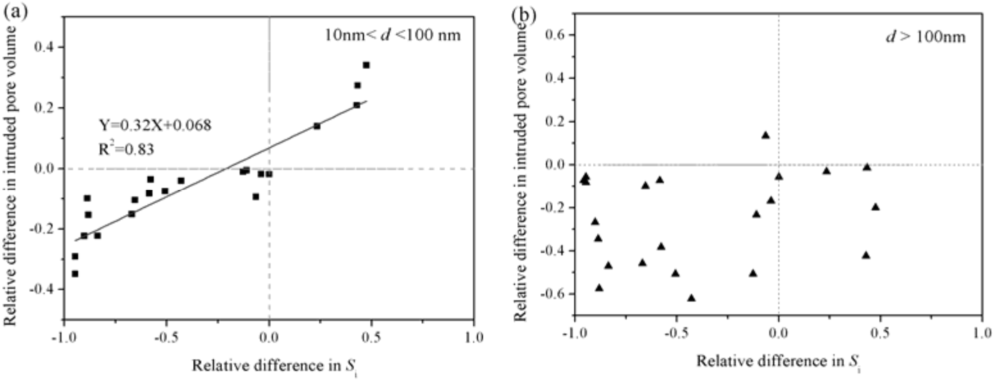

Fig. 4.69 Relation between the relative difference in the S_i values and, (a) the relative differences in the P2 ($10\,\text{nm} < d < 100\,\text{nm}$) volume and (b) the relative differences in the P3 (>100 nm) volume.

4.3.6 Discussion

It is widely accepted that the microstructure of the ITZ is initially determined by the packing of the anhydrous cement grains against the much larger aggregate particles. The well known “wall effect” leads to a depletion of larger anhydrous cement grains, approaching zero at the aggregate-paste interface, while a relatively high amount of smaller ones and a high W/C ratio [6, 162]. These very small particles hydrate rapidly and disappear in a short period. This phenomenon was confirmed by the quantitative BSE image analysis. The initial packing of anhydrous cement in the ITZ was estimated from the distributions and amounts of the remaining cement grains and the porosity after specific hydration times. Throughout the whole measurement period from 1 day to 6 months, the least changes in the anhydrous content occured at the first 10 µm from the interface. The smaller particles with a proportionally higher surface area per unit volume hydrated much more rapidly than larger particles, assuming that the reaction boundary moved at a constant rate at any given time. Within the first day the hydration of the anhydrous cement grains in the first 0-5 μm nearest to the interface were nearly finished, and showed the least changes in the time between 1 day and 6 months. While the smaller particles pack more closely to the interface, the region further away were dominated by the larger particles. In the anhydrous profiles of 1 day, there was a peak in the region between about 15 and 20 μm, which indicates the high amount of anhydrous cement grains. With continuous hydration, the relatively larger particles at the distance about 15-20 μm hydrate slowly and the peak did not exist at later ages. The particle size distribution beyond about 25-30 μm from the interface was similar to that of the bulk cement matrix. The anhydrous particles in the regions further away than about 25 μm from the interface, hydrated more uniformly than those in the region between about 0-25 μm. The diagram of this distribution was initially proposed by Crumbie [16], and adjusted in Fig. 4.70.

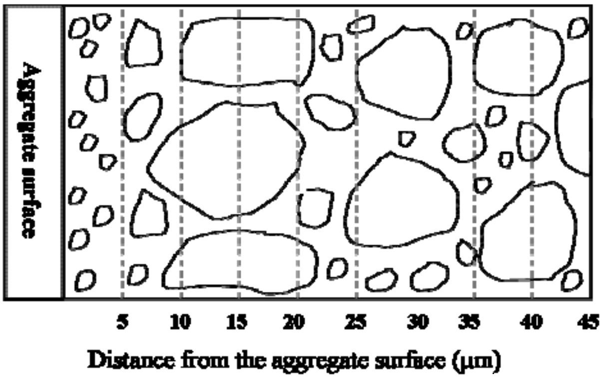

Fig. 4.70 Diagram of the initial particle packing based on the BSE image analysis and model proposed by Crumbie [16].

As a result of the initial particle packing, the most noticeable features of the ITZ are the high porosity and high concentration of CH which were detected in the BSE and X-ray line scanning analysis. These distinguished features suggest that the microstructure of the ITZ can be modified through disturbing the initial particle packing and filling secondary products in the pores of the ITZ. Therefore, two types of SCMs, i.e. LF with a fine particle size and GGBS with a high pozzolanic reactivity, were used. As the water to binder ratio was fixed, the addition of LF has two opposite effects, (i) the addition of inert LF powder can increase the effective W/C or W/(C+GGBS) ratio and results in a more porous structure; (ii) the positive one including nucleation sites effect, filler effect and transforming partial CH crystals with the remaining aluminates to hemi-carbonate [168]:

$$C_3A + 0.5C\bar{C} + 0.5CH + 11.5H \rightarrow C_4A\bar{C}_{0.5}H_{12}$$

At 5% LF of addition, the filler effect and nucleation effect dominate the adverse dilution effect, and produce a denser microstructure. Incorporating a higher amount of LF (10%), the dilution effect becomes prominent and leads to a more porous structure not only in the ITZ but also in the bulk cement matrix. Although the overall structure is weakened, the finer LF particles are also able to squeeze themselves closer to the aggregate surface and alter the nearby region to a higher extent, by replacing the large CH plates with smaller and less preferentially orientated crystals, and are contributing to a reduced difference between the ITZ and the bulk cement matrix. This was confirmed in the MIP, mechanical and transport measurements. The obtained results of L10 series showed a small variation to the aggregate size and volume fraction. The P3 pore volume in the L10-2 was also reduced slightly compared with that of the reference sample.

In the samples prepared with moderate amount of GGBS (35%), an improvement in the microstructure of both ITZ and bulk cement matrix was observed. The pozzolanic reaction between the GGBS and the hydration products of the cement hydration (CH) provided a more homogeneous microstructure. This was confirmed by the presence of a fairly constant Ca/Si ratio in the ITZ and bulk matrix. This is in consistence with previous literature results and some assumptions. The pozzolanic particles produce a fast saturation balance of CH and result in the formation of a dense cementitious matrix [164]. It was observed that the addition of GGBS significantly decreases the mean size of the CH crystal to 3-4 μm [164]. Meanwhile, the pozzolanic reaction of GGBS was limited by the amount of CH produced by cement hydration. For a higher GGBS replacement level (70%), the available CH content for pozzolanic reaction would reduce, and results in a higher total porosity. The other possible explanation could be that the addition of 70% GGBS increases the local W/C ratio. However, some pore refinements were still observed, in which the P3 and P2 pore volume decrease and P1 pore volume increases significantly. This refinement is essential for the ions and water movements.

Concerning the mechanical properties, the compressive strength was higher for the neat PC paste compared with the mortars and concretes. This presumably is due to the presence of the ITZ which results in a less effective transfer of stress from the bulk cement matrix to the aggregate grains [15]. For SCM incorporated groups, the strengths of the neat paste were always lower than the reference one. However, some improvements were captured in the mortars and concretes, such as group S35, L05 and S30L05. In mortars and concretes, the contribution of bulk matrix to the overall strengths was less and the effect of ITZ and aggregate became higher. Previous literature results also proposed other causes for the difference in effects of mineral additions on the strength of paste and mortars [21, 108, 115, 161, 188]. It is suggested that in cement paste, the fine cementitious additions cannot be effectively dispersed even in the presence of superplasticizers. For this reason, although the cement hydration may be accelerated, the pozzolanic reaction which occurs later is limited. In the mortars and concretes, the shearing of the aggregate grains with the fine cementitious particles during the mixing tends to break any clumps formed. In our study, however, the PSD of all the SCMs is of the same order of magnitude as that of the PC. The ineffective dispersion may not be the main reason for the different effect of SCMs on the paste and mortars. The improvement in the strength of mortars and concretes by the GGBS and LF are possible to be due to the modified ITZ.

On the other hand, significant decreases in the transport coefficients of chloride and water were observed in 5% LF blended and all samples containing GGBS. Two effects may contribute to these improvements, i.e. (i) improvement of the ITZ by the better particle packing and the pozzolanic reaction; (ii) densification of the bulk cement matrix also provided by the aforementioned acceleration, particle packing and pozzolanic reaction. The GGBS was more effective than the LF in limiting the movement of chloride and water. The weak zone of ITZ was also strengthened using ternary mixtures of GGBS and LF to partially replace PC. Compared with only GGBS partially replacing PC, the enhancement effect of GGBS and LF simultaneously substituting for a part of PC is less in the relation to the transport properties. From the results provided in the transport measurements, the differences in the transport coefficients between the reference series and the blended series were more apparent for the neat paste samples. Moreover, the variation of transport coefficients were highly dependent on the changes in the P2 ($10\text{ nm} < d < 100\text{ nm}$) rather the P3 (>100 nm) volume. This suggests that the observed improvement of ion and water resistance of the GGBS blended samples must be due in part to the improvement of the microstructure of the ITZ, but more importantly, to the marked densification of the bulk cement matrix.

4.4 Conclusions

In this chapter, the influences of GGBS and LF on the microstructure of the ITZ in relation to the macro-properties of the paste, mortar and concrete were determined. The development of the microstructure of the ITZ with hydration time was discussed based on the quantitative BSE image analysis and the initial particle packing of cement grains diagram was proposed. Correlating the mechanical properties, chloride migration coefficients and water sorptivities with the variations in the microstructure, the relative importance of the improved ITZ to the enhancement of the overall properties were determined. On the basis of the presented results, the main points of this chapter can be summarized as:

1) The initial particle packing of cement grains led to a depletion of larger anhydrous cement grains, approaching zero at the aggregate-paste interface, with a relatively high amount of smaller grains and a high W/C ratio. Throughout the whole measurement period from 1 day to 6 months, the least changes in the anhydrous content occured at the first 5 μm from the interface. The regions further away were dominated by the larger particles, which hydrated slowly and presented a peak in the region between about 15 and 20 μm in the anhydrous profiles, which disappeared at later ages. The

particle size distribution beyond about 25-30 μm from the interface was similar to that of the bulk cement matrix.

2) The critical pore diameters (d_1) of mortars prepared with 55% of aggregate were always less than the corresponding neat cement pastes regardless the binders. For the mortars prepared with 55% of aggregate, one of the most important observations was the presence of critical pores with diameter d_2 which was superior to 0.1 μm. The d_2 was more apparent for samples with the small aggregate size 0/2 mm, and shifted towards coarser for samples with coarser aggregates (combined 0/2 mm and 2/5.6 mm). The total porosity increased with increasing aggregate volume fraction, or with decreasing average aggregate size.

3) The incorporation of moderate amount of LF (5%) is able to compact the microstructure of both ITZ and bulk matrix by filling effect and nucleation sites effect. The reduction in P3 volume contributed to the largest decrease in the total pore volume. However, the addition of 10% LF in substitution of PC resulted in an increase in the total porosity and P2 pore volume, but a decrease in the P3 volume. Although the overall pore structure was weakened, it is still expected to have improvements in the microstructure of ITZ.

4) The effects of GGBS on the porosity were highly dependent on the replacement rate and the determined pore size regions. For 35% GGBS replacement, the total porosity, P3 and P2 volume were less, while the P1 volume was higher, than that of GGBS-free samples. Concerning the substitution of 70% GGBS for PC, the total porosity and the P1 volume increase significantly. However, the coarser pores were still observed to be refined and the P3 volume of S70 series arrived to 0.005, 0.031 and 0.069 mm^3/mm^3 for neat paste, mortar-1 and mortar-2. The high amount of GGBS substitution can increase total porosity but refine the pore size from the range of P3 and P2 to P1 size.

5) The neat cement paste C-P had the highest overall compressive

strength compared with the mortars and concretes. For the reference samples, there seemed to be an obvious trend towards reduced compressive strength with the higher ITZ quantity. Concerning the effect of the difference in the ITZ quantity on the compressive strengths, the variation was all the less appreciable as the amount of LF increases and the L10 series showed the least variation but the lowest overall strengths. The incorporation of 35% GGBS as a partial substitution for PC improved the compressive strengths of mortars and concretes, while the strengths of S70 blended mortars and concretes were reduced significantly. Incorporating of GGBS and LF as a substitute for PC did not show enhancement in the compressive strength of neat cement paste. The improvement in the strength of the mortars and concretes were presumably due to the densification of the ITZ.

6) The D_{nssm} and S_i values of the series containing GGBS decreased significantly when the replacement rate of GGBS increases. The influence of LF on the transport properties depended on the substitution rate. The addition of 5% LF tended to limit the movement of chloride ions and water slightly. The GGBS was more effective than the LF in limiting the movement of water and ions. By comparing the relative difference in the D_{nssm} and S_i with the relative difference in the intruded pore volume, a fairly obvious linear relationship between the variation of D_{nssm} (S_i) and that of P2 ($10\,\text{nm} < d < 100\,\text{nm}$) volume was observed. The observed improvement in limiting the movement of water and chloride ions for the GGBS blended samples could be due in part to the improvement of the microstructure of the ITZ, but more importantly, to the densification of the bulk cement matrix.

Chapter 5

The role of ITZ on the chloride diffusion in GGBS and LF blended cement composites

---

5.1 Introduction

The ingress of chlorides into concrete is of particular interest for the assessment of the durability characteristics of concrete. Resistance of concrete to chloride ingress is a key property for the durability of reinforced concrete structures exposed to de-icing salts or sea water [189-191]. The chlorides that are transported through the concrete pore network and microcracks depassivate the oxide film covering the reinforcing steel and accelerate the reaction of corrosion [192]. Even high-performance concrete may not necessarily ensure long-term durability in a severe environment unless it is designed for dimensional stability and soundness [193]. Chloride induced corrosion of the reinforcement is one of the main causes of structural concrete deterioration and therefore responsible for a large share of the cost for the rehabilitation of concrete structures [194].

Chloride transport through concrete is highly influenced by the pore structure [195-196]. It is determined by the w/c ratio, curing age, materials compositions and etc.. It is generally agreed that the pore structure of concrete is one of its most important characteristics and strongly affects the chloride movement [195, 197-198]. Besides, the influence of pH in the pore solution, Ca/Si ratio of calcium silica hydrates (C-S-H gel) etc. on the rate of chloride penetration have been widely investigated [199-202]. However, the relationship between the porous ITZ and the chloride movement remains uncertain.

Another influence on the rate of chloride penetration into concrete is affected by the chloride binding capacity [203]. With respect to the transport process two types of chloride in concrete must be distinguished. These are the free chloride ions dissolved in the concrete pore solution, and chloride ions that are combined in or bound to different hydration products of the cement. Both types of chloride normally exist simultaneously to maintain chemical equilibrium [201, 203]. For transport processes as well as for corrosive actions on the reinforcement, however, only the free chloride ions in the pore solution are of importance, and knowledge of the total chloride ions content of concrete is often insufficient unless the relation between the free chloride ion concentration and the total chloride concentration is known [146, 200]. The corresponding ratio bound/total chloride is usually referred to as the binding capacity. It is known that cement has the ability to bind chlorides, depending on its chemical composition [204-206]. Therefore, chloride is present in concrete both as ion in the pore solution as well as bound to cement hydration products in the form of Friedel's salt ($C_3A{\cdot}CaCl_2{\cdot}12H_2O$), adsorbing to C-S-H and the pore surface [20, 200]. Since only "free" chloride ions in the pore solution can move, chloride binding can affect resistance of concrete to chloride ingress by delaying the penetration process [201].

The incorporation of SCMs, such as fly ash, slag, silica fume, metakaolin and other natural pozzolans, as a partial substitute for PC have been found to be beneficial in resisting the ingress of chloride ions into concrete [204-205, 207-210]. This improvement in the chloride resistance is generally ascribed to the refined pore structure that results from the pozzolanic reaction or secondary hydration of these materials. The use of SCMs also alter the compositions, and hence the chloride binding capacity. Previous literature indicated that GGBS and fly ash generally shows increased chloride binding [208, 211], metakaolin improves the chloride binding to a large extent [204, 207] and silica fume shows a decrease in binding capacity [204]. Moreover, very few data are available regarding the effect of LF on the diffusion and binding of chloride ions despite its wide application.

From the literature studies and previous experiments, it was found that the variation of ITZ has a significant impact on the pore size distribution and the mineralogical compositions of bulk cement paste. The porous ITZ is normally accompanied by a denser bulk cement matrix with a finer critical pore diameter (d_1). The preferable deposition of CH within ITZ would lead to a lack of calcium ions in the matrix. The non-steady-state chloride migration measurements also indicated that the movement of chloride ions depends on the microstructure of the ITZ, and this influence varied significantly with the blended systems. However, several researches have pointed out that the RCM test has its drawbacks [156, 212]. It basically includes a conductivity of all ions in the pore solution which include OH^-, Cl^-, Na^+, K^+, SO_4^{2-} and Ca^{2+}, whose concentrations vary for concrete with different blended materials [213-214]. Therefore, the comparison of pozzolanic materials using various percentage blends with the RCM may not be representative because of the effect of the pore solution chemistry involved in the employed blended materials [215]. Other problems with this rapid chloride migration method include heat evolved during the test and alternation in the pore fluid characteristics when used with pozzolanic materials [215-216]. Moreover, very few data have been provided in the previous RCM tests and the published reports with respect to the relationship between the chloride binding capacity and the ITZ properties.

Therefore, the aim of this study is to investigate the effect of ITZ on the chloride diffusivity of various blended systems. The chloride resistance of concrete produced with various aggregate volume fractions and aggregate sizes is measured through a natural diffusion test. Whether the variation of the chloride diffusivity is mainly determined by the varied ITZ or the bulk cement matrix is evaluated and related to porosity. Furthermore, the chloride binding capacity obtained from the relation between free chloride and bound chloride is estimated, in order to investigate if/how its changes with the ITZ properties. This study will help to achieve a suitable mix design for more durable materials and contribute to the prediction of chloride-induced corrosion.

5.2 Experiments

5.2.1 Materials and mixtures

In this chapter, the same materials and mixtures as in chapter 4 were used. The detailed mixtures and the properties of the cementitious materials and aggregates were shown in Table 4.1 -4.4 and Fig.4.1-4.2.

5.2.2 Tests and analysis method

5.2.2.1 Diffusion process

For the ingress of chlorides into concrete, different physical mechanisms may be distinguished with respect to the driving force, i.e. permeation, capillary absorption, migration and wick action and diffusion. Of them, diffusion takes place under the influence of a concentration gradient, which mainly drives the transport of chloride ions in concrete exposed to a direct contact to seawater, for example, submerged, tidal and splash zones, where the moisture condition of the concrete is stable. Concerning the assessment of the corrosion protection of the reinforcement either concentration profiles for chlorides or the rate of progress of a given chloride concentration into a concrete section are of interest rather than the maximum depth of chloride ion penetration.

For modeling the diffusion of unreactive species into a semi-infinite medium, an error function solution to the Fick's second law is normally used as:

$$C(x,t) = C_{\mathrm{s}} - (C_{\mathrm{s}} - C_{\mathrm{i}}) erf(x / \sqrt{4 \cdot D_{\mathrm{a}} \cdot t}) \qquad (5.1)$$

Where $C(x,t)$ is the concentration at the depth x and the exposure time t, C_{i} is the initial chloride content in the specimens, C_{s} is the surface concentration, and *erf* is the error function. Theoretically, the D_{a} (apparent chloride diffusion coefficient) can be calculated by measuring the concentration of the C_{s} and the concentration of chloride ions $C(x,t)$ at the depth x and the exposure t.

5.2.2.2 Sample preparation

The effect of aggregate on chloride diffusion was investigated by a non-steady-state diffusion test [217]. The specimens were coated by epoxy at 56 days except the exposed surface. In order to avoid the casting surface effect, saw cut surfaces were chosen for contacting the chloride solution. After that, all the specimens were vacuum saturated with a saturated $Ca(OH)_2$ solution for 48 h. The technique of vacuum saturation ensured that the diffusion is the only mechanism for chloride transport. At last the saturated specimens were immersed in 165 g/L sodium chloride solution at 20±2 °C for 3 months, which means that the chloride profile testing age is 5 months. The exposed solution was stirred once every week and replaced with a new NaCl solution once every 30 days. The testing procedure is represented in the schematic diagram of Fig. 5.1.

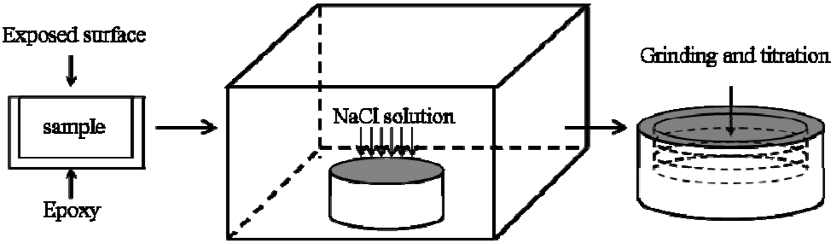

Fig. 5.1 Procedure of the chloride diffusion test.

5.2.2.3 Determination of chloride content

There are two stages in measuring the chloride content: sampling and analyzing. Sampling generally involves grinding the concrete and collecting dust at various depths. After 3 months of immersion, all specimens were ground immediately in layers with a thickness of 2 mm for each (see in Fig. 5.2). The grinding is performed within a diameter approximately 10 mm less than the full diameter of the core. This obviates the risk of edge effects and disturbances from the coating. It is essential to ensure that there is an approximately equal portion of cement paste in each sample, compared to a bulk concrete, since there is a risk of the sample being dominated by large aggregate sizes. The powder was then passed through 160 μm sieve, and was dried at 85°C to constant mass and cooled down to room temperature before titration. The chloride concentrations were determined by dissolving the powders in solution followed by titration [218].

Fig. 5.2 An example of the grinding process.

Total chloride concentration

The total chloride content in this work is defined as the acid soluble chloride. After cooling the ground powders down, a solution of 5 mL of 0.3 mol/L nitric acid, 40 mL distilled water, was prepared and mixed with 2 g powder to determine the acid soluble chloride content. The solution was stirred for 1 min, and then heated until boiling. After cooling down, the solution was filtered into 100 mL flask with distilled water. At last, 10 mL of the filtered solution was pipetted for the determination of the chloride content by titration. The titration was conducted by using a Metrohm MET 702 automatic titrator, and 0.01 mol/L silver nitrate solution. The total chloride content can be calculated by:

$$C_{\mathrm{t}}(\%) = \frac{10 \times 100 \times V \times 35.45 \times C_{\mathrm{AgNO_3}}}{1000 \times 2} \tag{5.2}$$

Where C_{t} is the acid soluble chloride content by the mass of concrete (in %); V is the consumed volume of silver nitrate solution (in mL); $C_{\mathrm{AgNO_3}}$ is the concentration of silver nitrate solution after calibration (in mol/L).

Water soluble chloride concentration

The water soluble (free) chloride concentration is measured from a solution obtained by dissolving the concrete/mortar powder in water. 2.5 g powder and 50 ml distilled water was used to prepare a solution. The solution was stirred for 1 min, sealed and stored at 20±2°C for 24 h. After that, 5 mL solution is pipetted to determine the water soluble chloride content by titration. The water soluble chloride content is given by:

$$C(\%)=\frac{10\times100\times V\times35.45\times C_{\mathrm{AgNO_3}}}{1000\times2.5} \tag{5.3}$$

Where C is the water soluble chloride content by the mass of concrete (in %); V is the consumed volume of silver nitrate solution (in ml); C_{AgNO3} is the concentration of silver nitrate solution after calibration (in mol/L).

Chloride binding isotherm

It has been proven that the chloride binding isotherm could be obtained from the diffusion cell experiments [219]. Based on the water soluble chloride content and total chloride content, the bound chloride content can be obtained by:

$$C_{\mathrm{b}}(\%)=C_{\mathrm{t}}(\%)-C(\%) \tag{5.4}$$

Since the unit of bound chloride content is given as the mass percentage of concrete samples, an equation is proposed to transform it to the mass percentage of binder content for the suitable chloride binding comparison between different samples [220-221].

$$W_{\mathrm{binder}}=\frac{W_{\mathrm{c}}+W_{\mathrm{w}}-\rho_{\mathrm{dry}}\times P_{\mathrm{m}}}{\rho_{\mathrm{dry}}} \tag{5.5}$$

Where W_{binder} is the binder content by the mass of concrete (%); W_{c} is the weight of cement for 1 m^3 concrete by the mass of concrete (%); W_{w} is the weight of water used for 1 m^3 concrete (%); ρ_{dry} is the density of dry concrete (105°C); p_{m} is water accessible porosity by mass of dry samples.

The unit of the determined water soluble chloride is percentage by the mass of sample. However, the free chloride content expressed in the unit of mol/L is more of interest in the case of chloride binding calculation. The unit of free chloride content can be transformed from % to mol/L by using the follow equation:

$$C(\text{mol/l})=\frac{1000\times C(\%)}{35.45\times P_{\text{m}}} \tag{5.6}$$

Where C (%) is the chloride content by the mass of concrete, P_{m} is the water accessible porosity by mass of dry samples.

Water accessible porosity

The water accessible porosity was determined on the parallel cylinders (Φ100 mm×50 mm) at the age of 5 months. The detailed procedure was presented in chapter 3 and the porosity by mass can be given by:

$$P_{\text{m}}=\frac{m_{\text{a}}-m_{\text{d}}}{m_{\text{d}}} \tag{5.7}$$

Where P_{m} is the water accessible porosity by mass of dry samples (%), m_{a} is the weight in air of saturated sample, m_{d} is the constant weight of oven-dried samples at 105°C.

5.3 Results and discussion

5.3.1 PC

5.3.1.1 Aggregate volume fraction

The effects of the aggregate volume fractions on the chloride penetration profiles of the reference samples and apparent diffusion coefficients are given in Fig. 5.3. The D values were obtained by fitting the experimental data to Eq. (5.1). The first point of the profile determined at the depth of 2 mm from the exposure surface was omitted in the regression analysis. From Fig. 5.3 (a), it can be seen that the chloride penetration profiles are highly dependent on the aggregate volume fractions. The water soluble chloride content in each layer is decreased with increasing aggregate volume content.

The effects of the aggregate volume fractions on the D are similar to the effects defined in chapter 3 and 4. Increasing aggregate volume fraction from 0 to 0.55 causes a reduction of about 60% in the D values. There is a slight increase in the D values while increasing V_{agg} from 0.2 to 0.55. Fig. 5.3 (b) presents the differences between the experimental results and the model line $D_{\mathrm{paste}}(1\text{-}V_{\mathrm{agg}})$ and $D_{\mathrm{paste}}(1\text{-}V_{\mathrm{agg}})^{3/2}$. The result of mortar C-1 below the Bruggeman-Hanai (B-H) law is presumable due to the densification of the bulk cement matrix. The dilution, tortuosity effect and the densification of the bulk cement matrix tends to be balanced by the ITZ effect when the aggregate content reaches to 55%, and the negative effect of ITZ becomes appreciable. A similar trend is also observed for the acid soluble chloride content and is given in the Appendix. As the free chloride in the pore solution is more related to the deterioration of the concrete, the apparent diffusion coefficients D presented in the following parts are obtained from the water soluble chloride penetration profile if no specific explanations are given.

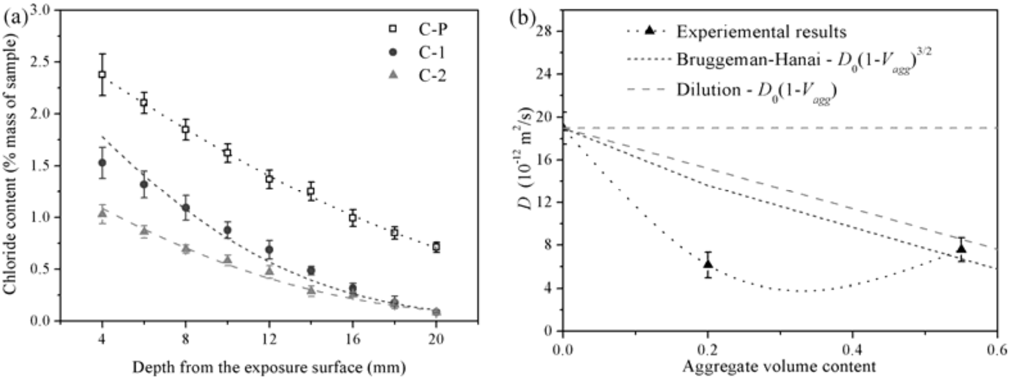

Fig. 5.3 Water soluble chloride penetration profiles (a) and calculated diffusion coefficients (b).

5.3.1.2 *Average grain size*

Fig. 5.4 (a) provides the water soluble chloride penetration profiles in relation to the average aggregate size. There is no detectable effect of the average aggregate size on the results. Concerning the D values in Fig. 5.4 (b), the results calculated are the order of $9\times10^{-12}\ \mathrm{m^2/s}$ and there seems to be an obvious trend of increasing D values for samples with coarser aggregate. This phenomenon may be attributed to: (i) using coarser aggregates would reduce the tortuosity and thus the effective movement paths; (ii) a denser bulk cement matrix is possible to be obtained in the sample prepared with finer aggregate; (iii) although no significant bleeding was observed in the specimens, some local microbleeding is still possible to occur around the coarse aggregates, leading to the presence of coarser pores. The effects (ii) and (iii) have been well defined in the MIP measurements.

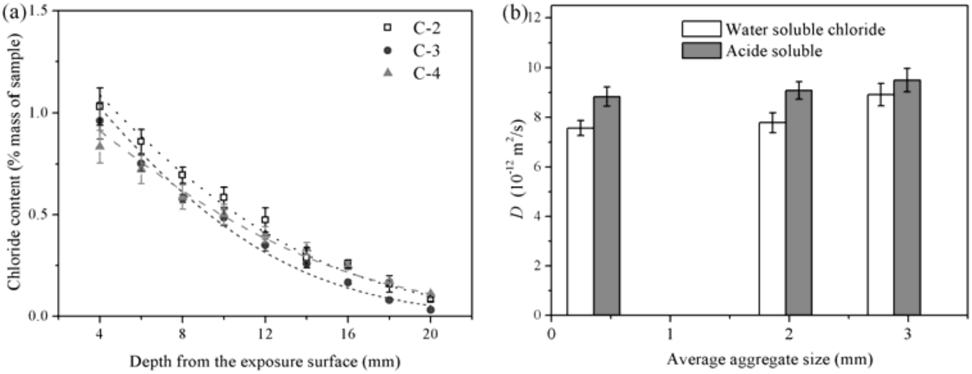

Fig. 5.4 Water soluble chloride penetration profiles (a) and calculated diffusion coefficients (b).

5.3.1.3 *Effect of aggregate on the chloride binding*

Chloride binding exerts a significant effect on the rate of chloride penetration, and hence on the time to corrosion initiation. It is desirable to include the influence of chloride binding in the predicting of service life for reinforced concrete structures [203, 222]. Therefore, this requires the knowledge of the binding isotherms for different parameters. Of them, the effect of materials, accompanied cations and curing period has been well studied [204-205, 207, 209], while the effect of ITZ or the related properties caused by the changes in the ITZ is still unknown.

In order to evaluate the binding capacity, the relationships between the bound chloride content and free chloride over a range of chloride concentrations can be given as the binding isotherm. Fig. 5.5 provides an example of chloride binding relationship for mortar C-1 and the following fitted isotherms:

$$\text{Linear isotherm: } C_\mathrm{b} = \alpha C_\mathrm{f} \tag{5.8}$$

$$\text{Langmuir isotherm: } C_\mathrm{b} = \alpha C_\mathrm{f} /(1+\beta C_\mathrm{f}) \tag{5.9}$$

$$\text{Freundlich isotherm: } C_\mathrm{b} = \alpha C_\mathrm{f}^{\beta} \tag{5.10}$$

Where α and β are binding constants. From Fig. 5.5, the binding is clearly non-linear and the “best-fit” isotherm is the Langmuir and Freundlich. Overall, the Feundlich isotherm provided better fit with higher coefficient of determination in all cases, thereby it is applied for comparison of results.

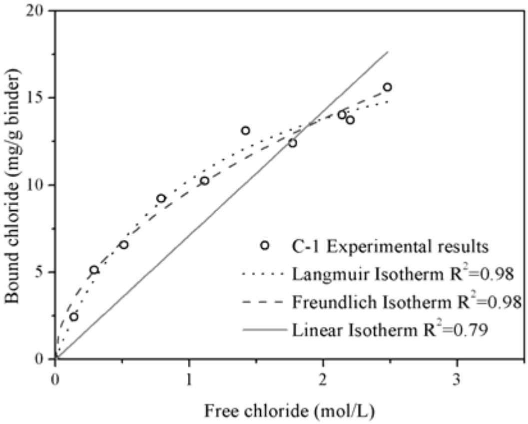

Fig. 5.5 An example of chloride binding relationship for mortar C-1.

Fig. 5.6 and Fig. 5.7 present the results for the samples with various aggregate volume fractions and sizes, respectively. In general, the binding capacity depends on the aggregate volume fractions and sizes, Mortar C-2 shows the highest binding compared with the paste and samples with coarser aggregates. The changes in the chloride binding might have two explanations. On the one hand, aggregate particles introduce changes in paste mineralogy within the ITZ. For instance, a relatively high concentration of portlandite deposited in the ITZ, may lead to a decreased concentration of Ca in the bulk cement matrix. SEM-EDX analysis results in Fig. 5.8 and Table 5.2 show that the average Ca/Si ratio of hydration products decreases as the aggregate volume increases from 0 to 0.55. This reduction is due to the mobility of calcium ions in solution. The more porous zone around the aggregate favors the deposition of more calcium hydroxide in this region. As the quantity of anhydrous material in the ITZ is low, most of this calcium hydroxide must form from calcium ions coming from the reaction of anhydrous cement outside the interfacial region, and thus less calcium ions are available for the formation of C-S-H and the Ca/Si ratio of C-S-H decreases. The reduction in Ca/Si ratio of C-S-H leads to a reduction in the amount of chloride that can be physically adsorbed on the surface of the C-S-H [223-224]. On the other hand, more porous ITZ is accompanied by denser bulk cement paste, so that more chlorides are bound. It may also be concluded that the influence of ITZ on the overall properties depends not only on its own properties, but also on other parameters accompanied by the presence of ITZ.

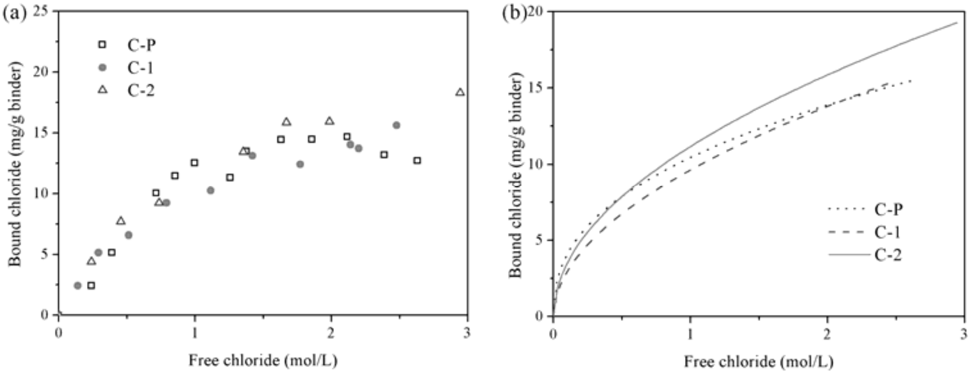

Fig. 5.6 Chloride binding relationship (a) and the fitted Freundlich isotherm (b) for samples with various aggregate volume fractions.

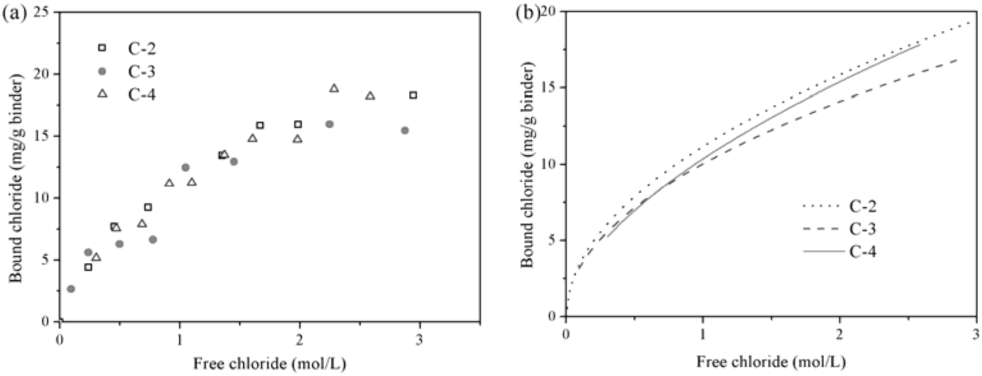

Fig. 5.7 Chloride binding relationship (a) and the fitted Freundlich isotherm (b) for samples with various aggregate sizes.

Table 5.1 The fitted binding coefficients for Freundlich isotherms.

Samples	α	β	R^2
C-P	10.45	0.41	0.903
C-1	9.64	0.50	0.979
C-2	11.17	0.51	0.982
C-3	10.04	0.49	0.929
C-4	10.91	0.50	0.962

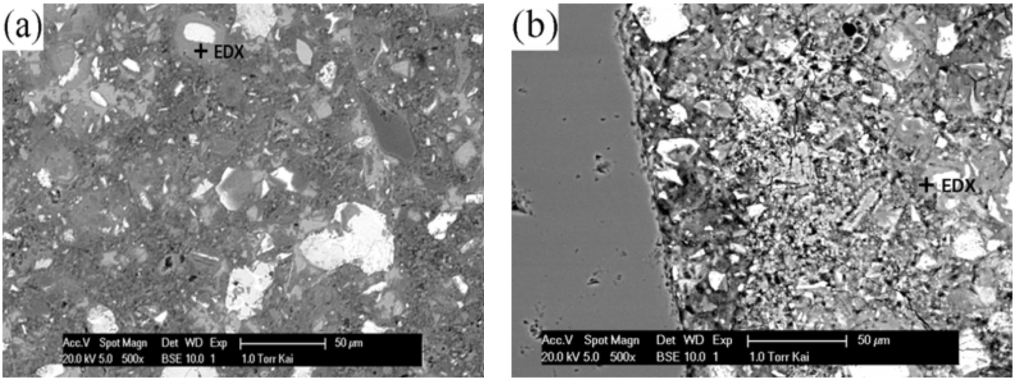

Fig. 5.8 SEM-EDX analysis of (a) C-P and (b) C-2

Table 5.2 The average Ca/Si ratio of hydration products in the paste and bulk cement matrix

	Ca/Si ratio
CP	2.61
C2	1.79

5.3.2 Effect of LF

5.3.2.1 Aggregate volume fraction

Fig. 5.9 (a) shows the chloride diffusion coefficient of reference and LF blended binary series versus the aggregate volume fraction. The results obtained were of the same order of magnitude, between 5-20$\times 10^{-12}$ m^2/s for the three series. For the three series, the *D* values of mortars are lower than those of the corresponding pastes.

For the binary series, the effect of LF on the overall *D* values depends on the substitution rate. The incorporation of 5% LF as a partial substitute for PC slightly decreases *D* of all samples, while *D* value increases significantly as the substitution rate of LF reaches to 10%. Additionally, *D* shows little variation as the aggregate volume content increases from 0.2 to 0.55. This is presumably due to the modification effect of LF on the ITZ. To support this conclusion, the differences calculated between the *D* of LF blended series and the reference samples are given in Fig. 5.9 (b). For L05 series, the most significant reduction in the *D* occurs for the sample with 55% aggregate. This further confirms the relatively importance of LF to the modification of ITZ. Concerning L10 series, there is no appreciable relation between the relative difference and the aggregate volume, the least increase is observed for the neat cement paste L10-P.

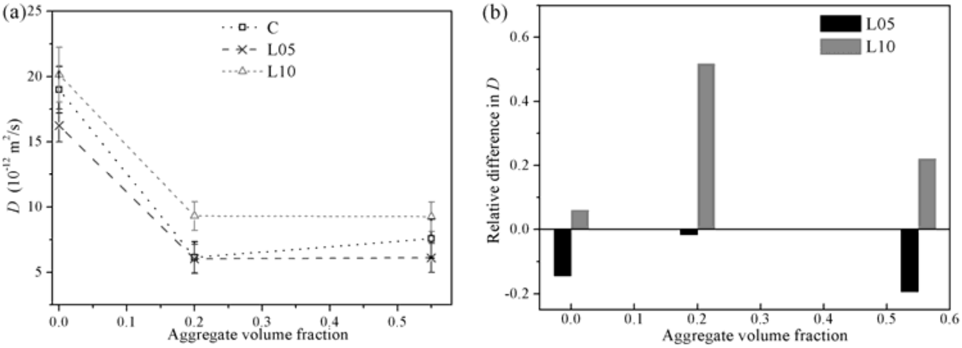

Fig. 5.9 Effect of aggregate volume fraction on *D* (a), and the relative difference in *D* of PC-LF binary series with respect to the reference C series (b).

5.3.2.2 Average grain size

Fig. 5.10 shows the relation between the obtained *D* values versus the average aggregate size. A similar trend is observed with respect to the effect of LF on the overall as observed in Fig. 5.9, namely *D* decreases for samples with 5% of LF and increases for samples with 10% of LF compared with the corresponding references. The values obtained are of the order of 7×10^{-12} m^2/s for the L05 series, and about 9×10^{-12} m^2/s for the L10 series. For the L05 series, the most significant reduction in *D* compared with the reference series occurs in the sample L05-2 (Fig. 5.10 (b)). Moreover, the *D* values of L10 series show the least variation with the average grain sizes. These findings are in consistence with the previous results.

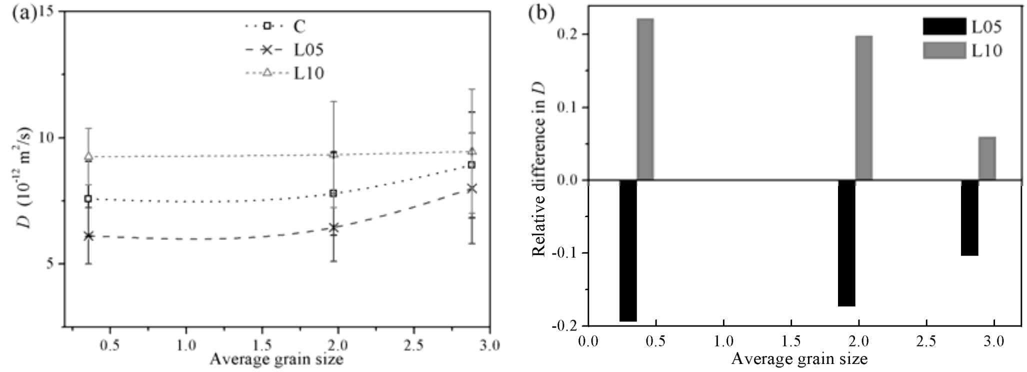

Fig. 5.10 Effect of average grain size on *D* (a), and the relative difference in *D* of PC-LF binary series with respect to the reference C series (b).

5.3.2.3 Chloride binding

The experimental results and regression analysis for L05 series and L10 series in relation to the aggregate volume fraction are given in Fig. 5.11. The fitted parameters are shown in Table 5.3. There is a slight increase in the chloride binding with the aggregate volume fraction. Fig. 5.12 shows the effect of aggregate size on the chloride binding capacity for L05 series and L10 series. Unlike the observations in the C series, there is no appreciable effect of the differences in aggregate size on chloride binding for both L05 and L10 series. For L05 series, the finer aggregate size increases chloride binding slightly. Concerning L10 series, the chloride binding of L10-2 is similar to that of L10-3, while it decreases slightly for L10-4. The lower sensitivity of chloride binding in samples containing LF to the aggregate properties, suggests a relatively more homogeneous microstructure for LF blended series than for the references.

Concerning the effect of LF on the chloride binding, the binding relationships for a combination of binders with and without LF are given in Fig. 5.13. LF decreases the chloride binding and its influence is more pronounced at lower free chloride concentration and higher LF substitution rate. The influences of LF on the chloride binding capacity can be mainly attributed to: (i) dilution of the C_3A content which may reduce the chloride binding. It is generally accepted that the amount of bound chlorides increases with increased alumina-bearing phase. This is mainly due to the reactions between chlorides and C_3A and the formation of Friedel's salt [200, 205-206]. Several studies have indicated that a higher C_3A content results in higher binding capacity [209, 225]. (ii) reducing the AFm phase quantity. Surgavanshi et al. [226] pointed out that the Friedel's salt can be formed by adsorption and anion-exchange. In the adsorption mechanism, the formation of Friedel's salt is due to the adsorption of chloride ion present in the pore solution into the interlayers, $[Ca_2Al(OH)_6 \cdot 2H_2O]^+$ of the AFm structure. In the anion-exchange mechanism, a fraction of the chloride ion replace OH^- ions present in the interlayers of the AFm hydrates to form Friedel's salt [200]. Therefore, the chloride binding capacity is highly dependent on the AFm phase content [204]. Weerdt et al. [168] found that the addition of LF tends to stable the ettringite and reduce the content of AFm. The remaining aluminates would react with calcium carbonate to form a combination of mono- and hemicarbonate and the decomposition of ettringite to AFm is limited. (iii) reducing pH value or the hydroxyl ions which could increase chloride binding. There is a competition between hydroxyl and chloride ion for adsorption sites on the surface of hydration products [227]. Additionally, a decrease in hydroxyl concentration could decrease the solubility of Friedel's salt, and enhance the chemically bound chloride as a result [200]. In this study, this positive influence was dominated by the reduction effects, thereby, the chloride binding was decreased as the substitution of LF increases. The reduction of chloride binding could be one of the reasons for the increased chloride diffusion coefficients in the LF blended series.

$$C_3A + C\bar{C} + 11\,H \rightarrow C_4ACH_{11}$$

$$C_3A + 0.5\,C\bar{C} + 0.5CH + 11.5\,H \rightarrow C_4A_{0.5}H_{12}$$

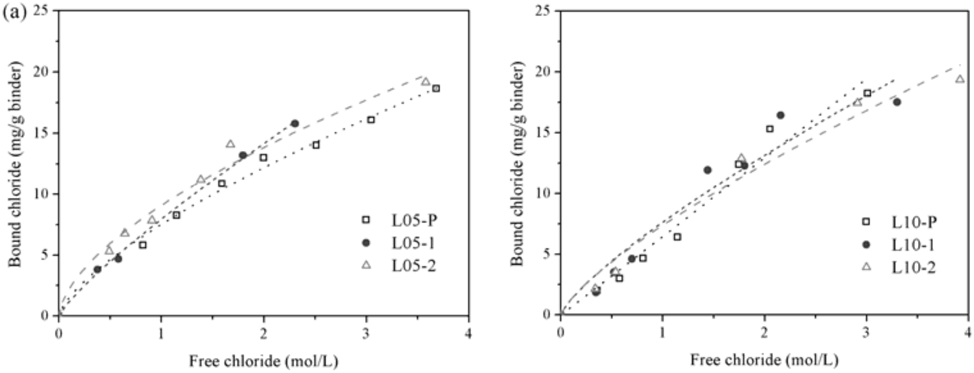

Fig. 5.11 Freundlich isotherms with experimental results in relation to aggregate volume fraction for (a) L05 series and (b) L10 series.

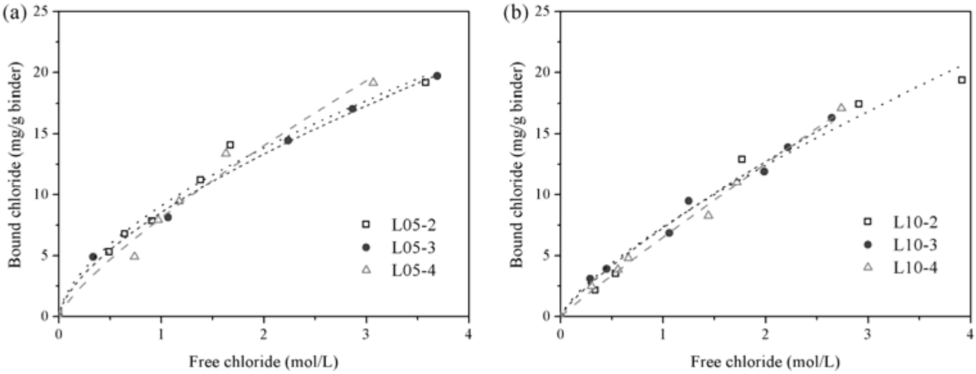

Fig. 5.12 Freundlich isotherms with experimental results in relation to aggregate size for (a) L05 series and (b) L10 series.

Table 5.3 The fitted binding coefficients for Freundlich isotherms.

	α	β	R^2		α	β	R^2
L05-P	7.51	0.70	0.992	L10-P	6.95	0.80	0.968
L05-1	7.95	0.83	0.997	L10-1	7.63	0.78	0.937
L05-2	9.07	0.61	0.980	L10-2	7.36	0.75	0.974
L05-3	8.54	0.64	0.995	L10-3	7.28	0.80	0.989
L05-4	8.11	0.79	0.974	L10-4	6.91	0.94	0.993

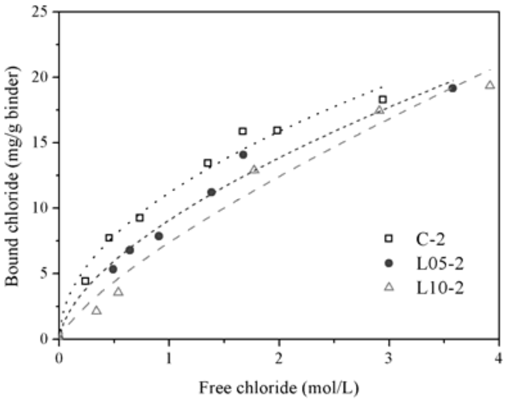

Fig. 5.13 Freundlich isotherm with experimental results for mortars with difference LF replacement rates.

5.3.3 Effect of GGBS

5.3.3.1 Aggregate volume fraction

Fig. 5.14 shows an example of chloride penetration profiles for 70% GGBS blended samples with various aggregate volume fractions. It can be clearly seen that the chloride concentrations reach a constant value at a distance of about 10 mm from the exposed surface regardless the aggregate content, and reaches the initial value. This suggests that the GGBS can limit the penetration of chloride significantly. The apparent chloride diffusion coefficients of GGBS blended binary samples are given versus the aggregate volume fraction in Fig. 5.15. The *D* values are significantly lower for samples containing GGBS than those for the pure PC series. The values obtained are between about 0.5×10^{-12} to 1.0×10^{-12} m^2/s for the binary series, and about 7.5×10^{-12} to 19×10^{-12} m^2/s for the reference series. Concerning the binary system, *D* increases continuously as the aggregate volume increase. This is in consistence with the findings in the chloride migration experiments, in which it was attributed to the prominent densification of the matrix.

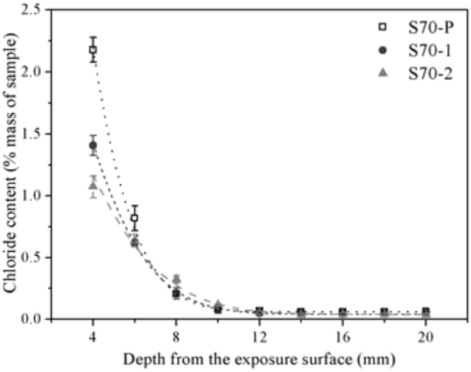

Fig. 5.14 Chloride penetration profiles for S70 with various aggregate volume fraction.

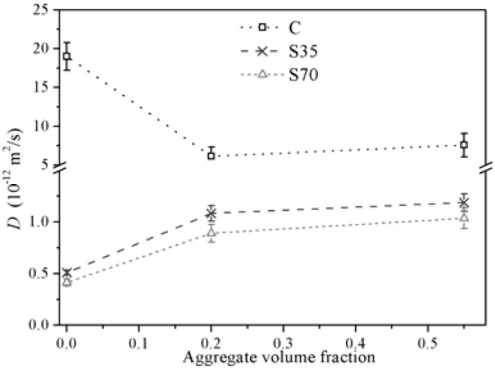

Fig. 5.15 Effect of aggregate volume fraction on D of PC-GGBS binary samples.

5.3.3.2 *Average grain size*

Fig. 5.16 shows the chloride diffusion coefficients of samples containing GGBS in relation to the average aggregate size. The D values obtained are between about 1.0×10^{-12} to 2.0×10^{-12} m^2/s for the S35 series, and consistently 1.1×10^{-12} m^2/s for the S70 series. Although a slight increase is observed as the average grain size increases, samples containing GGBS show little variation with the grain size.

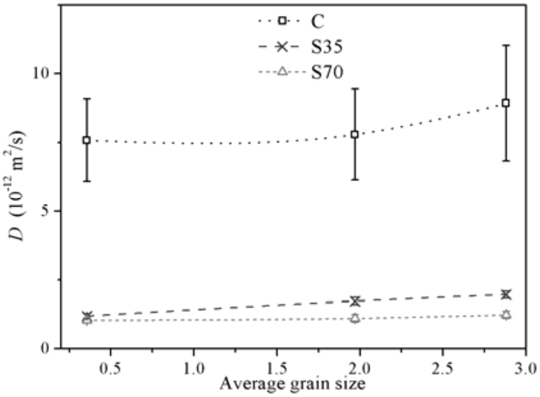

Fig. 5.16 Effect of aggregate size on D of PC-GGBS binary samples.

5.3.3.3 *Chloride binding*

Although the chloride binding relation in GGBS series was studied only at three different chloride concentrations, the experimental data were nevertheless fitted by Freundlich isotherms. The chloride binding relations with respect to the aggregate volume fraction and average aggregate size are given in Fig. 5.17 and Fig. 5.18, respectively. The regression analysis results are presented in Table 5.4. For S35 series, the chloride binding decreases slightly with increasing aggregate volume fraction, while there is no appreciable effect of the difference in aggregate grain size on the chloride binding. At higher rates of substitution (70%), the chloride binding shows the least variations with aggregate volume fraction and size. This again confirms the small influence of ITZ on the chloride binding in samples containing GGBS.

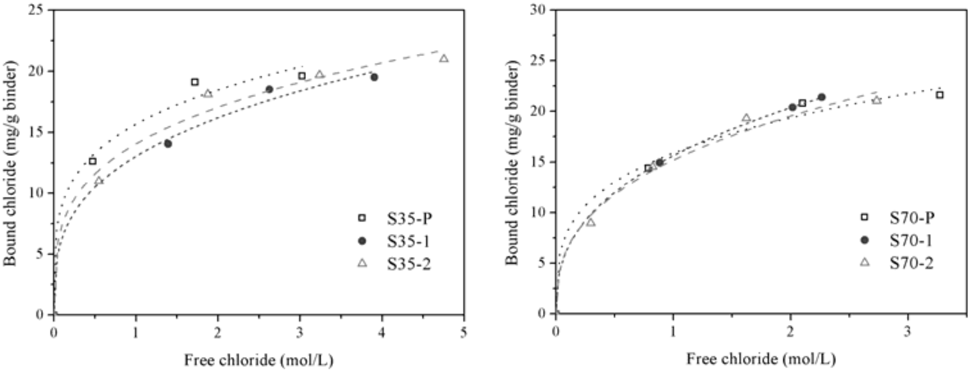

Fig. 5.17 Freundlich isotherms with experimental results in relation to aggregate volume fraction for (a) S35 series and (b) S70 series.

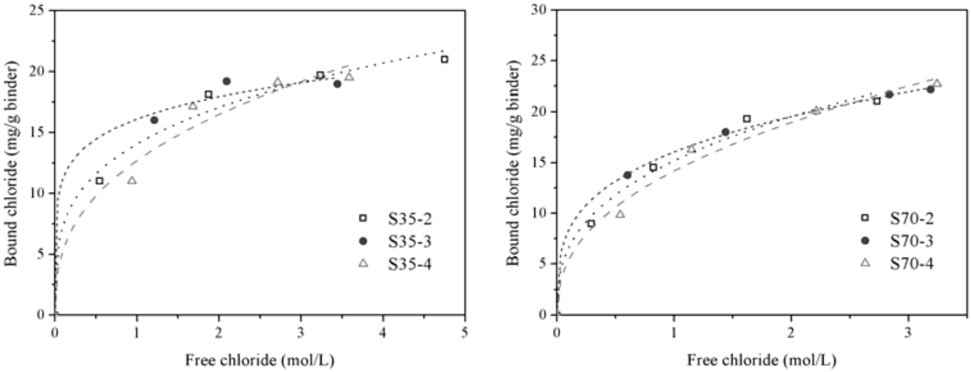

Fig. 5.18 Freundlich isotherms with experimental results in relation to aggregate size for (a) S35 series and (b) S70 series.

Table 5.4 The fitted binding coefficients for Freundlich isotherms.

	α	β	R^2		α	β	R^2
S35-P	14.67	0.24	0.985	S70-P	15.88	0.29	0.990
S35-1	14.04	0.31	0.993	S70-1	15.64	0.38	0.999
S35-2	14.06	0.28	0.986	S70-2	15.19	0.36	0.987
S35-3	15.10	0.16	0.989	S70-3	16.05	0.29	0.999
S35-4	13.69	0.38	0.969	S70-4	15.18	0.42	0.987

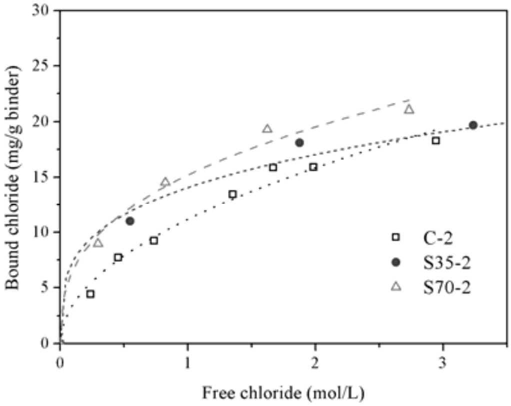

Fig. 5.19 Freundlich isotherm with experimental results for mortars with difference LF replacement rates.

Fig. 5.19 shows the effect of slag on the relationship between bound and free chlorides. The binding capacity of the mortars increases significantly as the substitution rate of GGBS increases. This could also be one of the reasons for the reduction of chloride diffusion coefficients in samples containing GGBS, besides the refinement of pore structure. Several researches have shown that partial substitution of cement with GGBS increases chloride binding both for external and internal chlorides [200, 204, 207-208]. The influence of GGBS on the chloride binding can be mainly attributed to three ways: (i) dilution of the C_3A which may reduce binding; (2) reduction of the pH of the pore solution which should increase chloride binding [222, 227-228]; (iii) the increase in the amount of C-S-H which should increase the adsorption sites for the chloride binding [204, 209, 221]; (iv) reducing the C/S ratio of the C-S-H which would reduce the binding capacity. However, the GGBS used in this study has a given amount of alumina contents (11.25 %) and the subsequent formation of C-A-S-H may result in increased binding [199, 204-205], in addition to the increased formation of Friedel's salt. Luo et al. [208] suggested that GGBS can increase the chloride binding capability because of the increased formation of Friedel's salt.

5.3.4 Effect of ternary binders

5.3.4.1 Apparent chloride diffusion coefficients

Fig. 5.20 shows the chloride diffusion coefficients for the binder S35 and S30L05 versus the aggregate volume fraction and sizes. Concerning the effect of aggregate on the D values, a similar trend to the corresponding binary series is observed for the S30L05 series, i.e. D increases continuously as the aggregate volume or the aggregate size increases. The presence of LF tends to increases D values slightly, and this increase is more noticeable in the case of pure paste. This can be mainly due to the dilution of the pozzolanic materials by LF. Although several researches have shown that the addition of moderate amount of LF can accelerate the hydration of GGBS by promoting the formation of CH, this acceleration was mainly limited in the case of early age [170-171]. The chloride diffusivity was measured at the age of 5 months, the acceleration effect might be dominated by the dilution effect. The results presented are in consistence with the migration tests in Chapter 3.

Fig. 5.21 shows the relation between the aggregate properties and the chloride diffusivity D for the binary and ternary binders with a fixed substitution rate of 70%. There is no trend with the LF replacement level as the D values of samples with ternary S65L05 are lower than both the corresponding binary binders and S60L10 series. The highest D values occur in the samples prepared with ternary binder S60L10 due to the prominent dilution of pozzolanic materials. Concerning the effect of aggregate volume fraction and grain size, a similar trend to the corresponding binary series is observed for both S65L05 and S60L10 series, namely D increases continuously as the aggregate volume or the aggregate size increases. From Fig. 5.21 (b), it can be seen that the samples prepared with ternary binder S65L05 show the least variation with the average aggregate size.

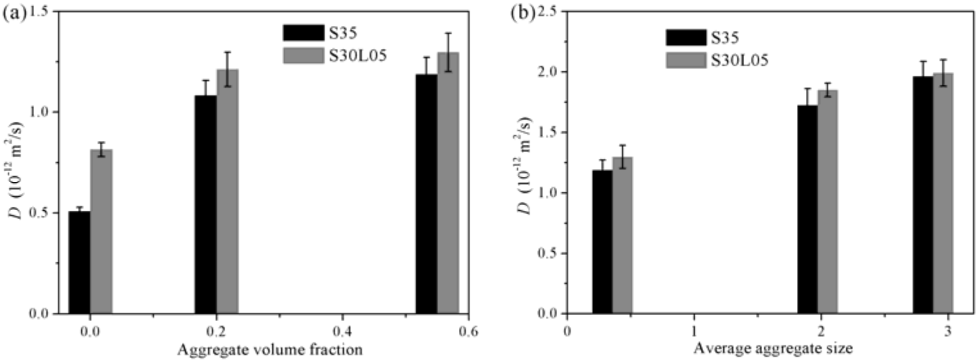

Fig. 5.20 Chloride diffusion coefficients for the binder S35 and S30L05 in relation to (a) aggregate volume fraction and (b) average aggregate size.

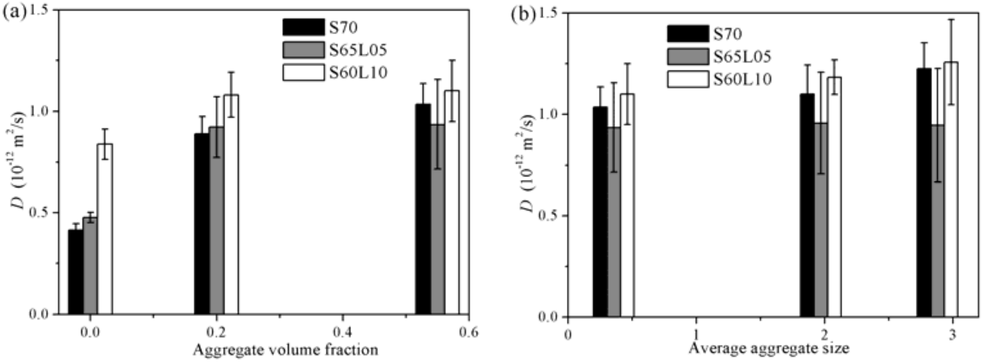

Fig. 5.21 Chloride diffusion coefficients for the binary and ternary binders with a fixed 70% of substitution rate in relation to (a) aggregate volume fraction and (b) average aggregate size.

5.3.4.2 Chloride binding

The binding coefficients for the Freundlich isotherm fitted to the experimental data for the ternary binders series are presented in Table 5.5. The detailed binding relationships are given in the Appendix. Concerning the effect of aggregate volume fraction and sizes, a similar trend to the corresponding binary series is observed in the ternary binders. For S30L05 series, The chloride binding decreases slightly with increasing aggregate volume fraction, while there is no appreciable effect of the difference in aggregate grain size on the chloride binding. At higher rates of SCMs substitution (70%), the chloride binding shows the least variations with aggregate volume fraction and size. This again confirms the small influence of ITZ on the chloride binding in samples containing GGBS.

Table 5.5 The fitted binding coefficients for Freundlich isotherms.

	α	*β*	R^2		*α*	*β*	R^2
S30L05-P	13.75	0.25	0.995	S65L05-P	13.41	0.41	0.944
S30L05-1	13.30	0.27	0.997	S65L05-1	13.47	0.40	0.955
S30L05-2	12.23	0.30	0.998	S65L05-2	14.02	0.42	0.986
S30L05-3	12.18	0.32	0.980	S65L05-3	13.68	0.37	0.999
S30L05-4	12.78	0.30	0.996	S65L05-4	13.29	0.43	0.998
				S60L10-P	13.11	0.42	0.987
				S60L10-1	13.41	0.45	0.982
				S60L10-2	12.99	0.45	0.985
				S60L10-3	12.34	0.47	0.997
				S60L10-4	12.31	0.44	0.958

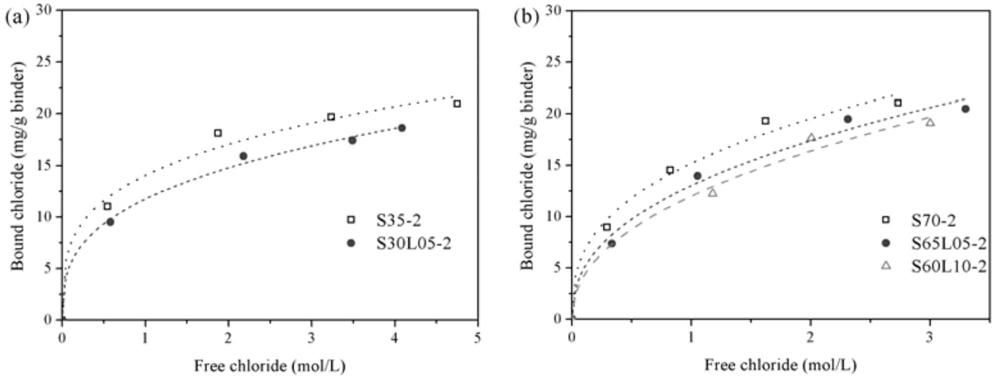

Fig. 5.22 Influence of substituting partially LF for GGBS on the chloride binding.

Fig. 5.22 shows the binding relationship for a combination of GGBS with and without LF. The comparisons of binding relationships between the ternary binders and the corresponding binary binders show that LF decreases chloride binding. In the pure PC system (Fig. 5.13), the reduction of chloride binding due to the presence of LF is more pronounced at lower free chloride concentration. However, this influence in the GGBS-PC systems is also observed even at higher concentration. The trend above can be explained by: (i) dilution of the alumina phase in the systems. (ii) limiting the formation of AFm phase. Although some researches suggested that the addition of LF is able to accelerate the hydration and promote the pozzolanic reaction of binders containing GGBS at early age [166, 168-169], it can not improve the chloride binding capability which is determined at later age.

5.3.5 Chloride diffusivity and porosity

In order to investigate the relationship between chloride diffusivity *D* and the characteristics of pore structure, Fig. 5.23 illustrates the relationships between the chloride diffusivity and the total porosity (mm^3/g) for all mortars. Two discernable relationships, one for the sample with binary binders containing LF and another for the reference and the samples containing GGBS, can be observed. The chloride diffusion coefficients (*D*) of samples with PC-LF binary binder increase slightly with the total porosity, while the *D* values of the reference samples and samples containing GGBS exhibit a reverse trend. The unit of total porosity is given as the volume by the mass of sample (mm^3/g). The results in MIP tests showed that the increase in the aggregate volume content decreases total porosity, which was mainly due to the reduction in the paste fraction. In order to present the results more clearly, the volume of non-porous aggregate was subtracted and the unit of the total porosity was transformed to volume percentage by the volume of the paste (mm^3/mm^3).

The relationships between *D* and total intruded pore volume (mm^3/mm^3) are given in Fig. 5.24. As can be seen in this figure, the *D* values are found to increase with increasing porosity regardless of the binders. In the MIP measurements, the increases in the total intruded pore volume (mm^3/mm^3 paste) are mainly due to the increased volume fraction of ITZ. Although the samples show a decreased chloride resistance with increasing the total intruded pore volume, the slope varies with the type of binders. Concerning the slope, the decrease of chloride resistance with increasing total intruded pore volume is lower for the samples with PC-LF binary binders than for the references. Samples with pure PC as the binder show the highest increasing rate. The increase of *D* values with increasing total intruded pore volume is lower for the samples with ternary binder than for the samples with PC-GGBS binary binder. This further confirms the differences in the modification of ITZ by GGBS and LF and suggests that the ternary systems show better results than the corresponding binary binders.

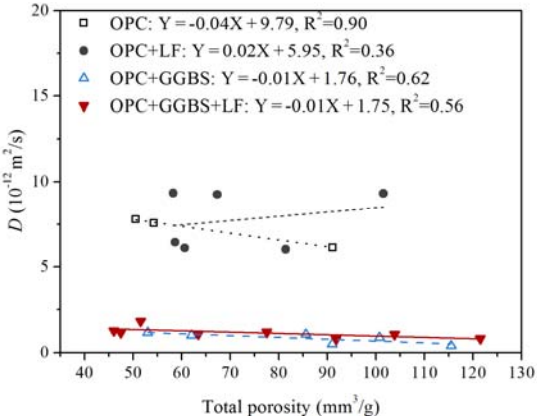

Fig. 5.23 Relationships between chloride diffusivity and total porosity in mm^3/g of samples.

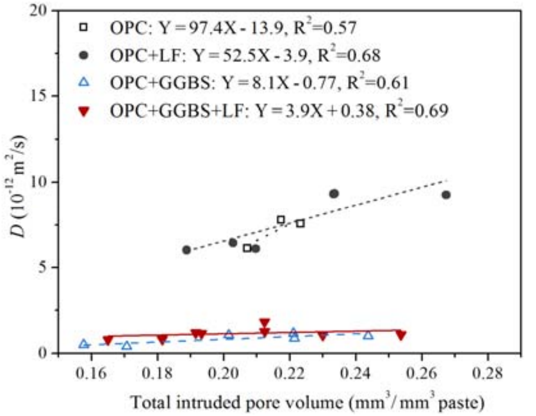

Fig. 5.24 Relationships between chloride diffusivity and total intruded pore volume in mm^3/ mm^3 of matrix.

5.3.6 ITZ vs. bulk matrix

In the previous pore structure investigations, it was found that one significant feature of ITZ is the relatively high pore volume in the range of

P3 (>100 nm). In the reference series, the increases in the total pore volume with increasing aggregate volume are mainly contributed by the pores in the scale larger than 100 nm. The intruded pore volume in this range (P3) can be reduced by incorporating moderate amount of SCMs, i.e. GGBS and LF in this study. As a result, the microstructure of ITZ is compacted and improved. Meanwhile, the pore volume in the range of P2 (10 nm < d < 100 nm), which predominates in the bulk cement matrix, was also altered by the presence of SCMs. To evaluate whether the changes in the D values of SCMs blended series are mainly contributed by the densification of the ITZ, or by the improvement of the bulk cement matrix, the relations between the relative difference in the D and the relative difference in the intruded pore volume are given in Fig. 5.25. Negative values represent a decrease, while positive values represent an increase of the corresponding parameters.

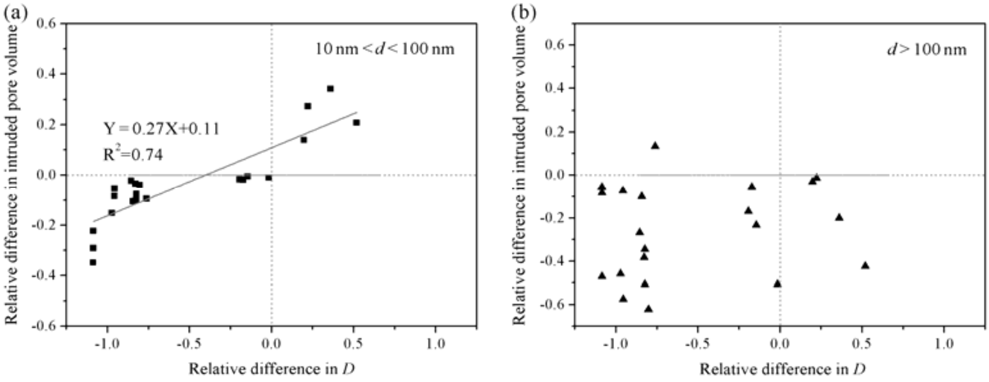

Fig. 5.25 Relation between the relative difference in the D values and, (a) the relative differences in the P2 (10 nm < d < 100 nm) volume and (b) the relative differences in the P3 (>100 nm) volume.

As can be seen in Fig. 5.25 (a), the variations of D values are strongly dependent on the P2 (10 nm < d < 100 nm) volume. However, there is no clear relation between the difference in the D and the difference in the P3 (>100 nm) volume in Fig. 5.25 (b). These observations are in consistence with the chloride migration tests. Therefore, the observed improvements of chloride resistance of the SCM blended samples, in particular the mixtures containing GGBS, must be due in part to the improvement of the microstructure of the ITZ, but more importantly, to the marked densification of the bulk cement matrix.

5.4 Conclusions

In this chapter, the influence of ITZ on the rate of chloride penetration for samples prepared with LF and GGBS blended binders was studied. The chloride resistance of samples produced with various aggregate volume fractions and aggregate sizes was measured through a natural diffusion test. The role of ITZ on the chloride binding relationships in different blended systems was discussed in detail. The analysis of the results leads to the following conclusions:

1) The chloride penetration profiles were highly dependent on the aggregate volume fractions. For the reference series, increasing aggregate volume fraction from 0 to 0.55 caused a reduction of about 60% in the D values. There was a slight increase in D when increasing V_{agg} from 0.2 to 0.55. There seemed to be an obvious trend toward increasing D for the samples with coarser aggregate.

2) For the LF blended binary series, the D values of mortars were lower than those of the corresponding pastes. D showed little variation as the aggregate volume content increased from 0.2 to 0.55 for both L05 and L10. Compared with the reference series and L05 series, the D values of L10 series showed the least variation with the average grain sizes. Concerning the effect of LF on the overall D values, the incorporation of 5% LF as a partial substitute for PC slightly decreased D for all samples, while the D value increased significantly as the substitution rate of LF reached to 10%.

3) For samples containing GGBS, the chloride concentrations reached a constant value at the distance of about 10 mm from the exposed surface regardless the aggregate volume fraction and sizes. The D values were significantly lower for samples containing GGBS than those for the pure PC series. Concerning the effect of aggregate volume fraction, D increased continuously as the aggregate volume increase for all binary and ternary series containing GGBS. Although

a slight increase in the diffusivity was observed as the average grain size increased, samples containing GGBS showed little variation with the grain size.

4) The binding capacity of the reference series depended on the aggregate volume fractions and sizes. Mortar C-2 showed the highest binding compared with the paste and samples with coarser aggregates. Although a similar trend to the reference series was observed in L05 series with respect to the effect of aggregate on the chloride binding, this influence was less noticeable in both L05 and L10 series. There was no appreciable effect of the differences in the aggregate volume fraction and size on chloride binding relationship for the samples containing GGBS.
5) The addition of LF and GGBS has been proven to significantly affect the chloride binding capacity. The partial substitution of PC with moderate amount of LF resulted in a reduction in the chloride binding especially at lower free chloride concentrations. Samples containing GGBS generally showed higher chloride binding capacities compared with the references. The incorporation of LF as a partial substitute for GGBS led to a reduction of chloride binding. This influence was observed both at lower and higher chloride concentrations.
6) The *D* values were found to increase with increasing porosity regardless of the binders. Although the samples showed a decreased chloride resistance with increasing total intruded pore volume, the slope varied with the type of binders. The decrease of chloride resistance with increasing total intruded pore volume was lower for the samples with PC-LF binary binders than for the references. Samples with pure PC as the binder showed the highest increasing rate. The increase of *D* values with increasing total intruded pore volume was lower for the samples with ternary binder than for the samples with PC-GGBS binary binder.
7) Comparing the relative difference in *D* with the relative difference in the intruded pore volume, a fairly obvious linear relationship between

the variation of D and that of P2 ($10\ \text{nm} < d < 100\ \text{nm}$) volume was observed. The observed improvement in limiting the movement of chloride ions in SCMs blended samples, particularly for the samples containing GGBS, could be due in part to the improvement of the microstructure of the ITZ, but more importantly, to the densification of the bulk cement matrix.

Chapter 6

Influence of ITZ on the sulfate resistance of LF and GGBS blended cement composites

6.1 Introduction

Sulfate attack is one of the major threats to concrete durability. Sulfate ions from surrounding water penetrate by diffusion and/or absorption in the concrete porous network and react with existing hydration products. The widespread occurrence and destruction caused by sulfate attack attracted researchers over the years into the study of the deterioration mechanism and methods to combat it. However, different theories about the mechanism still exist and the mechanism is not well understood.

The mechanism of degradation of concrete exposed to external sulfate attack depends on exposure conditions, such as temperature, associated cations and sulfate concentration. Calcium hydroxide and alumina-bearing phases of hydrated PC are more vulnerable to attack by sulfate ions. During hydration, PC with more than 5% potential C_3A will contain most of the alumina in the form of monosulfate hydrate ($C_3A \cdot C\$ \cdot H_{18}$). If the C_3A content of the cement is more than 8%, the hydration products will also contain $C_3A \cdot CH \cdot H_{18}$. Due to the presence of calcium hydroxide in hydrated PC paste, when a cement paste comes in contact with sulfate ions, both the alumina-containing hydrates are converted to the high-sulfate form (ettringite, $C_3A \cdot 3C\$ \cdot H_{32}$) by the following equations [1, 106, 229-232]:

$$C_3A \cdot CH \cdot H_{18} + 2CH + 3\bar{S} + 11H \rightarrow C_3A \cdot 3C\bar{S} \cdot H_{32} \qquad (6.1)$$

$$C_3A \cdot C\bar{S} \cdot H_{18} + 2CH + 2\bar{S} + 12H \rightarrow C_3A \cdot 3C\bar{S} \cdot H_{32} \qquad (6.2)$$

Gollop [233-234] explained that ettringite crystallization ends when the aluminium provided by AFm phase became insufficient. Moreover, the stability of ettringite is a pH dependant as reported in literature [235-236]. Ettringite is known to be unstable below a pH around 10.5 and dissolves as gypsum and aluminium sulfate [236]. The formation of these products may cause expansion, cracking, spalling, softening, loss of strength and other forms of damage.

In spite of dissolving from ettringite, gypsum formation as a result of cation-exchange reactions is also capable of causing expansion. However, it has been observed that deterioration of hardened PC paste by gypsum formation goes through a process that first leads to reduction of pH of the system and loss in the stiffness and strength, followed by expansion and cracking, and eventually transformation of the concrete into a mushy or non-cohesive mass. Depending on the cation type associated with the sulfate solution (i.e., Na^+, K^+, or Mg^{2+}), both calcium hydroxide and C-S-H presented in the hydrated Portland cement paste may be converted to gypsum by sulfate attack [1, 237-238]:

$$Na_2SO_4 + CH + 2H \rightarrow C\bar{S} \cdot 2H + 2NaOH \qquad (6.3)$$

$$MgSO_4 + CH + 2H \rightarrow C\bar{S} \cdot 2H + Mg(OH)_2 \qquad (6.4)$$

$$3MgSO_4 + 3CaO \cdot 2SiO_2 \cdot 3H_2O + 8H_2O \rightarrow 3(CaSO_4 \cdot 2H_2O) + 3Mg(OH)_2 + 2SiO_2 \cdot H_2O \qquad (6.5)$$

Moreover, $Mg(OH)_2$ and the silica hydrate can react together to form a noncementitious product [229]:

$$4MH + SH_n \rightarrow M_4SH_{8.5} + (N\text{-}4.5)H_2O \qquad (6.6)$$

In the case of sodium sulfate attack, the formation of sodium hydroxide as a by-product of the reaction ensures continuation of high alkalinity in the system, which is essential for the stability of the cementitious hydration product, C-S-H. On the other hand, in the case of magnesium sulfate attack, the conversion of calcium hydroxide to gypsum is accompanied by the simultaneous formation of magnesium hydroxide, which is insoluble and reduces the alkalinity of the system. In the absence of hydroxyl ions in the solution, C-S-H is no longer stable and is also attacked by the sulfate solution. The magnesium sulfate attack is, therefore, more severe on concrete.

Physical and chemical factors can influence the external sulphate attack, such as the properties of the solution (pH, concentration, the associated cation (sodium, calcium, magnesium)), the material properties (the type of cement, the w/c ratio) or the curing conditions [239-244]. Based on these assumptions, test parameters have been altered more frequently including cement composition, pozzolanic replacement and composition, solution concentration, pH value, temperature and w/c ratio in the mixture. Other factors, especially the properties of ITZ, should also be taken into account due to its distinguished microstructure, such as high porosity, less anhydrous and richness in the CH crystals.

The importance of ITZ with respect to the chemical aggression of concrete is obvious when one considers the relations existing between porosity, permeability, chemical composition and the sulfate attack. For Portland cement, several reports have observed that gypsum is localized preferably at the ITZ leading to the increase of cracking in this zone and the consequent decrease of modulus. Yang et al. [103] also studied the process of sulfate attack and the role of the ITZ during the attack process. They concluded that sulfate reacts with CH and AFm in the ITZ, leading to expansion and cracking. Wang [245] considered that more physical damage was caused by the formation of gypsum than by the formation of ettringite. Nielsen [246] found that the ettringite crystals observed in cracks formed after occurrence of the cracks. The researcher found that gypsum was the predominance reaction product while ettringite was rarely formed in an amount that was sufficient to be reasonably considered as a source for the formation of cracks. Irassar et al. [104] also emphasized that the deposition of ettringite and gypsum around the aggregate indicates the vulnerability of the ITZ to chemical attack. Mehta [29] explained the presence of gypsum in the ITZ by microcracks existing previously to sulfate exposure. These microcracks, larger than capillary pores, are a preferential path for the creation of interconnections leading to a more permeable system. So the sulfate ion diffusion is easier in this zone. Bonen [105] had also studied the replacement of CH by gypsum in the ITZ and they found thick deposits of gypsum up to 50 μm precipitating in this zone by a through-solution mechanism. These observations showed the important role of the ITZ that would be absent if the investigations was led on paste samples [106]. Bonakdar and Mobasher [247] suggested that the effectiveness of fly ash in mitigating damage from sulfate attack is expected to be more significant in mortar and concrete compared to the cement paste, due to the improved ITZ characteristics. The effect of size, content, surface texture and ITZ that are rarely quantified in these durability tests cannot be neglected. However, research specifically designed to study the effects of ITZ during sulfate attack is still limited.

The study of the role of ITZ in sulfate attack not only is important to the understanding of the sulfate attack mechanism, but also provides evidence for the modeling of deterioration process. Researchers have attempted to study sulfate attack effects using models [248-251]. Few of them base the analysis of the problem of sulfate on a wide database of experimental results. However, without understating the microstructural changes that accompany sulfate attack processes, it is not possible to accurately predict the damage using models. This further confirms the importance of the study of the role of ITZ in the sulfate attack.

This study is designed to understand better the interactions between sulfate and concrete with the aim of preventing it. The process of sulfate attack on pastes, mortars and concretes was studied from the influences of ITZ. One influence is the content of ITZ, which is studied by a comparison of resistance to sulfate attack among mortars and concretes prepared with different volume fractions and grain sizes of aggregate. The other influence is the microstructure of ITZ. Moderate amounts of GGBS and LF were blended with PC as binders to improve both the microstructure of the bulk cement matrix and the ITZ. With this approach, it should be possible to assess to what extent the ITZ are involved in the degradation mechanism. This study includes macroscopic and microscopic measurements. Observations were made on different pastes, mortars and concretes exposed to various concentrations of sulfate solutions. Mass and length measurements were registered every time the solution was renewed. Microstructural changes were investigated by an environmental scanning electron microscope and energy Dispersive X-ray analysis.

6.2 Experiments

6.2.1 Materials and mixtures

In this chapter, the same materials and similar mixtures as in the chapter 4 were used. The detailed mixtures and the properties of the cementitious materials and aggregates were shown in Table 4.1 -4.4 and Fig.4.1-4.2. Four types of binders, i.e. C, L10, S70 and S60L10 were used to evaluate the influence of SCMs on the process of sulfate attack. In addition to mortars with 20% and 55% of aggregate, an extra mixture with 35% of aggregate was prepared for each binder. Therefore, the name of each mixture was altered to S**L**-aggregate volume fraction”. For example, S60L10-35 refers to the binder containing 30% of PC, 60% GGBS and 10% LF, and the volume fraction of aggregate 0/2 mm is 0.35. Binder-3 and binder-4 have the same meaning as used in previous chapters, namely having 35% of 2/5.6 mm and 2/8 mm coarse aggregate, respectively.

6.2.2 Experimental procedure

6.2.2.1 Specimens preparation

A modified ASTM C 1012 [252] method was applied to estimate the potential of sulfate attack for mixes at 20±2°C. Each mixture consisted of 9 cubes of 50×50×50 mm^3 and 9 bars of 25×25×280 mm^3 in size. The bars had gauge studs at both ends in order to measure expansion with length comparators (Fig. 6.1). Immediately after molding, the molds were covered with a plastic sheet and stored in the chamber with a constant temperature of 20±2°C and a relative humidity of 95±5%. The specimens were demolded after 24h and immediately transferred to saturated limewater at 20±2°C.

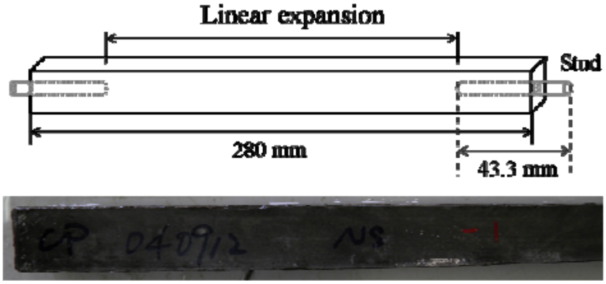

Fig. 6.1 Schematic (upper) and an example (bottom) of linear expansion measurement.

6.2.2.2 Sulfate attack tests

After 2 months of saturated limewater curing, the initial length and weight of the bars and cubes were recorded. Then, the specimens were divided into 3 groups and immersed in (i) 33.8 g/L SO_4^{2-} (50.0 g/L Na_2SO_4), (ii) 3.38 g/L SO_4^{2-} (5.0 g/L Na_2SO_4) and (iii) 33.8 g/L SO_4^{2-} (42.4 g/L $MgSO_4$) at 20±2°C. The ratio of solution volume to sample surface area was kept constant at 2.4 cm^3/cm^2, which for the mortar bars corresponds to the solution to sample volume ratio of 4. The solution was renewed after every length and weight measurements.

The measurements of the length and weight of the specimens were performed at 2, 4, 8, 13 and 15 weeks after immersed in solution. Thereafter, the measurements were carried out in intervals of 4 weeks. The final results presented were measured on three replicates per specimen type.

Visual observation of the specimens was performed monthly and all significant changes, such as spalling, cracking, expansion and disintegration were recorded.

6.2.2.3 Microstructure analysis

The microstructure of the attacked mortar samples with different immersion times was examined by scanning electron microscopy (SEMFEI QUANTA200FEG) using backscattered electron images and energy dispersive X-ray spectroscopy (EDX) including mapping. The specimens used for the SEM investigation were 1.5 cm thick slices from the 25×25×280 mm^3 mortar bars. Sample preparation involved freeze-drying, vacuum impregnation with epoxy resin, cutting, polishing and coating with carbon. The detailed procedure for sample preparation was provided in chapter 4. The accelerating voltage was 15 kV and the elemental mappings were obtained under a magnification of 500×, covering approximately a 301×277 μm^2 area.

6.3 Results and discussion

6.3.1 PC

6.3.1.1 Visual inspection

A visual inspection was carried out to evaluate the visible signs of surface deterioration such as spalling, cracking and softening in specimens exposed to sulfate attack. Fig. 6.2 shows examples of surface deterioration of C series cubes immersed in 50 g/L sodium sulfate solution for 3 months. The pure cement paste shows the first sign of deterioration in which the cracking along the edge is observed. While marginal deterioration is noted in C-35, no apparent deterioration is observed in C-55 and C-3.

Fig. 6.3 shows the samples of C series exposed to 50 g/L sodium sulfate solution for 12 months. As given in Fig. 6.3 (a), cracking is evident in specimen C-P while spalling of the corners, cracking localized at the edges, are noted in the mortar specimens. The severity of spalling is more intense in the specimens C-55 compared to the others. Concerning the effect of aggregate size in Fig. 6.3 (b), the extent of deterioration has a tendency to increase for the samples with finer aggregates. In other words, C-55 displays many wide cracks, spalling and substantial material loss at the surface as well as at the corner and edges, while C-3 and C-4 only exhibit cracks around corners and edges. This is also confirmed in Fig. 6.4, in which the C-55 shows more apparent expansion compared with the other samples.

Fig. 6.5 shows examples of cube samples exposed to 5.0 g/L sodium sulfate solution for 12 months. The surface of the specimens is covered by a white soft substance. No damage is noted in the specimens. It is clearly observed that the severity of deterioration in specimens exposed to 5.0 g/L sulfate solution is less than that in the specimens exposed to the solutions with higher sulfate concentrations (50 g/L). There is no apparent cracking, spalling at the surface as well as at the corner and edge for all specimens.

In 42.4 g/L magnesium sulfate solution, as shown in Fig. 6.6 (a), it can be observed that the pure cement paste C-P displays less cracks, spalling at the corner and edges compared with the mortar samples. Concerning the effect of aggregate size in Fig. 6.6 (b), C-55 displays severe surface deterioration in spite of the spalling and cracking localized at the corners and edges, while the samples with coarser aggregates only exhibit cracks around corners and edges. Moreover, it could be concluded that the surface deterioration modes are greatly associated with the type of exposure solution.

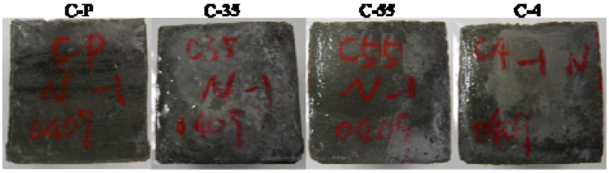

Fig. 6.2 C series specimens exposed to 50 g/L Na_2SO_4 for 3 months.

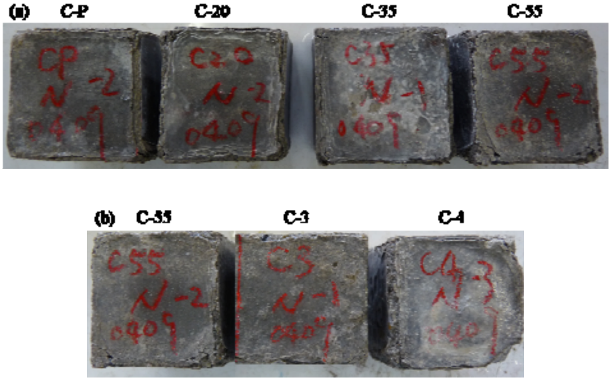

Fig. 6.3 C series specimens with respect to (a) aggregate volume fraction and (b) aggregate size exposed to 50 g/L Na_2SO_4 for 12 months.

Fig. 6.4 C series bars with respect to (a) aggregate volume fraction and (b) aggregate size exposed to 50 g/L Na_2SO_4 for 12 months.

Fig. 6.5 C series specimens exposed to 5.0 g/L Na_2SO_4 for 12 months.

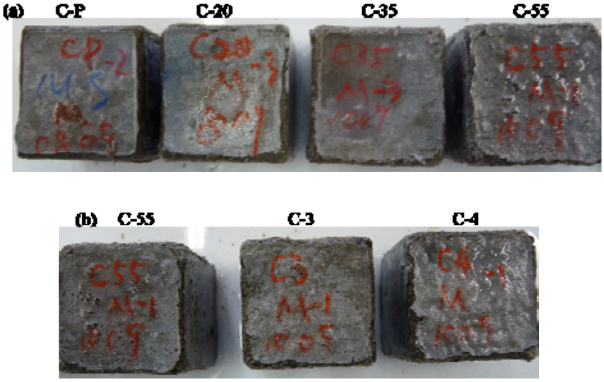

Fig. 6.6 C series specimens with respect to (a) aggregate volume fraction and (b) aggregate size exposed to 42.4 g/L $MgSO_4$ for 12 months.

6.3.1.2 Expansion

The linear expansions of the C series immersed in Na_2SO_4 with two solution concentrations are given in Fig. 6.7 and Fig. 6.8, respectively. In general, all specimens display more apparent expansion at high sulfate concentration by one year. At high sodium sulfate concentration (Fig. 6.7 (a)), the expansion behavior of pure cement paste (C-P) seemed to be more apparent until 150 days. Thereafter, C-55 starts to expand dramatically and exhibits the highest expansion. The others also start to expand rapidly after more than 240 days, but much less rapid than the C-55. In Fig. 6.7 (b), all samples exhibit similar expansion behaviors before 150 days. Subsequently, C-3 and C-4 shows a steady slow expansion and reaches to 0.73 mm/m and 0.97 mm/m after 12 month.

Regarding the lower sodium sulfate concentration in Fig. 6.8, the expansion of all samples is much less than those at the higher sulfate concentration. All samples exhibit a slow progressive expansion behavior and the expansions are lower than 1 mm/m by one year. No dramatic expansion is observed for C-55.

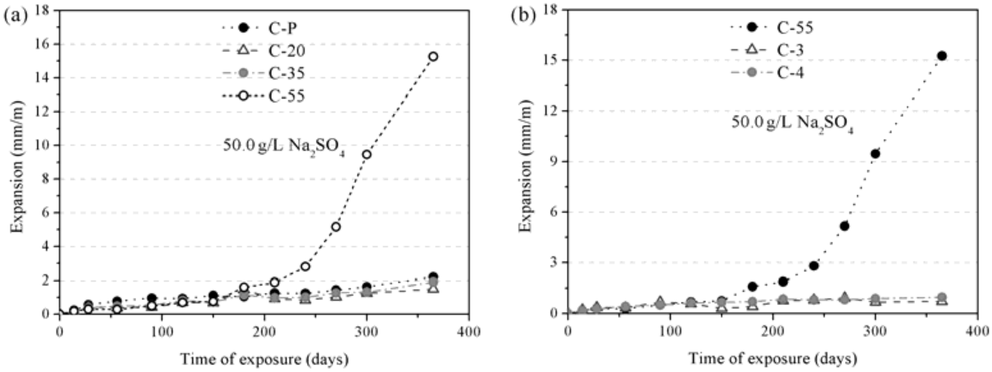

Fig. 6.7 Expansion of samples with various (a) aggregate volume fractions and (b) aggregate sizes immersed in 50 g/L Na_2SO_4.

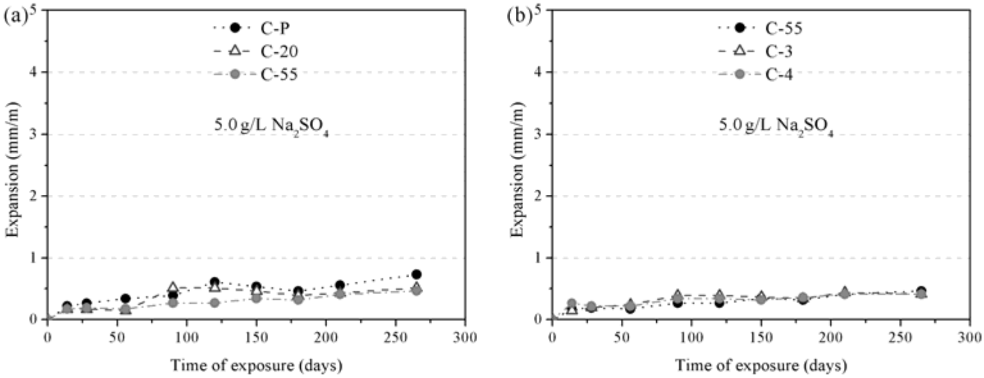

Fig. 6.8 Expansion of samples with various (a) aggregate volume fractions and (b) aggregate sizes immersed in 5.0 g/L Na_2SO_4.

The expansion is normally due to the formation of expansive products, such as gypsum and ettringite. As the sulfate source is external, the rate of expansive products formation is determined by the concentration and diffusivity of concentration. For the lower sulfate concentration or the early period of high sulfate concentration attack, the exposed surface and outer part of samples is important. For the sulfate to reach the inner part, it must move through the bulk cement matrix. As well defined in the previous chapters, the presence of more porous ITZ is normally accompanied by a denser bulk cement matrix. This could be the reason why the expansion is lower for mortar samples than that of pure cement paste at the lower sulfate concentration and the early period of higher sulfate concentration attack. After the sulfate penetrates into the interior of samples, the ITZ is expected to exert more significant influences on expansion. The availability of CH and the higher porosity of the ITZ can cause the preferred crystallization of gypsum in this region [247, 253-254]. Some researchers indicated that the formation of gypsum is responsible of the edge and corner deterioration [242, 253], which was also observed in the visual inspection in section 3.1.1. The formation of cracks around aggregates further opens up the interior microstructure to the sulfates and facilitates the deterioration.

Regarding the magnesium sulfate solution, the expansion in 90 days is lower for all samples compared with those immersed in the sodium sulfate attack. In Fig. 6.9 (a), C-P starts to expand rapidly after 210 days and exhibits the highest expansion at one year. The others also start to expand rapidly after more than 210 days, but much less rapid than the C-P. Samples with various aggregate sizes, as shown in Fig. 6.9 (b), display similar expansion behaviors. In this group, the expansion values at one year are in the increasing order: C-55 > C-3 > C-4.

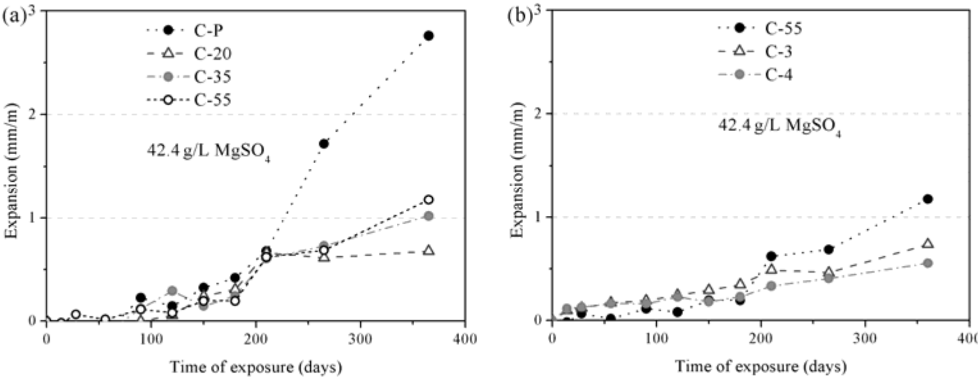

Fig. 6.9 Expansion of samples with various (a) aggregate volume fractions and (b) aggregate sizes immersed in 42.4 g/L $MgSO_4$.

When samples are subjected to magnesium sulfate attack, a layer of brucite (Magnesium hydroxide-$Mg(OH)_2$, forms on the surface by the reaction in (6.4) [255-257]. Santhanam et al. [257-258] suggested that the layer of brucite is often accompanied by a layer of gypsum that forms as a result of the reaction on the inside of the brucite layer. The presence of the relatively impermeable layer of MH leads to reducing the penetration of sulfate into the samples. This could be the reason for the relative low expansion at the early period of attack compared with the sodium sulfate. However, the MH can break down thereafter in several places due to the continued diffusion of sulfate ions. After that, a direct attack of the C-S-H can occur through the reaction in (6.5) and a different mechanism determines the expansion. As a result of the decomposition of C-S-H, the formation of M-S-H and gypsum takes place. The formed gypsum can react with calcium aluminate hydrate (C_4AH_{13}) and calcium monosulfoalimunate (C_4AH_{12}) to form ettringite and leads to further expansion [259-260]. Therefore, the quantity of expansive products is determined by the content of CH at early period and the content of C-S-H at later period of attack.

6.3.1.3 Mass change

The mass change of C series exposed to 50 g/L Na_2SO_4 in relation to the aggregate volume fraction and size is given in Fig. 6.10. There is a continuously mass increase for all samples with exposure age. However, there is no clear relation between the mass change and the aggregate properties. In this study, the main reaction occurs in the paste. An approximation has been made that the mass of aggregate is not changed during the sulfate attack. Therefore, the unit of mass change is transferred to the percentage of the mass of paste by subtracting the weight of aggregate. The normalized results are shown in Fig. 6.11.

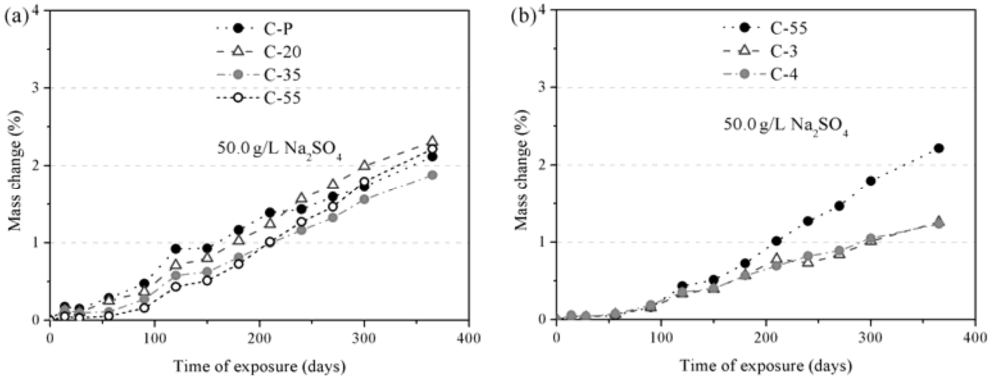

Fig. 6.10 Mass change of samples with various (a) aggregate volume fractions and (b) aggregate sizes immersed in 50 g/L Na_2SO_4.

As shown in Fig. 6.11 (a), there is an apparent trend toward increasing mass gain for the samples with higher aggregate volume fraction. A rapid increase in the mass gain is observed after 60 days of immersion for all samples. This point is earlier than that of expansion measurement. Regarding the effect of aggregate size in Fig. 6.11 (b), the mass increase is all the more apparent for a sample prepared with a finer aggregate. C-3 and C-4 exhibit a similar mass change behavior. A nearly similar trend is observed for the effect of aggregate on the mass change of samples exposed to lower sulfate concentration (Fig. 6.12). However, the mass gain of samples at lower sodium sulfate solution is much lower than that at higher concentration.

At the magnesium sulfate solution, the same trend as in sodium sulfate solution is observed with respect to the effect of aggregate on the mass change (see in Fig. 6.13). The most apparent difference is the mass variation between 90 days and 120 days. There are decreases in mass gain for all samples due to the deterioration. These variations are not appreciable in sodium sulfate solution.

Mass changes of cement based materials in sulfate solution are dependent on different physical and chemical processes, which can be summarized as [232, 259-262]: continuous hydration of binder, absorption of sulfate ions, withdrawal of water due to osmotic forces, leaching, and specimen deterioration and disintegration. The first two lead to increase in mass and the latter to decrease. When specimens are subjected to sulfate attack, calcium hydration converts to gypsum and brucite (occurs in $MgSO_4$ solution). In the presence of CH, the formed gypsum can react with C_4AH_{13} and C_4AH_{12} to form ettringite and result in further mass increase. Researchers have proven that the formation and deposition of gypsum and brucite result in mass increase [255, 260]. Thereafter, different mechanisms affect the mass changes. In sodium sulfate solution, the spalling, cracking and deterioration due to the formation of expansive products cause mass loss. In magnesium sulfate solution, the C-S-H gel converts to gypsum which would lead to mass loss. The mass change measurements in this study showed that factors leading to mass increase such as hydration and absorption of sulfate are prominent for the whole immersion period. No significant mass loss was observed even at high concentration of sulfate solution. This could be due to the insufficient exposure time.

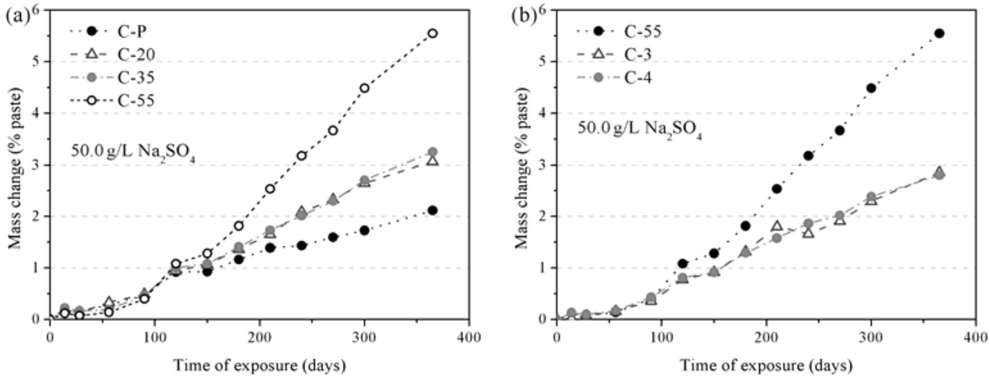

Fig. 6.11 Normalized mass change of samples with various (a) aggregate volume fractions and (b) aggregate sizes immersed in 50 g/L Na_2SO_4.

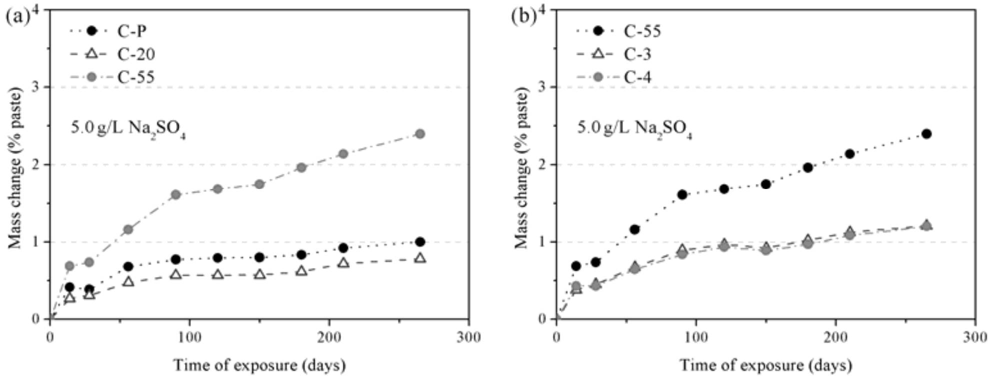

Fig. 6.12 Normalized mass change of samples with various (a) aggregate volume fractions and (b) aggregate sizes immersed in 5.0 g/L Na_2SO_4.

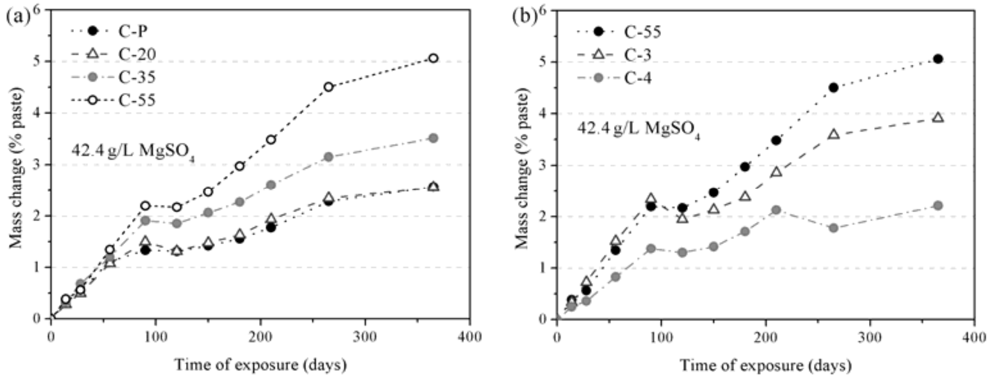

Fig. 6.13 Normalized mass change of samples with various (a) aggregate volume fractions and (b) aggregate sizes immersed in 42.4 g/L $MgSO_4$.

6.3.1.4 Microstructure analysis

Fig. 6.14 shows BSE images of C-P and C-55 immersed in the 50g/L Na_2SO_4 for 6 months, with the corresponding magnification. With respect to evidence of expansion and deterioration the pure cement paste shows the following characteristic: (i) the distinguished layer of expansive products (Fig. 6.14 (a)); (ii) the looser region under the surface layer shows signs of changes in the microstructure of the paste (Fig. 6.14 (a)); (iii) the cracks are perpendicular to the sample surface and generally empty; (iv) the interior parts characterized by a denser microstructure (Fig. 6.14 (b)).

Regarding mortar C-55, the crack patterns are more complex due to the presence of aggregates (Fig. 6.14 (c)). The cracks tend to open up around the aggregate. The formation of cracks around aggregates further improves the penetration of the sulfate solution. This could be the reason for the dramatic increase in expansion of C-55 after 6 month of immersion. In sulfate attack, the deterioration starts when the strength of the sample is unable to withstand the forces from the expanding [147]. The ITZ is less effective to transfer the stress from the bulk cement matrix to the aggregate grains. Therefore, the cracks tend to start form the ITZ. The region within the interior of C-55 also presents a loose microstructure and a few cracks propagated from the aggregate are observed (Fig. 6.14 (d)). This also illustrates quite well the expansion and mass change of C-55 as mentioned above.

The formation of gypsum in the ITZ has been actually observed at high magnification and confirmed by EDX analysis. Fig. 6.15 (left) shows an EDX analysis on an attacked C-55 (immersed in 50 g/L Na_2SO_4 for 6 months). The results consist in maps of calcium, silica, sulfur and aluminium relative concentration. The high calcium concentrations refer to the cement paste and the high silica concentrations correspond to the aggregate particles. Relatively high sulfur concentrations can be observed around aggregates. The mineralogical composition is further confirmed by EDX point analysis (Fig. 6.15). The atomic proportions and weight concentration given by quantitative analysis are close to the composition of gypsum. However, no clear signs of ettringite are observed since the aluminium concentration is not distinguishable in the paste. It is believed that ettringite is unstable below a pH around 10.5 and dissolves as gypsum and aluminium sulfate [235, 263-264].

The formation of gypsum in the ITZ could be associated with expansion, cracking and spalling. This would further open up cracks and facilitate the ingress of sulfate [106]. Yang et al. [103] also concluded that sulfate reacts with CH and AFm in the ITZ, leading to expansion and cracking. Wang [245] considered that more physical damage was caused by the formation of gypsum than by the formation of ettringite. Nielsen[246] found that gypsum was the predominance reaction product while ettringite was rarely formed in an amount that was sufficient to be reasonably considered as a source for the formation of cracks. Irassar et al. [104] also emphasized that the deposition of ettringite and gypsum around the aggregate indicate the vulnerability of the ITZ to chemical attack. Bonen [105] have also studied the replacement of CH by gypsum in the ITZ and they found thick deposits of gypsum up to 50 μm precipitating in this zone by a through-solution mechanism. However, Mehta [29] explained the presence of gypsum in the ITZ by microcracks existing previously to sulphate exposure. These microcracks were a preferential path for the creation of interconnections leading to a more permeable system. In this study, the gypsum was mainly localized in the ITZ and there was no products fill in the crack nearby (Fig. 6.15 (left)).

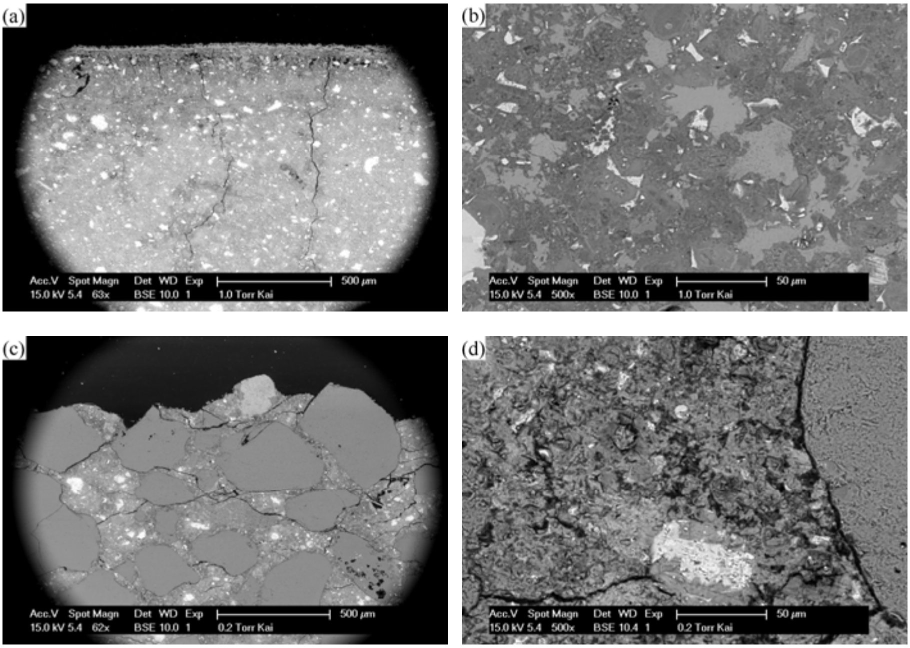

Fig. 6.14 BSE images of (a) C-P (63×), (b) C-P (500×), (c) C-55 (63×) and (d) C-55 (500×) immersed in 50 g/L Na_2SO_4 for 6 months.

The BSE images of mortar C-55 immersed in magnesium sulfate solution for 6 months are given in Fig. 6.16. The crack patterns at both the surface and interior are similar with those of samples immersed in the sodium sulfate. The brucite-gypsum double layer at the surface as indicated in ref. [258] is not observed due to the spalling. From the EDX analysis in

Fig. 6.15, the formation of gypsum is observed in the ITZ and in the paste. In magnesium sulfate attack, gypsum can form not only from the reaction between calcium hydroxide and magnesium sulfate, but also from the decomposition of C-S-H. The high magnesium concentrations among the cement paste further confirm the direct attack of C-S-H. Moreover, the comparison between magnesium concentration and sulfur concentration indicates that the movement of sulfate ions is faster than that of magnesium.

	C-55 (50 g/L Na_2SO_4 - 12 months)	C-55 (42.4 g/L $MgSO_4$ - 12 months)
BSE images	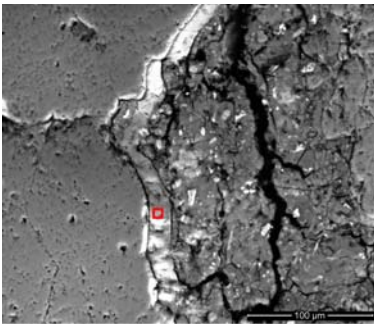	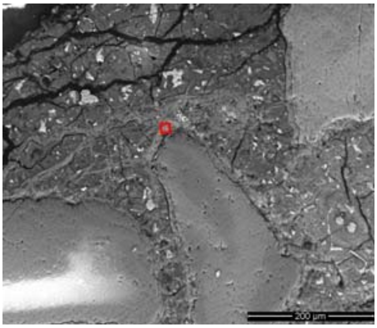
EDX spectrum	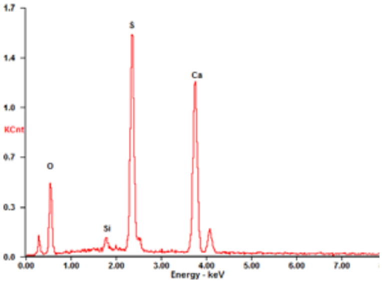	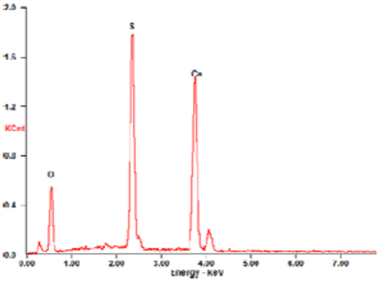
Ca	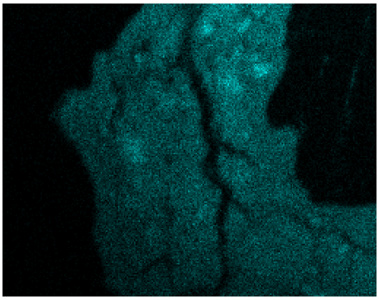	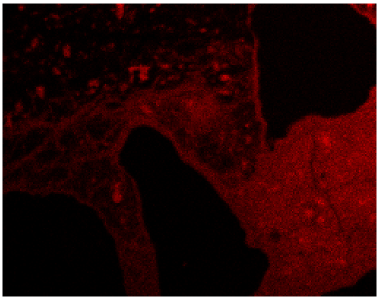

Si	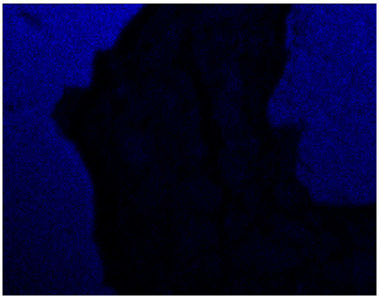	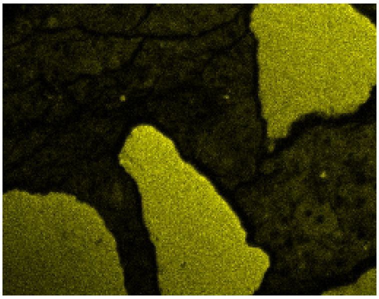
S	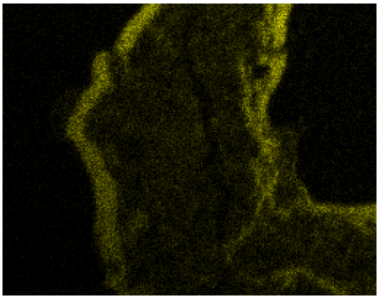	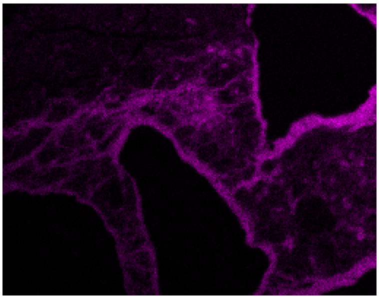
Al	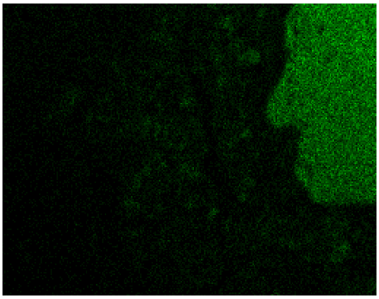	
Mg	-	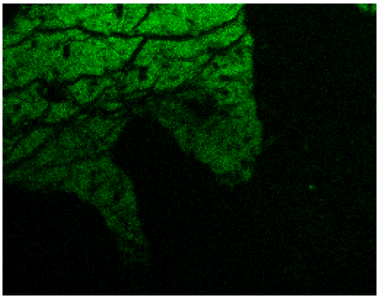

Fig. 6.15 EDX analysis of mortar C-55 after 12 months of immersion.

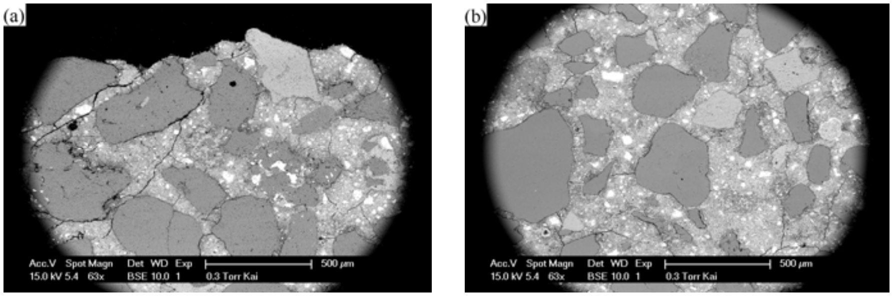

Fig. 6.16 BSE images (a) surface and (b) interior of C-55 immersed in 42.4 g/L $MgSO_4$ for 6 months.

6.3.2 PC-LF

6.3.2.1 Visual inspection

Fig. 6.17 shows the samples of L10 series exposed to 50 g/L sodium sulfate solution for 12 months. From Fig. 6.17 (a), it can be observed that the cracking at the corner, edge and surface is noted in L10-P, while spalling of the corners, cracking localized at the edge are noted in the mortars. In other words, the pure paste displays many wide cracks and spalling at the surface as well as at the corner and edges, while the mortar samples only exhibit cracks around corners and edges. However, as evident in Fig. 6.18, the L10-55 mortar bar shows the most significant expansion compared with the other samples. Concerning the effect of aggregate size in Fig. 6.17 (b), there is no appreciable effect of the differences in the aggregate sizes on the extent of deterioration. In high sodium sulfate solution, it is clearly observed that the degree of sulfate deterioration is more severe for the samples from L10 series compared with the corresponding references.

Fig. 6.19 shows examples of cube samples exposed to 42.4 g/L magnesium sulfate solution for 12 months. The surface of all specimens is covered by a white soft substance. Compared with the corresponding references, samples from L10 series show more severe deterioration and wider cracks are observed at the edges. These findings are in agreement with the published reports. Skaropoulou et al. [265] reported that the onset of deterioration were first observed on specimens with LF cement. Lee et al. [266] also reported that the negative effect of the higher replacement level of

LF was observed more remarkably in both sodium sulfate and magnesium sulfate solution.

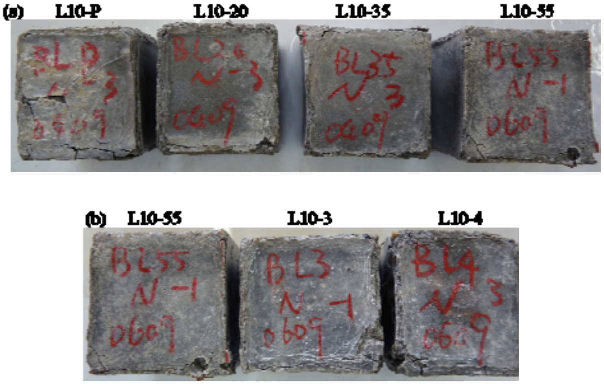

Fig. 6.17 L10 series specimens with respect to (a) aggregate volume fraction and (b) aggregate size exposed to 50 g/L Na_2SO_4 for 12 months.

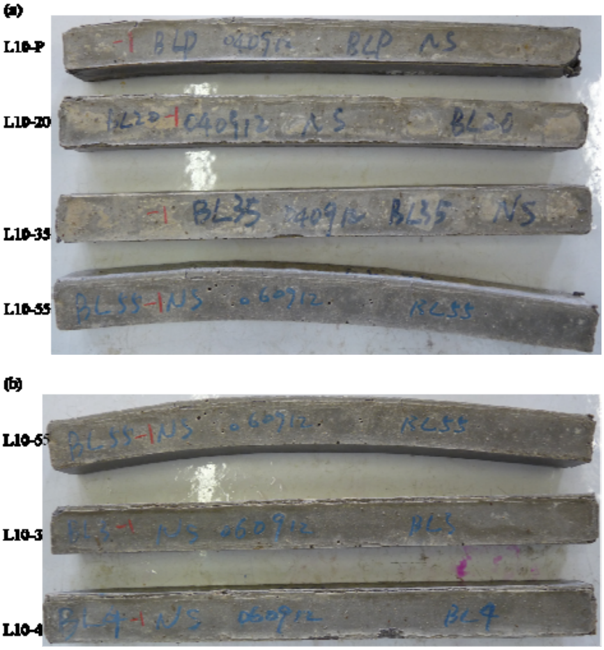

Fig. 6.18 L10 series bars with respect to (a) aggregate volume fraction and (b) aggregate size exposed to 50 g/L Na_2SO_4 for 12 months.

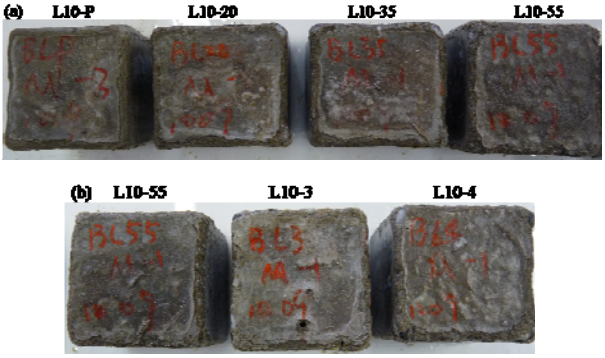

Fig. 6.19 L10 series specimens with respect to (a) aggregate volume fraction and (b) aggregate size exposed to 42.4 g/L $MgSO_4$ for 12 months.

6.3.2.2 Expansion

The linear expansions of the L10 series immersed in Na_2SO_4 with two solution concentrations are given in Fig. 6.20 and Fig. 6.21, respectively. In general, all specimens display more apparent expansion at high sulfate concentration in one year. At high sodium sulfate concentration (Fig. 6.20 (a)), there is an apparent trend toward increasing expansion for the samples with higher aggregate volume fraction. L10-55 starts to expand dramatically after 180 days of immersion and exhibit the highest expansion from then on. The others start to expand rapidly after more than 240 days, but less rapid than L10-55. In Fig. 6.20 (b), all samples exhibit a similar expansion behavior before 150 days. Thereafter, the mortar L10-55 starts to expand dramatically while L10-3 and L10-4 shows a steady continuous expansion. Compared with expansion behaviors of the reference samples, the onset of dramatic expansion of L10 series does not show any retardation which was observed in the ref. [267].

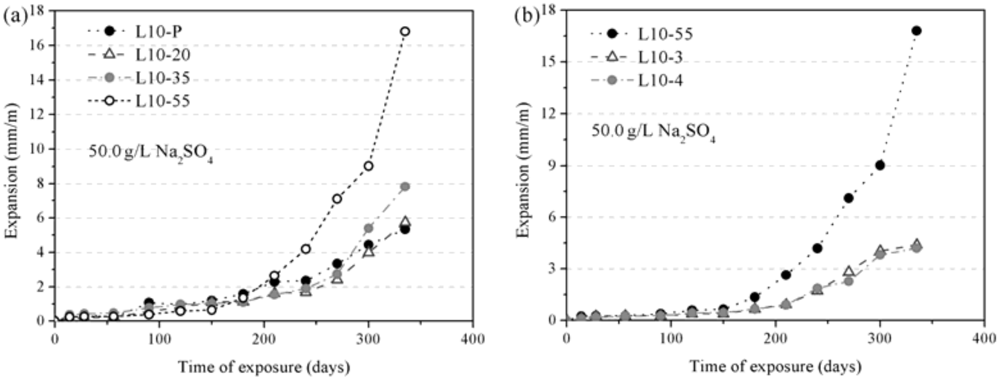

Fig. 6.20 Expansion of samples with LF in relation to (a) aggregate volume fractions and (b) aggregate sizes immersed in 50 g/L Na_2SO_4.

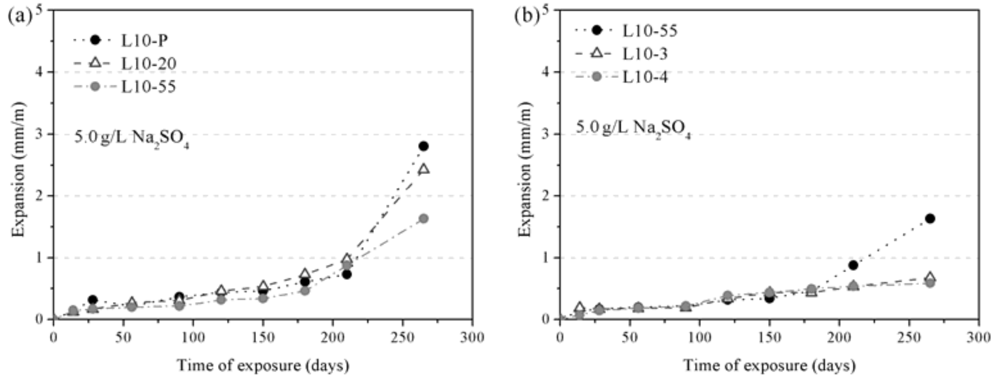

Fig. 6.21 Expansion of samples with LF in relation to (a) aggregate volume fractions and (b) aggregate sizes immersed in 5.0 g/L Na_2SO_4.

Regarding the lower sodium sulfate concentration in Fig. 6.21, the expansion of all samples is much less than at the higher sulfate concentration. In Fig. 6.21 (a), the pure paste and mortars exhibit similar expansion behaviors, which involve a steady slow expansion by 210 days and followed by a dramatic expansion. After 270 days of immersion, the expansion values follow the increasing order: L10-P > L10-20 > L10-55. The expansion data of 12 months is not presented here due to the insufficient immersion time. Fig. 6.21 (b) shows the relation between expansion with exposure time and the aggregate size. L10-3 and L10-4 shows a similar expansion behavior by 270 days and does not present a dramatic expansion.

Fig. 6.22 shows the expansion of L10 series in magnesium sulfate solution with exposure time. Regarding the effect of aggregate volume fraction in Fig. 6.22 (a), all samples exhibit a similar expansion behavior and the expansion values at one year is in the increasing order: L10-P > L10-55 > L10-35 > L10-20. Samples with different aggregate sizes, as shown in Fig. 6.22 (b), display a continuous expansion until 180 days and followed by a dramatic expansion. In this group, L10-55 exhibits the highest expansion after 12 months of immersion.

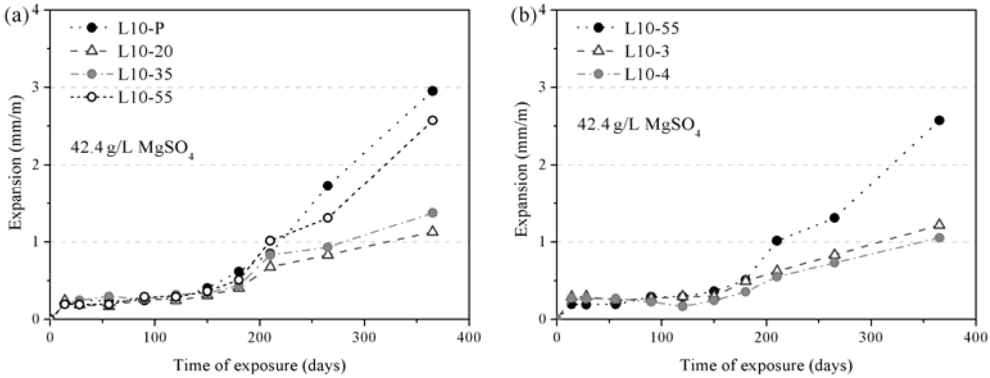

Fig. 6.22 Expansion of samples with LF in relation to (a) aggregate volume fractions and (b) aggregate sizes immersed in 42.4 g/L $MgSO_4$.

Regarding the effect of LF, the 12 months expansion values of the references and L10 groups obtained from sodium sulfate and magnesium sulfate solution are given in Fig. 6.23. In 50 g/L sodium sulfate solution, addition of LF results in a higher expansion. However, this increase is less apparent in case of mortar with 55% aggregate. In magnesium sulfate solution, although an increase in the expansion is observed for LF blended samples, the most significant increase is observed in the mortar L10-55. Moreover, there is no clear evidence that the negative effect of LF in the magnesium sulfate attack is more pronounced than that in the sodium sulfate. This is in contradiction to the findings in literature [266]. The researchers attribute the primary cause for the deterioration of mortar incorporating LF to the formation of gypsum as well as thaumasite [104,268].

For the effect of LF, previous researches both presented positive and negative effect which was dependent on the replacement level. There are several mechanism need to be considered with the addition of LF: (i) the modification of pore structure which could affect the permeability. In the chapter 4, it was observed that the incorporation of 10% LF increases porosity and permeability which could lead to a higher degradation. Schmidt et al. also [147] suggested that the impacts of LF on degradation in sulfate solutions are dominated by their impact on the cement porosity and on the rate of sulfate ingress; (ii) the phase compositions of hydration products. The addition of LF to PC tends to convert the monosulfate to monocarboaluminate which could reduce the possibility of expansion during the sulfate attack [269-270]; (iii) dilution of the C_3A content in the binder which could increase sulfate resistance. Moreover, the sulfate resistance of LF blended cement at low temperature should take the possible thaumasite formation into consideration [265, 271].

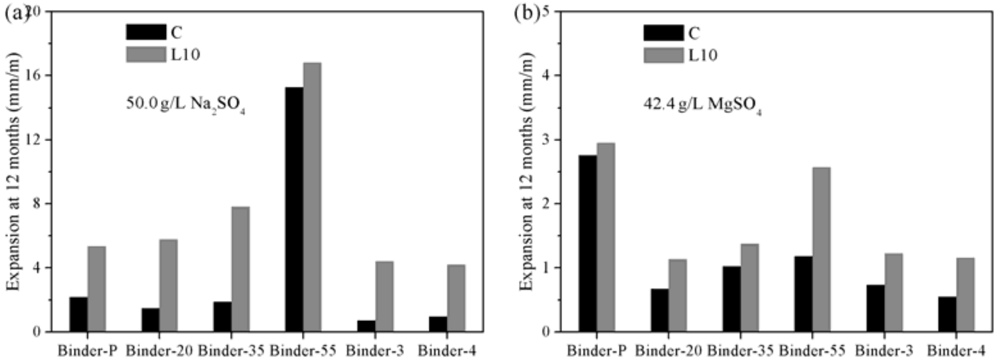

Fig. 6.23 Comparison of 12 months expansion values of C and L10 series exposed to (a) 50 g/L Na_2SO_4 and (b) 42.4 g/L $MgSO_4$.

Compared to the same samples exposed to magnesium sulfate solution, immersion in sodium sulfate solution leads to more significant expansion. This is largely related to the kinds of products formed by different solutions. In case of magnesium sulfate attack, decalcification of C-S-H contributes to the reduction of pH values [235]. Even if ettringite succeeds in forming during the sulfate attack, the product is prone to be unstable in the low alkalinity provided by the brucite formation and the C-S-H decomposition [268, 272]. For sodium sulfate attack, the sodium hydroxide formed compensates for the loss of alkalinity caused by the consumption of CH [266]. In this study, it was observed that a great amount of gypsum formed both under sodium sulfate and magnesium sulfate attack might be partly responsible for the expansion. However, the possibility of expansion due to the formation of ettringite remains uncertain.

6.3.2.3 Mass change

The normalized mass change of L10 series exposed to 50 g/L Na_2SO_4 in relation to the aggregate volume fraction and aggregate size is given in Fig. 6.24. As shown in Fig. 6.24 (a), a rapid increase in the mass gain is observed after 90 days of immersion for all samples. This point is retarded by around 1 month compared with the references, although the mass increase after 12 months is higher for the samples containing LF. Regarding the effect of aggregate size in Fig. 6.24 (b), there is a trend toward increasing mass gain for the samples with finer aggregate. L10-3 and L10-4 exhibit a similar mass change behavior.

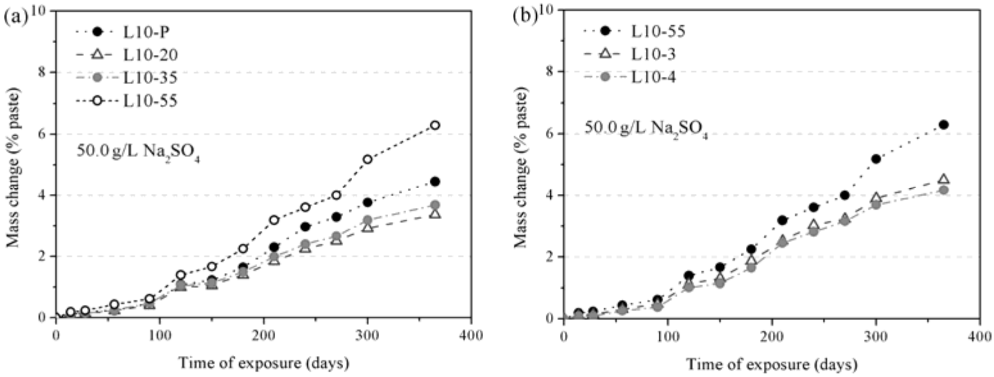

Fig. 6.24 Normalized mass change of samples with LF in relation to (a) aggregate volume fractions and (b) aggregate sizes immersed in 50 g/L Na_2SO_4.

At low sodium sulfate concentration solution (Fig. 6.25), a characteristic of the mass change curves of all samples is a period of rapid mass gain until 14 days, followed by a steady mass increasing. Moreover, the mass gain of samples at lower sodium sulfate solution is much lower than that at higher concentration.

In case of magnesium sulfate attack, as shown in Fig. 6.26, the mass gain after 12 months of immersion is all the more apparent for the sample prepared with higher aggregate volume fraction or finer aggregate.

Additionally, there is a nearly stable process in mass change from 270 days to 360 days for all samples. This can be due to the increased deterioration which could partially offset the mass increase by sulfate absorption.

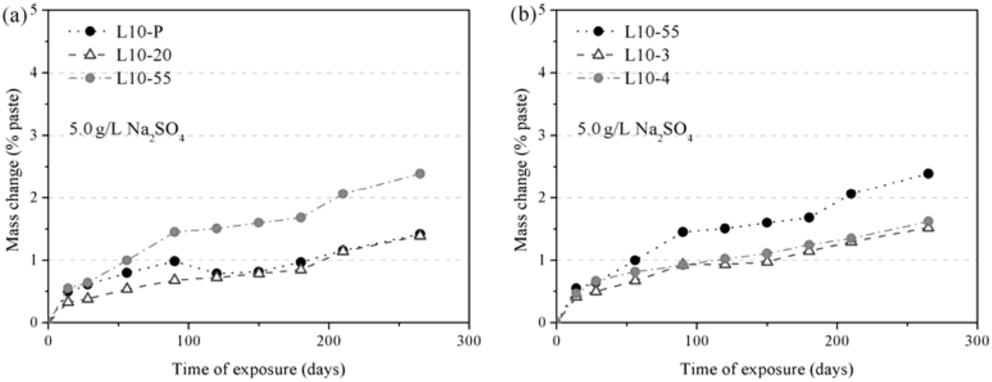

Fig. 6.25 Normalized mass change of samples with LF in relation to (a) aggregate volume fractions and (b) aggregate sizes immersed in 5.0 g/L Na_2SO_4.

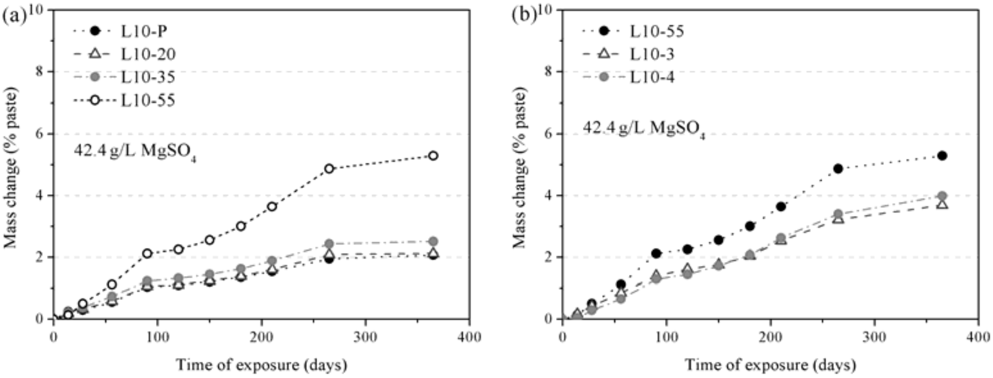

Fig. 6.26 Normalized mass change of samples with LF in relation to (a) aggregate volume fractions and (b) aggregate sizes immersed in 42.4 g/L $MgSO_4$.

6.3.3 PC-GGBS

6.3.3.1 Visual inspection

Fig. 6.27 shows the samples of S70 series exposed to 50 g/L sodium sulfate solution for 12 months. In general, the GGBS blended samples display much less deterioration and are very effective in resisting the sodium sulfate attack. This is believed to be associated with the permeability reduction associated with the presence of slag [273]. As evident in the chapter 4 and 5, the diffusivity of slag blended samples were much less than that of plain samples. Besides, there might be other relevant effects. The incorporation of high amount of GGBS increased the fine porosity, and this could enhance the ability of the microstructure to accommodate a greater increase in solid volume without undergoing server damage [274]. From Fig. 6.27 (a), it can be observed that S70-P presents the most significant damage at the corner and edge, while no spalling at the corners, cracking at the edge is noted in the mortar S70-35 and S70-55. Mortar S70-20 displays only one corner spalling after 12 months of immersion. Regarding the effect of aggregate size in Fig. 6.27 (b), there is no appreciable effect of the differences in the aggregate sizes on the extent of deterioration.

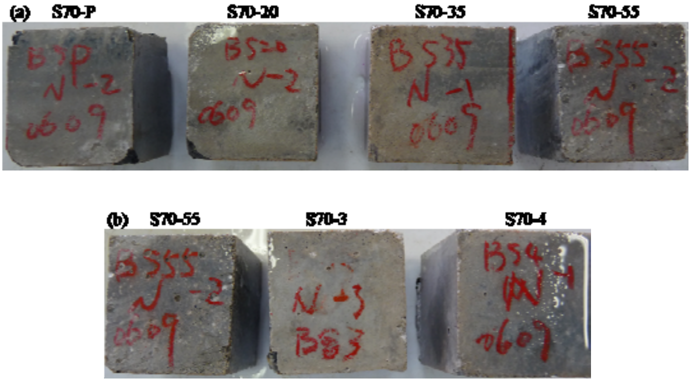

Fig. 6.27 S70 series specimens with respect to (a) aggregate volume fraction and (b) aggregate size exposed to 50 g/L Na_2SO_4 for 12 months.

Fig. 6.28 shows examples of cube samples exposed to 42.4 g/L magnesium sulfate solution for 12 months. Although no significant expansion is noted, all specimens exhibit signs of deterioration by showing severe softening and disintegration. Besides, mortar S70-55 displays wider cracks at the edge and the coarse aggregate in S70-3 and S70-4 is noted due to the disintegration. The deterioration of GGBS blended samples under magnesium sulfate attack is much more severe than that of plain samples. Therefore, the presence of GGBS is detrimental to the magnesium sulfate attack resistance.

It is well known that the major deterioration of cement based materials in magnesium sulfate solution is softening and disintegration. This progress can be considerable aggravated by incorporating GGBS to PC. With magnesium sulfate solution, decomposition of C-S-H is intensified due to the remarkable reduction of pH associated with the precipitation of brucite and M-S-H [235, 274]. In the case of pure PC samples, the decalcification of C-S-H can be limited due to the relatively high concentration of CH. However, the calcium hydroxide is low in the samples containing large amount of slag and the source of calcium ions for the formation of gypsum comes directly from the decalcification of C-S-H. This may be why the GGBS blended samples tend to fail firstly by softening and disintegration.

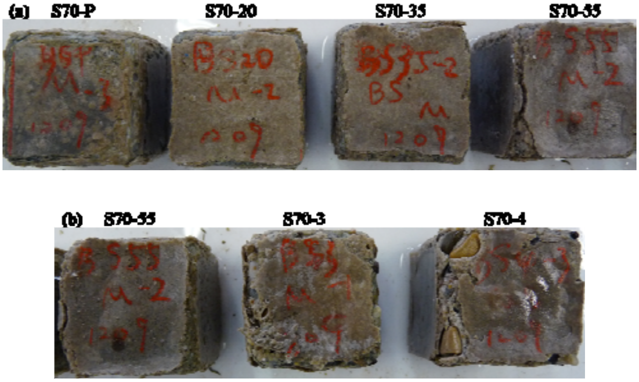

Fig. 6.28 S70 series specimens with respect to (a) aggregate volume fraction and (b) aggregate size exposed to 42.4 g/L $MgSO_4$ for 12 months.

6.3.3.2 Expansion

Fig. 6.29 shows the expansion data with exposure time of GGBS blended samples exposed to sodium sulfate solution. In general, there is no appreciable effect of the difference in the aggregate on the expansion behavior. All specimens remain stable with a small expansion value of about 0.5 mm/m in 12 months.

The highly improved sodium sulfate resistance by adding GGBS can be mainly due to: (i) reduction of the permeability since the involved reaction proceeds by the inward movement of sulfate ions; (ii) reduction of the calcium hydroxide which provides the preferred source of calcium ions for the formation of gypsum and ettringite; (iii) low Ca/Si ratio of C-S-H in GGBS blended samples. Due to the lack of calcium hydroxide, the calcium ions needed for the formation of expansive products are mainly contributed by decalcification of the C-S-H. For gypsum to be stable, relatively high concentration of both calcium ions and sulfate ions are required. These could occur in the presence of CH or C-S-H of high Ca/Si ratio, but not in that of C-S-H of low Ca/Si ratio [274]. In the visual inspection, only minor spalling was noted at the corner of S70-P and S70-20 while no deterioration was noted for the others. This could suggest that the quantity of gypsum is much less or none at all in some cases. Ettringite was not taken into account since it can only be the dominant effect if $Al(OH)_4^-$ and calcium hydroxide are available. Although there is much alumina in the GGBS blended system, not much is available [166, 274].

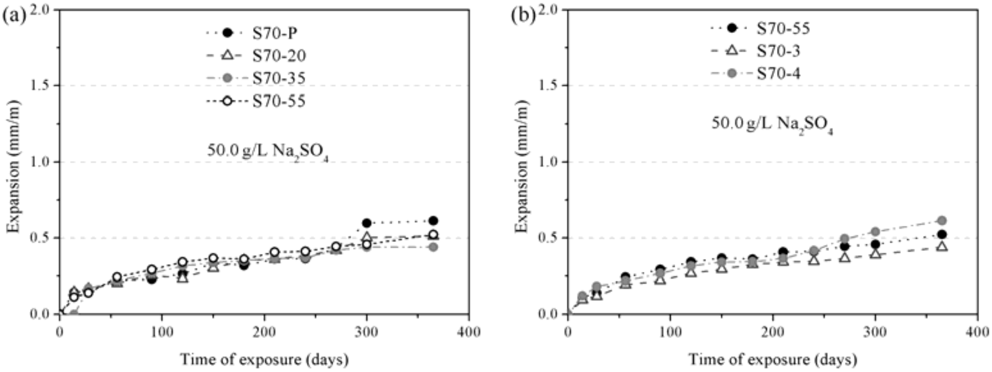

Fig. 6.29 Expansion of samples with GGBS in relation to (a) aggregate volume fractions and (b) aggregate sizes immersed in 50 g/L Na_2SO_4.

Fig. 6.30 shows the expansion of S70 series in magnesium sulfate solution with exposure time. All specimens exhibit a similar expansion curves as in the sodium sulfate solution which is characterized by a steady state expansion. In Fig. 6.30 (a), the paste S70-P displays the highest expansion in 12 month which could be due to the formation of relatively high content of expansive products.

The reactions involved in the deterioration of GGBS blended samples exposed to magnesium sulfate attack are generally similar to those occurred in the reference samples, but are associated with more intensified decomposition of the C-S-H and lead to more significant softening and disintegration [259-260, 275-276]. Due to the releasing calcium ions from the decalcification of the C-S-H, gypsum can form readily in the paste and results in a relatively high expansion compared with the results in sodium sulfate solution. However, the quantity of gypsum is possibly still less than that in the plain PC system, because the expansion of GGBS blended samples is less apparent than that of the reference. Moreover, the insoluble of brucite formed in the plain PC system, which could protect the C-S-H gel from further magnesium sulfate attack, is absence in high GGBS blended samples. This could be the reason for the relatively high expansion rate by one month noted in Fig. 6.30.

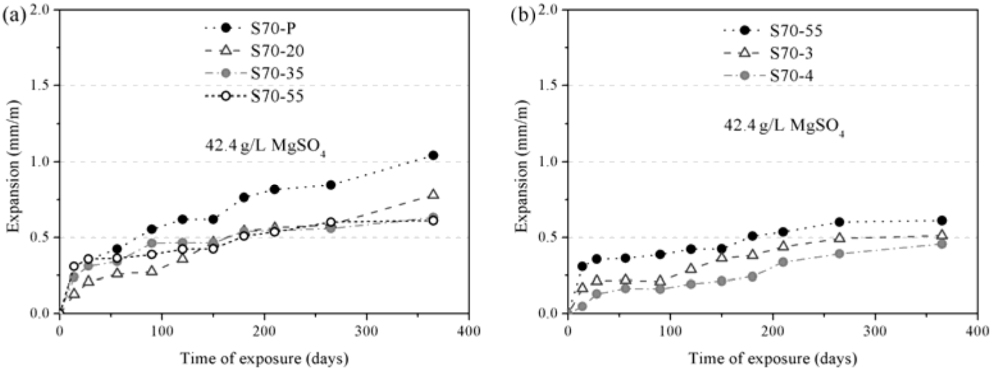

Fig. 6.30 Expansion of samples with GGBS in relation to (a) aggregate volume fractions and (b) aggregate sizes immersed in 42.4 g/L $MgSO_4$.

6.3.3.3 Mass change

The normalized mass change of S70 series exposed to 50 g/L Na_2SO_4 in relation to the aggregate volume fraction and aggregate size is given in Fig. 6.31. In general, there is no appreciable effect of the aggregate on the mass change for all specimens. As shown in Fig. 6.31 (a), the paste S70-P displays a clear mass loss at 12 months, with corresponding spalling at the corner as observed in the visual inspection. The mass change of GGBS blended samples exposed to sodium sulfate solution for 12 months is much less than that of plain PC samples. This further confirms the positive influence of GGBS on the sodium sulfate resistance. Moreover, the less mass change indicates that the absorption of sulfate ions is slow in the samples containing

GGBS-PC binary binders. In this study, it can be concluded that the improvement of sodium sulfate resistance by GGBS is mainly through reducing the permeability.

Fig. 6.32 shows the normalized mass change of S70 series exposed to 50 g/L 42.4 g/L $MgSO_4$ in relation to the aggregate volume fraction and aggregate size. In Fig. 6.32 (a), there is an obvious trend toward increasing mass gain for the samples with higher aggregate volume fraction. For S70-P, it can be clearly seen that there is a mass loss from 120 days to 210 days, with corresponding softening and degradation at the corner and edge. Thereafter, a stable mass gain is noted again. In Fig. 6.32 (b), S70-3 and S70-4 displays a nearly same mass change curve while S70-55 exhibits the highest mass gain, especially after 180 days. A similar trend is also observed with respect to the effect of aggregate volume fraction, as shown in Fig. 6.32 (a), the difference in the mass gain among the samples is more apparent after 150 days. This might suggest that the increased ITZ content could increase absorption of sulfate and magnesium ions and facilitate the degradation as a result. This negative effect starts to be notable when the interior structure of samples is exposed to the sulfate and magnesium ions.

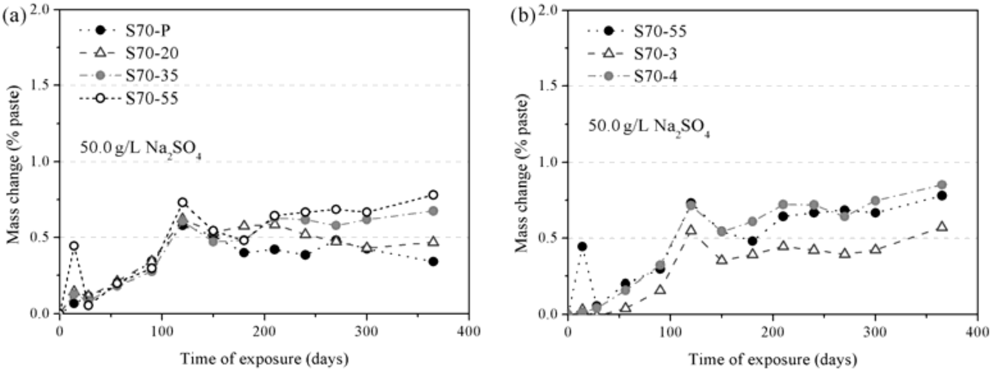

Fig. 6.31 Normalized mass change of samples with GGBS in relation to (a) aggregate volume fractions and (b) aggregate sizes immersed in 50 g/L Na_2SO_4.

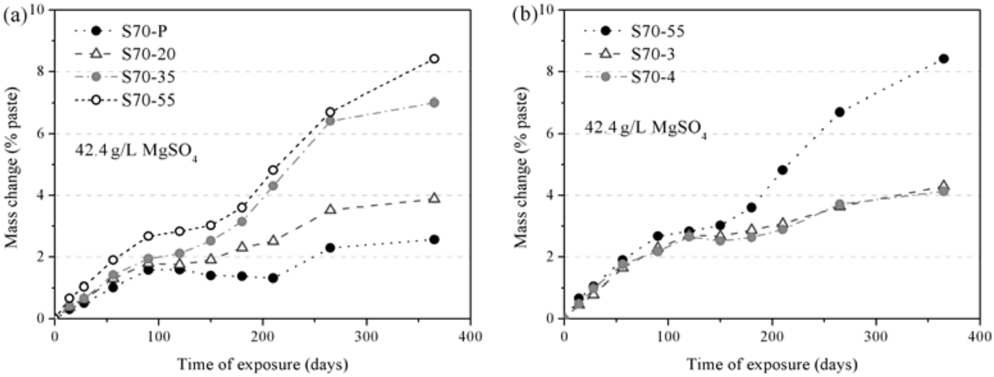

Fig. 6.32 Normalized mass change of samples with GGBS in relation to (a) aggregate volume fractions and (b) aggregate sizes immersed in 42.4 g/L $MgSO_4$.

6.3.3.4 Microstructure analysis

Fig. 6.33 shows low magnification images of the mortar S70-55 immersed in high sodium sulfate concentration for 6 months. The surface region in Fig. 6.33 (a) only exhibits a loose and porous microstructure which could be due to the decalcification of C-S-H. Compared with the BSE images of C-55 in Fig. 6.14, the microcracks are much less for S70-55. This finding is coincidence with the expansion and mass change measurements, of which no apparent expansion and mass gain was noted. As shown in Fig. 6.33 (b), the core region is unaltered and characterized by a dense and compact microstructure and a good binding between the bulk matrix and aggregates.

The surface region of S70-55 stored in magnesium sulfate solution for 6 months is given in Fig. 6.34. It can be seen that the region close to the surface is darker than the core zone. This deterioration is inward for more than 500 µm from the surface. Some severe cracks which are mainly parallel to the surface are noted. These cracks could be formed due to the decomposition of C-S-H and the formation of expansive products.

Fig. 6.35 shows the BSE image and EDX analysis on mortar S70-55 exposed to magnesium sulfate solution for 12 months. As for the references, relatively high sulfur concentrations is observed in the ITZ and in the cracks. The spectrum of area A confirms that the atomic proportions and weight concentration are closed to the composition of gypsum. It could be the reason for the relatively high expansion and mass gain of mortar S70-55. This confirms the role of ITZ and gypsum in expansion due to sulfate attack. Comparing the relatively concentration of magnesium with that of calcium, it is interesting to note that a relatively high magnesium concentration is observed in the bulk matrix where the calcium is insufficient, and vice versa. This could be due to the decalcification of C-S-H and formation of M-S-H, and is further confirmed by the EDX analysis on area B. Moreover, the aluminium concentrations in the ITZ and cracks are much less than those in the bulk matrix. Combining the concentrations maps of calcium, sulfur and aluminium, it could be concluded that there is no evidence for the formation of ettringite during the sulfate attack. The formation of gypsum could be the main reason for the observed expansion.

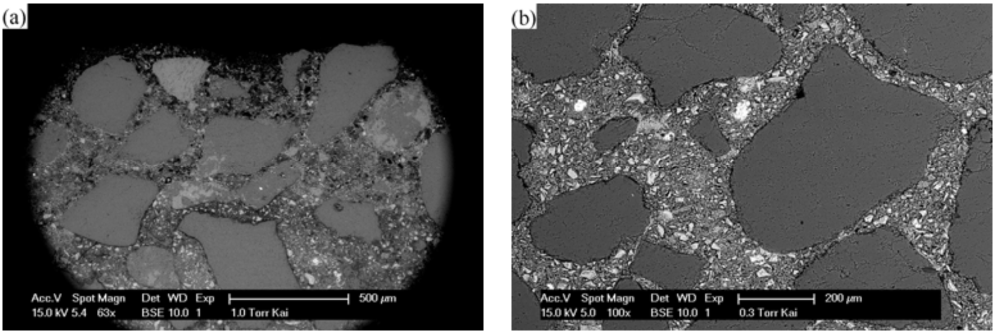

Fig. 6.33 BSE images (a) surface region and (b) core region of S70-55 immersed in 50 g/L Na_2SO_4 for 6 months.

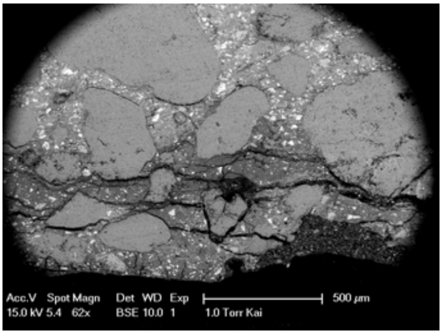

Fig. 6.34 BSE images of surface region of S70-55 immersed in 42.4 g/L $MgSO_4$ for 6 months.

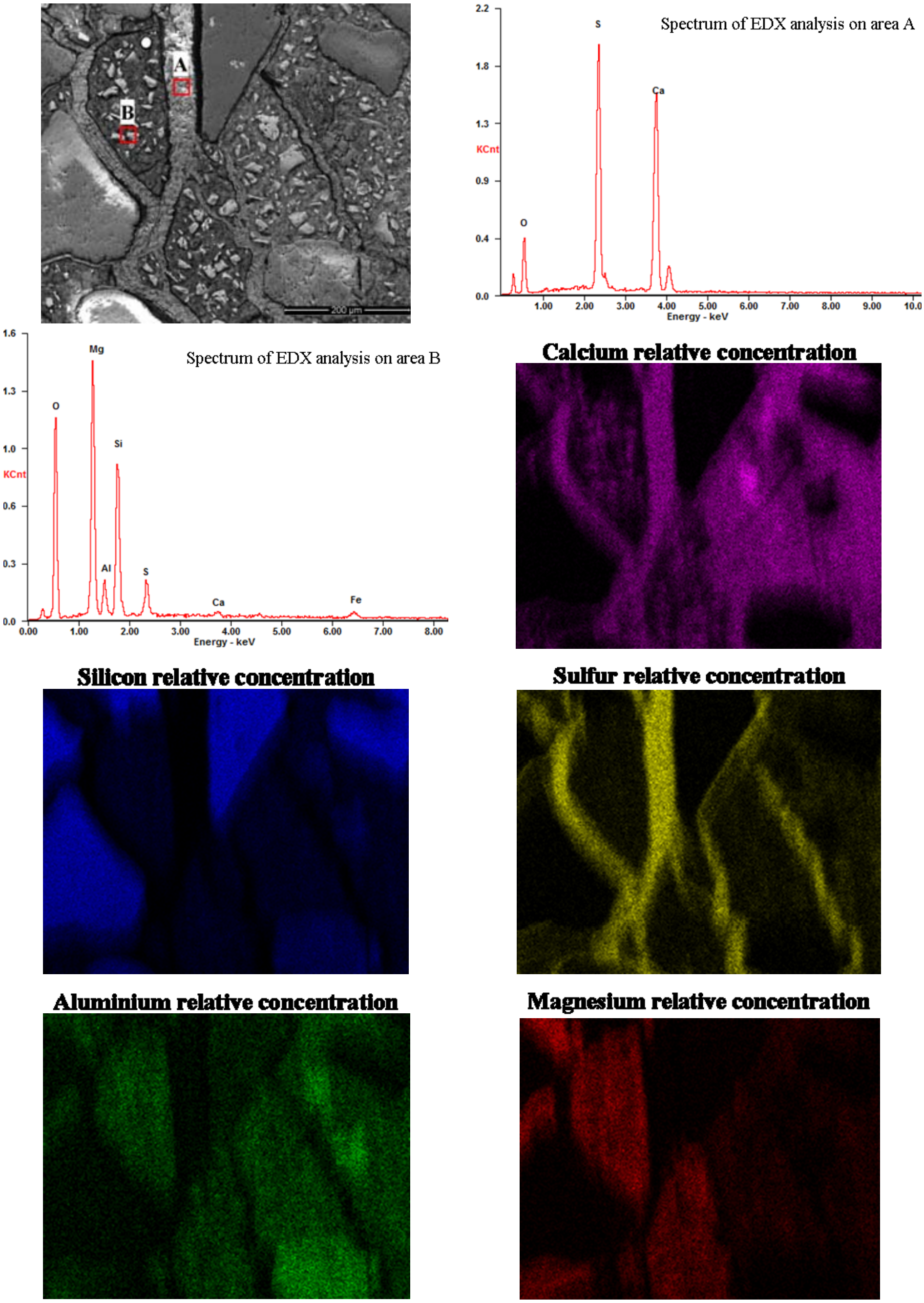

Fig. 6.35 EDX analysis of mortar S70-55 immersed in 42.4 g/L $MgSO_4$ for 6 months.

6.3.4 PC-GGBS-LF

6.3.4.1 Visual inspection

Fig. 6.36 shows the samples of S60L10 series exposed to 50 g/L sodium sulfate solution for 12 months. After one year of exposure, only minor signs of deterioration in the form of fine cracks appeared at the corner of the neat paste S60L10-P. The incorporation of 10% LF as a partial substitute for GGBS does not reduce the sodium sulfate resistance. This is in consistence with the permeability measurements, as evident in the chapter 4 and 5, the diffusivity of the ternary binders was comparable to the corresponding binary binders.

Fig. 6.37 shows examples of cube samples exposed to 42.4 g/L magnesium sulfate solution for 12 months. Although no significant expansion is noted, all specimens exhibit similar signs of deterioration as in case of S70 series, such as wide cracks on the edges, spalling at the corners, softening and disintegration.

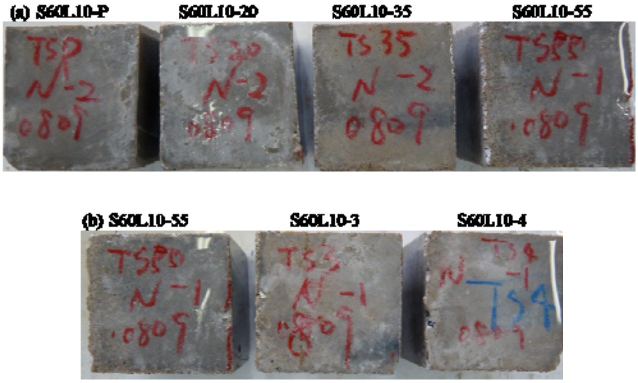

Fig. 6.36 S60L10 series specimens with respect to (a) aggregate volume fraction and (b) aggregate size exposed to 50 g/L Na_2SO_4 for 12 months.

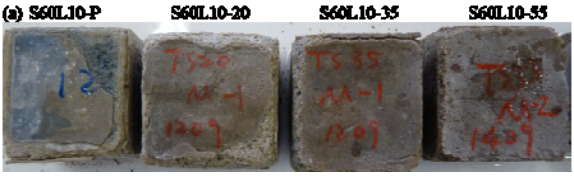

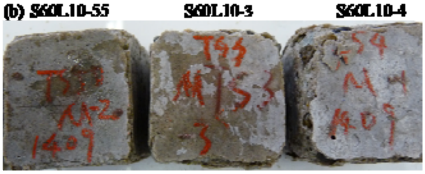

Fig. 6.37 S60L10 series specimens with respect to (a) aggregate volume fraction and (b) aggregate size exposed to 42.4 g/L $MgSO_4$ for 12 months.

6.3.4.2 Expansion and mass change

The differences of expansion and normalized mass change after one year of exposure between the binary and ternary series are given in Fig. 6.38 and Fig. 6.39, respectively. Except for S70-P in magnesium sulfate solution, after one year of exposure, all samples exhibit average expansion of less than 1 mm/m regardless of the type of solution. The expansion values at 12 months of the bars decreases by adding 10% of LF to the binders. This decrease is more apparent in case of magnesium sulfate attack. On the other hand, a reverse trend is observed for the normalized mass change. As shown in Fig. 6.39, there is a general trend toward increasing normalized mass gain with the addition of LF. This effect is more noticeable in case of magnesium sulfate attack.

As given in chapter 4 and 5, the incorporation of 10% LF as a partial substitute for GGBS tended to increase porosity and the diffusivity slightly. This corresponds well with the trend in mass gain in Fig. 6.39. Concerning expansion, it mainly determined by the formation of expansive products. In GGBS blended samples containing LF, the hydration products are different from those in the corresponding binary and plain samples. Hoshno et al. [277] found that ettringite generated at early ages does not transform into monosulfate, while monocarboaluminate and hemicarboaluminate were generated. Based on this conclusion, Ogawa et al. [267] suggested that the additional ettringite tends to react with LF and transform to monocarboaluminate and hemicarboaluminate instead of monosulfate, and thereby reduce or delay the formation of expansive ettringite when exposed to external sulfate ions. However, the ettringite was not observed in the previous microstructure analysis, and the formation of gypsum could be the main force for the expansion. On the other hand, some researchers also indicated that monocarboaluminate, hemicarboaluminate would be transformed into ettringite and gypsum slowly in the presence of excessive sulfate and high C_3A content cement, leading to extended deterioration [176, 278]. This was not observed in the present study. Therefore, the mechanism related to the effect of LF on the expansion of GGBS blended binders needs to be further investigated.

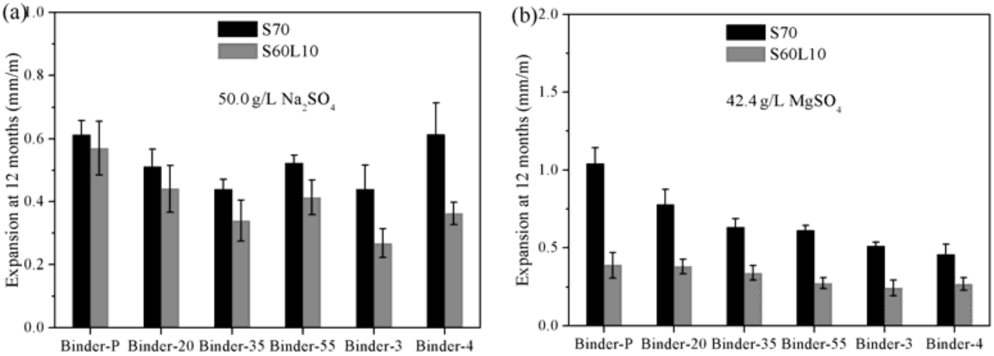

Fig. 6.38 Comparison of 12 months expansion values of S70 and S60L10 series exposed to (a) 50 g/L Na_2SO_4 and (b) 42.4 g/L $MgSO_4$.

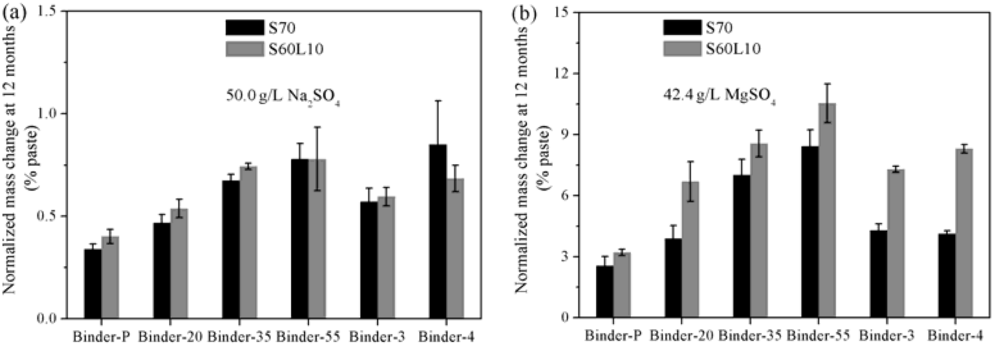

Fig. 6.39 Comparison of 12 months mass change of S70 and S60L10 series exposed to (a) 50 g/L Na_2SO_4 and (b) 42.4 g/L $MgSO_4$.

6.3.5 Relation between ITZ and expansion, mass change

In order to evaluate the role of ITZ in the process of sulfate attack, the expansion values and normalized mass change at different immersion time (1, 3, 6 and 12 months) are plotted against the ITZ volume fraction in Fig. 6.40 - Fig. 6.42. Linear regressions are also fitted to the data to find any possible correlation or trends. The ITZ volume fraction was calculated according to the Eq. (3.15) with an assumed ITZ thickness of averaged particle size of binders. Fig. 6.40 (a) and (b) show the effect of ITZ on expansion of the reference and L10 series exposed to 50g/L sodium sulfate solution. While the data are highly scattered, a general trend is observed that the negative effect of ITZ is prominent at the exposure age of 12 months. In 6 months of exposure, the expansion values seem to be independent of the ITZ content since it is determined by the expansive products formed close to the surface region. The relation between normalized mass change in sodium sulfate solution and ITZ volume fraction exhibits a similar trend. In magnesium sulfate attack (Fig. 6.42), the negative effect of ITZ starts to be appreciable at the exposure age of 3 months regardless of the binders. This point is much earlier than that in the sodium sulfate attack. According to these findings, one may use a similar approach to estimate the desirable aggregate proportion for improving the sulfate resistance during the mix design. This could also be used for the estimation of sulfate attack through modeling.

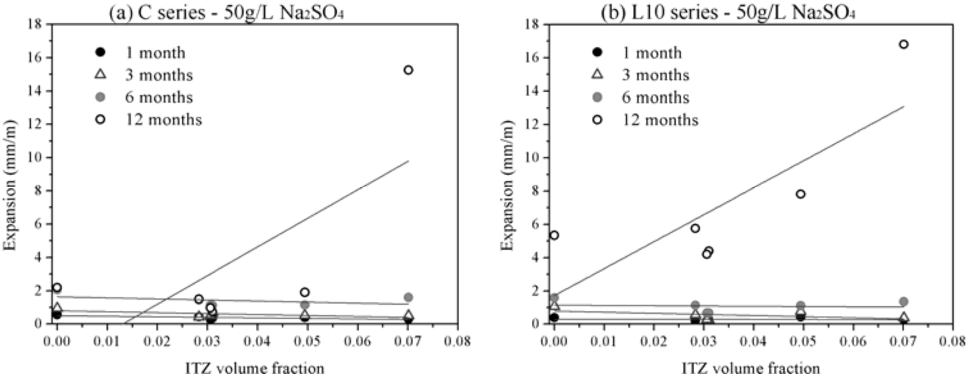

Fig. 6.40 The relationship between expansion values with ITZ volume fraction.

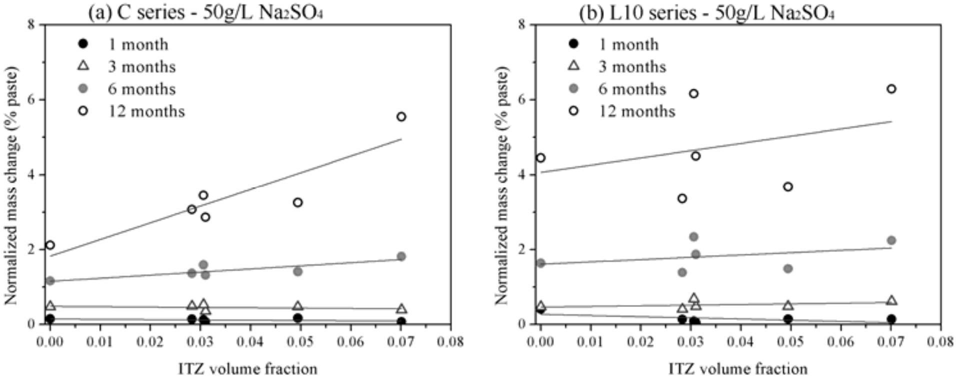

Fig. 6.41 The relationship between normalized mass change with ITZ volume fraction.

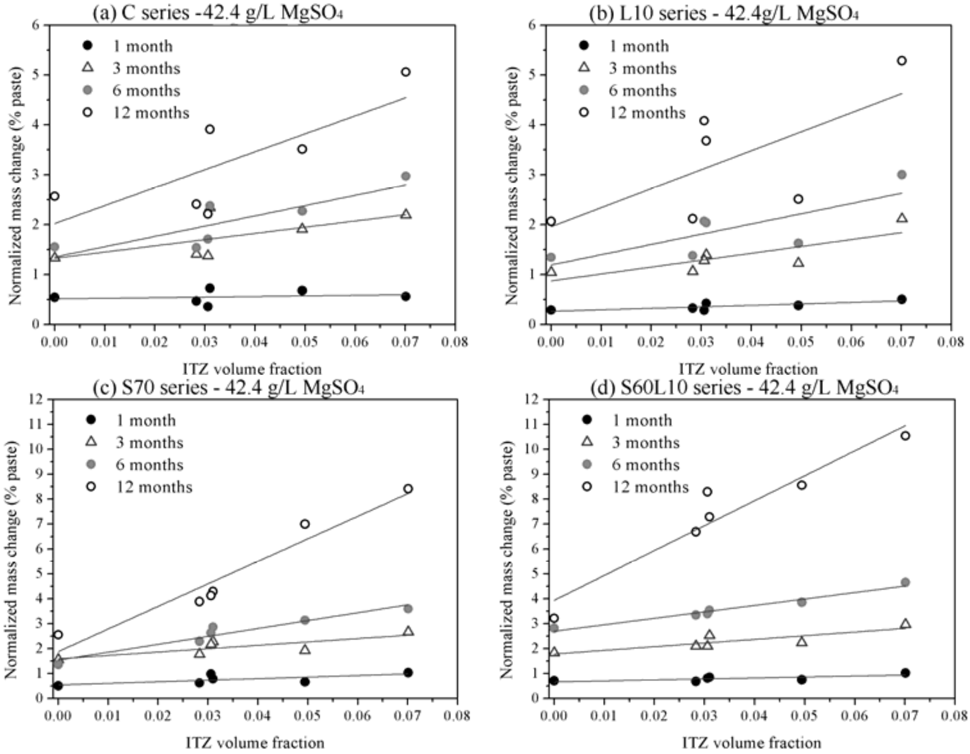

Fig. 6.42 The relationship between normalized mass change with ITZ volume fraction.

6.4 Conclusions

In order to understand better the interactions between sulfate and concrete with the aim of preventing it, several parameters were studied from the influences of ITZ. One is the content of ITZ, which is studied by a comparison of resistance to sulfate attack among mortars and concretes prepared with different volume fractions and grain sizes of aggregate. The other influence is the binders. Moderate amounts of GGBS and LF were blended with PC as binders to modify both the microstructure of the bulk cement matrix and the ITZ. Four series of samples were exposed to sodium sulfate solution with two concentrations (50 and 5.0 g/L Na_2SO_4) and a magnesium sulfate solution (42.2 g/L $MgSO_4$). This work includes macroscopic measurements and microscopic analysis. The following conclusions pertain to this study:

1) In case of high sodium sulfate concentration, the extent of deterioration had a slight tendency to increase for the samples with finer aggregates or higher aggregate volume fraction. C-55 displayed many wide cracks, spalling and substantial material loss at the surface as well as at the corner and edges, while C-3 and C-4 only exhibited cracks around corners and edges. For the lower sulfate concentration or the early period of high sulfate concentration attack, the exposed surface and outer part of samples was important. For the sulfate to reach the interior of the samples, it must move through the bulk cement matrix. The presence of more porous ITZ was normally accompanied by a denser bulk cement matrix. This could limit the ingress of sulfate ions and delay the formation of expansive products. After the sulfate penetrates into the interior of the samples, the ITZ was expected to exert more significant influences on the deterioration.

2) In magnesium sulfate attack, there was an apparent trend toward increasing the normalized mass gain for the samples with higher aggregate volume fraction or finer aggregatre. The presence of the relatively impermeable layer of MH led to reducing the penetration of sulfate into the samples of C series, and reduced expansion at the early period of attack compared with the sodium sulfate. After the broken of

MH, a direct attack of the C-S-H could occur and resulted in softening and disintegration.

3) Gypsum was mainly observed in the ITZ for sodium sulfate attack, and both in the ITZ and the bulk matrix for the magnesium sulfate attack. The expansion of samples in sodium sulfate attack was influenced by the changes in aggregate to a higher extent compared with that in the magnesium sulfate solution. From the microstructure analysis, no clear signs of ettringite were observed since it is unstable below a pH around 10.5 and dissolves as gypsum and aluminium sulfate.

4) Compared with the corresponding references, the samples of L10 series showed more severe deterioration in both sodium sulfate and magnesium sulfate solution. In case of sodium sulfate attack, the addition of LF resulted in a higher expansion. This increase was less apparent in the mortar with 55% of aggregate. In magnesium sulfate solution, although an increase in expansion was observed for LF blended samples, the most significant increase was observed in the mortar L10-55. There was no clear evidence that the negative effect of LF in the magnesium sulfate attack is more pronounced than that in the sodium sulfate attack.

5) The GGBS blended samples were very effective in resisting the sodium sulfate attack. This was partial due to the permeability reduction by slag. The incorporation of high amount of GGBS increased fine porosity which could enhance the ability of the microstructure to accommodate a greater increase in solid volume without undergoing server damage. On the other hand, the deterioration of GGBS blended samples under magnesium sulfate attack was much more severe than that of plain samples. From microstructure analysis on mortar S70-55 exposed to magnesium sulfate, a high concentration of gypsum was also observed in the ITZ. The aluminium concentrations in the ITZ and cracks were much less than those in the bulk matrix. There is no evidence for the formation of ettringite during the sulfate attack. The formation of gypsum could

be the main reason for the expansion of the samples containing GGBS exposed to magnesium sulfate solution.

6) The effect of ITZ can only be notable when the interior structure of samples was exposed to the sulfate and magnesium ions. In sodium sulfate attack, the negative effect of ITZ was prominent at the exposure age of 12 months, and the expansion values seem to be independent of the ITZ in 6 months of exposure. In magnesium sulfate attack, the negative effect of ITZ started to be appreciable at the exposure age of 3 months regardless of the binders. This point was much earlier than that in the sodium sulfate attack. According to these findings, one may use a similar approach to estimate the desirable aggregate proportion for improving the sulfate resistance during the mix design.

Chapter 7

Conclusions and perspectives

7.1 Conclusions

This work was focus on the effect of ITZ on the overall performance of concrete made with pure PC and blended materials. The ITZ volume fraction was controlled by either varying the aggregate volume fraction at a fixed PSD, or varying the size distribution at a fixed volume fraction. Besides, the microstructure features of ITZ in mortars made with different types of binders were determined by quantitative BSE image analysis, EDX analysis and MIP measurement. According to this approach, the role of ITZ on transport properties (gas permeability, water absorption, chloride migration and diffusion), strength and sulfate attack was evaluated by a comparison among mortars and concretes with systematically varied aggregate volume fraction and size. Moreover, the main force for the improvement of the overall performance of concrete with blended binders was presented. The main conclusions can be drawn as follows:

Effect of ITZ on the transport properties of Portland cement-based composites

For the effect of ITZ and its percolation on the transport properties, several other factors should be taken into account with the variation in aggregate: (i) the dilution and tortuosity of the bulk cement matrix by using high aggregate volume fraction or finer aggregate size decreases permeability; (ii) the densification of bulk cement matrix associated with the presence of ITZ decrease permeability; (iii) the presence of ITZ and its percolation increases transport properties. Additionally, other parameters such as bleeding, cracks from drying exerted significant effects on the overall transport properties. This misunderstanding was more apparent for gas permeability which is dominated by pressure-induced flow than for the sorptivity and migration.

The relatively importance of ITZ to the overall transport properties depended on the mechanism governing the transport process. The gas permeability, initial and secondary sorptivity decreased continuously when the aggregate volume content increased. An increase of the sand volume fraction led to a decrease of migration coefficient until 0.35 due to the densification, dilution and tortuosity effect induced by the inclusions. Then a significant increase in the migration coefficient was observed when the aggregate content increased from 0.35 to 0.60 due to the increased ITZ and percolation effect. The ratio of mass transport between ITZ and bulk cement matrix increased with increasing ITZ volume and width. The influence of ITZ was also becoming remarkable as the adjacent ITZ percolates.

From the microstructure analysis, the visual difference in the porosity between the region of ITZ and that of bulk cement matrix at the side of concrete with maximum aggregate size of 16 mm and 20 mm was fairly similar, while high porosity and large pore size could be easily observed at the bottom of these coarse aggregates. A contrast microstructure was obtained in one image with respect to the position effect. Therefore, a fixed ITZ thickness is not correct for analyzing the ITZ effect in the samples containing coarse aggregates.

Influence of GGBS and LF on the microstructure of ITZ

The initial particle packing of cement grains led to a depletion of larger anhydrous cement grains, approaching zero at the aggregate-paste interface, with a relatively high amount of smaller grains and a high W/C ratio. Throughout the whole measurement period from 1 day to 6 months, the least changes in the anhydrous content occurred at the first 5 μm from the interface. The regions further away were dominated by the larger particles, which hydrated slowly and presented a peak in the region between about 15 and 20 μm in the anhydrous profiles at 1 day. The particle size distribution beyond about 25-30 μm from the interface was similar to that of the bulk cement matrix.

Regarding the MIP data, one of the most important observations for the presence of ITZ was the presence of critical pores with diameter d_2 which is superior to 0.1 μm. The d_2 was more apparent for samples with the small aggregate size 0/2 mm, and shifted towards coarser for samples with coarser aggregates (combined 0/2 mm and 2/5.6 mm). The total porosity given by the percentage of paste volume increased with increasing aggregate volume fraction, or with decreasing average aggregate size.

The incorporation of moderate amount of LF (5%) was able to compact the microstructure of both ITZ and bulk matrix by filling effect and nucleation sites effect. Although the overall pore structure was weakened by substituting 10% LF for PC, it is still expected to have improvements in the microstructure of ITZ. The addition of 35% of GGBS reduced the porosity at all distances from the aggregate surface and produced a denser microstructure both in the ITZ and bulk cement matrix. The high amount of GGBS substitution (70%) can increase total porosity but refine the pore size from coarser (>0.1 μm and 10 to 100 nm) to finer (<10 nm) size. For the ternary binders, a synergy effect of combined GGBS and LF was observed on the ITZ when a moderate amount of GGBS (30%) and LF (5%) substituted for PC.

Effect of GGBS and LF on the ITZ in relation to the overall performance

For the reference samples, there seemed to be an obvious trend towards reduced compressive strength with higher ITZ quantity. Incorporating of GGBS and LF as a substitute for PC did not show enhancement in the compressive strength of neat cement paste. The improvement in the strength of the mortars and concretes were presumably due to the densification of the ITZ. A reverse trend was observed for the water absorption, chloride migration and diffusion. The relations between the relatively difference in the transport coefficients and the relatively difference in the intruded pore volume with respect to the reference samples, the variations of transport coefficients were highly determined by the variations of pore in the range between 10 nm and 100 nm rather than those of pore superior to 100 nm. The observed improvement in limiting the movement of water and chloride ions for the GGBS blended samples could be due in part to the improvement of the microstructure of the ITZ, but more importantly, to the densification of the bulk cement matrix.

The chloride diffusivity was found to strongly depend on the total intruded pore volume for all the binders. Although the samples showed a decreased chloride resistance with increasing total intruded pore volume, the increasing rate varied with the type of binders. Samples with pure PC as the binder showed the highest increasing rate. This rate was lower for the samples with blended binders. The ternary binders showed the least variation with the increasing total intruded pore volume.

Effect of ITZ on the sulfate resistance of LF and GGBS blended concrete

The incorporation of GGBS is beneficial to the sodium sulfate resistance, but detrimental to the magnesium sulfate attack. The samples containing 10% of LF showed more severe deterioration in both sodium sulfate and magnesium sulfate solution than the references.

Gypsum was mainly observed in the ITZ for sodium sulfate attack, and both in the ITZ and the bulk matrix for the magnesium sulfate attack. The expansion of samples in sodium sulfate attack was influenced by the changes in aggregate to a higher extent compared with that in the magnesium sulfate solution. From the microstructure analysis, no clear signs of ettringite were observed in the ITZ.

For the lower concentration or the early period of high sodium sulfate concentration attack, the exposed surface and outer part of samples was important, the deterioration was mainly determined by the ingress rate of sulfate ions. After the sulfate penetrates into the interior of the samples, the ITZ was expected to exert more significant influences on the deterioration. In sodium sulfate attack, the negative effect of ITZ was prominence at the exposure age of 12 months, and the expansion seems to be independent on the ITZ quantity in 6 months of exposure.

In magnesium sulfate attack, there was an apparent trend toward increasing normalized mass gain after 12 months of exposure for the samples with higher ITZ volume fraction. The negative effect of ITZ started to be appreciable at the exposure age of 3 months regardless the binders. This point was much earlier than that in the sodium sulfate attack. According to these findings, one may use a similar approach to estimate the desirable aggregate proportion for improving the sulfate resistance during the mix design.

7.2 Perspectives

This study has presented the relationship between the ITZ and the overall performance of concrete. The items involved are transport properties, strength and sulfate attack. However, durability is a complex problem because it is the crossed between physical and chemical and it exists different scales in concrete. The service condition for real concrete structure is more complex than the experiments carried out in the lab. Therefore, it is recommended that further research be carried out to explore the role of ITZ in concrete under multivariate impact or in real structures.

Compared with the real concrete, the mixture designed in this chapter are somewhat simplified. In real structure, coarser aggregate size, higher aggregate volume fraction, and other raw materials such as superplasticizer are commonly used. These factors should also be taken into account in the future study.

One of the objectives of the study was to investigate the factors leading to the microstructure of ITZ. These findings apply to normal concrete, which is prepared with normal weight aggregates. Recently, there is a great deal of interest in utilizing other types of aggregate, such as lightweight aggregate, recycled aggregate or other more porous aggregates. It is recommended that the present investigation could be extended to cover these concretes. A study using quantitative BSE image analysis and MIP measurements performed on the mortars with varying aggregate quantity may be useful in studying the ITZ.

Moreover, further studies could be expanded to explore the use of other solid wastes powders, to evaluate the feasibility of improving the structure of ITZ and the overall performance of concrete. This is not only beneficial to the improvement of the properties, but also helpful to the sustainability development of concrete.

Appendix

A.1 Water absorption results for chapter 3

The following figures show the detailed water absorption data in relation to the curing age and preconditioning regime.

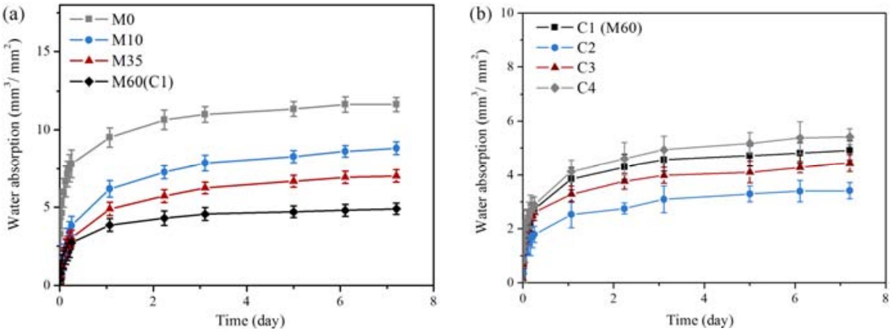

Fig.A.1-1 Absorbed water (tested at the age of 28 d) in relation to (a) aggregate volume fraction and (b) aggregate size.
Preconditioning: drying at 35°C for 1 week and then at 50°C until mass equilibrium

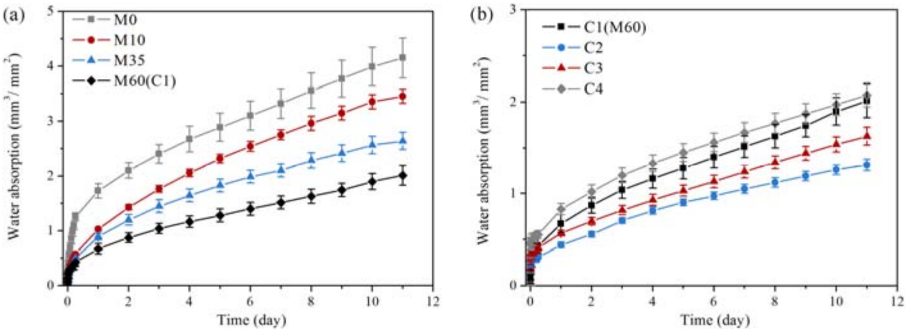

Fig.A.1-2 Absorbed water (tested at the age of 12 months) in relation to (a) aggregate volume fraction and (b) aggregate size.
Preconditioning: curing in the chamber for 12 months

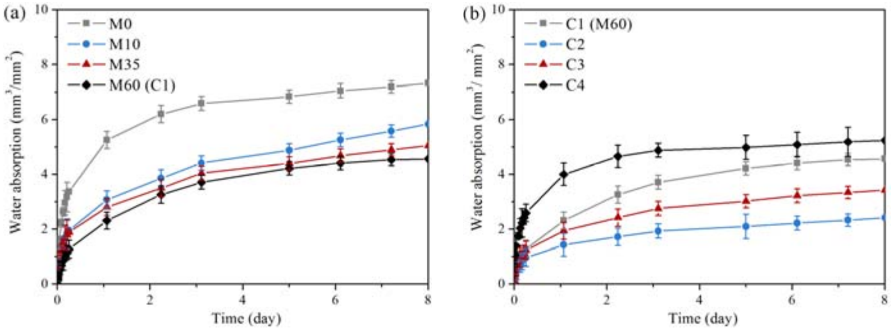

Fig.A.1-3 Absorbed water (tested at the age of 12 months) in relation to (a) aggregate volume fraction and (b) aggregate size.

Preconditioning: drying at 35°C for 1 week and then at 50°C until equilibrium

A.2 Water absorption results for chapter 4

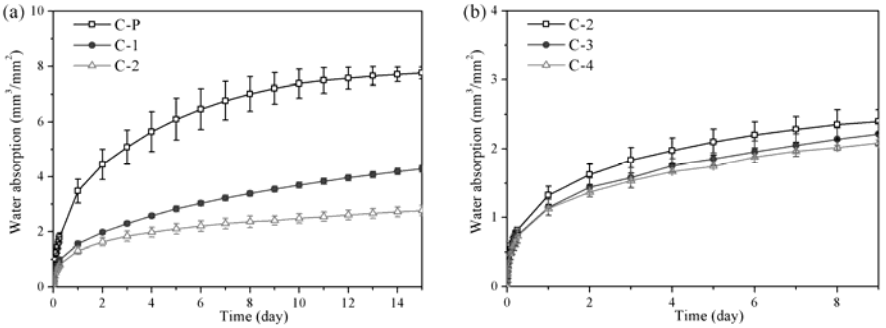

Fig.A.2-1 Absorbed water of C series (tested at the age of 12 months) in relation to (a) aggregate volume fraction and (b) aggregate size.

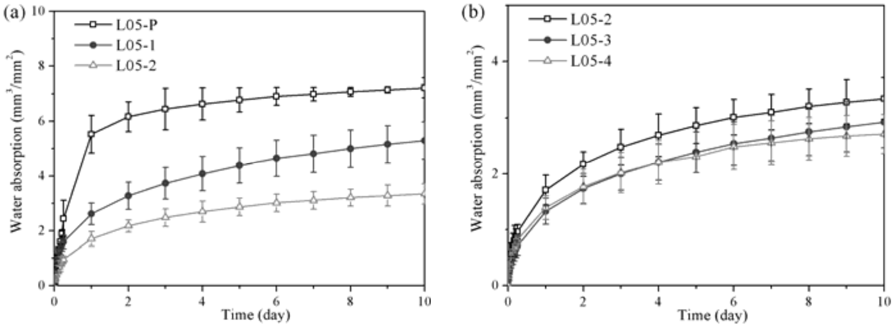

Fig.A.2-2 Absorbed water of L05 series (tested at the age of 12 months) in relation to (a) aggregate volume fraction and (b) aggregate size.

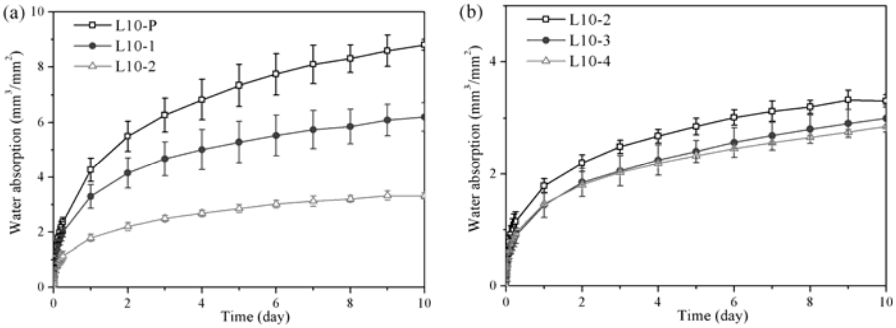

Fig.A.2-3 Absorbed water of L10 series (tested at the age of 12 months) in relation to (a) aggregate volume fraction and (b) aggregate size.

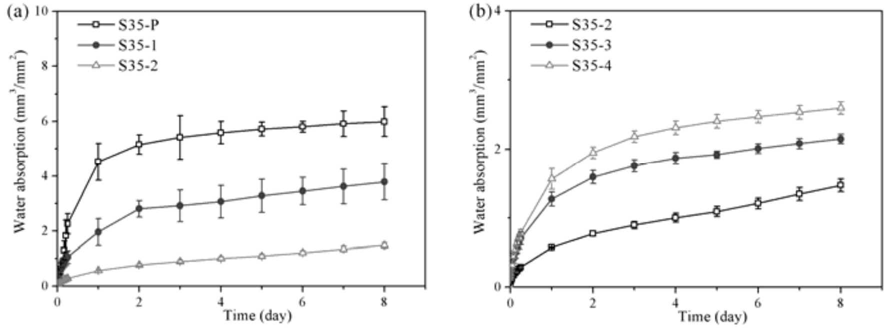

Fig.A.2-4 Absorbed water of S35 series (tested at the age of 12 months) in relation to (a) aggregate volume fraction and (b) aggregate size.

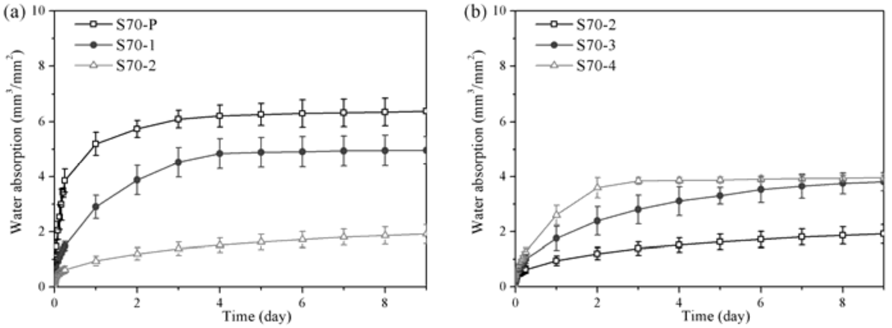

Fig.A.2-5 Absorbed water of S70 series (tested at the age of 12 months) in relation to (a) aggregate volume fraction and (b) aggregate size.

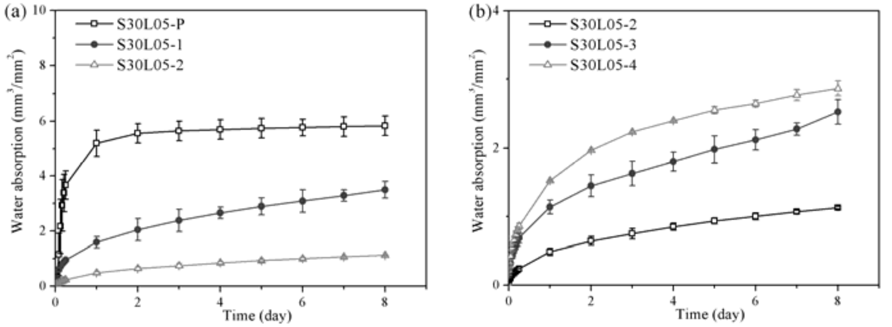

Fig.A.2-6 Absorbed water of S30L05 series (tested at the age of 12 months) in relation to (a) aggregate volume fraction and (b) aggregate size.

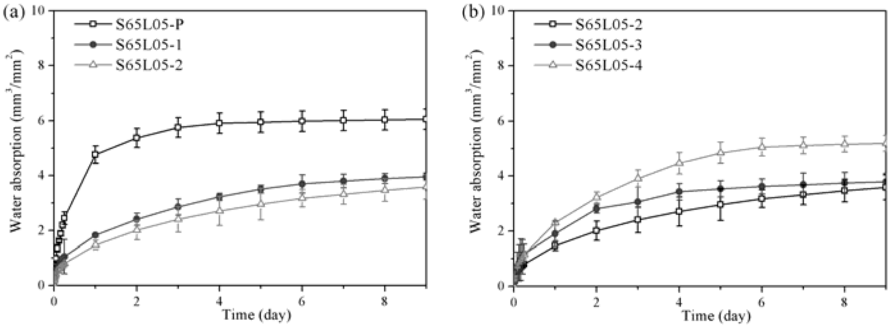

Fig.A.2-7 Absorbed water of S65L05 series (tested at the age of 12 months) in relation to (a) aggregate volume fraction and (b) aggregate size.

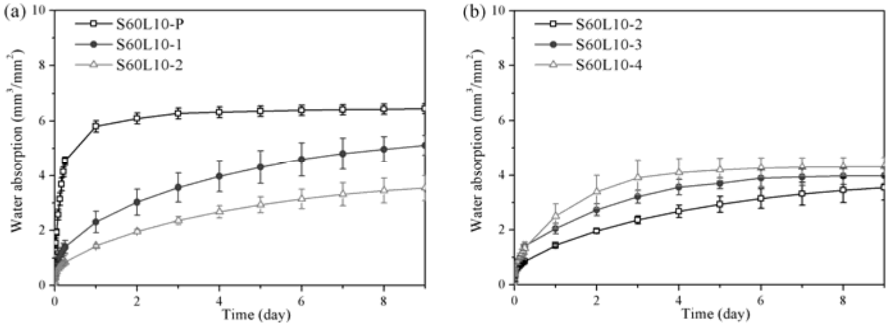

Fig.A.2-8 Absorbed water of S60L10 series (tested at the age of 12 months) in relation to (a) aggregate volume fraction and (b) aggregate size.

A.3 Water soluble chloride penetration profiles

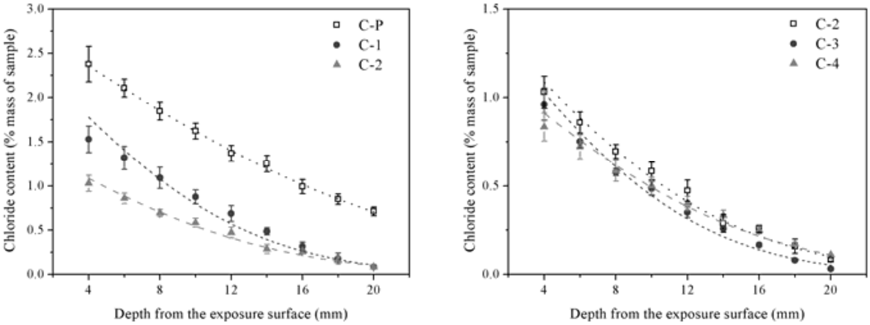

Fig.A.3-1 Water soluble chloride penetration profiles for C in relation to (left) aggregate volume fraction and (right) the average aggregate size.

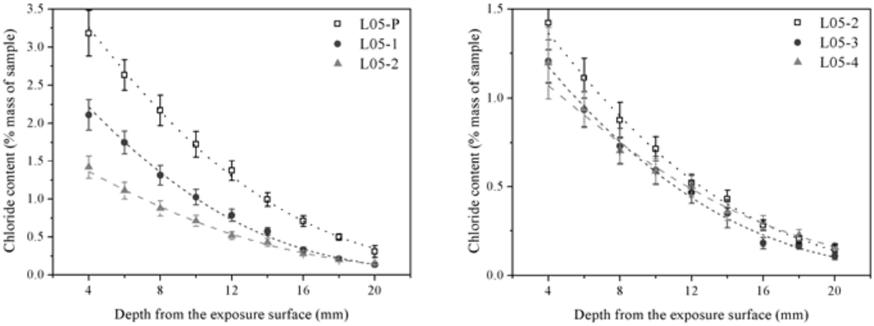

Fig.A.3-2 Water soluble chloride penetration profiles for L05 in relation to (left) aggregate volume fraction and (right) the average aggregate size.

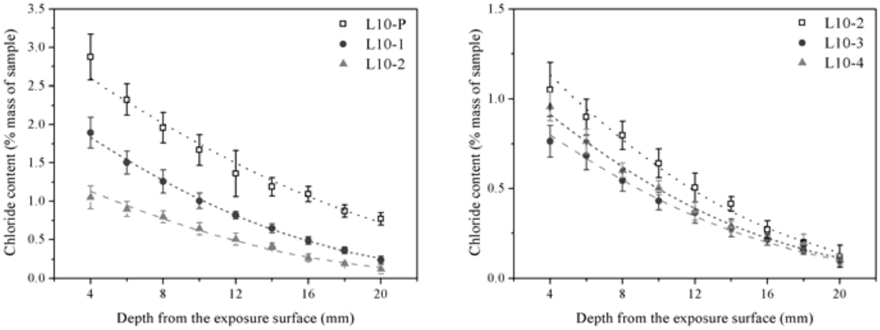

Fig.A.3-3 Water soluble chloride penetration profiles for L10 in relation to (left) aggregate volume fraction and (right) the average aggregate size.

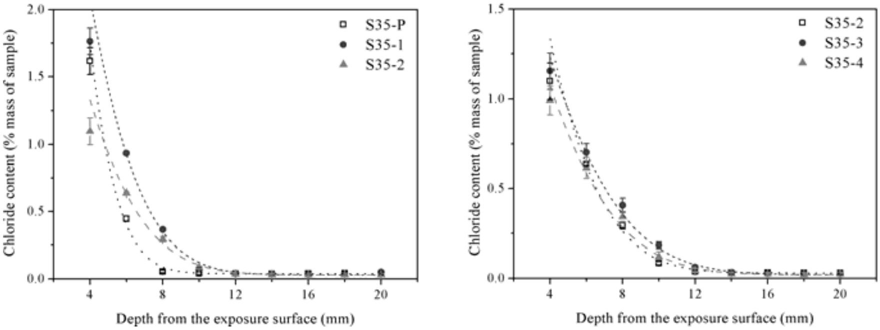

Fig.A.3-4 Water soluble chloride penetration profiles for S35 in relation to (left) aggregate volume fraction and (right) the average aggregate size.

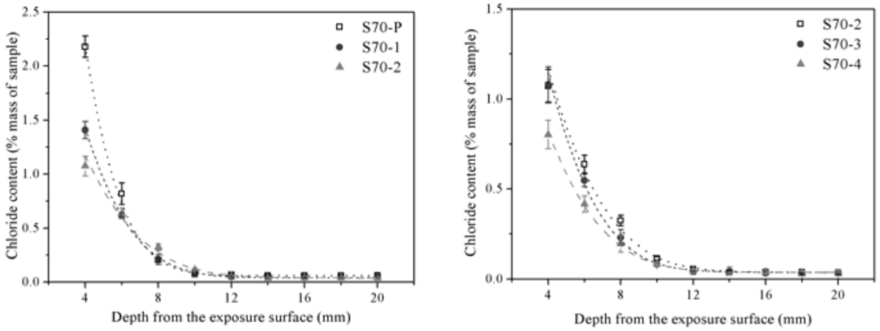

Fig.A.3-5 Water soluble chloride penetration profiles for S70 in relation to (left) aggregate volume fraction and (right) the average aggregate size.

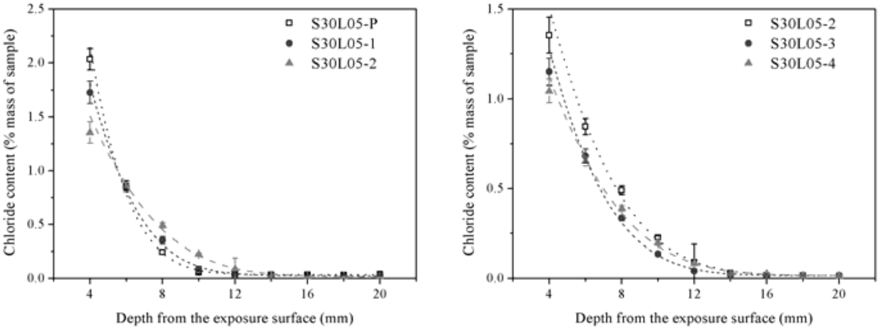

Fig.A.3-6 Water soluble chloride penetration profiles for S30L05 in relation to (left) aggregate volume fraction and (right) the average aggregate size.

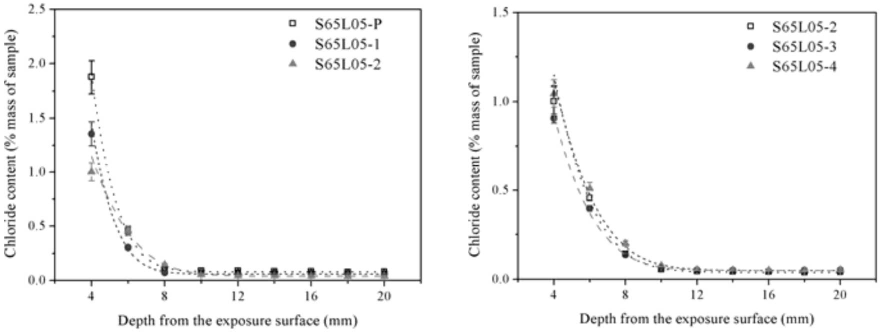

Fig.A.3-7 Water soluble chloride penetration profiles for S65L05 in relation to (left) aggregate volume fraction and (right) the average aggregate size.

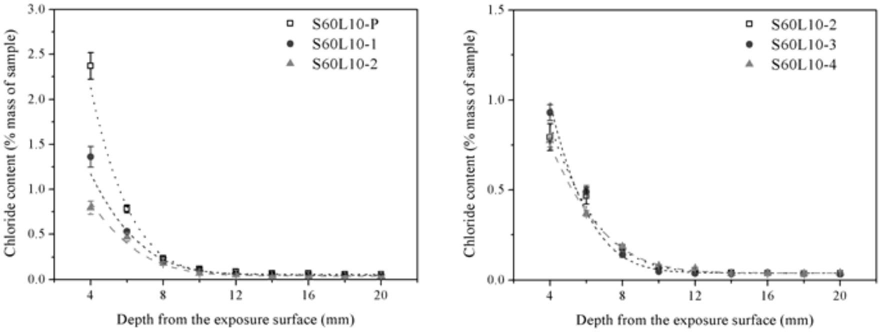

Fig.A.3-8 Water soluble chloride penetration profiles for S60L10 in relation to (left) aggregate volume fraction and (right) the average aggregate size.

A.4 Acid soluble chloride penetration profiles

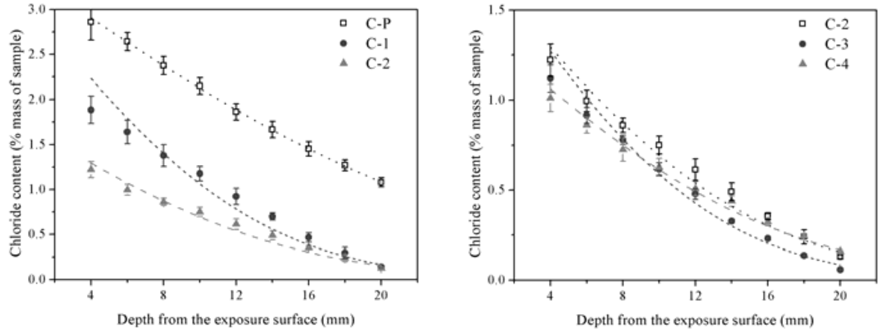

Fig.A.4-1 Acid soluble chloride penetration profiles for C in relation to (left) aggregate volume fraction and (right) the average aggregate size.

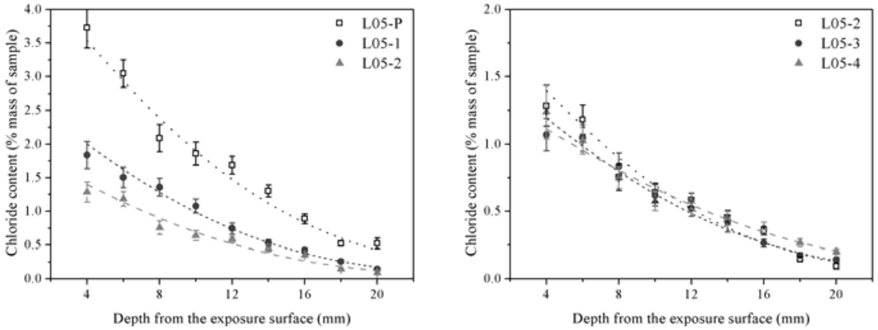

Fig.A.4-2 Acid soluble chloride penetration profiles for L05 in relation to (left) aggregate volume fraction and (right) the average aggregate size.

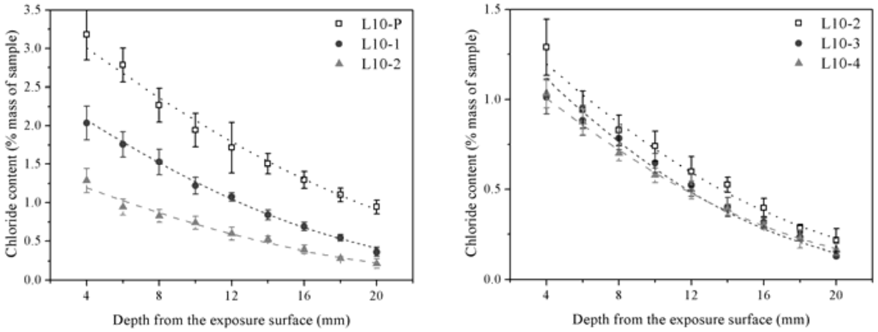

Fig.A.4-3 Acid soluble chloride penetration profiles for L10 in relation to (left) aggregate volume fraction and (right) the average aggregate size.

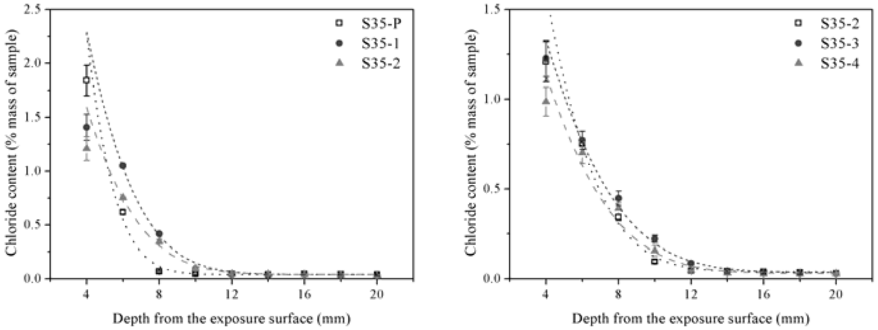

Fig.A.4-4 Acid soluble chloride penetration profiles for S35 in relation to (left) aggregate volume fraction and (right) the average aggregate size.

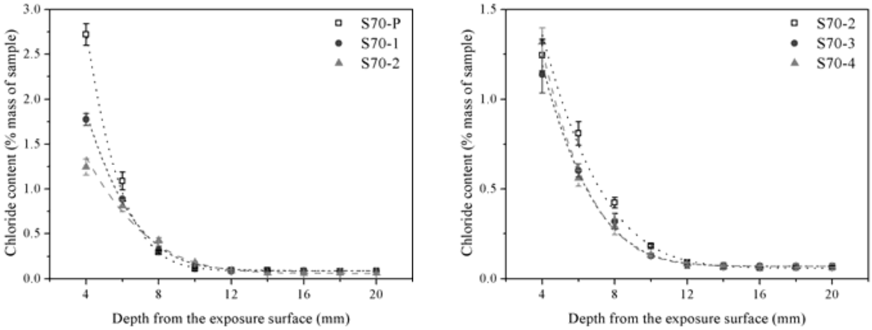

Fig.A.4-5 Acid soluble chloride penetration profiles for S70 in relation to (left) aggregate volume fraction and (right) the average aggregate size.

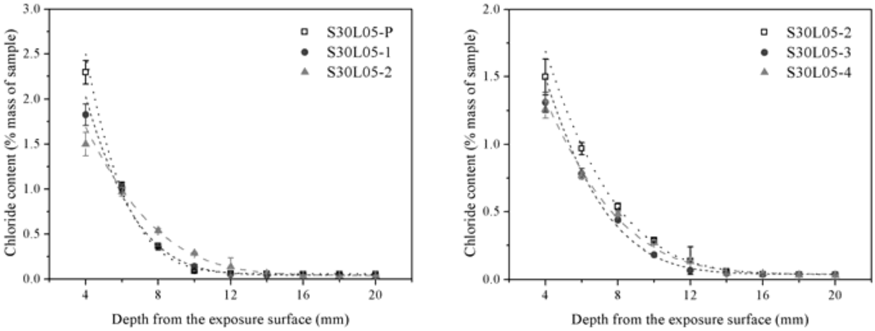

Fig.A.4-6 Acid soluble chloride penetration profiles for S30L05 in relation to (left) aggregate volume fraction and (right) the average aggregate size.

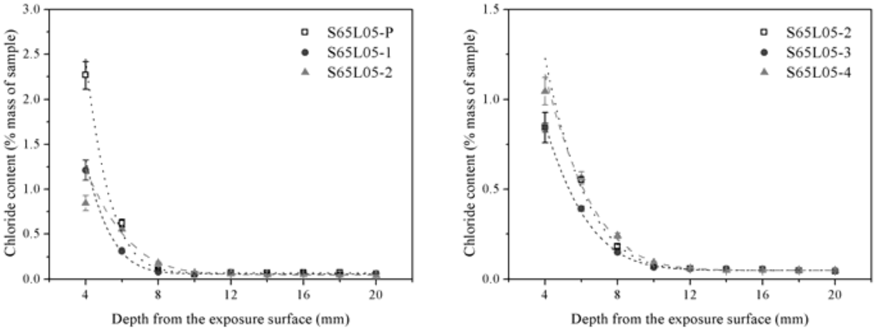

Fig.A.4-7 Acid soluble chloride penetration profiles for S65L05 in relation to (left) aggregate volume fraction and (right) the average aggregate size.

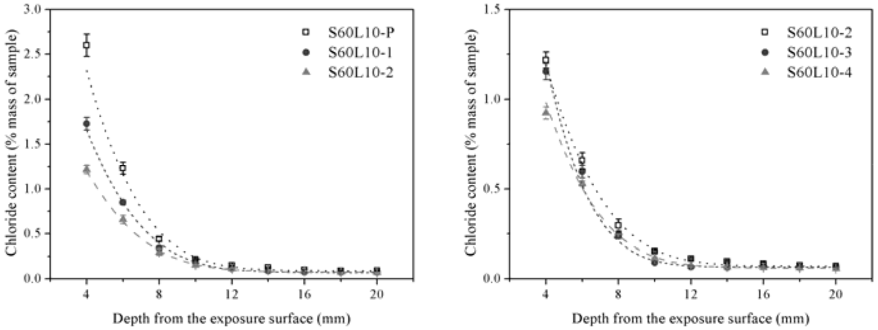

Fig.A.4-8 Acid soluble chloride penetration profiles for S60L10 in relation to (left) aggregate volume fraction and (right) the average aggregate size.

A.5 Chloride binding relationships and fitted Freundlich isotherm

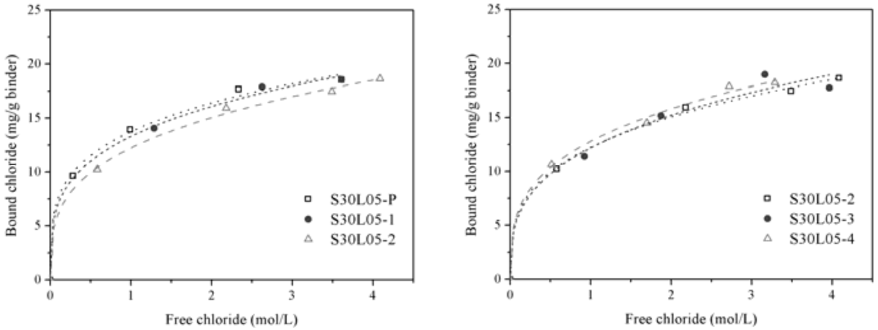

Fig.A.5-1 Freundlich isotherm with experimental data for S30L05 in relation to (left) aggregate volume fraction and (right) the average aggregate size.

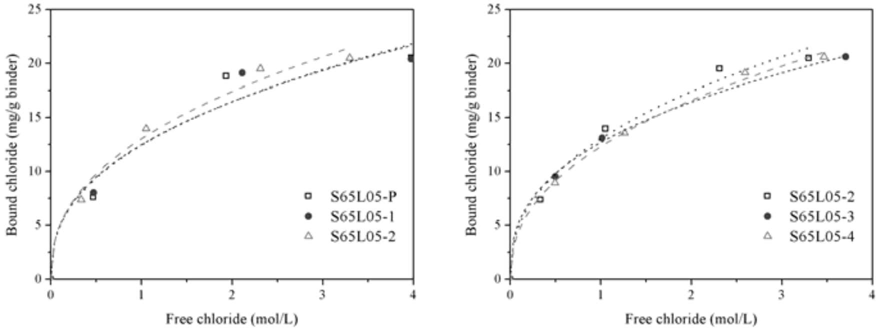

Fig.A.5-2 Freundlich isotherm with experimental data for S65L05 in relation to (left) aggregate volume fraction and (right) the average aggregate size.

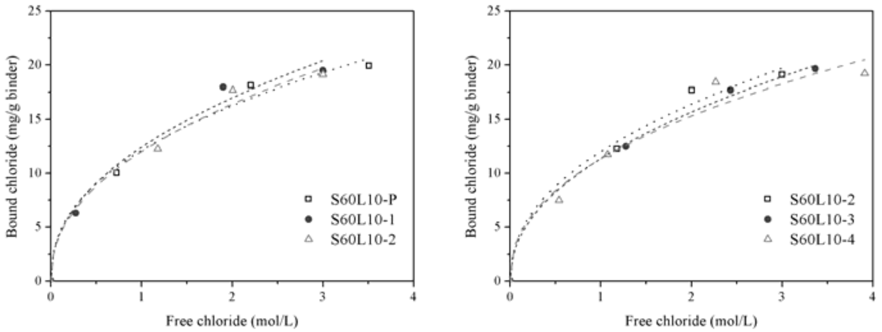

Fig.A.5-3 Freundlich isotherm with experimental data for S60L10 in relation to (left) aggregate volume fraction and (right) the average aggregate size.

References

[1] Mehta PK, Monteiro PJM. Microstructure and Properties of Hardened Concrete. 2006;3rd edition.

[2] Alexander MG, Magee BJ. Durability performance of concrete containing condensed silica fume. Cement Concrete Res. 1999;29(6):917-22.

[3] Sabir BB, Wild S, Bai J. Metakaolin and calcined clays as pozzolans for concrete: a review. Cement Concrete Comp. 2001;23(6):441-54.

[4] Glasser FP, Marchand J, Samson E. Durability of concrete - Degradation phenomena involving detrimental chemical reactions. Cement Concrete Res. 2008;38(2):226-46.

[5] Scrivener KL, Crumbie AK, Laugesen P. The interfacial transition zone (ITZ) between cement paste and aggregate in concrete. Interface Sci. 2004;12(4):411-21.

[6] Ollivier JP, Maso JC, Bourdette B. Interfacial Transition Zone in Concrete. Adv Cem Based Mater. 1995;2(1):30-8.

[7] Breton D, Carlesgibergues A, Ballivy G, Grandet J. Contribution to the Formation Mechanism of the Transition Zone between Rock-Cement Paste. Cement Concrete Res. 1993;23(2):335-46.

[8] Bonen D. Calcium Hydroxide Deposition in the near Interfacial Zone in Plain Concrete. J Am Ceram Soc. 1994;77(1):193-6.

[9] Nemati KM. Mechanical behavior and percolation of pore space in the interfacial transition zone of concrete. Proceedings of 2nd International Conference on Concrete and Development, 1984.

[10] Scrivener KL, Nemati KM. The percolation of pore space in the cement paste aggregate interfacial zone of concrete. Cement Concrete Res. 1996;26(1):35-40.

[11] Barnes B, Diamond S, Dolch W. The contact zone between Portland cement paste and glass “aggregate” surfaces. Cement Concrete Res. 1978;8(2):233-43.

[12] Barnes B, Diamond S, Dolch W. Micromorphology of the interfacial zone around aggregates in Portland cement mortar. J Am Ceram Soc. 1979;62(1-2):21-4.

[13] Diamond S. Cement paste microstructure in concrete. Microstructural development during hydration of cement Mater Res Soc Symp Proc: Cambridge Univ Press; 1987. pp. 21-3.

[14] Zimbelmann R. A Contribution to the Problem of Cement-Aggregate Bond. Cement Concrete Res. 1985;15(5):801-8.

[15] Larbi J. The Cement Paste-Aggregate lnteriacial Zone in Concrete. Delft, The Netherlands: TU Delft; 1991.

[16] Crumbie AK. Characterization of the microstructure of concrete. London: University of London; 1994.

[17] Richardson IG. The nature of C-S-H in hardened cements. Cement Concrete Res. 1999;29(8):1131-47.

[18] Richardson IG. The calcium silicate hydrates. Cement Concrete Res. 2008;38(2):137-58.

[19] ASTM 469. Standard test method for static modulus of elasticity and Poisson's ratio of concrete in compression. 2001.

[20] Taylor HFW. Cement chemistry. Thomas Telford Publishing. 1997;2nd edition.

[21] Scrivener KL, Bentur A, Pratt PL. Quantitative characterisation of the transition zone in high strength concretes[J]. Advanced Cement Res, 1988, (1):230-238.

[22] Scrivener KL, Gartner EM. Microstructure gradients in cement paste and aggregate particles in bonding in cementitious composites[J]. Pro Mat Res Sco Symp, 1988, (114):77-87.

[23] Shane JD, Mason TO, Jennings HM, Garboczi EJ, Bentz DP. Effect of the interfacial transition zone on the conductivity of portland cement mortars. J Am Ceram Soc. 2000;83(5):1137-44.

[24] Yang CC. Effect of the percolated interfacial transition zone on the chloride migration coefficient of cement-based materials. Mater Chem Phys. 2005;91(2-3):538-44.

[25] Leemann A, Loser R, Munch B. Influence of cement type on ITZ porosity and chloride resistance of self-compacting concrete. Cement Concrete Comp. 2010;32(2):116-20.

[26] Khokhrin N. The durability of lightweight concrete structural members. Kuibyshev, USSR. 1973;4:40-53.

[27] Bentur A, Cohen MD. Effect of condensed silica fume on the microstructure of the interfacial zone in Portland cement mortars. J Am Ceram Soc. 1987;70(10):738-43.

[28] Winslow DN, Cohen MD, Bentz DP, Snyder KA, Garboczi EJ. Percolation and Pore Structure in Mortars and Concrete. Cement Concrete Res. 1994;24(1):25-37.

[29] Mehta PK, Monteiro PJM. Concrete, Structure, Properties and Materials: Prentice-Hall, Englewood Cliffs, N.J.; 1993.

[30] Zampini D, Jennings HM, Shah SP. Characterization of the Paste-Aggregate Interfacial Transition Zone Surface-Roughness and Its Relationship to the

Fracture-Toughness of Concrete. J Mater Sci. 1995;30(12):3149-54.

[31] Hadley DW. The Nature of the Paste-aggregate Interface: Interim Report. Purdue University; 1972.

[32] Grandet J, Ollivier JP. Etude de la formation du monocarboaluminate de calcium hydrate au contact d'un granulat calcaire dans une pate de ciment portland[J]. Cement Concrete Res, 1980, 10(6):759-770.

[33] Yuan CZ, Odler I. The interfacial zone between marble and tricalcium silicate paste. Cement Concrete Res. 1987;17(5):784-92.

[34] Gao Y, De Schutter G, Ye G, Huang HL, Tan ZJ, Wu K. Porosity characterization of ITZ in cementitious composites: Concentric expansion and overflow criterion. Constr Build Mater. 2013;38:1051-7.

[35] Wong HS, Buenfeld NR. Euclidean Distance Mapping for computing microstructural gradients at interfaces in composite materials. Cement Concrete Res. 2006;36(6):1091-7.

[36] Ke Y, Ortola S, Beaucour AL, Dumontet H. Identification of microstructural characteristics in lightweight aggregate concretes by micromechanical modelling including the interfacial transition zone (ITZ). Cement Concrete Res. 2010;40(11):1590-600.

[37] Elsharief A, Cohen MD, Olek J. Influence of aggregate size, water cement ratio and age on the microstructure of the interfacial transition zone. Cement Concrete Res. 2003;33(11):1837-49.

[38] Diamond S, Huang JD. The ITZ in concrete - a different view based on image analysis and SEM observations. Cement Concrete Comp. 2001;23(2-3):179-88.

[39] Brough AR, Atkinson A. Automated identification of the aggregate-paste interfacial transition zone in mortars of silica sand with Portland or alkali-activated slag cement paste. Cement Concrete Res. 2000;30(6):849-54.

[40] Bourdette B, Ringot E, Ollivier JP. Modeling of the Transition Zone Porosity. Cement Concrete Res. 1995;25(4):741-51.

[41] Care S, Derkx F. Determination of relevant parameters influencing gas permeability of mortars. Constr Build Mater. 2011;25(3):1248-56.

[42] Panesar DK, Francis J. Influence of limestone and slag on the pore structure of cement paste based on Mercury intrusion porosimetry and water vapour sorption measurements. Constr Build Mater. 2014;52:7.

[43] Hamami AA, Turcry P, Ait-Mokhtar A. Influence of mix proportions on microstructure and gas permeability of cement pastes and mortars. Cement Concrete Res.

2012;42(2):490-8.

[44] Duan P, Shui ZH, Chen W, Shen CH. Effects of metakaolin, silica fume and slag on pore structure, interfacial transition zone and compressive strength of concrete. Constr Build Mater. 2013;44:1-6.

[45] Li WG, Xiao JZ, Sun ZH, Kawashima S, Shah SP. Interfacial transition zones in recycled aggregate concrete with different mixing approaches. Constr Build Mater. 2012;35:1045-55.

[46] Mitsui K, Li ZJ, Lange DA, Shah SP. Relationship between Microstructure and Mechanical-Properties of the Paste-Aggregate Interface. ACI Mater J. 1994;91(1):30-9.

[47] Rao GA, Prasad BKR. Influence of the roughness of aggregate surface on the interface bond strength. Cement Concrete Res. 2002;32(2):253-7.

[48] Cohen MD, Goldman A, Chen WF. The Role of Silica Fume in Mortar - Transition Zone Versus Bulk Paste Modification. Cement Concrete Res. 1994;24(1):95-8.

[49] Ramesh G, Sotelino ED, Chen WF. Effect of transition zone on elastic moduli of concrete materials. Cement Concrete Res. 1996;26(4):611-22.

[50] Jiang LH. The interfacial zone and bond strength between aggregates and cement pastes incorporating high volumes of fly ash. Cement Concrete Comp. 1999;21(4):313-6.

[51] Wong YL, Lam L, Poon CS, Zhou FP. Properties of fly ash-modified cement mortar-aggregate interfaces. Cement Concrete Res. 1999;29(12):1905-13.

[52] Kuroda M, Watanabe T, Terashi N. Increase of bond strength at interfacial transition zone by the use of fly ash. Cement Concrete Res. 2000;30(2):253-8.

[53] Chan YW, Chu SH. Effect of silica fume on steel fiber bond characteristics in reactive powder concrete. Cement Concrete Res. 2004;34(7):1167-72.

[54] Poon CS, Shui ZH, Lam L. Effect of microstructure of ITZ on compressive strength of concrete prepared with recycled aggregates. Constr Build Mater. 2004;18(6):461-8.

[55] Zhang JX, Sun HH, Wan JH, Yi ZL. Study on microstructure and mechanical property of interfacial transition zone between limestone aggregate and Sialite paste. Constr Build Mater. 2009;23(11):3393-7.

[56] Herve E, Care S, Seguin JP. Influence of the porosity gradient in cement paste matrix on the mechanical behavior of mortar. Cement Concrete Res. 2010;40(7):1060-71.

[57] Akcaoglu T, Tokyay M, Celik T. Effect of coarse aggregate size and matrix quality on ITZ and failure behavior of concrete under uniaxial compression. Cement Concrete Comp. 2004;26(6):633-8.

[58] Akcaoglu R, Tokyay M, Celik T. Assessing the ITZ microcracking via scanning

electron microscope and its effect on the failure behavior of concrete. Cement Concrete Res. 2005;35(2):358-63.

[59] Lee T-FF, Cohen MD, Chen W, Zhang Y. Strength and durability of concrete: effects of cement paste-aggregate interfaces, Part II: significance of transition zones on physical and mechanical properties of portland cement mortar, Purdue University: 1998.

[60] Prokopski G, Langier B. Effect of water/cement ratio and silica fume addition on the fracture toughness and morphology of fractured surfaces of gravel concretes. Cement Concrete Res. 2000;30(9):1427-33.

[61] Tasong WA, Lynsdale CJ, Cripps JC. Aggregate-cement paste interface Part I. Influence of aggregate geochemistry. Cement Concrete Res. 1999;29(7):1019-25.

[62] Xie P, Beaudoin JJ. Effects of transition zone microstructure on bond strength of aggregate-portland cement paste interfaces. Cement Concrete Res. 1992;22(1):23-6.

[63] Ozturan T, Cecen C. Effect of coarse aggregate type on mechanical properties of concretes with different strengths. Cement Concrete Res. 1997;27(2):165-70.

[64] Wang XH, Jacobsen S, Lee SF, He JY, Zhang ZL. Effect of silica fume, steel fiber and ITZ on the strength and fracture behavior of mortar. Mater Struct. 2010;43(1-2):125-39.

[65] Asbridge AH, Page CL, Page MM. Effects of metakaolin, water/binder ratio and interfacial transition zones on the microhardness of cement mortars. Cement Concrete Res. 2002;32(9):1365-9.

[66] Wei S, Mandel JA, Said S. Study of the Interface Strength in Steel Fiber-Reinforced Cement-Based Composites. J Am Concrete I. 1986;83(4):597-605.

[67] Igarashi S, Bentur A, Mindess S. Microhardness testing of cementitious materials. Adv Cem Based Mater. 1996;4(2):48-57.

[68] Constantinides G, Ulm F, Van Vliet K. On the use of nanoindentation for cementitious materials. Mater Struct. 2003;36(257):191-6.

[69] Zhu W, Sonebi M, Bartos PJM. Bond and interfacial properties of reinforcement in self-compacting concrete. Mater Struct. 2004;37(271):442-8.

[70] Saito M, Kawamura M. Resistance of the Cement-Aggregate Interfacial Zone to the Propagation of Cracks. Cement Concrete Res. 1986;16(5):653-61.

[71] Delagrave A, Bigas JP, Ollivier JP, Marchand J, Pigeon M. Influence of the interfacial zone on the chloride diffusivity of mortars. Adv Cem Based Mater. 1997;5(3-4):86-92.

[72] Ballivy G. In relationship between ITZ transport properties and durability of

cementitious composites, RILEM report 20: Engineering and transport properties of the interfacial transition zone in cementitious composites, 1999, pp 337-345.

[73] Halamickova P, Detwiler RJ, Bentz DP, Garboczi EJ. Water Permeability and Chloride-Ion Diffusion in Portland-Cement Mortars - Relationship to Sand Content and Critical Pore Diameter. Cement Concrete Res. 1995;25(4):790-802.

[74] Rangaraju PR, Olek J, Diamond S. An investigation into the influence of inter-aggregate spacing and the extent of the ITZ on properties of Portland cement concretes. Cement Concrete Res. 2010;40(11):1601-8.

[75] Shane JD, Mason TO, Jennings HM. Conductivity and microstructure of the interfacial transition zone measured by impedance spectroscopy[R]. RILEM publicatioins report 20: Engineering and transport properties of the interfacial transition zone in cementitious materials, 1999, pp 173-203.

[76] Ping X, Beaudoin JJ, Brousseau R. Flat-aggregate portland-cement paste interfaces .2. Transition zone formation. Cement Concrete Res. 1991;21(5):718-26.

[77] Ping X, Beaudoin JJ, Brousseau R. Flat-aggregate portland-cement paste interfaces .1. Electrical-conductivity models. Cement Concrete Res. 1991;21(4):515-22.

[78] Yang CC, Cho SW. Approximate migration coefficient of percolated interfacial transition zone by using the accelerated chloride migration test. Cement Concrete Res. 2005;35(2):344-50.

[79] Breton D, Ollivier J P, Ballivy G, Maso. Interfaces in Cementitious Composites, RILEM International Conference, Toulouse. 1992.

[80] Yang CC, Su JK. Approximate migration coefficient of interfacial transition zone and the effect of aggregate content on the migration coefficient of mortar. Cement Concrete Res. 2002;32(10):1559-65.

[81] Hornain H, Marchand J, Dohot V, Moranvilleregourd M. Diffusion of Chloride-Ions in Limestone Filler Blended Cement Pastes and Mortars. Cement Concrete Res. 1995;25(8):1667-78.

[82] Buenfeld NR, Okundi E. Effect of cement content on transport in concrete. Mag Concrete Res. 1998;50(4):339-51.

[83] Ye G. Percolation of capillary pores in hardening cement pastes. Cement Concrete Res. 2005;35(1):167-76.

[84] Bentz DP, Hwang JTG, Hagwood C, Garboczi EJ, Snyder KA, Buenfeld N, et al. Interfacial zone percolation in concrete: Effects of interfacial zone thickness and aggregate shape. Microstructure of Cement-Based Systems/Bonding and Interfaces in

Cementitious Materials, 1995:437-442.

[85] Bonneau O, Vernet C, Moranville M, Aitcin PC. Characterization of the granular packing and percolation threshold of reactive powder concrete. Cement Concrete Res. 2000;30(12):1861-7.

[86] Sun GW, Sun W, Zhang YS, Liu ZY. Quantitative analysis and affecting factors of the overlapping degree of interfacial transition zone between neighboring aggregates in concrete. J Wuhan Univ Technol. 2011;26(1):147-53.

[87] Garboczi EJ, Schwartz LM, Bentz DP. Modeling the influence of the interfacial zone on the DC electrical-conductivity of mortar. Adv Cem Based Mater. 1995;2(5):169-81.

[88] Zheng JJ, Wong HS, Buenfeld NR. Assessing the influence of ITZ on the steady-state chloride diffusivity of concrete using a numerical model. Cement Concrete Res. 2009;39(9):805-13.

[89] Wong HS, Zobel M, Buenfeld NR, Zimmerman RW. Influence of the interfacial transition zone and microcracking on the diffusivity, permeability and sorptivity of cement-based materials after drying. Mag Concrete Res. 2009;61(8):571-89.

[90] Garboczi EJ, Bentz DP. Digital-simulation of the aggregate-cement paste interfacial zone in concrete. J Mater Res. 1991;6(1):196-201.

[91] Garboczi EJ. Computational materials science of cement-based materials. Mater Struct. 1993;26(158):191-5.

[92] Garboczi EJ, Bentz DP. Modelling of the microstructure and transport properties of concrete. Constr Build Mater. 1996;10(5):293-300.

[93] Garboczi EJ, Bentz DP. Analytical formulas for interfacial transition zone properties. Adv Cem Based Mater. 1997;6(3-4):99-108.

[94] Garboczi EJ, Bentz DP. Multiscale analytical/numerical theory of the diffusivity of concrete. Adv Cem Based Mater. 1998;8(2):77-88.

[95] Asbridge AH, Chadbourn GA, Page CL. Effects of metakaolin and the interfacial transition zone on the diffusion of chloride ions through cement mortars. Cement Concrete Res. 2001;31(11):1567-72.

[96] Sun GW, Zhang YS, Sun W, Liu ZY, Wang CH. Multi-scale prediction of the effective chloride diffusion coefficient of concrete. Constr Build Mater. 2011;25(10):3820-31.

[97] Watson AJ, Oyeka CC. Oil Permeability of hardened cement pastes and concrete. Mag Concrete Res. 1981;33(115):85-95.

[98] Nyame BK. Permeability of normal and lightweight mortars. Mag Concrete Res.

1985;37(130):44-8.

[99] Princigallo A, Lura P, van Breugel K, Levita G. Early development of properties in a cement paste: A numerical and experimental study. Cement Concrete Res. 2003;33(7):1013-20.

[100] Care S. Influence of aggregates on chloride diffusion coefficient into mortar. Cement Concrete Res. 2003;33(7):1021-8.

[101] Basheer L, Basheer PAM, Long AE. Influence of coarse aggregate on the permeation, durability and the microstructure characteristics of ordinary Portland cement concrete. Constr Build Mater. 2005;19(9):682-90.

[102] Castro J, Bentz D, Weiss J. Effect of sample conditioning on the water absorption of concrete. Cement Concrete Comp. 2011;33(8):805-13.

[103] Yang S, Xu ZZ, Tang MS. The process of sulfate attack on cement mortars. Adv Cem Based Mater. 1996;4(1):1-5.

[104] Irassar EF, Bonavetti VL, Gonzalez M. Microstructural study of sulfate attack on ordinary and limestone Portland cements at ambient temperature. Cement Concrete Res. 2003;33(1):31-41.

[105] Bonen D, Sarkar SL. Replacement of portlandite by gypsum in the interfacial zone and cracking related to crystalization pressure. Ceram Trans. 1993;37:49-59.

[106] El-Hachem R, Roziere E, Grondin F, Loukili A. Multi-criteria analysis of the mechanism of degradation of Portland cement based mortars exposed to external sulphate attack. Cement Concrete Res. 2012;42(10):1327-35.

[107] Leemann A, Munch B, Gasser P, Holzer L. Influence of compaction on the interfacial transition zone and the permeability of concrete. Cement Concrete Res. 2006;36(8):1425-33.

[108] Zhang MH, Lastra R, Malhotra VM. Rice-husk ash paste and concrete: Some aspects of hydration and the microstructure of the interfacial zone between the aggregate and paste. Cement Concrete Res. 1996;26(6):963-77.

[109] Vivekanandam K, Patnaikuni I. Transition zone in high performance concrete during hydration. Cement Concrete Res. 1997;27(6):817-23.

[110] Rossignolo JA. Interfacial interactions in concretes with silica fume and SBR latex. Constr Build Mater. 2009;23(2):817-21.

[111] Kong DY, Lei T, Zheng JJ, Ma CC, Jiang J, Jiang J. Effect and mechanism of surface-coating pozzalanics materials around aggregate on properties and ITZ microstructure of recycled aggregate concrete. Constr Build Mater. 2010;24(5):701-8.

[112] Tuan NV, Ye G, van Breugel K, Copuroglu O. Hydration and microstructure of ultra high performance concrete incorporating rice husk ash. Cement Concrete Res. 2011;41(11):1104-11.

[113] Xie P, Beaudoin JJ. Modification of transition zone microstructure - silica fume coating of aggregate surfaces. Cement Concrete Res. 1992;22(4):597-604.

[114] Xuan DX, Shui ZH, Wu SP. Influence of silica fume on the interfacial bond between aggregate and matrix in near-surface layer of concrete. Constr Build Mater. 2009;23(7):2631-5.

[115] Bui DD, Hu J, Stroeven P. Particle size effect on the strength of rice husk ash blended gap-graded Portland cement concrete. Cement Concrete Comp. 2005;27(3):357-66.

[116] Gutteridge WA, Dalziel JA. Filler cement - the effect of the secondary component on the hydration of portland-cement .1. A fine nonhydraulic filler. Cement Concrete Res. 1990;20(5):778-82.

[117] Bonavetti V, Donza H, Menendez G, Cabrera O, Irassar EF. Limestone filler cement in low w/c concrete: A rational use of energy. Cement Concrete Res. 2003;33(6):865-71.

[118] Allahverdi A, Salem S. Simultaneous Influences of microsilica and limestone powder on properties of Portland cement paste. Ceram-Silikaty. 2010;54(1):65-71.

[119] Kadri EH, Aggoun S, De Schutter G, Ezziane K. Combined effect of chemical nature and fineness of mineral powders on Portland cement hydration. Mater Struct. 2010;43(5):665-73.

[120] Siddique R, Bennacer R. Use of iron and steel industry by-product (GGBS) in cement paste and mortar. Resour Conserv Recy. 2012;69:29-34.

[121] Van den Heede P, De Belie N. Environmental impact and life cycle assessment (LCA) of traditional and 'green' concretes: Literature review and theoretical calculations. Cement Concrete Comp. 2012;34(4):431-42.

[122] Li Y, Bao JL, Guo YL. The relationship between autogenous shrinkage and pore structure of cement paste with mineral admixtures. Constr Build Mater. 2010;24(10):1855-60.

[123] Moon HY, Kim HS, Choi DS. Relationship between average pore diameter and chloride diffusivity in various concretes. Constr Build Mater. 2006;20(9):725-32.

[124] Li K, Zeng Q, Luo M, Pang X. Effect of self-desiccation on the pore structure of paste and mortar incorporating 70% GGBS. Constr Build Mater. 2014;51:9.

[125] Hadjsadok A, Kenai S, Courard L, Michel F, Michelc J. Durability of mortar and

concretes containing slag with low hydraulic activity. Cement Concrete Comp. 2012;34(5):671-7.

[126] Gruyaert E, Van den Heede P, Maes M, De Belie N. Investigation of the influence of blast-furnace slag on the resistance of concrete against organic acid or sulphate attack by means of accelerated degradation tests. Cement Concrete Res. 2012;42(1):173-85.

[127] Vejmelkova E, Pavlikova M, Kersner Z, Rovnanikova P, Ondracek M, Sedlmajer M, et al. High performance concrete containing lower slag amount: A complex view of mechanical and durability properties. Constr Build Mater. 2009;23(6):2237-45.

[128] Bleszynski R, Hooton RD, Thomas MDA, Rogers CA. Durability of ternary blend concrete with silica fume and blast-furnace slag: Laboratory and outdoor exposure site studies. ACI Mater J. 2002;99(5):499-508.

[129] Sakai E, Sugita J. Composite mechanism of polymer-modified cement. Cement Concrete Res. 1995;25(1):127-35.

[130] Ollitrault-Fichet R, Gauthier C, Clamen G, Boch P. Microstructural aspects in a polymer-modified cement. Cement Concrete Res. 1998;28(12):1687-93.

[131] De Schutter G. Hydration, Microstructure and durability of self-compacting concrete. Rilem Proc. 2008;61:15-24.

[132] De Schutter G, Committee RT. Final report of RILEM TC 205-DSC: durability of self-compacting concrete. Mater Struct. 2008;41(2):225-33.

[133] Bentz DP, Stutzman PE, Garboczi EJ. Experimental and simulation studies of the interfacial zone in concrete. Cement Concrete Res. 1992;22(5):891-902.

[134] Liao KY, Chang PK, Peng YN, Yang CC. A study on characteristics of interfacial transition zone in concrete. Cement Concrete Res. 2004;34(6):977-89.

[135] Princigallo A, van Breugel K, Levita G. Influence of the aggregate on the electrical conductivity of Portland cement concretes. Cement Concrete Res. 2003;33(11):1755-63.

[136] Garboczi EJ, Bentz D. Microstructure of Portland cement-based materials: Computer simulation and percolation theory. Computational and mathematical models of microstructural evolution, Materials Research Society Syposium Proceedings. April 13-17 ed. San Francisco1998. p. 12.

[137] Van den Heede P, Gruyaert E, De Belie N. Transport properties of high-volume fly ash concrete: Capillary water sorption, water sorption under vacuum and gas permeability. Cement Concrete Comp. 2010;32(10):749-56.

[138] RILEM TC 116-PCD. Permeability of concrete as a criterion of its durability. Mater Struct, 1999.

[139] Gruyaert E. Effect of blast-furnace slag as cement replacement on hydration, microstructure, strength and durability of concrete. Ghent: Ghent University; 2011.

[140] ASTM C 1585. Standard test method for measurement of rate of absorption of water by hydraulic-cement concretes. 2004.

[141] Hall C. Water sorptivity of mortars and concretes-a review. Mag Concrete Res. 1989;41(147):51-61.

[142] Martys NS, Ferraris CF. Capillary transport in mortars and concrete. Cement Concrete Res. 1997;27(5):747-60.

[143] NT Build 492. Concrete, mortar and cement-based repair materials: chloride migration coefficient from non-steady-state migration experiments[S]. Nordtest method, 1999.

[144] Tang LP. Concentration dependence of diffusion and migration of chloride ions - Part 1. Theoretical considerations. Cement Concrete Res. 1999;29(9):1463-8.

[145] Castellote M, Andrade C, Alonso C. Measurement of the steady and non-steady-state chloride diffusion coefficients in a migration test by means of monitoring the conductivity in the anolyte chamber - Comparison with natural diffusion tests. Cement Concrete Res. 2001;31(10):1411-20.

[146] Spiesz P, Ballari MM, Brouwers HJH. RCM: A new model accounting for the non-linear chloride binding isotherm and the non-equilibrium conditions between the free- and bound-chloride concentrations. Constr Build Mater. 2012;27(1):293-304.

[147] Schmidt T, Lothenbach B, Romer M, Neuenschwander J, Scrivener K. Physical and microstructural aspects of sulfate attack on ordinary and limestone blended Portland cements. Cement Concrete Res. 2009;39(12):1111-21.

[148] Galle C. Effect of drying on cement-based materials pore structure as identified by mercury intrusion porosimetry - A comparative study between oven-, vacuum-, and freeze-drying. Cement Concrete Res. 2001;31(10):1467-77.

[149] Ye G. Experimental Study and Numerical Simulation of the Development of the Microstructure and Permeability of Cementitious Materials. Delft, the Netherlands: Delft University of Technology; 2003.

[150] Lu BL, Torquato S. Nearest-surface distribution-functions for polydispersed particle-systems. Phys Rev A. 1992;45(8):5530-44.

[151] Thomas C. HTT. Mathematical analysis of shrinkage stresses in a model of hardened concrete. ACI Mater J, 1963, 60(3):371-390.

[152] Bisschop J, van Mier JGM. Effect of aggregates on drying shrinkage microcracking

in cement-based composites. Mater Struct. 2002;35(252):453-61.

[153] Sanjuan MA, MunozMartialay R. Oven-drying as a preconditioning method for air permeability test on concrete. Mater Lett. 1996;27(4-5):263-8.

[154] Mclachlan DS, Blaszkiewicz M, Newnham RE. Electrical-Resistivity of Composites. J Am Ceram Soc. 1990;73(8):2187-203.

[155] Gao Y, De Schutter G, Ye G. Micro- and meso-scale pore structure in mortar in relation to aggregate content. Cement Concrete Res. 2013;52:149-60.

[156] Cam HT, Neithalath N. Moisture and ionic transport in concretes containing coarse limestone powder. Cement Concrete Comp. 2010;32(7):486-96.

[157] Akhavan A, Shafaatian SMH, Rajabipour F. Quantifying the effects of crack width, tortuosity, and roughness on water permeability of cracked mortars. Cement Concrete Res. 2012;42(2):313-20.

[158] Wong HS, Pappas AM, Zimmerman RW, Buenfeld NR. Effect of entrained air voids on the microstructure and mass transport properties of concrete. Cement Concrete Res. 2011;41(10):1067-77.

[159] Monteiro PJM. Microstructure of concrete and its influence on the mechanical properties. California: University of California, Berkeley; 1985.

[160] Erdem S, Dawson AR, Thom NH. Influence of the micro- and nanoscale local mechanical properties of the interfacial transition zone on impact behavior of concrete made with different aggregates. Cement Concrete Res. 2012;42(2):447-58.

[161] Bentz DP, Garboczi EJ. Simulation Studies of the Effects of Mineral Admixtures on the Cement Paste-Aggregate Interfacial Zone. ACI Mater J. 1991;88(5):518-29.

[162] Zampini D, Shah SP, Jennings HM. Early age microstructure of the paste-aggregate interface and its evolution. J Mater Res. 1998;13(7):1888-98.

[163] Xu G, Beaudoin JJ, Jolicoeur C, Page M. The effect of a polynaphthalene sulfonate superplasticizer on the contribution of the interfacial transition zone to the electrical resistivity of mortars containing silica and limestone fine aggregate. Cement Concrete Res. 2000;30(5):683-91.

[164] Gao JM, Qian CX, Liu HF, Wang B, Li L. ITZ microstructure of concrete containing GGBS. Cement Concrete Res. 2005;35(7):1299-304.

[165] Siddique R. Utilization of silica fume in concrete: Review of hardened properties. Resour Conserv Recy. 2011;55(11):923-32.

[166] Menendez G, Bonavetti V, Irassar EF. Strength development of ternary blended cement with limestone filler and blast-furnace slag. Cement Concrete Comp.

2003;25(1):61-7.

[167] Oner A, Akyuz S. An experimental study on optimum usage of GGBS for the compressive strength of concrete. Cement Concrete Comp. 2007;29(6):505-14.

[168] De Weerdt K, Ben Haha M, Le Saout G, Kjellsen KO, Justnes H, Lothenbach B. Hydration mechanisms of ternary Portland cements containing limestone powder and fly ash. Cement Concrete Res. 2011;41(3):279-91.

[169] De Weerdt K, Kjellsen KO, Sellevold E, Justnes H. Synergy between fly ash and limestone powder in ternary cements. Cement Concrete Comp. 2011;33(1):30-8.

[170] Mounanga P, Khokhar MIA, El Hachem R, Loukili A. Improvement of the early-age reactivity of fly ash and blast furnace slag cementitious systems using limestone filler. Mater Struct. 2011;44(2):437-53.

[171] Carrasco MF, Menendez G, Bonavetti V, Irassar EF. Strength optimization of "tailor-made cement" with limestone filler and blast furnace slag. Cement Concrete Res. 2005;35(7):1324-31.

[172] Githachuri Ku, Alexander MG. Durability performance potential and strength of blended Portland limestone cement concrete. Cement and Concrete Composites. 2013;39:7.

[173] Camiletti J, Soliman AM, Nehdi ML. Effects of nano- and micro-limestone addition on early-age properties of ultra-high-performance concrete. Mater Struct. 2013;46(6):881-98.

[174] Bouasker M, Mounanga P, Turcry P, Loukili A, Khelidj A. Chemical shrinkage of cement pastes and mortars at very early age: Effect of limestone filler and granular inclusions. Cement Concrete Comp. 2008;30(1):13-22.

[175] Lothenbach B, Le Saout G, Gallucci E, Scrivener K. Influence of limestone on the hydration of Portland cements. Cement Concrete Res. 2008;38(6):848-60.

[176] Bonavetti VL, Rahhal VF, Irasser EF. Studies on the carboaluminate formation in limestone filler-blended cements. Cement Concrete Res. 2001;31(6):853-9.

[177] Tan Z, De Schutter G, Ye G, Gao Y, Machiels L. Influence of particle size on the early hydration of slag particle activated by Ca(OH)2 solution. Constr Build Mater. 2014;52(0):488-93.

[178] Hussin A, Poole C. Petrography evidence of the interfacial transition zone (ITZ) in the normal strength concrete containing granitic and limestone aggregates. Constr Build Mater. 2011;25(5):2298-303.

[179] Head MK, Wong HS, Buenfeld NR. Characterising aggregate surface geometry in

thin-sections of mortar and concrete. Cement Concrete Res. 2008;38(10):1227-31.

[180] Diamond S. Considerations in image analysis as applied to investigations of the ITZ in concrete. Cement Concrete Comp. 2001;23(2-3):171-8.

[181] Wong HS, Head MK, Buenfeld NR. Pore segmentation of cement-based materials from backscattered electron images. Cement Concrete Res. 2006;36(6):1083-90.

[182] Scrivener KL. Backscattered electron imaging of cementitious microstructures: understanding and quantification. Cement Concrete Comp. 2004;26(8):935-45.

[183] Kumar R, Bhattacharjee B. Study on some factors affecting the results in the use of MIP method in concrete research. Cement Concrete Res. 2003;33(3):417-24.

[184] Uysal M, Yilmaz K, Ipek M. The effect of mineral admixtures on mechanical properties, chloride ion permeability and impermeability of self-compacting concrete. Constr Build Mater. 2012;27(1):263-70.

[185] Wu K, De Schutter G, Shi H, Ye G, Gao Y. Influence of the interfacial transition zone on the chloride migration coefficient of portland cement concrete. 1st International Conference on Concrete Sustainability (ICCSH-2013)2013. p. 612-7.

[186] Bentur A, Alexander MG, Comm RT. A review of the work of the RILEM TC 159-ETC: Engineering of the interfacial transition zone in cementitious composites. Mater Struct. 2000;33(226):82-7.

[187] Hall C. Barrier Performance of Concrete - a review of fluid transport-theory. Mater Struct. 1994;27(169):291-306.

[188] Godman A, Bentur A. Bond effects in high-strength silica fume concretes. ACI Mater J. 1989;86(5):440-449.

[189] Pack SW, Jung MS, Song HW, Kim SH, Ann KY. Prediction of time dependent chloride transport in concrete structures exposed to a marine environment. Cement Concrete Res. 2010;40(2):302-12.

[190] Page CL. Degradation of reinforced concrete: Some lessons from research and practice. Mater Corros. 2012;63(12):1052-8.

[191] Page CL. Mechanism of corrosion protection in reinforced concrete marine structure. Nature. 1975;256:12.

[192] Page CL, Sergi G. Developments in cathodic protection applied to reinforced concrete. J Mater Civil Eng. 2000;12(1):8-15.

[193] Angst UM, Hooton RD, Marchand J, Page CL, Flatt RJ, Elsener B, et al. Present and future durability challenges for reinforced concrete structures. Mater Corros. 2012;63(12):1047-51.

[194] Vidal T, Castel A, Francois R. Corrosion process and structural performance of a 17 year old reinforced concrete beam stored in chloride environment. Cement Concrete Res. 2007;37(11):1551-61.

[195] Neithalath N, Jain J. Relating rapid chloride transport parameters of concretes to microstructural features extracted from electrical impedance. Cement Concrete Res. 2010;40(7):1041-51.

[196] Song HW, Lee CH, Ann KY. Factors influencing chloride transport in concrete structures exposed to marine environments. Cement Concrete Comp. 2008;30(2):113-21.

[197] Siegwart M, Lyness JF, McFarland BJ. Change of pore size in concrete due to electrochemical chloride extraction and possible implications for the migration of ions. Cement Concrete Res. 2003;33(8):1211-21.

[198] Zhang MH, Li H. Pore structure and chloride permeability of concrete containing nano-particles for pavement. Constr Build Mater. 2011;25(2):608-16.

[199] Balonis M, Lothenbach B, Le Saout G, Glasser FP. Impact of chloride on the mineralogy of hydrated Portland cement systems. Cement Concrete Res. 2010;40(7):1009-22.

[200] Yuan Q, Shi CJ, De Schutter G, Audenaert K, Deng DH. Chloride binding of cement-based materials subjected to external chloride environment - A review. Constr Build Mater. 2009;23(1):1-13.

[201] Loser R, Lothenbach B, Leemann A, Tuchschmid M. Chloride resistance of concrete and its binding capacity - Comparison between experimental results and thermodynamic modeling. Cement Concrete Comp. 2010;32(1):34-42.

[202] Angst U, Elsener B, Larsen CK, Vennesland O. Critical chloride content in reinforced concrete - A review. Cement Concrete Res. 2009;39(12):1122-38.

[203] Martin-Perez B, Zibara H, Hooton RD, Thomas MDA. A study of the effect of chloride binding on service life predictions. Cement Concrete Res. 2000;30(8):1215-23.

[204] Zibara H, Hooton RD, Thomas MDA, Stanish K. Influence of the C/S and C/A ratios of hydration products on the chloride ion binding capacity of lime-SF and lime-MK mixtures. Cement Concrete Res. 2008;38(3):422-6.

[205] Florea MVA, Brouwers HJH. Chloride binding related to hydration products Part I: Ordinary Portland Cement. Cement Concrete Res. 2012;42(2):282-90.

[206] Tritthart J. Chloride binding in cement .1. Investigations to determine the composition of porewater in hardened cement. Cement Concrete Res. 1989;19(4):586-94.

[207] Thomas MDA, Hooton RD, Scott A, Zibara H. The effect of supplementary

cementitious materials on chloride binding in hardened cement paste. Cement Concrete Res. 2012;42(1):1-7.

[208] Luo R, Cai YB, Wang CY, Huang XM. Study of chloride binding and diffusion in GGBS concrete. Cement Concrete Res. 2003;33(1):1-7.

[209] Delagrave A, Marchand J, Ollivier JP, Julien S, Hazrati K. Chloride binding capacity of various hydrated cement paste systems. Adv Cem Based Mater. 1997;6(1):28-35.

[210] Boddy A, Hooton RD, Gruber KA. Long-term testing of the chloride-penetration resistance of concrete containing high-reactivity metakaolin. Cement Concrete Res. 2001;31(5):759-65.

[211] Thomas MDA, Bamforth PB. Modelling chloride diffusion in concrete - Effect of fly ash and slag. Cement Concrete Res. 1999;29(4):487-95.

[212] Feldman RF, Chan GW, Brousseau RJ, Tumidajski PJ. Investigation of the Rapid Chloride Permeability Test. ACI Mater J. 1994;91(3):246-55.

[213] Snyder KA, Feng X, Keen BD, Mason TO. Estimating the electrical conductivity of cement paste pore solutions from OH^-, K^+ and Na^+ concentrations. Cement Concrete Res. 2003;33(6):793-8.

[214] Suryavanshi AK, Swamy RN, Cardew GE. Estimation of diffusion coefficients for chloride ion penetration into structural concrete[J]. ACI Mater J, 2003, 100(1): 441-449.

[215] Ahmed MS, Kayali O, Anderson W. Chloride penetration in binary and ternary blended cement concretes as measured by two different rapid methods. Cement Concrete Comp. 2008;30(7):576-82.

[216] Liu Z, Beaudoin JJ. The permeability of cement systems to chloride ingress and related test methods. Cement Concrete Aggr. 2000;22(1):16-23.

[217] NT Build 443. Concrete, hardened: accelerated chloride penetration[S]. Nordtest method, 1995.

[218] NT Build 208. Concrete, hardened: chloride content by volhard titration[S], Nordtest method, 1996.

[219] Glass GK, Wang Y, Buenfeld NR. An investigation of experimental methods used to determine free and total chloride contents. Cement Concrete Res. 1996;26(9):7.

[220] Mu S, De Schutter G, Ma BG. Non-steady state chloride diffusion in concrete with different crack densities. Mater Struct. 2013;46(1-2):123-33.

[221] Tang LP, Nilsson LO. Chloride binding-capacity and binding isotherms of OPC pastes and mortars. Cement Concrete Res. 1993;23(2):247-53.

[222] Sandberg P. Studies of chloride binding in concrete exposed in a marine environment. Cement Concrete Res. 1999;29(4):473-7.

[223] Beaudoin JJ, Ramachandran VS, Feldman RF. Interaction of chloride and C-S-H. Cement Concrete Res. 1990;20(6):875-83.

[224] Glass GK, Hassanein NM, Buenfeld NR. Neural network modelling of chloride binding. Mag Concrete Res. 1997;49(181):323-35.

[225] Rasheeduzzafar, Hussain SE, Alsaadoun SS. Effect of Cement Composition on Chloride Binding and Corrosion of Reinforcing Steel in Concrete. Cement Concrete Res. 1991;21(5):777-94.

[226] Suryavanshi AK, Scantlebury JD, Lyon SB. Mechanism of Friedel's salt formation in cements rich in tri-calcium aluminate. Cement Concrete Res. 1996;26(5):11.

[227] Tritthart J. Chloride Binding in Cement .2. The influence of the hydroxide concentration in the pore solution of hardened cement paste on chloride binding. Cement Concrete Res. 1989;19(5):683-91.

[228] Ipavec A, Vuk T, Gabrovsek R, Kaucic V. Chloride binding into hydrated blended cements: The influence of limestone and alkalinity. Cement Concrete Res. 2013;48:74-85.

[229] Cohen MD, Bentur A. Durability of Portland cement-silica fume pastes in magnesium and sodium sulfate solutions. ACI Mater J. 1988;85(3):10.

[230] Mehta P. Mechanism of expansion associated with ettringite formation. Cement Concrete Res. 1973;3(1):1-6.

[231] Lothenbach B, Bary B, Le Bescop P, Schmidt T, Leterrier N. Sulfate ingress in Portland cement. Cement Concrete Res. 2010;40(8):1211-25.

[232] Lawrence C. Sulphate attack on concrete. Mag Concrete Res. 1990;42(153):249-64.

[233] Gollop RS, Taylor HFW. Microstructural and microanalytical studies of sulfate attack .1. Ordinary Portland-cement paste. Cement Concrete Res. 1992;22(6):1027-38.

[234] Gollop RS, Taylor HFW. Microstructural and Microanalytical studies of sulfate attack .2. Sulfate-resisting Portland-cement ferrite composition and hydration chemistry. Cement Concrete Res. 1994;24(7):1347-58.

[235] Santhanam M, Cohen MD, Olek J. Sulfate attack research - whither now? Cement Concrete Res. 2001;31(6):845-51.

[236] Damidot D, Stronach S, Kindness A, Atkins M, Glasser FP. Thermodynamic investigation of the CaO-Al_2O_3-$CaCO_3$-H_2O closed-System at 25°C and the influence of Na_2O. Cement Concrete Res, 1994, 24(3):563-572.

[237] Santhanam M, Cohen MD, Olek J. Effects of gypsum formation on the performance

of cement mortars during external sulfate attack. Cement Concrete Res. 2003;33(3):325-32.

[238] Tian B, Cohen MD. Does gypsum formation during sulfate attack on concrete lead to expansion? Cement Concrete Res. 2000;30(1):117-23.

[239] Lee ST, Moon HY, Hooton RD, Kim JP. Effect of solution concentrations and replacement levels of metakaolin on the resistance of mortars exposed to magnesium sulfate solutions. Cement Concrete Res. 2005;35(7):1314-23.

[240] Khatri RP, Sirivivatnanon V, Yang JL. Role of permeability in sulphate attack. Cement Concrete Res. 1997;27(8):1179-89.

[241] Prasad J, Jain D, Ahuja A. Factors influencing the sulphate resistance of cement concrete and mortar. Asian Journal of Civil Engineering, 2006, 7(8): 259-268.

[242] Mangat PS, Elkhatib JM. Influence of initial curing on sulfate resistance of blended cement concrete. Cement Concrete Res. 1992;22(6):1089-100.

[243] Al-Dulaijan SU, Maslehuddin M, Al-Zahrani MM, Sharif AM, Shameem M, Ibrahim M. Sulfate resistance of plain and blended cements exposed to varying concentrations of sodium sulfate. Cement Concrete Comp. 2003;25(4-5):429-37.

[244] Monteiro PJM, Kurtis KE. Time to failure for concrete exposed to severe sulfate attack. Cement Concrete Res. 2003;33(7):987-93.

[245] Wang JG. Sulfate Attack on hardened cement paste. Cement Concrete Res. 1994;24(4):735-42.

[246] Nielsen J. Investigation of resistance of cement paste to sulfate attack[R]. Highway Research Record, 1966, (113): 114-117.

[247] Bonakdar A, Mobasher B. Multi-parameter study of external sulfate attack in blended cement materials. Constr Build Mater. 2010;24(1):61-70.

[248] Kurtis KE, Monteiro PJM, Mandanat SM. Empirical models to predict concrete expansion caused by sulfate attack. ACI Mater J. 2000;97(2):156-61.

[249] Oliveira I, Cavalaro SHP, Aguado A. New kinetic model to quantify the internal sulfate attack in concrete. Cement Concrete Res. 2013;43:95-104.

[250] Idiart AE, Lopez CM, Carol I. Chemo-mechanical analysis of concrete cracking and degradation due to external sulfate attack: A meso-scale model. Cement Concrete Comp. 2011;33(3):411-23.

[251] Maltais Y, Samson E, Marchand J. Predicting the durability of Portland cement systems in aggressive environments - laboratory validation. Cement Concrete Res. 2004;34(9):1579-89.

[252] ASTM C 1012. Standard test method for length change of hydraulic-cement mortars exposed to a sulfate solution, 1995.

[253] Gonzalez MA, Irassar EF. Ettringite formation in low C_3A Portland cement exposed to sodium sulfate solution. Cement Concrete Res. 1997;27(7):1061-71.

[254] Roziere E, Loukili A, El Hachem R, Grondin F. Durability of concrete exposed to leaching and external sulphate attacks. Cement Concrete Res. 2009;39(12):1188-98.

[255] Cohen MD, Bentur A. Durability of Portland cement-silica fume pastes in magnesium-sulfate and sodium-sulfate solutions. ACI Mater J. 1988;85(3):148-57.

[256] Bonen D, Cohen MD. Magnesium-sulfate attack on Portland-cement paste .1. microstructural analysis. Cement Concrete Res. 1992;22(1):169-80.

[257] Santhanam M, Cohen MD, Olek J. Mechanism of sulfate attack: A fresh look Part 2. Proposed mechanisms. Cement Concrete Res. 2003;33(3):341-6.

[258] Santhanam M, Cohen MD, Olek J. Mechanism of sulfate attack: A fresh look Part 1: Summary of experimental results. Cement Concrete Res. 2002;32(6):915-21.

[259] Hekal EE, Kishar E, Mostafa H. Magnesium sulfate attack on hardened blended cement pastes under different circumstances. Cement Concrete Res. 2002;32(9):1421-7.

[260] Biricik H, Akoz F, Turker F, Berktay I. Resistance to magnesium sulfate and sodium sulfate attack of mortars containing wheat straw ash. Cement Concrete Res. 2000;30(8):1189-97.

[261] El-Hachem R, Roziere E, Grondin F, Loukili A. New procedure to investigate external sulphate attack on cementitious materials. Cement Concrete Comp. 2012;34(3):357-64.

[262] Girardi F, Vaona W, Di Maggio R. Resistance of different types of concretes to cyclic sulfuric acid and sodium sulfate attack. Cement Concrete Comp. 2010;32(8):595-602.

[263] Poellmann H, Kuzel HJ, Wenda R. Solid-solution of ettringites.1. Incorporation of OH^- and CO_3^{2-} in $3CaO{\cdot}Al_2O_3{\cdot}3CaSO_4{\cdot}32H_2O$. Cement Concrete Res. 1990;20(6):941-7.

[264] Damidot D, Glasser FP. Thermodynamic investigation of the CaO-Al_2O_3-$CaSO_4$-H_2O system at 50°C and 85°C. Cement Concrete Res. 1992;22(6):1179-91.

[265] A. Skaropoulou KS, G. Kakali, S. Tsivilis. Use of mineral admixtures to improve the resistance of limestone cement concrete against thaumasite form of sulfate attack[J]. Cement and Concrete Composites, 2013, 37:267-275.

[266] Lee ST, Hooton RD, Jung HS, Park DH, Choi CS. Effect of limestone filler on the

deterioration of mortars and pastes exposed to sulfate solutions at ambient temperature. Cement Concrete Res. 2008;38(1):68-76.

[267] Ogawa S, Nozaki T, Yamada K, Hirao H, Hooton RD. Improvement on sulfate resistance of blended cement with high alumina slag. Cement Concrete Res. 2012;42(2):244-51.

[268] Brown PW, Hooton RD, Clark BA. The co-existence of thaumasite and ettringite in concrete exposed to magnesium sulfate, at room temperature and the influence of blast-furnace slag substitution on sulfate resistance. Cement Concrete Comp. 2003;25(8):939-45.

[269] Chatterji SK. Mechanism of sulphate expansion of hardened cement pastes[C]. The 5th international symposium on the chemistry of cement, 1968, Part III: 336-341.

[270] Zelic J, Krstulovic R, Tkalcec E, Krolo P. Durability of the hydrated limestone-silica fume Portland cement mortars under sulphate attack. Cement Concrete Res. 1999;29(6):819-26.

[271] Sotiriadis K, Nikolopoulou E, Tsivilis S. Sulfate resistance of limestone cement concrete exposed to combined chloride and sulfate environment at low temperature. Cement Concrete Comp. 2012;34(8):903-10.

[272] Bonen D, Cohen MD. Magnesium-sulfate attack on Portland-cement paste .2. Chemical and mineralogical analyses. Cement Concrete Res. 1992;22(4):707-18.

[273] Brown P, Hooton RD, Clark B. Microstructural changes in concretes with sulfate exposure. Cement Concrete Comp. 2004;26(8):993-9.

[274] Gollop RS, Taylor HFW. Microstructural and microanalytical studies of sulfate attack .4. Reactions of a slag cement paste with sodium and magnesium sulfate solutions. Cement Concrete Res. 1996;26(11):1013-1028.

[275] Turker F, Akoz F, Koral S, Yuzer N. Effects of magnesium sulfate concentration on the sulfate resistance of mortars with and without silica fume. Cement Concrete Res. 1997;27(2):205-14.

[276] Al-Dulaijan SU. Sulfate resistance of plain and blended cements exposed to magnesium sulfate solutions. Constr Build Mater. 2007;21(8):1792-802.

[277] Hoshno S, Yamada K, Hirao H. XRD/Rietveld analysis of the hydration and strength development of slag and limestone blended cement. J Adv Concr Technol. 2007;4(3):11.

[278] Matschei T, Lothenbach B, Glasser FP. The AFm phase in Portland cement. Cement Concrete Res. 2007;37(2):118-30.

Curriculum vitae

Personal data

First name	Kai
Last name	Wu
Date of birth	02/12/1987
Place of birth	Anqing city, Anhui province, China
Email	kai.wu@ugent.be wukaitj@gmail.com

Education

2011~2014	PhD: Civil Engineering The Magnel Laboratory for Concrete Research, Department of Structural Engineering, Faculty of Architecture and Engineering, Ghent University, Belgium
2010~2014	PhD: Materials Science Institute of Environmental Materials, School of Materials Science and Engineering, Tongji University, China
2007~2010	Master: Materials Science School of Materials Science and Engineering, Tongji University, China
2003~2007	Bachelor: Materials Science and Engineering School of Materials Science and Engineering, Tongji University, China

Publications

A1

Wu K., Shi H., Xu L., Guo X., De Schutter G., et al., Influence of heavy metals on the early hydration of calcium sulfoaluminate, Journal of Thermal Analysis and Calorimetry, 2013, 9, DOI: 10.1007/s10973-013-3376-9.

Wu K., Shi H., De Schutter G., Guo X., Ye G., Experimental study on alinite ecocement clinker preparation from municipal solid waste incineration fly ash, Materials and Structures, 2012, 45(8): 1145-1153.

Wu K., Shi H., De Schutter G., Guo X., Ye G., Preparation of Sulphoaluminate Cement-Based Material from Municipal Solid Waste Incineration (MSWI) Fly Ash, Advanced Science Letters, 2012, 5(1): 232-234.

Wu K., Shi H., De Schutter G., Guo X., Ye G., Preparation of alinite cement from municipal solid waste incineration fly ash, Cement and Concrete Composites, 2012, 34(3): 322-327.

Wu K., Shi H., Guo X., Utilization of municipal solid waste incineration fly ash for sulfoaluminate cement clinker production, Waste Management, 2011, 31(9-10): 2001-2008.

Under preparation

Wu K., Shi H., De Schutter G., Ye G., Gao Y., influence of ITZ and interconnection on the chloride migration of portland cement mortar, Advanced Concrete Technology, Under review.

Wu K., De Schutter G., Shi H., Ye G., Gao Y., Influence of ITZ and precondition on the transport properties of Ordinary cement-based materials, submitted

Wu K., De Schutter G., Shi H., Ye G., Gao Y., Microstructural modification of ITZ using blended materials: slag and limestone filler, submitted

Wu K., De Schutter G., Shi H., Ye G., Gao Y., Influence of ITZ on the degradation of concrete exposed to sulfate solution, submitted

A3

Wu K., Shi H., De Schutter G., Guo X., Ye G., Influence of aggregate on the chloride diffusion in the cement-based materials (in English), Journal of Chinese Ceramic Society, 2013,41(11): 56-62.

Shi H., Wu K., Guo X., Preparation of sulphoaluminate cement from MSWI fly ash and its hydration properties (in Chinese), Journal of Building Materials, 2011, (6): 730-735.

Wu K., Shi H., Guo X., Suphoaluminate cement prepared with Municipal Solid Waste Incineration Fly Ash and Its Hydration Heat Evolution Characteristics (in Chinese), Journal of Chinese Ceramic Society , 2011, 39(4): 670-675.

Shi H., Wu K., Deng K., Yuan F., Preparation of alinite cement clinker from MSWIfly ash (in Chinese), Journal of Chinese Ceramic Society, 2009, 37(7): 1092-1096.

Shi H., Wu K., Deng K., Yuan F., Experimental study on the preparation of alinite cement from MSWI fly ash (in Chinese), Cement, 2009, (8): 9-13.

Wu K., Shi H., Guo X., Formation process of alinite prepared from MSIW fly ash and its hydration properties (in Chinese), Cement Technology, 2010, (6): 23-27.

Conference and oral presentations

Shi H., Wu K., Guo X., Behaviour of calcium sulfoaluminate cement in the presence of heavy metals. First International Conference on Sulphoaluminate Cement: Materials and Engineering Technology, 23-24 October, 2013, Wuhan, China.

Wu K., De Schutter G., Shi H., Ye G., Gao Y., Influence of the interfacial transition zone on the chloride migration coefficient of Portland cement concrete, The First International Conference on Concrete Sustainability, 27-29 May 2013, Tokyo, Japan. (Best paper award).

Wu K., De Schutter G., Shi H., Ye G., Gao Y., Experimental study on the influence of ITZ on the durability of concrete made with different kinds of blended materials, 3rd Magnel lab seminar, 30 May 2013.

Wu K., De Schutter G., Shi H., Ye G., Gao Y., Effect of ITZ on durability of cement concrete exposed to chloride solutions, The Seventh

International Conference on Concrete under Severe Conditions-Environment and Loading, 23-25 Sep., 2013, Nanjing, China.

Wu K., Shi H., De Schutter G., Ye G., Gao Y., Study on properties of sulfoaluminate cement-based materials made from municipal solid waste incineration fly ash, The 2nd International Conference on Microstructural-related Durability of Cementitious Composites, 11-13 April, 2012, Amsterdam, the Netherlands.

Book

《Mixture design for the ready mixed concrete - Manual Info》 (2nd edition, In Chinese), Deng K., Wang H., Wu K., Beijing: China Building Materials Press, 2012.